12-18-2015

Flame Combustion Synthesis of Nano-materials for Catalysts and Sensors

Rishabh Jain
University of Connecticut - Storrs, rishabh.jain@uconn.edu

Flame Combustion Synthesis of Nano-materials for Catalysts and Sensors

Rishabh Jain, Ph.D.

University of Connecticut, 2015

Synthesis of functional nanomaterial thin films using a scalable flame combustion technique called Reactive Spray Deposition Technology (RSDT) was explored. Nanomaterials were used as sensing film for local gas monitoring and human breath analysis for medical diagnosis (different phases of WO_3) and catalysts for water-gas shift (WGS) reaction (Pt supported on ceria). Areas of application include: handheld portable devices for immediate breath composition monitoring, medical diagnosis, and environment monitoring (workplace, residence and automobile). Two case studies will be explained in detail: (1) acetone sensing in human breath for blood glucose monitoring and (2) NO_2 sensing for air quality monitoring. A study of the RSDT synthesis technique and control of crystal structure, porosity, and nanoparticle size will be demonstrated. The detailed study of acetone and NO_2 sensing mechanism will be explained in detail, including sensor performance and stability testing.

Flame Combustion Synthesis of Nano-materials for Catalysts and Sensors

Rishabh Jain

B.Tech., Haldia Institute of Technology, 2007

M.S., University of Southern California, 2009

A Dissertation

Submitted in Partial Fulfillment of the

Requirements for the Degree of

Doctor of Philosophy

at the

University of Connecticut

2015

2015

APPROVAL PAGE

Doctor of Philosophy Dissertation

Flame Combustion Synthesis of Nano-materials for Catalysts and Sensors

Presented by

Rishabh Jain, B.Tech., M.S.

Major Advisor _____

Radenka Maric

Associate Advisor _____

C. Barry Carter

Associate Advisor _____

S. Pamir Alpay

Associate Advisor _____

Yu Lei

Associate Advisor _____

Ken Furusaki

University of Connecticut

2015

To my parents

Ramesh Chand Jain and Anuradha Jain

and my sisters

Ekta Jain and Shweta Senthil Jain

ACKNOWLEDGEMENTS

I owe everything to my parents for their sacrifices in providing me the opportunity and platform to obtain a high quality education from kindergarten till doctorate studies. I can't thank them enough for their efforts in supporting me throughout their life. I am grateful to my sisters Ekta (baddijiji) and Shweta (little) for looking after me and supporting me as their little brother! It is the strong bonding between all five of us in my family which keeps me going!

I want to thank Prof. Radenka Maric, my Ph.D. advisor for showing faith in me and hiring me as a student in her research group at University of Connecticut. It is worth noting here that after I sent her a two page email explaining my compatibility with her research interests along with my résumé, she took <1 min. in deciding that she is going to hire me with full scholarship in her research group!

I want to express my gratitude to my advisory committee members: Prof. C. Barry Carter, Prof. S. Pamir Alpay, Prof. Y. Lei and Mr. K. Furusaki for agreeing to serve in my committee. Special thanks to Mr. Leonard Bonville who contributed countless hours of his time in reviewing my manuscripts and thesis for errors, grammatical mistakes and discrepancies.

I would also like to acknowledge University of Connecticut for the fall 2011 pre-doctoral fellowship, the UConn Graduate School for the fall 2014 doctoral dissertation fellowship and the fall 2014 travel award, the General Electric (GE) Company for the 2015 GE fellowship for innovation, the Phi Kappa Phi (PKP) society (University of Connecticut chapter) for the 2015 PKP graduate student award, and Alpha Sigma Mu (ASM) society (University of Connecticut chapter) for the honorary membership.

I want to thank my other colleagues in the Maric group (Justin, Haoran, Tony, Yang, Siwon, Abhinav, Ryan, Tim, Na and Thomas), colleagues at the Center for Clean Energy Engineering (Sapna, Venkata, Manoj, and Keling) and at the Institute of Materials Science (Louis, Kan, Austin, Greg, Matthew, Sriram, Arun, Bahareh, Haibo, Kuo-ting and Sarah) for making my time so enjoyable at UConn. Staff members at the machine shop (Mark, Joe and Daryl) and C2E2 (Sheila, Terry, Mark and Gary) were indispensable part of this journey.

I would also like to thank the entire NTK team at Nagoya, Japan (Ken san, Suzuki san, Kojima san, Taniguchi san, Ishikawa san, Sato san, Ueki san, Kida san and Ito san) for their hospitality during my visit to Japan in the summer of 2014.

I dedicate this thesis to my family.

TABLE OF CONTENTS

LIST OF FIGURES

LIST OF TABLES

LIST OF ACRONYMS

ACAC: acetylacetonate

AcAc: acetoacetate

AIDS: acquired immune deficiency symdrome

ASM: Alpha Sigma Mu

BET: Brunauer-Emmett-Teller

CCVD: combustion chemical vapor deposition

C2E2: Center for Clean Energy Engineering

CMOS: complementary metal oxide semiconductor

COPD: chronic obstructive pulmonary disease

CRDS: cavity ring down spectroscope/spectroscopy

CVD: chemical vapor deposition

DC: direct current

DEGME: diethylene glycol monobutyl ether

DFT: density functional theory

DOAS: differential optical absorption spectroscope/spectroscopy

DRIFTS: diffuse reflectance infrared Fourier transform spectroscope/spectroscopy

DSC: differential scanning coulorimeter/coulorimetry

ECS: Electrochemical Society

EDS: energy dispersive spectroscope/spectroscopy

EDX: energy dispersive X-ray spectroscope/spectroscopy

EFTEM: energy filtered transmission electron microscope/microscopy

ESEM: environmental scanning electron microscope/microscopy

ESR: electron spin resonance spectroscope/spectroscopy

ETEM: environmental transmission electron microscope/microscopy

FEG: field emission gun

FEI company: Field Electron and Ion company

FESEM: field emission scanning electron microscope/microscopy

FWHM: full width at half maximum

GC: gas chromatograph/chromatography

GE company: General Electric company

GFF: glass fiber filter

GHSV: gas hourly space velocity

HIV: Human immunodeficiency virus

HMDSO: hexamethyene disiloxane

HRTEM: high resolution transmission electron microscope/microscopy

HTS: high temperature shift

ICDD: International Center for Diffraction Data

ICP-OES: inductively coupled plasma optical emission spectroscope/spectroscopy

ID: internal diameter

IMS: Institute of Materials Science

JEOL: Japan Electron Optics Laboratory

LOD: limit of detection

LOPAP: long path absorption photometer/photometry

LTS: low temperature shift

MATLAB: matrix laboratory

MEMS: microelectromechanical systems

MFC: mass flow controller

MTS: medium temperature shift

MRS: Materials Research Society

MS: mass spectrometer/spectrometry

NASICON: natrium superionic conductor

NGK: Nippon (Japan) Gaishi (insulator) Kaisha (company)

NSA: near surface alloy

NSI: needle stick injuries

OD: outside diameter

OSC: oxygen storage capacity

OSHA: occupational safety and health administration

PEC: photo electrochemical cell

PECVD: plasma-enhance chemical vapor deposition

PEL: permissible exposure limit

PEMFC: proton exchange membrane fuel cell

PKP: Phi Kappa Phi

PMOD: photochemical metal-organic deposition

PPB: parts per billion

PPM: parts per million

PP: polypropylene

PVD: physical vapor deposition

PVDF: polyvinylidene fluoride

REMPI: resonance enhanced multi photon ionization

RSDT: reactive spray deposition technology

RTD: resistance temperature detector

RWGS: reverse water-gas shift

SADP: selected area diffraction pattern

SAXS: small angle X-ray scattering

SCAC: single crystal adsorption calorimeter/calorimetry

SDD: silicon drift detector

SEM: scanning electron microscope/microscopy

SIDS: sudden infant death syndrome

SiLi: silicon lithium detector

SMBG: self-monitoring blood glucose

SMSI: strong metal-support interaction

S/TEM: scanning/transmission electron microscope/microscopy

TCD: thermal conductivity detector

TEM: transmission electron microscope/microscopy

TGA: thermogravimetric analysis

THF: tetrahydrofuran

TPB: triple phase boundary

TPD: temeprature programmed desorption

TPR: temperature programmed reduction

UConn/UCT: University of Connecticut

UHV: ultra high vaccuum

UV: ultra violet

VOC: volatile organic compound

WGS: water-gas shift

XRD: X-ray diffraction

XEDS: X-ray energy dispersive spectroscope/spectroscopy

XPS: X-ray photoelectron spectroscope/spectroscopy

YSZ: yttria stabilized zirconia

LIST OF SYMBOLS

Å: angstrom

α: alfa (as in tetragonal α-WO_3)

β: beta (as in orthorhombic β-WO_3)

β: line broadening at half the maximum intensity (FWHM) for X-ray diffraction

°C: degree centigrade

c: centi

d: diameter of the crystal grain

d_{XRD}: average diameter of the crystal grain determined from XRD analysis

d_{TEM}: diameter of the crystal grain determined from TEM point analysis

d_{BET}: average diameter of the particle determined from BET analysis

δ: delta (as in triclinic δ-WO_3)

ε_0: permitivity of free space

ε_r: dielectric constant

ε: epsilon (as in monoclinic ε-WO_3)

e: electron charge

Ec: conduction band energy

E_F: fermi level energy

E_V: valence band energy

E_{vac}: oxygen vacancy formation energy

esu: electro static unit

F: Fahrenheit

γ: gamma (as in monoclinic γ-WO_3)

G: conductance

ΔG: Gibb's free energy change

$\Delta H°_c$: enthalpy of combustion

ΔH: enthalpy of reaction

h: hour

J: Joule

K_p: equilibrium constant

k_B: Boltzmann's constant

K: Kelvin

k: kilo

k: shape factor

λ_D: Debye length

L: litre

m: mili

min: minute

M: molar

m: meter

μ: micro

μ: electron mobility

μ: polarity

n: nano

n_c: carrier concentration

ή: molar flow rate

Λ : electron depletion layer or Schottky barrier

P: pressure

Φ: equivalence ratio

qV_s: height of band bending

R_a: resistance of air

R_g: resistance of analyte/gas

S: sensitivity/response

sq: square

s: second

T: temperature

τ: average diameter of the crystal grain determined from XRD analysis

θ: half Bragg's angle

V: volume

vol: volume

wt: weight

W: Watt

X: Pauling's electronegativity

This page has been intentionally kept blank

SECTION I:

INTRODUCTION

CHAPTER 1:

Reactive Spray Deposition Technology

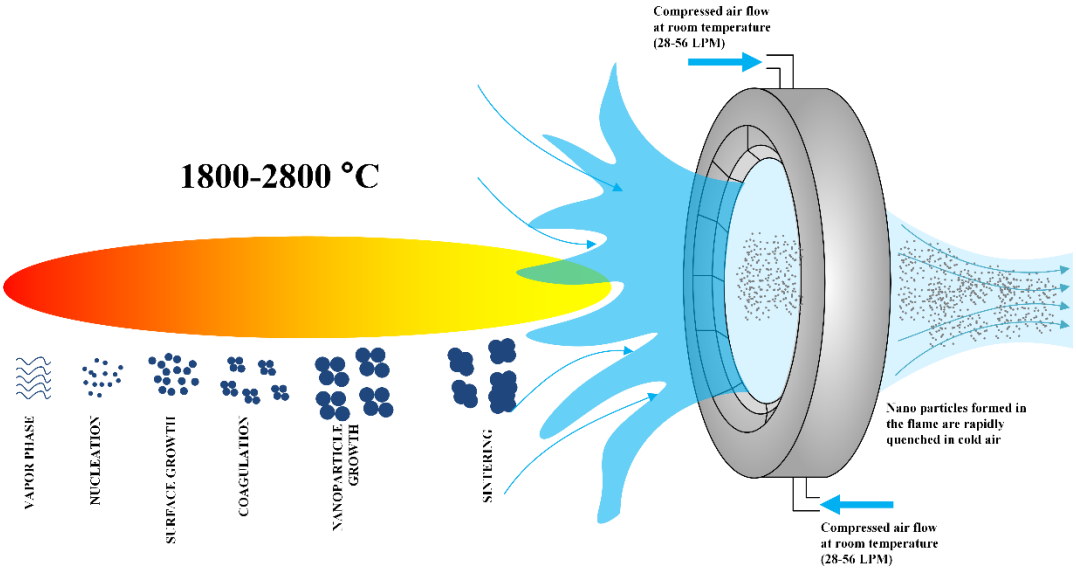

1.1 Introduction:

The identification of next-generation materials with improved properties has been a continuing quest for the human race, resulting in fascinating discoveries that have improved the quality of life. Over the last century, materials used in chemical processes have attracted significant attention due to their potential for broader impact on process improvement. Catalysts, which typically increase the reaction rate without being consumed, are the workhorses of such chemical processes, and offer a plethora of opportunities for discovery of improved materials due to essentially infinite combinations of elements in various compositions. For example, less than 5% of the estimated 160,000 ternary systems (three elements) have been investigated experimentally and the number drops to less than 1% for the estimated 4 million quaternary systems (four elements) [1]. With such limited knowledge and the vast chemical composition space still unexplored, the challenging question faced by engineers, chemists, and physicists is how to efficiently identify a limited number of algorithms to discover improved catalysts (materials) for a chemical process. Production of high value materials in the form of powders and thin coatings is a large multibillion dollar manufacturing enterprise. Specific functional materials have been synthesized by different processes including spray drying and pyrolysis [2] as well as combustion and plasma processing [3]. Flame based materials prepared in well controlled conditions are high surface area materials that can have some unique properties e.g. higher activity, lower melting point, good thermal stability, and faster mass transfer during catalysis [4]. There are a number of researchers working on the flame spray pyrolysis (FSP) technology for the synthesis of ceria [5, 6], alumina [7], titania [8], Pt [9], UO_2 [10], SnO_2 [11], IrO_2 [12], RuO_2 [12], WO_3 [4] etc. either in the manufacturing or in the modeling and optimization phase. While some of these material developments are in the research phase, materials like titania, silica and carbon black are already

in mass production. Fig. 1.1 shows some of the powder synthesis unit operations worldwide and also the products available to the end user which uses one or more components made by flame spray pyrolysis. Some of them are: carbon black as a reinforcement agent for tires [13], printer toners, pigments for cosmetics such as eyeliners, mascara and other beauty products [14], fumed silica as a thickening agents for body lotions and creams and also as an additive for food and beverage industry [15] and optical fibers [16], titania for the paint and cosmetic applications [17].

Fig. 1.1: Products for end users generated by flame based processes.

It is clear that most of the elements of the periodic table can be converted into oxides, metals or salts in the powder as well as thin film form [18, 19]. Reactive Spray Deposition Technology (RSDT), which can employ a broader selection of precursors compared to

conventional vapor-fed flame reactors [4,6,9,12,20–31] was developed by Maric et al. for synthesis of nanoparticle thin films with atomic-level precision and control of properties such as phase, structure, shape, particle size distribution (0.5–500 nm), density and porosity. The reactive spray synthesis of nanoparticles relies on combustion of a solvent which also acts as a fuel and aids in the decomposition of a precursor to form nanoparticles. RSDT provides adjustable process variables such as flame temperature, stoichiometry, residence time, and downstream quenching rates that coupled with solvent and metal precursor concentrations, affect particle: nucleation, growth, annealing, and oxidation. Since the droplets produced by this process are mostly sub-micron—due to energetic inputs of heat, pressure, and supercritical propane diluent—the precursor is confined to the nanoscale regime during formation. During the particle formation process the precursor heats up, decomposes, and then undergoes a phase transition to vapor followed by concurrent reduction of the metal ions to metal or metal oxides.

A picture of RSDT is shown in Fig. 1.2. RSDT is a single-step, open atmosphere flame process for synthesizing nanomaterials, whereby nanoparticles are synthesized in the reaction zone of the flame and directly deposited on the substrate as a film [6, 9] or collected as nanoparticles [24, 31], thereby eliminating the intermediate steps of filtration, drying, and calcination. No precursor or precursor solution waste is generated because the solvent is combusted in the flame, yielding CO_2 and H_2O. Precise control of particle size and crystallinity can be achieved by adjusting flame conditions [4], including precursor concentration, chemistry, and flow rate; length of reaction zone; equivalence ratio (stoichiometric oxidant and fuel flow rate to actual oxidant and fuel flow rate); quench air flow rate, and the substrate temperature [23]. In addition to these conditions, flame dynamics is also dependent on the solvent boiling point, enthalpy of combustion and the combustion nozzle geometry. The RSDT process bypasses

traditional wet chemical routes by simultaneously nucleating the catalyst on a support and sequential deposition of catalyst layer via gas-phase. Results from Roller et al. [9, 30] using RSDT, for Pt based electro-catalysts has clearly shown that the process can be adjusted to give precise control (<1 nm) of metallic nanoparticle diameters and film thickness (~100 nm to 10 μm), directly deposited onto Nafion® membranes. Results from Roller et al. [9, 30] using RSDT, for Pt based electro-catalysts has clearly shown that the process can be adjusted to give precise control (<1 nm) of metallic nanoparticle diameters and film thickness (~100 nm to 10 μm), directly deposited onto Nafion® membranes.

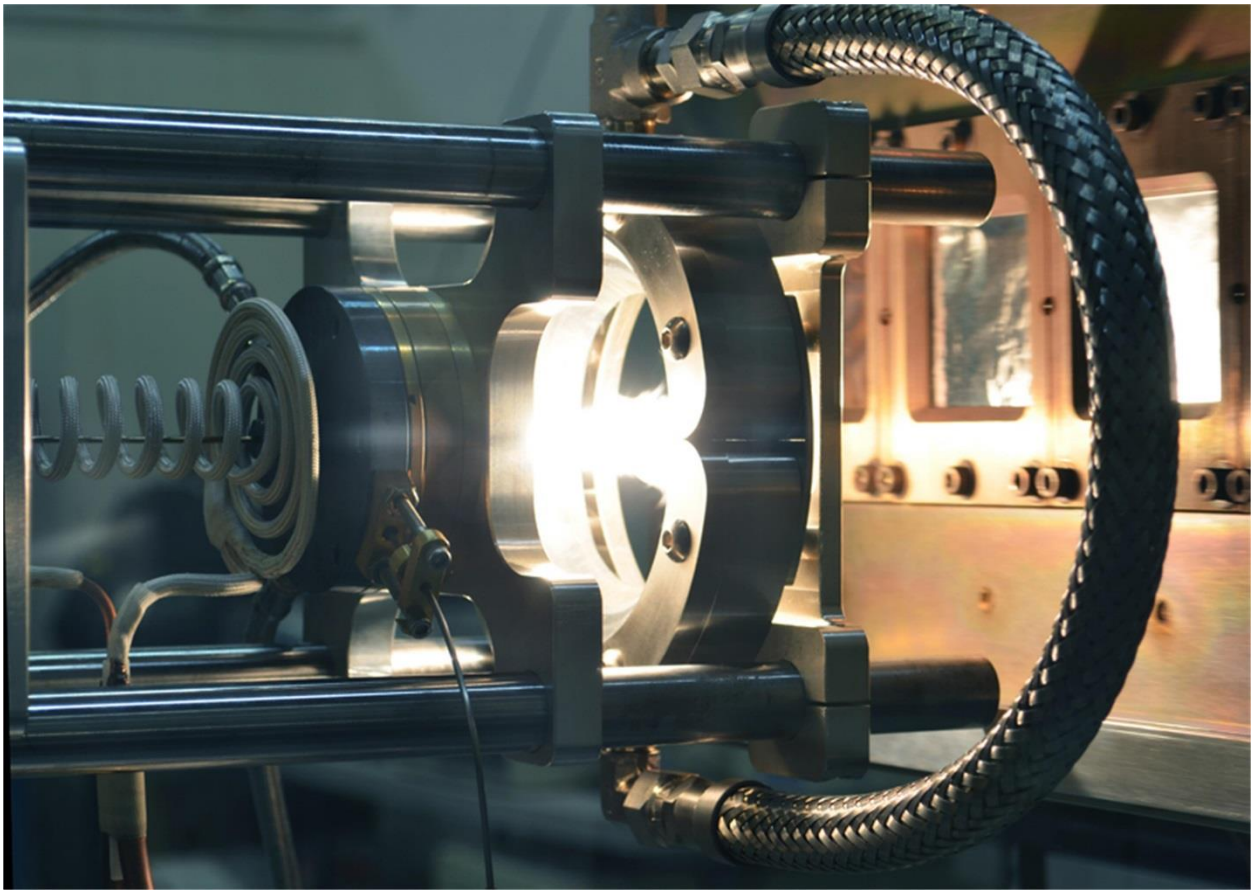

Fig. 1.2: The real time photograph of RSDT during a thin film deposition.

RSDT has several advantages over the traditional wet chemistry processes such as sol-gel, incipient wetness impregnation, co-precipitation, screen printing and drop coating especially for the synthesis of catalysts materials. Some of these advantages as compared to the traditional wet chemistry processes are as follows: (1) RSDT is a one step process in which the precursor solution is atomized to form a mist and decomposed in the flame to form fine sinterable particles and therefore it eliminates the steps of filtration, drying and calcination. (2) Better control on particle size and distribution and crystallinity can be achieved in RSDT by changing the flame conditions, precursor concentration and flow rate of gases. (3) Flame based materials are high surface area materials and can give some unique phases, good thermal stability and mass transfer during catalysis since these particles are exposed to rapid heating and cooling zones in the flame. (4) No solvent waste is produced in RSDT since the solvent is combusted in the flame.

1.2 Explanation of the RSDT components:

The fundamental design space for RSDT is given in table 1.1. A schematic of the RSDT is shown in with the role of its components in determining the structure and property of the synthesized material is shown in Fig. 1.6 and also described below:

1.2.1 Precursor concentration, temperature and pressure:

Precursors for the nanomaterial synthesized by RSDT are chosen according to their decomposition temperature and low vapor pressure [23]. Generally acetates, nitrates and acetylacetonates are the preferred choice because their decomposition temperature is less than 500°C. They are dissolved in a non-aqueous and high enthalpy solvent such as xylene ($\Delta H^{\circ}_{c,\ 298K}$ = -4301 kJ/mol), acetone ($\Delta H^{\circ}_{c,\ 298K}$ = -1658 kJ/mol), tetrahydrofuran (THF) ($\Delta H^{\circ}_{c,\ 298K}$ = -2501 kJ/mol), or diethylene glycol monobutyl ether (DEGME) ($\Delta H^{\circ}_{c,\ 298K}$ = -5234 kJ/mol).

A concentration of 3–20 mmol/L is maintained to avoid precipitation in the capillary. Lower concentration, in addition to lower flow rate, favors the formation of fully dense coatings. Adding 20–25 wt% liquefied propane ($\Delta H^{\circ}_{c,\ 298K}$ = -2202 kJ/mol) in the precursor solution, in addition to creating a pressure drop of 130 psi by means of a reducer and temperature of 60°C by an induction heater, confines it in the supercritical regime. Hence, droplets of (10–20 μm) in diameter are formed at the point of exit of the capillary tube which is a required parameter for the formation of nanoparticles in the flame.

1.2.2 Precursor solution flow rate:

A flow rate of 4 mL/min of the precursor solution is maintained to obtain a pressure drop of around 130 psi at the point of exit. The flow rate of the solution is one of the determining factor for the morphology of the deposited film (either fully dense at low flow rate or porous at high flow rate).

1.2.3 Tip O_2 flow rate and equivalence ratio:

Oxygen is directed in a co-flow pattern with respect to the precursor solution which results in an equivalence ratio [32] defined as follows:

$$\varphi = \left(\frac{\dot{n}_{oxidant}}{\dot{n}_{fuel}}\right)_{stoichiometric} / \left(\frac{\dot{n}_{oxidant}}{\dot{n}_{fuel}}\right)_{real} \quad \text{(E1.1)}$$

Where $\dot{n}_{oxidant}$ and $\dot{n}_{fuel}$ are the molar flow rate of oxygen and precursor solution (fuel) respectively. Equivalence ratio determines the oxidation or reduction condition of the flame since φ >1 (reducing flame), φ = 1 (stoichiometric flame), φ <1 (oxidizing flame). While calculating the value of φ, consideration for the entrainment of atmospheric O_2 must be made.

1.2.4 Pilot O_2 and CH_4:

A set of six flames comprised of a premixed CH_4 and O_2, surrounds the capillary tube concentrically. The pilot light keeps the flame burning and is also responsible for the control of temperature at the tip of the needle. The position of the capillary tube with respect to the combustion nozzle is adjusted in order to prevent overheating of the tip and formation of buildup which can block the capillary opening, and distort the main flame.

1.2.5 Standoff distance:

Standoff distance is defined as the distance between the combustion nozzle and the substrate. This distance is adjusted on the basis of the desired temperature of the substrate for denser film (high temperature), porous film (low temperature) or powder collection (room temperature). Standoff distance also dictates the collection efficiency of the nanoparticles on the substrate.

1.2.6 Air quench flow rate and position with respect to flame:

The air quench is a circular metallic ring with an internal annular chamber as shown in Fig. 1.3. The compressed air at room temperature enters the two nozzles and is directed towards that chamber. The chamber has a narrow ring nozzle through which the air adopts the coanda profile and flows along the angled surface of the air quench. This also creates a low pressure region behind the air quench causing the entrainment of the surrounding air into the primary air stream. A 360° cone of air is formed which cools the nanoparticles instantly and prevents growth, agglomeration, and sintering, thereby keeping the particle size small, maintaining high surface area. The distance between the combustion nozzle and the air quench is the reaction zone, and the length of the reaction zone is proportional to the residence time of the nanoparticles in the zone. The reaction zone is the region where all the major reactions takes place in the flame.

Here the combustion of the precursor takes place followed by the formation of the nanoparticles. This is possible because formation of the particles in the flame occurs through the following steps: (1) vapor, (2) particle nucleation, (3) surface growth, (4) coagulation, (5) nanoparticle growth, (6) sintering. Adjusting the length of the reaction zone and the flow rate of compressed air gives conditions to obtain an assortment of phases and structures of nanomaterials. One or more of the last steps of the combustion products formation can be prevented by reducing the length of the reaction zone. Position of the air quench and the air flow rate determines the point at which no further surface growth, coagulation, nanoparticle growth, and sintering of the particle is desirable and the particles are collected as it is on the substrate holder. This rapid cooling effect also causes a rapid decrease in the temperature of nanoparticles from about 500°C to 30°C in 7 s. This nanoparticle quenching effect causes the formation of some metastable phases [4]. Various configurations of RSDT is shown in Fig. 1.5.

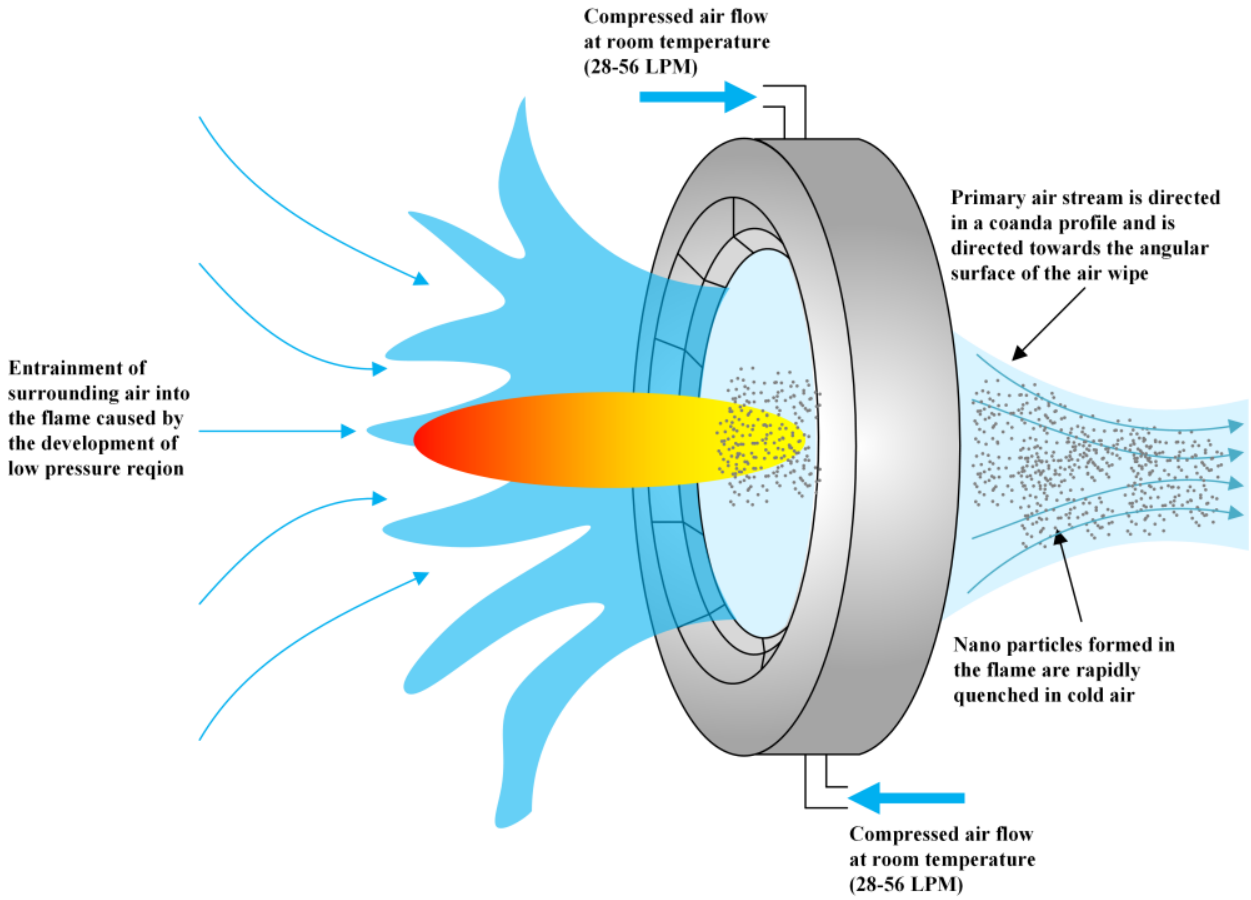

Fig. 1.3: Schematic of air quenching mechanism and the coanada profile in RSDT.

1.2.7 Slurry flow rate and concentration:

In catalysis application for the synthesis of noble metal supported oxides, an oxide slurry is prepared and sprayed perpendicularly to the flame by means of a pair of spray nozzles. Nanoparticles generated from the flame are condensed on the slurry particles which can be collected on the substrate of choice. The flow rate and concentration of the oxide is maintained according to the desired loading value of noble metal. A binder such as Nafion™ or polyvinylidene fluoride (PVDF) can be added to the slurry for proper adhesion of the film. This technology enables independent control of the support, binder and metal for the synthesis of the catalysts [6, 30].

1.2.8 Substrate motion pattern:

Substrates are mounted on a substrate holder as shown in Fig. 1.4. This can be placed on a platform which can be moved in the x-y-z pattern, and can be programmed using a MATLAB code. This allows for a large (400 sq. cm) and uniform deposition area.

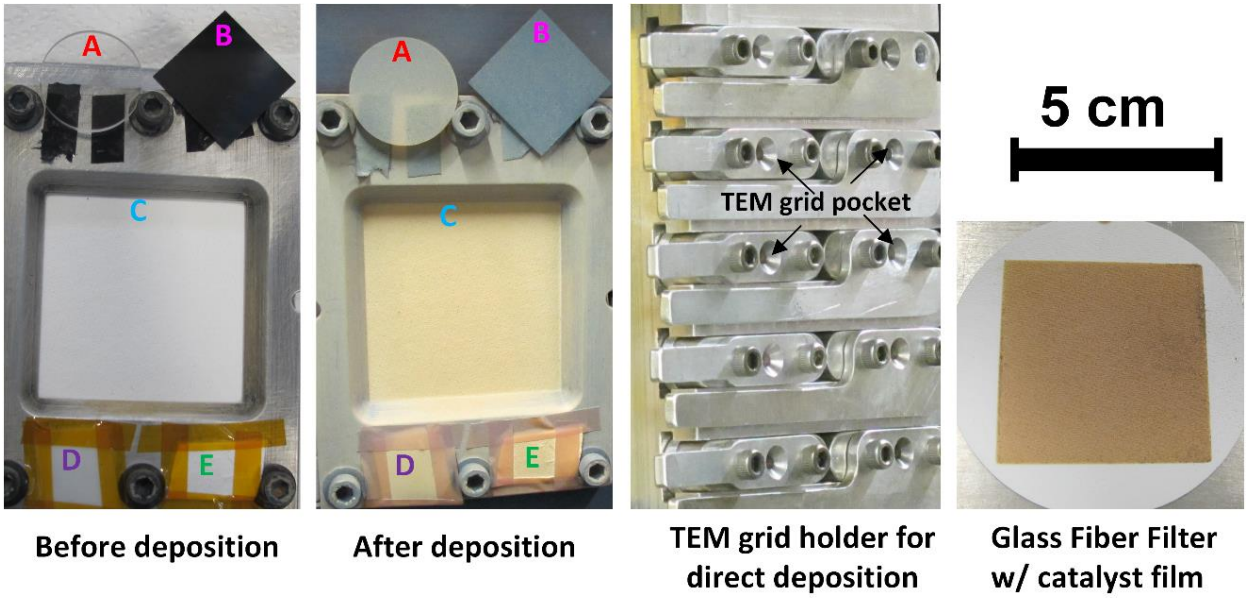

Fig. 1.4: Arrangement of substrates on the deposition platform in RSDT. A: no background quartz disc, B: conductive glassy carbon, C: glass fiber filter (GFF), D: polypropylene coupon, E: GFF coupon.

Table 1.1: Synthesis parameters in RSDT with their typical values.

	Component	Function	Typical range
Chemical parameters	**Precursor**	Decomposition to produce nanoparticles. Low decomposition temperature precursors (<500°C) are preferred.	platinum acetylacetonate (Pt acac) :5–20 mmol/L tungsten hexacarbonyl (WO_3): 5–10 mmol/L
	Solvent	Determines flame luminosity and temperature. Non aqueous, high enthalpy solvent(s) are used.	xylene, acetone, tetrahydrofuran, diethylene glycol monobutyl ether
	Propane content	Maintains the pressure drop at the point of exit of the precursor solution to the atmosphere and reduces the droplet size.	17–22 wt%

	Component	Function	Typical range
	Slurry flow rate and concentration	Maintains concentration of support material vs flame sprayed (e.g. Pt supported on ceria)	1.5 mL/min
Physical parameters	**Precursor solution flow rate**	Determines the deposition rate, film density, pressure drop, flame length, and particle residence time in the combustion zone.	4–6 mL/min
	Air quench flow rate	Determines the preference for a particular phase (e.g. ε-WO_3 vs γ-WO_3), crystallinity and momentum for the flow of secondary spray. It also influences the mixing of the phases.	0–100 L/min
	Pilot O_2 and CH_4 flow rate	Ignition source for the flame and the amount of heat produced at the tip.	O_2: 0.55 L/min; CH_4: 0.42 L/min
	Tip O_2 flow rate	Equivalence ratio (oxidizing, reducing or stoichiometric flame), flame temperature and flame turbulence.	5–7 L/min
	Combustion nozzle to air quench ring distance	Length of reaction zone. Particle growth halts at the point of air quench. It also determines the crystallinity of the deposited film	10–14 cm
	Standoff distance	Combustion nozzle to substrate distance. Determines substrate temperature and residence time of particles in flame.	16–18 cm
	Substrate holder	A variety of materials and configurations can be used for mounting substrates depending upon the desired temperature of deposition (e.g. water cooled or back heated substrate holder)	20–1000°C
	Motion of the substrate platform	Enables wide and uniform deposition area (400 sq. cm.)	2–400 sq. cm.

Based on the above parameters and, the combustion nozzle can be modified to suit a particular application's need. This has been drawn in the Fig 1.4.

1.2.9 Quartz shroud:

This method of constraining the flame was suggested by Waser et al. [33]. Enclosing a quartz tube (shroud) around the flame (shrouding) significantly reduces the

entrainment of atmospheric oxygen towards the flame and causes the equivalence ratio to shift towards higher value (Φ>1). Modification in the quartz tube can also be made to enable the controlled supply of oxygen by which a precise control of the equivalence ratio can be achieved [33]. This method also increases the particle collection efficiency and sintering of the particles. Adding or removing the air quench mechanism at the end of the quartz shroud provides an additional option to obtain porous film with micron size particles or fully dense film respectively.

1.2.10 Substrate cooling and heating:

Substrate temperature in the RSDT can be varied from 20–1200°C by various methods. This provides the possibility for using a diverse set of substrates depending upon their melting point. Some of the lower melting point substrates used for the deposition are Nafion® membranes with thickness from ~100 nm to 10 μm, polypropylene, teflon, and glass fiber filter. The substrate cooling is achieved by using a hollow stainless steel block which is connected to a water chiller. By this arrangement achieving the substrate temperature as low as 20°C is possible. Since RSDT is an open atmosphere process, the dew point for the atmosphere is very important to avoid any water condensation on the substrate. Lower temperature also enables the collection of nano-powder which is useful for the BET surface area measurements. Similarly, for higher temperature operation, a ceramic substrate is used. The high temperature can be obtained by either impinging the flame directly on the substrate or by using a substrate heater.

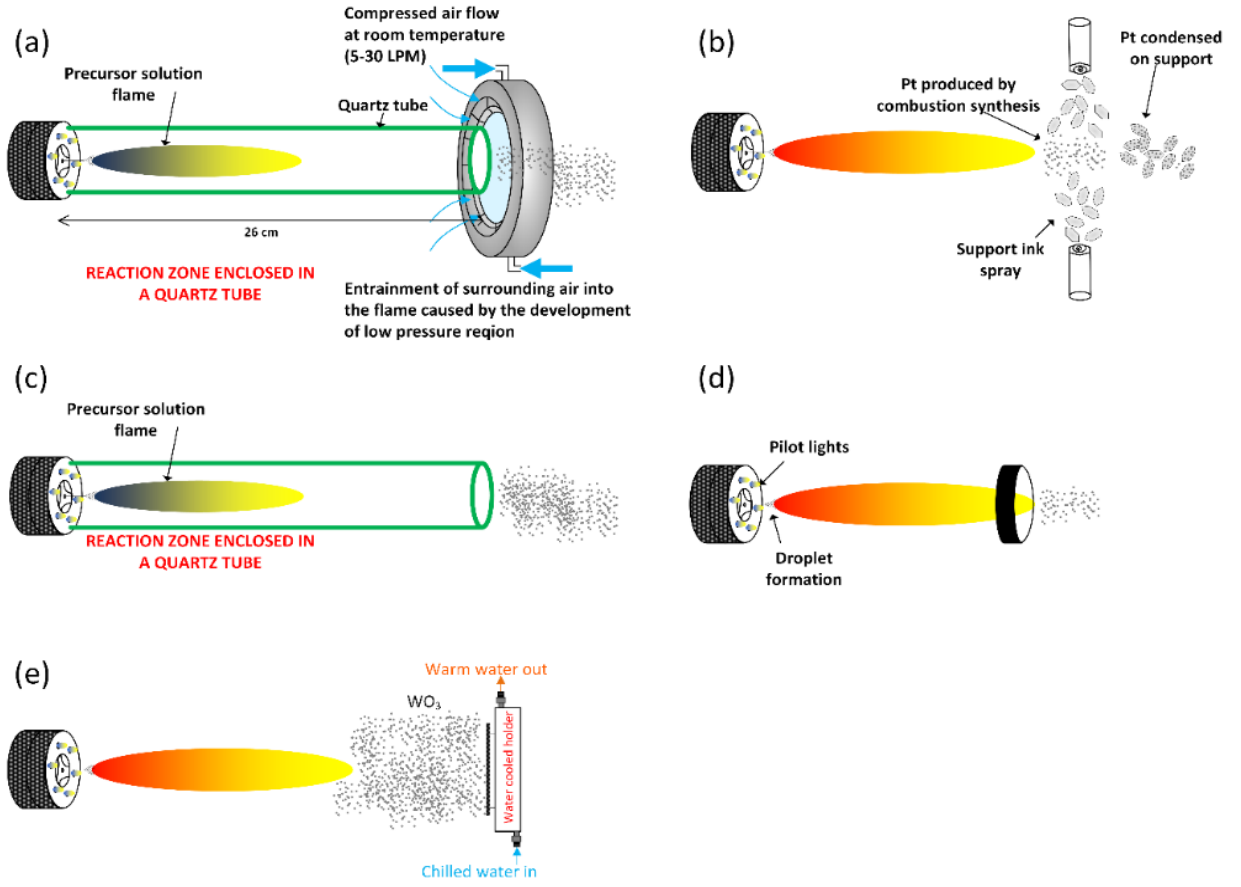

Fig. 1.5: Different configurations of RSDT: (a) for porous but micron size particles film, (b) use of secondary spray to deposited nanoparticles on support, (c) for dense film, (d) option to change the length of the reaction zone (distance between combustion nozzle and air quench, (e) deposition on a chilled substrate to enable the collection of nanopowder.

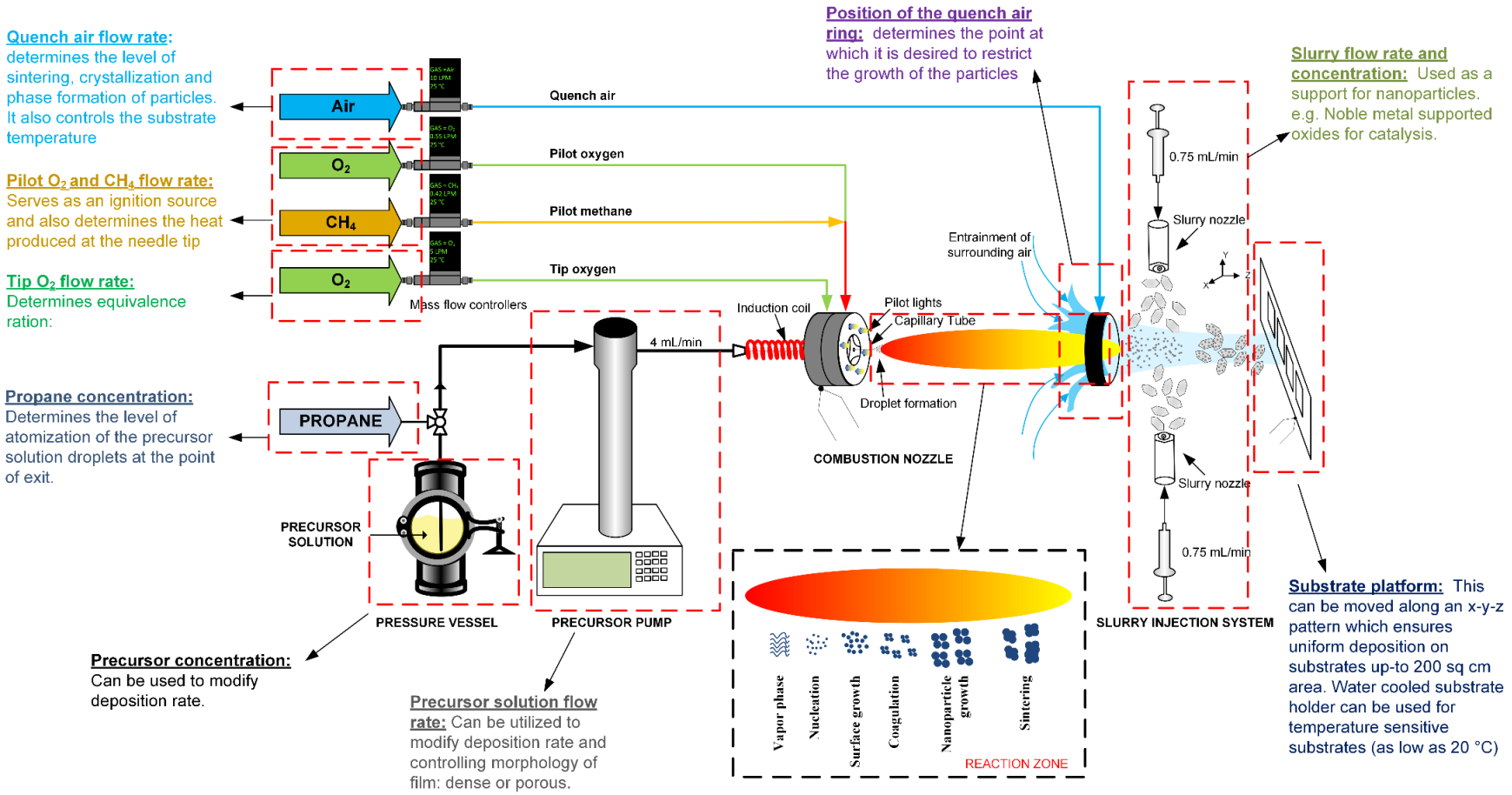

Fig. 1.6: Schematic of Reactive Spray Deposition Technology with the function of each component explained in details.

1.3 References:

[1] J.R. Rodgers, D. Cebon, Materials Informatics, MRS Bulletin. 31 (12) (2006) 975-980.

[2] C.J. King Dean, Spray Drying Handbook, Fourth Edition By K. Masters, Halstead Press, New York, 1985, 696 pp, AIChE Journal. 33 (1) (1987) 172-173.

[3] L. Pawlowski, The Science and Engineering of Thermal Spray Coatings, Second Edition ed., John Wiley & Sons, Ltd, 2008.

[4] R. Jain, Y. Wang, R. Maric, Tuning of WO_3 Phase Transformation and Structural Modification by Reactive Spray Deposition Technology, Journal of Nanotechnology and Smart Materials. 1 (2014) 1-7.

[5] R. Jain, A.S. Poyraz, D.P. Gamliel, J. Valla, S.L. Suib, R. Maric, Comparative study for low temperature water-gas shift reaction on Pt/ceria catalysts: Role of different ceria supports, Applied Catalysis A: General. 507 (2015) 1-13.

[6] R. Jain, R. Maric, Synthesis of nano-Pt onto ceria support as catalyst for water-gas shift reaction by Reactive Spray Deposition Technology, Applied Catalysis A: General. 475 (2014) 461-468.

[7] J. Huang, Y. Liu, J. Yuan, H. Li, Al/Al_2O_3 Composite Coating Deposited by Flame Spraying for Marine Applications: Alumina Skeleton Enhances Anti-Corrosion and Wear Performances, Journal of Thermal Spray Technology. 23 (4) (2014) 676-683.

[8] W.J. Stark, S.E. Pratsinis, A. Baiker, Flame Made Titania/Silica Epoxidation Catalysts, Journal of Catalysis. 203 (2) (2001) 516-524.

[9] J.M. Roller, R. Neagu, F. Orfino, R. Maric, Supported and unsupported platinum catalysts prepared by a one-step dry deposition method and their oxygen reduction reactivity in acidic media, Journal of Materials Science. 47 (11) (2012) 4604-4611.

[10] E.J. Lahoda, Two step dry UO_2 production process utilizing a positive sealing valve means between steps, US Patent. US 12/465,729(US7824640 B1) (2010).

[11] L. Mädler, T. Sahm, A. Gurlo, J.-. Grunwaldt, N. Barsan, U. Weimar, S.E. Pratsinis, Sensing low concentrations of CO using flame-spray-made Pt/SnO_2 nanoparticles, Journal of Nanoparticle Research. 8 (6) (2006) 783-796.

[12] J.M. Roller, J. Arellano-Jiménez, R. Jain, H. Yu, R. Maric, C.B. Carter, Processing, Activity and Microstructure of Oxygen Evolution Anodes Prepared by a Dry and Direct Deposition Technique, ECS Transactions. 45 (21) (2013) 97-106.

[13] A. Henni, Top 10 Catalysts Companies, http://www.arabianoilandgas.com/article-9496-top-10-catalysts-companies/1/print/#.UYZyybW-2uI. 2013 (May/05) (2011).

[14] Food and Drug Administration, Listing of Color Additives Subject to Certification, Code of Federal Regulations Title 21. Volume 1(21CFR74.2052) (2015) 74.2052 D&C Black No. 2.

[15] T. Johannessen, J.R. Jensen, M. Mosleh, J. Johansen, U. Quaade, H. Livbjerg, Flame Synthesis of Nanoparticles: Applications in Catalysis and Product/Process Engineering, Chemical Engineering Research and Design. 82 (11) (2004) 1444-1452.

[16] S.A. Khan, M.A. Maruca, I.M. Plitz, Rheology of fumed silica dispersions for fiber-optic cables, Polymer Engineering & Science. 31 (24) (1991) 1701-1707.

[17] H.K. Kammler, L. Mädler, S.E. Pratsinis, Flame Synthesis of Nanoparticles, Chemical Engineering & Technology. 24 (6) (2001) 583-596.

[18] W.Y. Teoh, R. Amal, L. Mädler, Flame spray pyrolysis: An enabling technology for nanoparticles design and fabrication, Nanoscale. 2(8) (2010) 1324-1347.

[19] K. Wegner, B. Schimmoeller, B. Thiebaut, C. Fernandez, T.N. Rao, Pilot Plants for Industrial Nanoparticle Production by Flame Spray Pyrolysis, KONA Powder and Particle Journal. 29 (2011) 251-265.

[20] K. Fatih, R. Neagu, V. Alazate, V. Neburchilov, R. Maric, W. Haijiang, Activity of Pt-Sn Catalyst Prepared by Reactive Spray Deposition Technology for Ethanol Electro-oxidation, ECS Transactions. 25 (1) (2009) 1177-1183.

[21] R. Hui, R. Maric, C. Decès-Petit, E. Styles, W. Qu, X. Zhang, J. Roller, S. Yick, D. Ghosh, K. Sakata, M. Kenji, Proton conduction in ceria-doped $Ba_2In_2O_5$ nanocrystalline ceramic at low temperature, Journal of Power Sources. 161 (1) (2006) 40-46.

[22] R. Maric, C. Deces-Petit, R. Hui, X. Zhang, D. Ghosh, K. Sakata, M. Kenji, Preparation and Characterization of Nanocrystalline $Ba_2In_{2-x}M_xO_{5-\delta}$ $(M = Ce, Zr)$, Journal of Electroceramic Society. 153 (8) (2006) A1505-A1510.

[23] R. Maric, J. Roller, R. Neagu, Flame-Based Technologies and Reactive Spray Deposition Technology for Low-Temperature Solid Oxide Fuel Cells: Technical and Economic Aspects, Journal of Thermal Spray Technology. 20 (4) (2011) 696-719.

[24] R. Maric, M. Oljaca, B. Vukasinovic, A.T. Hunt, Synthesis of Oxide Nanopowders in NanoSpraySM Diffusion Flames, Materials and Manufacturing Processes. 19 (6) (2004) 1143-1156.

[25] R. Maric, J.M. Roller, R. Neagu, K. Fatih, A. Tuck, Low Pt Thin Cathode Layer Catalyst Layer by Reactive Spray Deposition Technology, ECS Transactions. 12 (1) (2008) 59-63.

[26] R. Maric, R. Neagu, Y. Zhang-Steenwinkel, F.P.F. van Berkel, B. Rietveld, Reactive Spray Deposition Technology – An one-step deposition technique for Solid Oxide Fuel Cell barrier layers, Journal of Power Sources. 195 (24) (2010) 8198-8201.

[27] R. Maric, K. Furusaki, D. Nishijima, R. Neagu, Thin Film Low Temperature Solid Oxide Fuel Cell (LTSOFC) by Reactive Spray Deposition Technology (RSDT), ECS Transactions. 35 (1) (2011) 473-481.

[28] R. Neagu, X. Zhang, R. Maric, J.M. Roller, Characterisation and Performance of SOFC Components made by Reactive Spray Deposition Technology, ECS Transactions. 25 (2) (2009) 2481-2486.

[29] R. Nédélec, R. Neagu, S. Uhlenbruck, R. Maric, D. Sebold, H.-. Buchkremer, D. Stöver, Gas phase deposition of diffusion barriers for metal substrates in solid oxide fuel cells, Surface & Coatings Technology. 205 (16) (2011) 3999-4004.

[30] J.M. Roller, M.J. Arellano-Jiménez, H. Yu, R. Jain, C.B. Carter, R. Maric, Catalyst nanoscale assembly from the vapor phase on corrosion resistant supports, Electrochimica Acta. 107 (0) (2013) 632-655.

[31] Z. Wang, R. Hui, N. Bogdanovic, Z. Tang, S. Yick, Y. Xie, I. Yaroslavski, A. Burgess, R. Maric, D. Ghosh, Plasma spray synthesis of ultra-fine YSZ powder, Journal of Power Sources. 170 (1) (2007) 145-149.

[32] S.R. Turns, An Introduction to Combustion: Concepts and Applications, 3rd ed., McGraw-Hill, New York, 2012.

[33] O. Waser, A.J. Groehn, M.L. Eggersdorfer, S.E. Pratsinis, Air Entrainment During Flame Aerosol Synthesis of Nanoparticles, Aerosol Science and Technology. 48 (11) (2014) 1195-1206.

CHAPTER 2:

Catalysts for Water-Gas Shift Reaction

2.1 Water-gas shift reaction:

Water gas was discovered by Italian physicist Felice Fontana in 1780. Water gas was made in England from 1828 by blowing steam through white-hot coke maintained at 1000°C. However the major limitation of that process was the additional processing step required (Cu liquor scrubbing) to remove CO. It was Mond Langer who patented [1] the WGS reaction in 1888, and thereafter it was commercially used for the generation of H_2 as a raw material for the Haber process for production of ammonia.

Applications of water-gas shift (WGS) and reverse water-gas shift (RWGS) reactions are generally found in the large-scale industrial processes, such as ammonia/urea production (approx. 202 million tonnes/year—estimated $75 billion/year industry) and methanol synthesis (approx. 100 million metric tons/year—estimated $36 billion/year industry). WGS reaction is also a critical component in hydrocarbon reforming and Fischer-Tropsch synthesis [2-5], automotive exhaust catalysis [6], H_2 production for fuel cells [7, 8], and CO_2 capture from power plants [9]. WGS catalysts is especially important for automotive applications because of various reasons. Exhaust of a vehicle equipped with an internal combustion engine, has CO_2, H_2O and N_2. However there is a possibility that the combustion is fuel rich (little air) because of the fault in the car's onboard computer and the oxygen sensor, which causes the formation of poisonous CO [10]. With the water-gas shift, CO concentration can be reduced from 10% to <0.1% and at the same time hydrogen (H_2) can be produced which can be utilized in a wide array of applications including Proton exchange membrane fuel cells (PEMFC). CO can be converted using the water-gas shift (WGS) reaction ($CO\ (g) + H_2O\ (g) \rightarrow CO_2\ (g) + H_2\ (g)$) in the presence of a catalyst to yield H_2 and CO_2. Good catalytic systems (in terms of stability, reactivity, and selectivity) are known for some of these processes. Yet, the fundamental understanding of what

makes a good catalyst, how it acts in the catalytic process, and why one catalytic system is superior to another is often ill defined [11]. Interest in WGS reaction has grown exponentially in the past decade as a result of the advancement in fuel cell technology and the need to develop small-scale fuel processors [12]. Fuel cell technology has the potential to revolutionize the existing transportation system as well as fulfill the most rigorous exhaust gas emission requirements [13]. Fuel cells require H_2 which is obtained by reforming synthesis gas (mixture of CO, and H_2). When hydrogen is used in the fuel cell operation, the WGS catalyst should be both active and stable in cyclic operation. The presence of CO as low as 30 ppm in H_2 can poison the Pt electrode of a fuel cell resulting in complete shutdown [14].

Novel methods for preparation of WGS catalysts have emerged in the past few years due to the rapid development of fuel cell technology and a need for small scale and mobile PEMFC systems in vehicles [15].

A review paper by Ratnasamy et al. [16] describes three types of WGS catalysts that are currently available in the market as shown in the flow chart in Fig. 2.2. The high temperature shift (HTS) catalysts which employs iron-oxide catalysts with alumina and chromium as promoters has a reaction temperature in the range of 400–500°C. In this case the rate is proportional to the first order of the partial pressure of CO. The second one is the low temperature shift (LTS) catalyst consisting of copper-zinc oxide and is used at relatively low temperature range of 190–250°C. Equilibrium constant for WGS reaction increases with the decrease in temperature as shown in Fig. 2.1. Hence low temperature is thermodynamically favorable for WGS reaction. Here the rate is proportional to zeroth order of the partial pressure of CO.

High temperature shift catalysts: $r \propto [PCO]^1$

Low temperature shift catalysts: catalysts, r $\propto [PCO]^0$

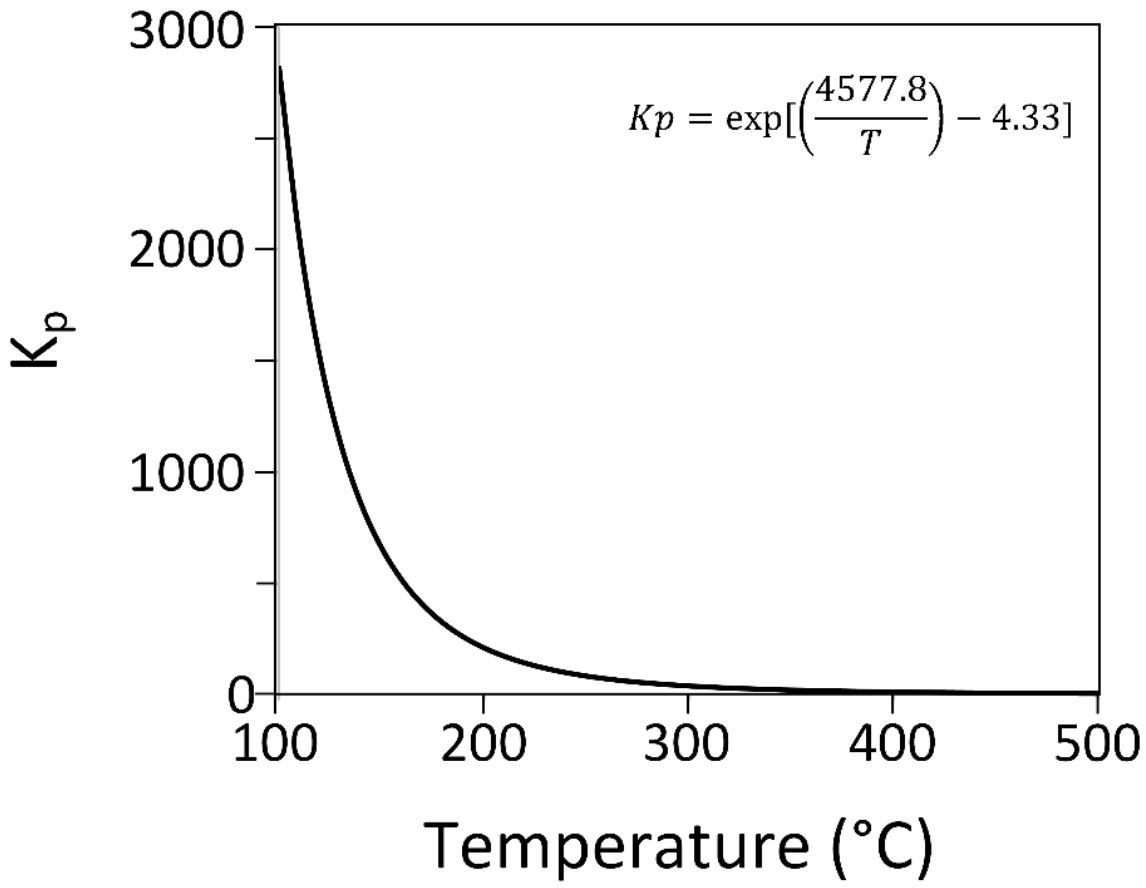

Fig. 2.1: Relationship between equilibrium constant (K_p) and temperature for the water-gas shift reaction.

The obvious advantages of LTS over HTS is the low temperature of operation and low volume requirement. The third type of catalyst can be called medium temperature shift (MTS) and they operate in the temperature range from 275–350°C. These catalysts are the LTS which are mixed with HTS to slightly increase the temperature of reaction. In addition to these, there are WGS catalysts which are sulfur tolerant, such as cobalt and molybdenum sulfides based. Catalysts of this type can be used when the reaction gas contains sulfur especially in the exhaust of the vehicles burning low quality gasoline.

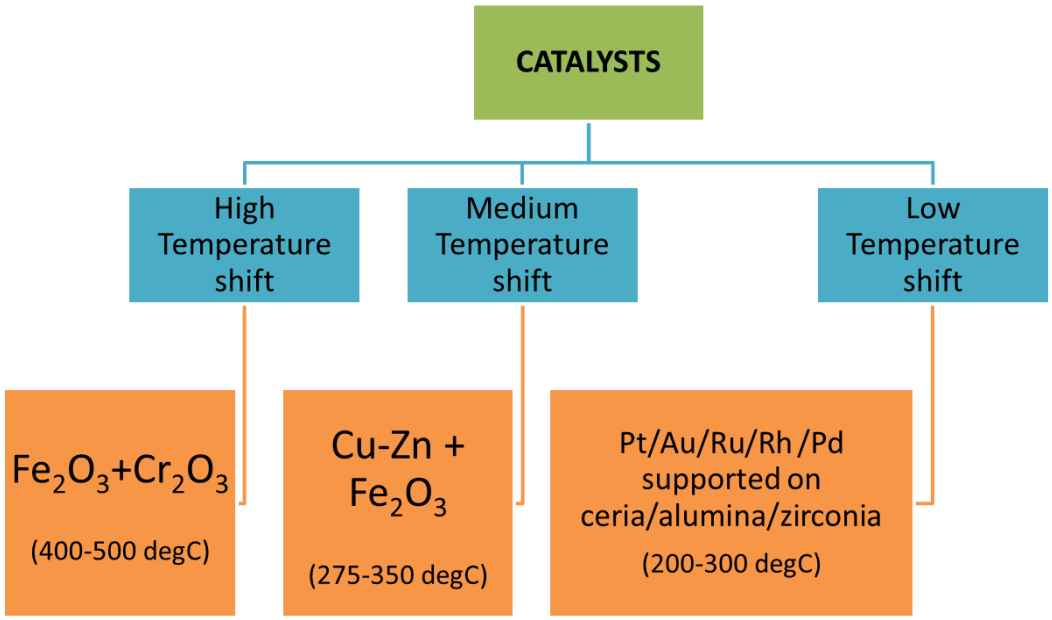

Fig. 2.2: Different types of water-gas shift catalysts and their temperature of operation.

However commercial HTS and LTS catalysts although ideal for industrial scale H_2 production, are not suitable for on-board fuel processing because of the need of sophisticated activation process, activity deterioration due to temperature change and the need to isolate the catalyst during shutdown to prevent oxidation [17]. The most important of all the catalyst types for WGS are noble metal catalysts (Pt and Au based). They have application in hydrogen production for the fuel cell industry including possibility of onboard H_2 production in fuel cell vehicles [18].

Uniformly distributed nanoparticles of noble metal supported on high surface area oxides have been shown to be highly effective for many important catalytic reactions. Catalysts are complex materials where achieving the desired properties (i.e. activity, selectivity, and stability) depends on exploiting many degrees of freedom such as surface vs bulk composition, geometry, defects, interactions with the support material, and control of the reacting environment. Many of these factors are currently poorly understood [19–24]. Process catalysts are a $13 billion-

per-year industry and the value of products dependent on process catalysts, which include refined products, chemicals and petrochemical products, and many others, is around $500–600 billion per year. Despite the large number of applications, WGS reaction remains one of the most difficult chemical processes due to kinetic limitations of commercial catalysts at low temperature and equilibrium limitations at high temperature [16, 25]. Moreover, the commercially used Cu and ZnO based WGS reaction catalysts are pyrophoric, and require pretreatment [26]. While currently used commercial catalysts require a two-stage operation and operate at temperature greater than 300°C, (Au) and platinum (Pt)-based catalysts supported on ceria (CeO_2) offer a promising alternative due to their single-state operation and low temperature (<250°C) activity [27–29]. The design of novel catalysts to potentially eliminate the two-stage operation is a challenging task.

The majority of the reactions in catalysis take place on the surface. Hence the efficiency of a catalytic process is largely determined by the quality of the catalysts used, i.e. the exposed surface area and the stability of the active phase [30]. The importance of metal oxide interfaces has long been recognized [31, 32], however they have not been explored until recently [33]. Different kinds of metal atoms, ranging from metallic to ionic, are available at the interface which along with the oxide support create reaction sites for WGS reaction [34]. The synergy of metal and oxide at the reaction interface plays an essential role in tuning activity and selectivity. The recent discovery of University of Connecticut mesoporous materials (UCT-1 to UCT-53) by Poyraz et al. has led to a wide range of over 50 families of materials that have very high adsorption capacities that surpass all known materials, excellent mono-modal pore size distributions, as well as superior thermal stability [35]. Among these, the most interesting observation is the pore expansion on heat treatment which has not been reported before [35]. The low temperature WGS reaction occurs between 180°C and 250°C with noble metals (Pt, Au, Ru, Rh, Pd) supported on

ceria, alumina, zirconia, vanadium or titania. However ceria has stood out to be the most favorable support for noble metals based LTS reactions because of its unique properties of high oxygen storage capacity [36] and its ability to exist in multiple oxidation states (Ce^{4+}/Ce^{3+}) which results in an increase in oxygen vacancies [37,38]. The oxygen storage capacity (OSC) of ceria is strongly dependent on the microstructure that results from the selected processing technique, because the oxygen vacancy formation energy (E_{vac}) decreases with grain size, resulting in greater non stoichiometry [39]. The presence of noble metal [40] also increases the oxygen-ion conductivity of ceria which provides the driving force for the transfer of oxygen from the bulk to the surface [41].

Of all the catalysts available for low temperature WGS reaction, Pt/ceria has been identified as the front runner because of its high activity and structural stability at low temperature [42]. Pt supported on ceria has been commercially utilized as a three way catalyst in the catalytic converter of the automobiles [43] and ceria has been established as an ideal support for WGS reaction catalysts in comparison with alumina (Al_2O_3), yttria stabilized zirconia (YSZ), and, vanadium oxide because of its oxygen storage capacity (OSC) and higher surface oxygen diffusion (280 times higher than γ-Al_2O_3 and 100 times than ZrO_2) [44]. The ceria unit cell has been shown in Fig. 2.3. In a ceria (CeO_2) molecule, each cerium (Ce) atom is surrounded by 8 oxygen (O) atoms. If the structure is extended so that O occupies the corner of the cube every alternate unit cell has an either empty center or is occupied by a Ce atom. Hence the formation of vacancies eases the movement of O atoms [45]. In this way ceria can be reduced (Ce^{+3}) or oxidized (Ce^{+4}) in fuel rich and lean conditions respectively [16, 41]. This unique property of ceria is particularly useful for automotive applications because the noble metal based ceria catalysts is used in the catalytic convertor. This allows the engine to operate at stoichiometric air to fuel ratio [41]. WGS

reaction activity is strongly dependent upon the structure of the ceria support as well as the nature of the interaction between the metal/metal oxide and the support [46]. Only strongly bound metal-ceria is active for WGS because they are associated with the surface oxygen vacancies of ceria. Hence the synthesis technique of ceria is directly related to the WGS reaction activity. Many syntheses have been proposed for ceria including flame spray pyrolysis [47, 48], incipient wetness impregnation [49, 50], co-precipitation [51, 52], sol-gel [53, 54], hydrothermal [55, 56] and micro-emulsion [57, 58].

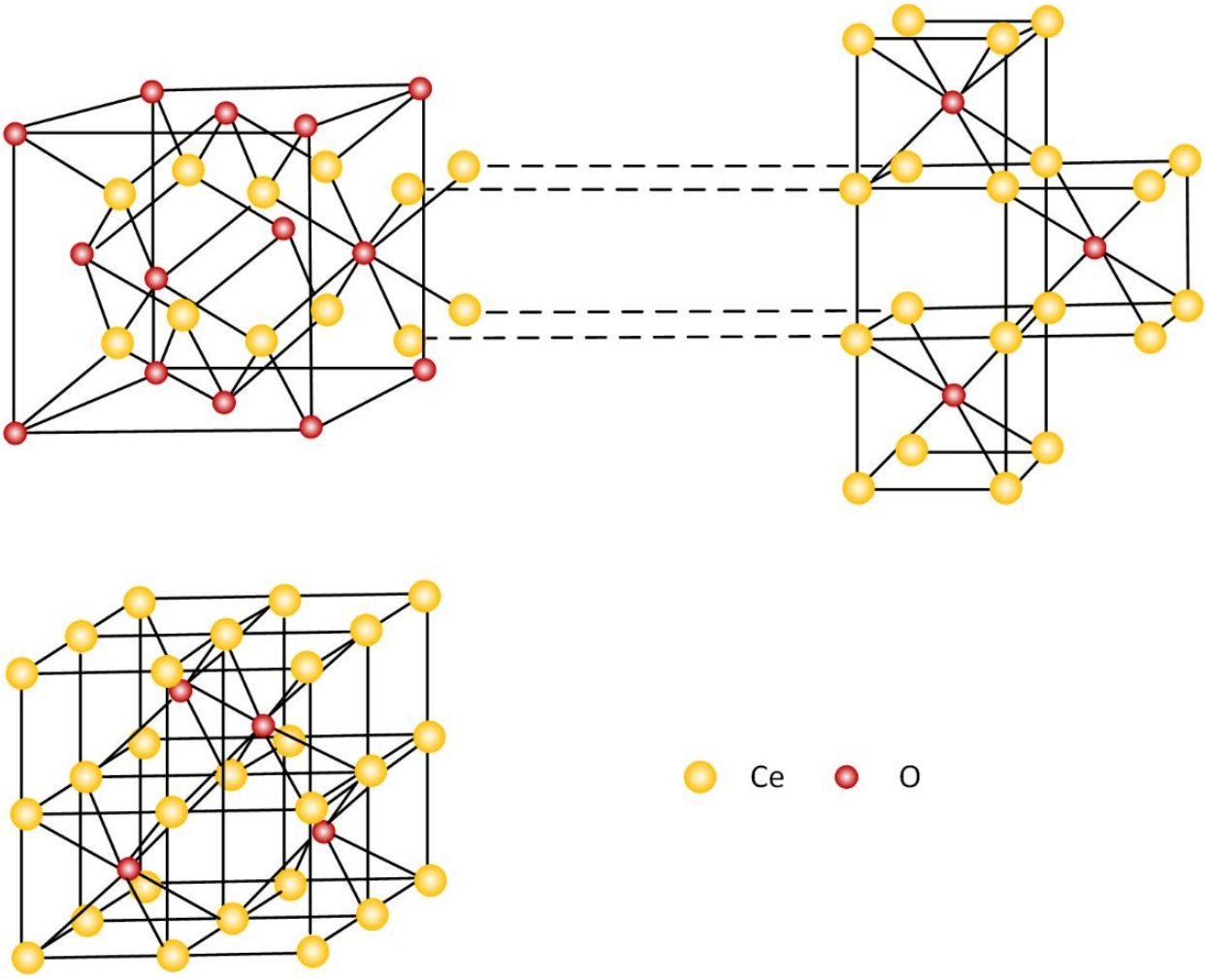

Fig. 2.3: A ceria unit cell with voids or "holes" if the Ce atom occupies the corner positions of the cube.

2.2 Mechanism of water-gas shift reaction on Pt/ceria:

There is a general disagreement on the role of ceria and noble metals for the WGS reaction [34], and two main mechanisms: (1) a redox mechanism [59], and (2) a formate mechanism [60] have been proposed based upon theory and developed models [61].

2.2.1 Redox mechanism:

This is the most widely accepted mechanism. Bunluesin et al. [62] reported the redox mechanism of WGS reaction. This mechanism is also known as a ceria mediated redox process. The WGS reaction takes place at the triple phase boundary (TPB) of the noble metal, ceria and the incoming gas [63]. In the ceria mediated redox process the incoming CO is adsorbed on the Pt which reduces the support (two Ce^{4+} ions are reduced to the Ce^{3+} state) by extracting oxygen from the Pt-ceria interface. This results in the formation of an oxygen vacancy in the ceria and the formation of Ce_2O_3 and CO_2. Ce_2O_3 is then oxidized back to CeO_2 through the dissociation of the H_2O into H^+ and OH^-. The oxygen vacancy is refilled and H_2 is released in the process. This work is also supported by infra-red and kinetic studies [13, 42]. The mechanism has been described in detail in Fig. 2.4 and is expressed in equations E2.3–E2.5:

$$CO + H_2O \overset{\text{catalyst}}{\Longleftrightarrow} CO_2 + H_2 \quad \text{(E2.1)}$$

$$CO + Pt^* \rightarrow CO_{ads} \text{ (*represents adsorption site on Pt)} \quad \text{(E2.2)}$$

$$CO_{ads} + 2CeO_2 \rightarrow CO_2 + Ce_2O_3 \quad \text{(E2.3)}$$

$$H_2O + Pt^* \rightarrow 2H^+ + OH^- \quad \text{(E2.4)}$$

$$H^+ + OH^- + Ce_2O_3 \rightarrow 2CeO_2 + H_2 \quad \text{(E2.5)}$$

$$\Delta H^{o}_{298K} = -41.4\ \text{kJ/mol}\ [11] \quad \text{(E2.6)}$$

$$\Delta G^{o}_{298K} = -32.197 + 0.03104T - \frac{1774.7}{T}\ [11] \quad \text{(E2.7)}$$

$$\log(K) = -2.4198 + 0.0003855T + \frac{2180.6}{T}\ [11] \quad \text{(E2.8)}$$

As shown in the equations E2.1 and E2.6–E2.8, the WGS reaction is a mildly exothermic and reversible reaction and the tendency of the equilibrium constant is to decrease with increase in temperature.

2.2.2 Formate mechanism:

The formate mechanism was proposed and supported by Shido and Iwasawa [33] as shown in equation E2.10–E2.15. Oxygen vacancies in ceria provide a site for platinum-catalyzed H_2O dissociation, which generate atomic hydrogen and OH species. Oxygen vacancies in ceria provide a site for Pt-catalyzed H_2O dissociation, which generate atomic hydrogen and OH species. Adsorbed CO on Pt reacts with OH groups (unidentates, bidentates, and tridentates) which act as WGS reaction intermediate groups, to generate a formate or formic acid (HCOOH). Formates enables the regeneration of adsorbed hydrogen atoms, which on reaction with ambient water, generates additional H_2 and unidentate carbonate prior to CO_2 formation. This theory was also supported by the studies of the decomposition of formic acid on the ceria surface [37] and by density-functional theory (DFT) calculations by Kinch et al. [38].

$$CO + H_2O \overset{\text{catalyst}}{\Longleftrightarrow} CO_2 + H_2 \quad \text{(E2.9)}$$

$$CO + Pt^{*} \rightarrow CO_{ads}\ (\text{*represents adsorption site on Pt}) \quad \text{(E2.10)}$$

$$H_2O + Pt^{*} \rightarrow 2H^{+} + OH^{-} \quad \text{(E2.11)}$$

$$CeO_2 + H^+ + OH^- \rightarrow Ce(OH) + Ce(OH)_2 + Ce(OH)_3 \quad \text{(E2.12)}$$

$$Ce(OH) + Ce(OH)_2 + Ce(OH)_3 + CO_{ads} \rightarrow HCOO + HCOOH \quad \text{(E2.13)}$$

$$HCOO + HCOOH \rightarrow OC + OCO + H^+ \quad \text{(E2.14)}$$

$$OC + OCO + H^+ \rightarrow CO_2 + H_2 \quad \text{(E2.15)}$$

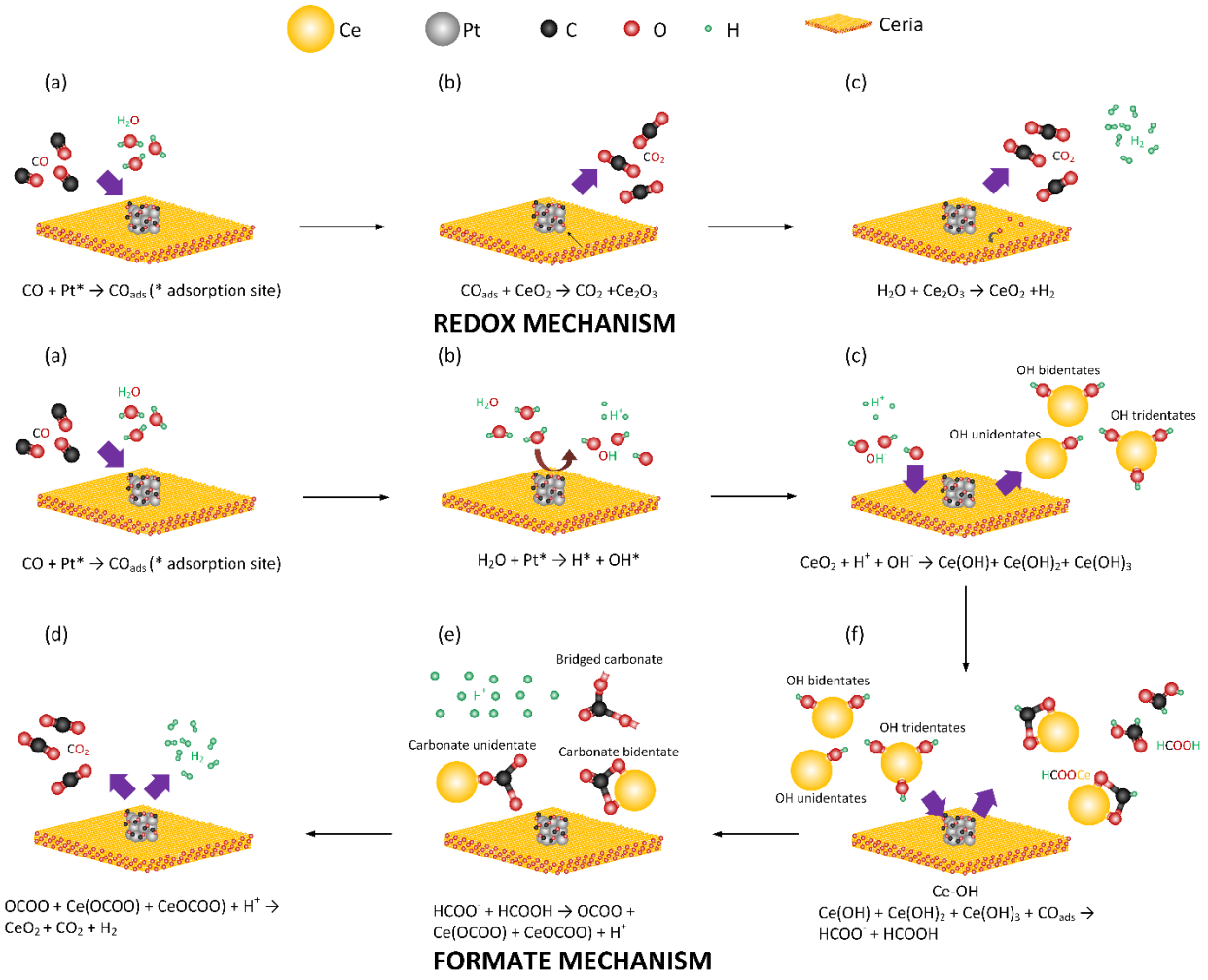

Fig. 2.4: Representation of the water-gas shift reaction redox mechanism on ceria/Pt catalysts shown in atomic scale.

2.3 References:

[1] L. Mond, C. Langer, Improvements in obtaining hydrogen, British Patent 12608. (1888).

[2] M.E. Dry, Practical and theoretical aspects of the catalytic Fischer-Tropsch process, Applied Catalysis A: General. 138 (2) (1996) 319–344.

[3] P. Kaiser, R. Unde, C. Kern, A. Jess, Production of Liquid Hydrocarbons with CO_2 as Carbon Source based on Reverse Water-Gas Shift and Fischer-Tropsch Synthesis, Chemie Ingenieur Technik. 85 (4) (2013) 489–499.

[4] A.K. Dalai, B.H. Davis, Fischer–Tropsch synthesis: A review of water effects on the performances of unsupported and supported Co catalysts, Applied Catalysis A: General. 348 (1) (2008) 1–15.

[5] H. Schulz, Short history and present trends of Fischer–Tropsch synthesis, Applied Catalysis A: General. 186 (1–2) (1999) 3–12.

[6] B.I. Whittington, C.J. Jiang, D.L. Trimm, Vehicle exhaust catalysis: I. The relative importance of catalytic oxidation, steam reforming and water-gas shift reactions, Catalysis Today. 26 (1) (1995) 41–45.

[7] C. Song, Overview of Hydrogen Production Options for Hydrogen Energy Development, Fuel-Cell Fuel Processing and Mitigation of CO_2 Emissions, 40–3 (2003).

[8] S. Gupta, M.K. Mahapatra, P. Singh, Lanthanum chromite based perovskites for oxygen transport membrane, Materials Science and Engineering: R: Reports. 90 (2015) 1–36.

[9] M.C. Carbo, J. Boon, D. Jansen, H.A.J. van Dijk, J.W. Dijkstra, R.W. van den Brink, A.H.M. Verkooijen, Steam demand reduction of water-gas shift reaction in IGCC power plants with pre-combustion CO_2 capture, International Journal of Greenhouse Gas Control. 3 (6) (2009) 712–719.

[10] G.A. Bishop, D.H. Stedman, Measuring the Emissions of Passing Cars, Accounts of Chemical Research. 29 (10) (1996) 489–495.

[11] Caitlin A. Callaghan. Kinetics and Catalysis of the Water-Gas-Shift Reaction: A Microkinetic and Graph Theoretic Approach (Doctoral dissertation). Worcester Polytechnic Institute. Retrieved from: https://www.wpi.edu/Pubs/ETD/Available/etd-050406-023806/unrestricted/ccallaghan.pdf (2006).

[12] B.I. Whittington, C.J. Jiang, D.L. Trimm, Vehicle exhaust catalysis: I. The relative importance of catalytic oxidation, steam reforming and water-gas shift reactions, Catalysis Today. 26 (1) (1995) 41-45.

[13] Y. Li, Q. Fu, M. Flytzani-Stephanopoulos, Low-temperature water-gas shift reaction over Cu- and Ni-loaded cerium oxide catalysts, Applied Catalysis B: Environmental. 27 (3) (2000) 179-191.

[14] T. E. Springer, T. Rockward, T. A. Zawodzinski* and S. Gottesfeld, Model for Polymer Electrolyte Fuel Cell Operation on Reformate Feed: Effects of CO, H_2 Dilution, and High Fuel Utilization, Journal of Electroceramic Society. 148 (1) (2001) A11-A23.

[15] L. F. Brown, A comparative study of fuels for on-board hydrogen production for fuel-cell-powered automobiles, International Journal of Hydrogen Energy. 26 (4) (2001) 381-397.

[16] C. Ratnasamy, J.P. Wagner, Water Gas Shift Catalysis, Catalysis Reviews. 51 (3) (2009) 325-440.

[17] S.Y. Choung, J. Krebs, M. Ferrandon, R. Souleimanova, D. Myers, T. Krause, Hydrogen, Fuel Cells, and Infrastructure Technologies. US DOE FY 2003 Progress Report (2003) 1-4.

[18] R. Farrauto, S. Hwang, L. Shore, W. Ruettinger, J. Lampert, T. Giroux, Y. Liu, O. Ilinich, New Materials Needs For Hydrocarbon Fuel Processing: Generating Hydrogen for the PEM Fuel Cell, Annual Review of Materials Research. 33 (1) (2003) 1-27.

[19] J. Shi, X. Li, Q. Wang, Y. Zhang, Y. Tang, Platinum-encapsulated zeolitically microcapsular catalyst for one-pot dynamic kinetic resolution of phenylethylamine, Journal of Catalysis. 291 (0) (2012) 87-94.

[20] Z. Qin, B. Shen, Z. Yu, F. Deng, L. Zhao, S. Zhou, D. Yuan, X. Gao, B. Wang, H. Zhao, H. Liu, A defect-based strategy for the preparation of mesoporous zeolite Y for high-performance catalytic cracking, Journal of Catalysis. 298 (0) (2013) 102-111.

[21] M. Badawi, J.F. Paul, S. Cristol, E. Payen, Y. Romero, F. Richard, S. Brunet, D. Lambert, X. Portier, A. Popov, E. Kondratieva, J.M. Goupil, J. El Fallah, J.P. Gilson, L. Mariey, A. Travert, F. Maugé, Effect of water on the stability of Mo and CoMo hydrodeoxygenation catalysts: A combined experimental and DFT study, Journal of Catalysis. 282 (1) (2011) 155-164.

[22] T. Valdes-Solis, P. Valle-Vigon, M. Sevilla, A.B. Fuertes, Encapsulation of nanosized catalysts in the hollow core of a mesoporous carbon capsule, Journal of Catalysis. 251 (1) (2007) 239–243.

[23] V. Nallathambi, J. Lee, S.P. Kumaraguru, G. Wu, B.N. Popov, Development of high performance carbon composite catalyst for oxygen reduction reaction in PEM Proton Exchange Membrane fuel cells, Journal of Power Sources. 183 (1) (2008) 34-42.

[24] S. Guo, S. Han, H. Mao, S. Dong, C. Wu, L. Jia, B. Chi, J. Pu, J. Li, Structurally controlled ZnO/TiO_2 heterostructures as efficient photocatalysts for hydrogen generation from water without noble metals: The role of microporous amorphous/crystalline composite structure, Journal of Power Sources. 245 (0) (2014) 979-985.

[25] A.M. Duarte de Farias, A.P.M.G. Barandas, R.F. Perez, M.A. Fraga, Water-gas shift reaction over magnesia-modified Pt/CeO_2 catalysts, Journal of Power Sources. 165 (2) (2007) 854-860.

[26] A. Faur Ghenciu, Review of fuel processing catalysts for hydrogen production in PEM fuel cell systems, Current Opinion in Solid State and Materials Science. 6 (5) (2002) 389-399.

[27] R. Burch, Gold catalysts for pure hydrogen production in the water-gas shift reaction: activity, structure and reaction mechanism, Physical Chemistry Chemical Physics. 8 (47) (2006) 5483-5500.

[28] D. Tibiletti, A.A. Fonseca, R. Burch, Y. Chen, J.M. Fisher, A. Goguet, C. Hardacre, P. Hu, D. Thompsett, DFT and in situ EXAFS investigation of gold/ceria-zirconia low-temperature water gas shift catalysts: identification of the nature of the active form of gold, Journal of Physical Chemistry B. 109 (47) (2005) 22553-22559.

[29] H. Roh, D. Jeong, K. Kim, I. Eum, K. Koo, W. Yoon, Single Stage Water-Gas Shift Reaction Over Supported Pt Catalysts, Catalysis Letters. 141 (1) (2011) 95-99.

[30] G. Mul, J.A. Moulijn, Preparation of supported metal catalysts, in: J.A. Anderson, M.F. García (Eds.), Supported Metals in Catalysis, Imperial College Press, eprint: http://www.worldscientific.com/doi/pdf/10.1142/9781860947476_0001, 2013, pp. 1-32.

[31] G.-. Schwab, Boundary-Layer Catalysis, Angewandte Chemie International Edition. 6(4) (1967) 375.

[32] K. Hayek, R. Kramer, Z. Paal, Metal-support boundary sites in catalysis, Applied Catalysis A: General. 162 (1-2) (1997) 1-15.

[33] Y.Y. Wu, N.A. Mashayekhi, H.H. Kung, Au-metal oxide support interface as catalytic active sites, Catalysis Science & Technology. 3 (11) (2013) 2881-2891.

[34] S.C. Ammal, A. Heyden, Water-Gas Shift Catalysis at Corner Atoms of Pt Clusters in Contact with a TiO_2 (110) Support Surface, ACS Catalysis. 4 (10) (2014) 3654-3662.

[35] A.S. Poyraz, C. Kuo, S. Biswas, C.K. King'ondu, S.L. Suib, A general approach to crystalline and monomodal pore size mesoporous materials, Nature Communications. 4 (2013) 2952.

[36] V. Pitchon, F. Garin, O. Maire, Influence of the surrounding atmosphere upon the catalytic performances of three-way catalysts, Applied Catalysis A: General. 149 (1) (1997) 245-256.

[37] T. Tabakova, F. Boccuzzi, M. Manzoli, D. Andreeva, FTIR study of low-temperature water-gas shift reaction on gold/ceria catalyst, Applied Catalysis A: General. 252 (2) (2003) 385-397.

[38] T.R. Reina, W. Xu, S. Ivanova, M.Á Centeno, J. Hanson, J.A. Rodriguez, J.A. Odriozola, In situ characterization of iron-promoted ceria–alumina gold catalysts during the water-gas shift reaction, Catalysis Today. 205 (0) (2013) 41-48.

[39] E.B. Lavik, I. Kosacki, H.L. Tuller, Y. Chiang, J.Y. Ying, Nonstoichiometry and Electrical Conductivity of Nanocrystalline $CeO_{\{2-x\}}$, Journal of Electroceramics. 1 (1) (1997) 7-14.

[40] K. Eguchi, T. Setoguchi, T. Inoue, H. Arai, Electrical properties of ceria-based oxides and their application to solid oxide fuel cells, Solid State Ionics. 52 (1–3) (1992) 165-172.

[41] R.J. Gorte, Ceria in catalysis: From automotive applications to the water-gas shift reaction, AIChE Journal. 56 (5) (2010) 1126-1135.

[42] S. Hilaire, X. Wang, T. Luo, R.J. Gorte, J. Wagner, A comparative study of water-gas-shift reaction over ceria supported metallic catalysts, Applied Catalysis A: General. 215 (1–2) (2001) 271-278.

[43] A. Trovarelli, Catalytic Properties of Ceria and CeO_2-Containing Materials, Catalysis Reviews. 38 (4) (1996) 439-520.

[44] Sara Aranifard. Theoretical Investigation of the Water-Gas Shift Reaction At the Three Phase Boundary of Ceria Supported Platinum Metal Clusters (Doctoral dissertation). University of South Carolina. Retrieved from: http://scholarcommons.sc.edu/etd (2013).

[45] D. Duprez, C. Descorme, Oxygen Storage/Redox Capacity and Related Phenomena on Ceria-based Catalysts, in: A. Trovarelli (Ed.), Catalysis by Ceria and Related Materials, 2nd ed.,

Published by: Imperial College Press, Distributed by: World Scientific Publishing Co., London, UK, 2002, pp. 243-280.

[46] R. Si, J. Raitano, N. Yi, L. Zhang, S. Chan, M. Flytzani-Stephanopoulos, Structure sensitivity of the low-temperature water-gas shift reaction on Cu–CeO_2 catalysts, Catalysis Today. 180 (1) (2012) 68-80.

[47] J. Christensen, D. Deiana, J. Grunwaldt, A. Jensen, Ceria Prepared by Flame Spray Pyrolysis as an Efficient Catalyst for Oxidation of Diesel Soot, Catalysis Letters. 144 (10) (2014) 1661-1666.

[48] W.J. Stark, J. Grunwaldt, M. Maciejewski, S.E. Pratsinis, A. Baiker, Flame-Made Pt/Ceria/Zirconia for Low-Temperature Oxygen Exchange, Chemistry of Materials. 17 (13) (2005) 3352-3358.

[49] F. Balıkçı Derekaya, C. Kutar, Ç Güldür, Selective CO oxidation over ceria supported CuO catalysts, Materials Chemistry and Physics. 115 (2–3) (2009) 496-501.

[50] H. Roh, D. Jeong, K. Kim, I. Eum, K. Koo, W. Yoon, Single Stage Water-Gas Shift Reaction Over Supported Pt Catalysts, Catalysis Letters. 141 (1) (2011) 95-99.

[51] D. Hari Prasad, H.-. Kim, J.-. Park, J.-. Son, B.-. Kim, H.-. Lee, J.-. Lee, Superior sinterability of nano-crystalline gadolinium doped ceria powders synthesized by co-precipitation method, Journal of Alloys and Compounds. 495 (1) (2010) 238-241.

[52] K. Higashi, K. Sonoda, H. Ono, S. Sameshima, Y. Hirata, Synthesis and sintering of rare-earth-doped ceria powder by the oxalate coprecipitation method, Journal of Materials Research. 14 (03) (1999) 957-967.

[53] A. Luengnaruemitchai, S. Osuwan, E. Gulari, Comparative studies of low-temperature water-gas shift reaction over Pt/CeO_2, Au/CeO_2, and Au/Fe_2O_3 catalysts, Catalysis Communications. 4 (5) (2003) 215-221.

[54] C. Laberty-Robert, J.W. Long, E.M. Lucas, K.A. Pettigrew, R.M. Stroud, M.S. Doescher, D.R. Rolison, Sol−Gel-Derived Ceria Nanoarchitectures: Synthesis, Characterization, and Electrical Properties, Chemistry of Materials. 18 (1) (2006) 50-58.

[55] Q. Dong, S. Yin, C. Guo, T. Kimura, T. Sato, Hydrothermal synthesis of tin doped ceria-zirconia solid solutions with enhanced thermal stability and oxygen storage capacity, RSC Advances. 2 (33) (2012) 12770-12774.

[56] R. Divakar, J. Basu, C. Carter, Hydrothermal Synthesis of Cuboidal Nanocrystalline Ceria, Microscopy and Microanalysis. 13 (Supplement S02) (2007) 980-981.

[57] C.M. Yeung, F. Meunier, R. Burch, D. Thompsett, S.C. Tsang, Comparison of new microemulsion prepared "Pt-in-Ceria" catalyst with conventional "Pt-on-Ceria" catalyst for water-gas shift reaction, Journal of Physical Chemistry B. 110 (17) (2006) 8540-8543.

[58] O.H. Laguna, M.A. Centeno, M. Boutonnet, J.A. Odriozola, Fe-doped ceria solids synthesized by the microemulsion method for CO oxidation reactions, Applied Catalysis B: Environmental. 106 (3–4) (2011) 621-629.

[59] T. Bunluesin, R.J. Gorte, G.W. Graham, Studies of the water-gas-shift reaction on ceria-supported Pt, Pd, and Rh: Implications for oxygen-storage properties, Applied Catalysis B: Environmental. 15 (1–2) (1998) 107-114.

[60] T. Shido, Y. Iwasawa, Reactant-Promoted Reaction Mechanism for Water-Gas Shift Reaction on Rh-Doped CeO_2, Journal of Catalysis. 141 (1) (1993) 71-81.

[61] A.B. Mhadeshwar, D.G. Vlachos, Microkinetic Modeling for Water-Promoted CO Oxidation, Water-Gas Shift, and Preferential Oxidation of CO on Pt, Journal of Physical Chemistry B. 108 (39) (2004) 15246-15258.

[62] T. Bunluesin, R.J. Gorte, G.W. Graham, Studies of the water-gas-shift reaction on ceria-supported Pt, Pd, and Rh: Implications for oxygen-storage properties, Applied Catalysis B: Environmental. 15 (1–2) (1998) 107-114.

[63] S. Aranifard, S.C. Ammal, A. Heyden, On the importance of metal–oxide interface sites for the water-gas shift reaction over Pt/CeO_2 catalysts, Journal of Catalysis. 309 (0) (2014) 314-324.

CHAPTER 3:

Metal-oxide based Gas Sensors

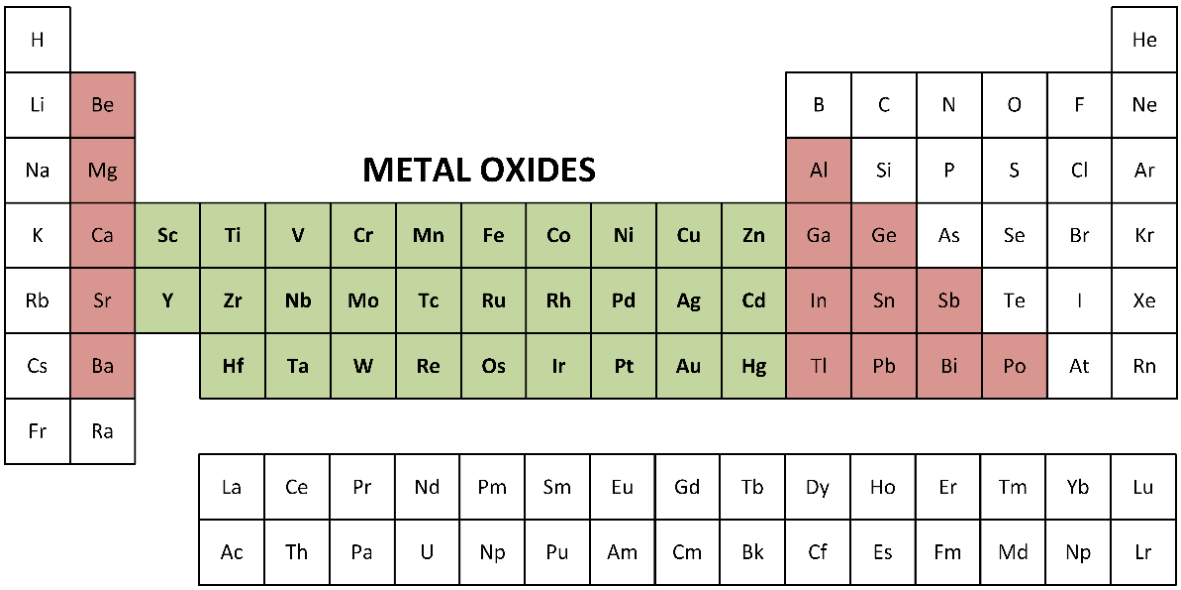

3.1 Gas sensor:

The word sensor means to sense or "perceive". A sensor is a device which detects the change in a physical stimulus and converts it into a signal which can be measured and decoded. All living objects have sensors. A traditional example of a sensor is human body which can sense heat, temperature, humidity, pressure, light, smell, touch, and sound to name a few. The more complicated sensors exists inside the human body in the form of organs which can sense the chemical composition of the bodily fluids. Flowers such as sunflower can sense the sunlight and respond by moving toward the sun. There are sensors in automobiles which prevent accidental injury by deploying the airbags in case of a collision. Oxygen sensors in the car engine exhaust, control the amount of oxygen for the combustion of gasoline to provide a rich or lean combustion. There are smoke detectors and water sprinklers in households and offices which detect the possibility of a fire and alerts accordingly. As we progress into the 21st century, the use of sensors for different applications have increased many fold. The worldwide market for sensors was worth $56.3 billion in 2010, which increased to $62.8 billion in 2011 and is expected to rise to $91.5 billion in 2016 [1]. A gas sensor is a device which is generally used for sensing a potentially hazardous gas. After a predetermined threshold for a gas is reached in the environment, the gas sensor responds with a previously determined signal. Some sensors are programmed to automatically start a preventive process to remove the cause which started the alarm. A common example of gas sensor is the CO sensor which detects the abnormal level of CO in an environment.

The integration of gas sensor components into smart phones, tablets and wrist watches will revolutionize the environmental health and safety industry by providing individuals the ability to detect harmful chemicals and pollutants using always-on hand-held or wearable devices [2]. Gas sensors based on conductometric principle which uses a metal oxide based

element is one of such device which has been used since 1960. The device consists of Au or Pt interdigitated line electrodes on a silicon or alumina base [3]. A metal oxide semiconductor film with narrow band gap is deposited onto the interdigitated lines and resistance across them is measured externally. The resistance increases in presence of oxidizing analytes and reduces in presence of reducing analytes (for n-type semiconductor metal oxide film). The process of conversion of sensory inputs to electrical signals is utilized by many devices such as heart in-plants, digital blood pressure monitor, blood glucose monitors, and body fat monitors. Fig. 3.1 shows the components of a sensing device. The essential components of a gas sensing device are: a metal-oxide sensing layer deposited on gold or platinum interdigitated electrodes which are attached to, an alumina or silicon substrate, consisting of a heater and a temperature probe to increase and control the temperature of the sensing layer.

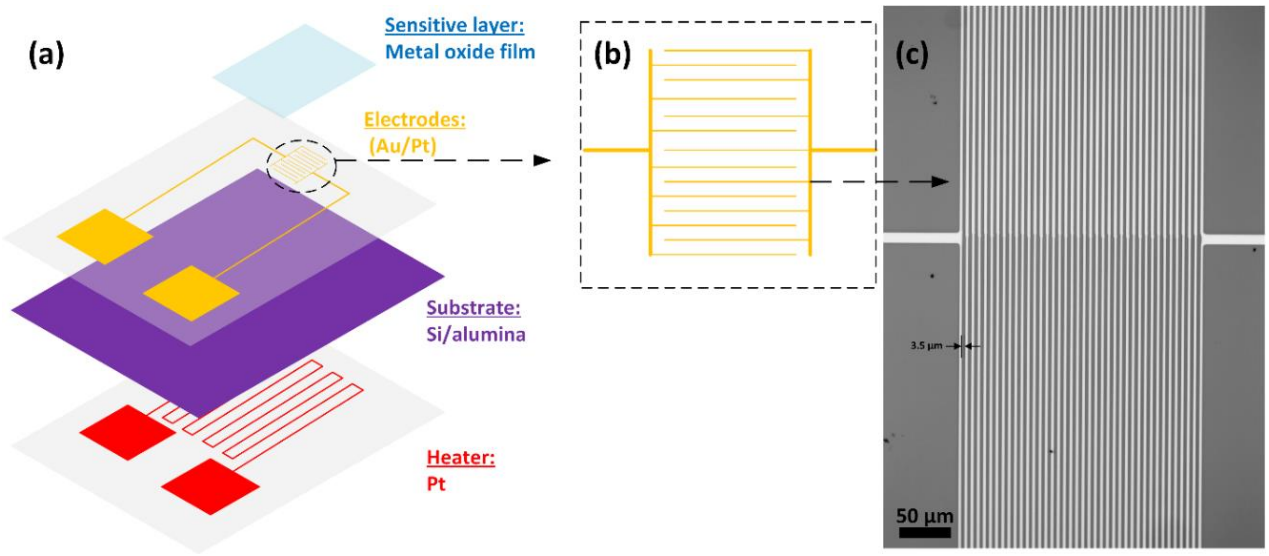

Fig. 3.1: (a) Different parts of the gas sensing device, (b) architecture of the gold interdigitated electrodes, (c) optical microscopy image of the gold interdigitated electrodes.

3.2 Mechanism of sensing (oxidizing and reducing analytes):

The mechanism of analyte sensing by metal oxide based sensors was described by Barsan and Weimar [4] and proved by temperature programmed desorption (TPD), Fourier transform infrared spectroscopy (FTIR), and electron spin resonance (ESR) spectroscopy [4]. The metal oxide film deposited on interdigitated electrodes possess both receptor and transducer function. Sensing of an analyte on the metal oxide surface takes place by the adsorption and desorption process. The reaction of the analyte species takes place on the film surface (receptor function) and the adsorbed analyte changes the resistance of the interdigitated electrode (transducer function). This change in resistance can be correlated with the concentration of the analyte. The resistance increases in presence of oxidizing analyte and decreases in presence of reducing analyte. This is because the change in resistance is related to the concentration of the ionosorbed oxygen. An oxidizing analyte increases the ionosorbed oxygen concentration which causes the formation of a large electron depletion layer or space charge layer $\Lambda_{oxidizing}$ [5] between two individual metal oxide grains. At the junction of two particles a larger electron depletion layer ($2 * \Lambda_{oxidizing}$) is formed causing bending of the metal oxide conduction band and the generation of a surface potential barrier (height of band bending qV_S, also called Schottky barrier) [6]. Since the electrons flow along a percolation path from grain to grain, the electron depletion layer restricts this movement causing an increase in the film resistance. On the other hand, the reducing analytes are oxidized on the metal oxide surface which causes the reduction in the ionosorbed oxygen concentration and reduction in the electron depletion layer ($\Lambda_{reducing}$). Hence the resistance is lowered. This has been explained in Fig. 3.5. $\Lambda_{oxidizing}$ is always larger than $\Lambda_{reducing}$. The resistance of the metal oxide is related to the surface potential barrier by the following equation [6, 7]:

$R = \frac{1}{\exp\left(\frac{-qV_S}{k_B T}\right)}$, where R = resistance of metal oxide film, (E3.1)

qV_s = height of band bending

k_B = Boltzmann' s constant = $1.38 * 10^{-23} \frac{J}{K}$, T = temperature

The response (S) for oxidizing and reducing gases are calculated according to the following equations:

$S_{oxidizing} = \frac{R_{analyte}}{R_{air}}$; $S_{reducing} = \frac{R_{air}}{R_{analyte}}$ (E3.2)

3.3 Sensor terminology:

In the sensor field, there are few terms and definitions that are often used. Some of them are defined below:

3.3.1 Analyte:

Analyte is the gas or the chemical which is to be detected by the sensor.

3.3.2 Limit of detection (LOD):

A sensor is designed to work over a particular range. The lower limit of that range is called limit of detection (LOD). Below this limit, the sensor will produce inaccurate readings. Similarly, if the upper limit of the sensor is exceeded, the reading will be erroneous or it may lead to permanent damage to its instrumentation. The performance of a gas sensor is measured by its (LOD) [5].

3.3.3 Sensitivity:

Sensitivity of a sensor is defined as the change in output of the sensor per unit change in the parameter being measured [6].

3.3.4 Selectivity:

Selectivity is defined as the preferential detection of the target analyte among a mixture of gases. Selectivity to other gases, which can lead to false alarm or incorrect gas concentration determination, is a major concern for a sensor to be commercially viable.

3.3.5 Response time:

The sensor responds to a change in the concentration of analyte in its surroundings. The time taken by the sensor to reach 90% of its saturation value is known as response time [6]. It is desirable to have the lowest possible response time for an ideal sensor.

3.3.6 Recovery time:

After the analyte is removed from the environment, the sensor tends to recover to its original baseline. The time required for the sensor to reach 90% of its original baseline is known as recovery time. Generally recovery time is larger than response time for metal oxide based gas sensors. This is because those sensors are adsorption and desorption based in which, the analyte molecules are adsorbed on the surface of metal oxide. The activation energy for adsorption is smaller than the activation energy for desorption which causes a delay in the recovery of the sensor [8].

3.3.7 Drift:

Drift is defined as the variation in the signal for the same concentration of analyte. This introduces an error in the measurement. This is caused by large difference in the activation energy for analyte adsorption and desorption. There may be other factors responsible for drift such as changes of temperature, electronics instability, or aging of the electronic components. Drift of the metal oxides based sensors have been recognized and various suggestions to counter this limitation have been proposed as described in chapter 8.

3.3.8 Calibration:

A sensor might need calibration from time to time to confirm that the concentration of the analyte detected represents the actual concentration. The calibration schedule must be fixed for the best possible performance.

3.3.9 Resolution:

Resolution is defined as the smallest change that can be detected by a sensor.

3.3.10 Operating temperature or working temperature:

A gas sensor generally operates at a temperature which is called its operating temperature. It is the temperature at which it responds in a most efficient manner. At low working temperature, the activation barrier for the generation of ionosorbed oxygen is higher while at high temperature, desorption of analytes exceeds adsorption resulting in lower response. Also at higher temperature the chemisorption of the analytes onto the surface of the metal oxide film is accelerated and the activation energy of the reaction is reduced. Hence an optimum temperature is required which is a function of the analyte and metal oxide properties. As shown in Fig. 3.1, a sensor has a heating element, and a resistance temperature detector (RTD) for the control of heat to the metal oxide film. The reactions at the heated metal oxide surface changes the concentration of electrons in the film depletion layer, and this in turn changes the conductance of these devices as a function of gas concentration. Generally speaking, lower operating temperature is desirable which reduces the power consumption, however the efficient micro hot plate designs significantly reduces the power consumption [9]. On the other hand there are applications in the industry which require sensing an analyte at high temperature. A review by Liu et al. has described the recent progress in the development of such high temperature solid-state gas sensors [10].

3.4 Gas sensors-from research to market:

Like any other device, a gas sensor requires extensive research and development in the laboratory before it can be made available for its end use. There are various steps for this process as described in the Fig. 3.2. These are: (1) defining the architecture, geometry and material for the interdigitated electrode, (2) metal oxide film synthesis, characterization and property optimization, (3) performing lab trials and errors with simulated atmosphere, (4) performing lab trials with near real type atmosphere, (5) performing lab trials with real sample (human breaths or field samples), (6) arranging necessary approvals, (7) commercial production. This thesis will be entirely focused on the material development and testing.

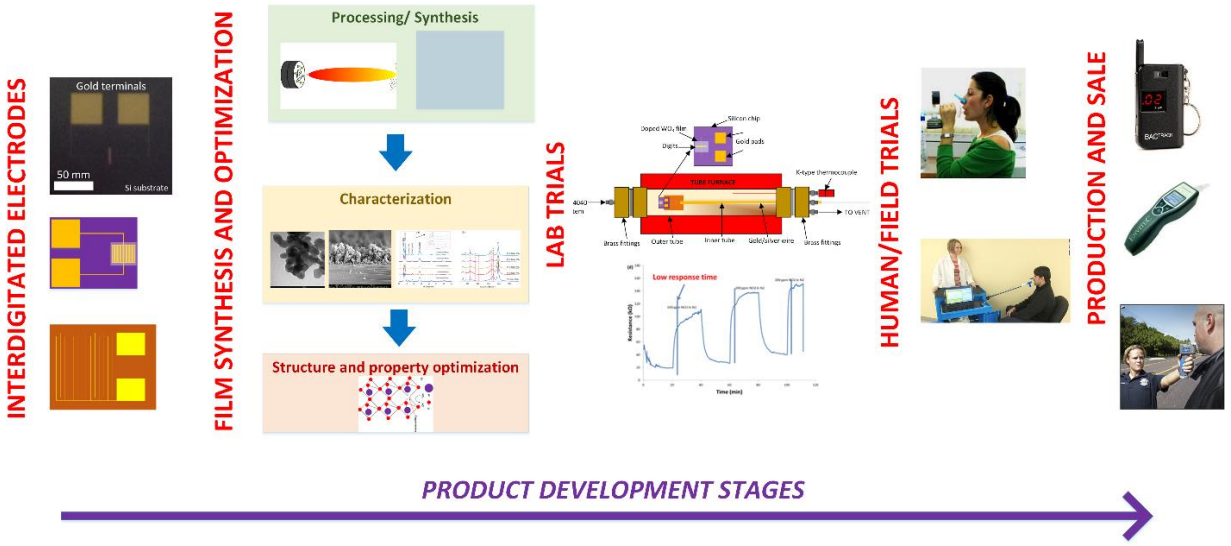

Fig. 3.2: Different stages for the development of the gas sensing device.

3.5 Materials selection for metal oxide based gas sensor films:

A detailed review by Korotcenkov on choosing the correct metal-oxide for the sensing film was published in 2007 [8]. If we consider binary metal oxides for gas sensor films,

then there are two types: (1) transitional metal oxides having d^0 - d^{10} symmetry and (2) non-transitional metal oxides having s or p symmetry. Transitional metal oxides have unfilled d-orbital, hence they have a tendency to attract electrons. Also the energy difference between a cation d^n configuration and, d^{n+1} or d^{n-1} configuration is small. The cation d^0 configuration represents the highest oxidation state (can only be reduced to form defects) and d^{10} configuration represents the lowest oxidation state (can only be oxidized). Hence transition metal oxides can easily form different oxides with varying stoichiometry and it is easier to form defects in the transitional metal oxides. Non-transitional metal oxides have only one preferred oxidation state. Other states are inaccessible because adding or removing an electron from a cation which is coordinated with O^{2-} ligand, will require significant amount of energy. They are quite inert and are difficult to oxidize or reduce. However, the transitional metal oxides with a partially filled d orbitals ($0<d<10$) are not preferred for sensing application, in spite of possessing a better catalytic activity [11], because of their structure instability at high temperatures and non-optimality of other parameters necessary for conductometric gas sensing such as band gap energy and electro conductivity [8]. Transition-metal oxides with d^0 or d^{10} electronic configurations are generally preferred for gas sensing applications.

3.6 Application of gas sensors in healthcare:

Human breath is a complex mixture of N_2, CO_2, O_2, water vapor and traces of 200 other organics and inorganics [12] which are the product of one or more biological phenomenon occurring in the human body. Deviation of the concentration of these organic and inorganic vapors from their normal value is caused by a slight change in the chemistry of human body and could be used as a biomarker for an onset of disease. Few examples of the most commonly occurring organics and inorganics in the human breath are provided in table 3.1. Quantifying low

concentration of these organics with high selectivity and cross sensitivity with other gases can prove challenging with the presently available conductometric sensing capabilities. The healthcare sector for diagnostics and patient monitoring using non-invasive breathalyzers is still in its infancy, but has a huge potential for growth in the next 10 years following the publication of this thesis.

Table 3.1: Analytes in human breath and the respective disease biomarker.

Compound in human breath	Biomarker	Reference
acetone	diabetes	[13–21]
carbonyl sulfide, carbon disulphide, isoprene	liver diseases	[22]
naphthalene,1-methyl-, 3-heptanone, methylcyclododecane, etc.	pulmonary tuberculosis	[23]
nonane, tridecane, 5-methyl, undecane, 3-methyl, etc.	breast cancer	[24]
benzene,1,1-oxybis-, 1,1-biphenyl,2,2-diethyl, furan,2,5-dimethyl-, etc.	lung cancer	[25]
ammonia	renal disease	[26]
octane,4-methyl, decane, 4-methyl, hexane, etc.	unstable angina	[27]
propane,2-methyl, octadecane, octane, 5-methyl, etc.	heart transplant rejection	[28]
pentane, carbon disulfide	schizophrenia	[29]
pentane	acute myocardial infarction	[30]
pentane	acute asthma	[31]
pentane	rheumatoid arthritis	[32]
ethane	active ulcerative colitis	[33]
nitric oxide	asthmatic inflammation	[34]
nitric oxide	bronchiectasis	[35]
carbon monoxide	bronchiectasis	[36]
nitric oxide	COPD	[37]
ethane, propane, pentane, etc.	cystic fibrosis	[38]

3.7 Important factors for analyte sensing:

3.7.1 Adsorption:

Gas detection by metal-oxide based sensors is an adsorption and desorption process of the oxygen to the metal oxide surface as described in section 3.2. Adsorption is caused by the attractive force between the adsorbed species (adsorbate) and the solid surface of the metal oxide and must be stronger than the disordering effect of the thermal motion. Thermodynamically, adsorption is a spontaneous process, which means that the change in Gibb's free energy of the system is negative ($\Delta G<0$). This is because the translational freedom of the adsorbate is reduced when it is adsorbed causing the change in the entropy to be negative [39]. Adsorption can be of two types: physisorption and chemisorption which can be represented by the potential energy (PE) diagram (PE vs distance of adsorbate from the surface of the metal-oxide) as shown in Fig. 3.3. Physisorption is caused by the weak van der Waal's force with the enthalpy of adsorption ($\Delta H_{ads,\ phy}$) in the range -0.1 to -0.2 eV. In this case the weak forces give rise to a shallow PE well over a large distance from the surface (>0.3 nm), which is easily overwhelmed by the strong repulsive forces arising from the surface of the metal-oxide. Due to the low enthalpy change, physisorption does not cause a chemical reaction and this process is invariably fast [40]. Enthalpy of physisorption can be measured by the controlled monitoring of the rise in temperature of the sample of known thermal capacity [39]. Physisorption is represented by the Lennard-Jones potential. Chemisorption is caused by charge exchanges between the gaseous species, and the metal oxide and it is characterized by the dissociation of the adsorbate. Chemisorption also requires an activation energy. In the PE diagram, it is represented by the Morse potential and is characterized by the deep PE well over a short distance between the adsorbate and the metal oxide surface. The depth of the PE well corresponds to the enthalpy of chemisorption ($\Delta H_{ads,chem}$), a

typical value of which is around -2 eV. The activation energy of for chemisorption ($\Delta E_{ads,chem}$) ranges between -1 to -10 eV and it is represented by the transition from physisorption to chemisorption. Enthalpy of chemisorption can be measured by using single crystal adsorption calorimetry [41]. The equilibrium bond distance (z_e) between the adsorbate and the metal oxide surface is at the minimum PE. In the gas sensors described in this thesis (NO_2 sensing by γ-WO_3 in chapter 9 and acetone sensing by ε-WO_3 in chapter 10) the dominant adsorbate is oxygen. Hence the discussion henceforth will focus on oxygen adsorption. The bond dissociation energy of oxygen ($\Delta E_{diss,\,O}$) is 5.16 eV at 298K [42]. The oxygen is in molecular form (O_2^-) below 150°C and ionic form (O^-, O^{2-}) between 100–500°C. Oxygen chemisorption can be represented by the following equation [4]:

$$\frac{\beta}{2} O_2^{gas} + \alpha * e^- + S \leftrightarrow O_{\beta S}^{-\alpha} \quad \text{(E3.1)}$$

Where, O_2^{gas} = oxygen molecule in the atmosphere

e^- = electron with enough energy to reach the surface (surface charge)

S = surface oxygen vacancy or unoccupied chemisorption site for oxygen

$O_{\beta S}^{-\alpha}$ = chemisorbed oxygen species

α = 1 (singly ionized form), α = 2 (doubly ionized form),

β = 1 (atomic form), β = 2 (molecular form),

In the beginning before the adsorption process commence, there is an unlimited availability of electrons on the surface. Hence there is no band bending. After the adsorption of oxygen on the surface of the metal oxide, the space charge layer is developed (Schottky barrier) which needs to be overcome by the electron to reach the surface [4].

Rate of adsorption can be expressed as the following equation [40]:

$$R_{ads} = k_{ads} * P \quad \text{(E3.2)}$$

Where, k_{ads} = rate constant of adsorption and P = partial pressure of the adsorbate.

This can also be written in the Arrhenius form as:

$$R_{ads} = A * \exp(\frac{-E_{a,ads}}{RT}) * P \quad \text{(E3.3)}$$

Where, A = pre-exponential (frequency) factor; $E_{a,ads}$ = activation energy of adsorption, R = universal gas constant, T = temperature.

3.7.2 Desorption:

Desorption is controlled by both electronic and chemical parts from the beginning. In order for the adsorbate to desorb from the surface, a significant barrier is encountered. As shown in Fig. 3.3, $\Delta E_{dis} >> \Delta E_{ads}$. It can also be seen from Fig. 3.3 that $\Delta E_{des} \sim \Delta H_{ads, chem}$.

Rate of desorption can be expressed as the following equation [40]:

$$R_{des} = k_{des} * N \quad \text{(E3.4)}$$

Where, k_{ads} = rate constant of adsorption and N = surface concentration of the adsorbate.

This can also be written in the Arrhenius form as:

$$R_{des} = A * \exp(\frac{-E_{a,des}}{RT}) * N \quad \text{(E3.5)}$$

Where, A = pre-exponential (frequency) factor; $E_{a,des}$ = activation energy of desorption, R = universal gas constant, T = temperature.

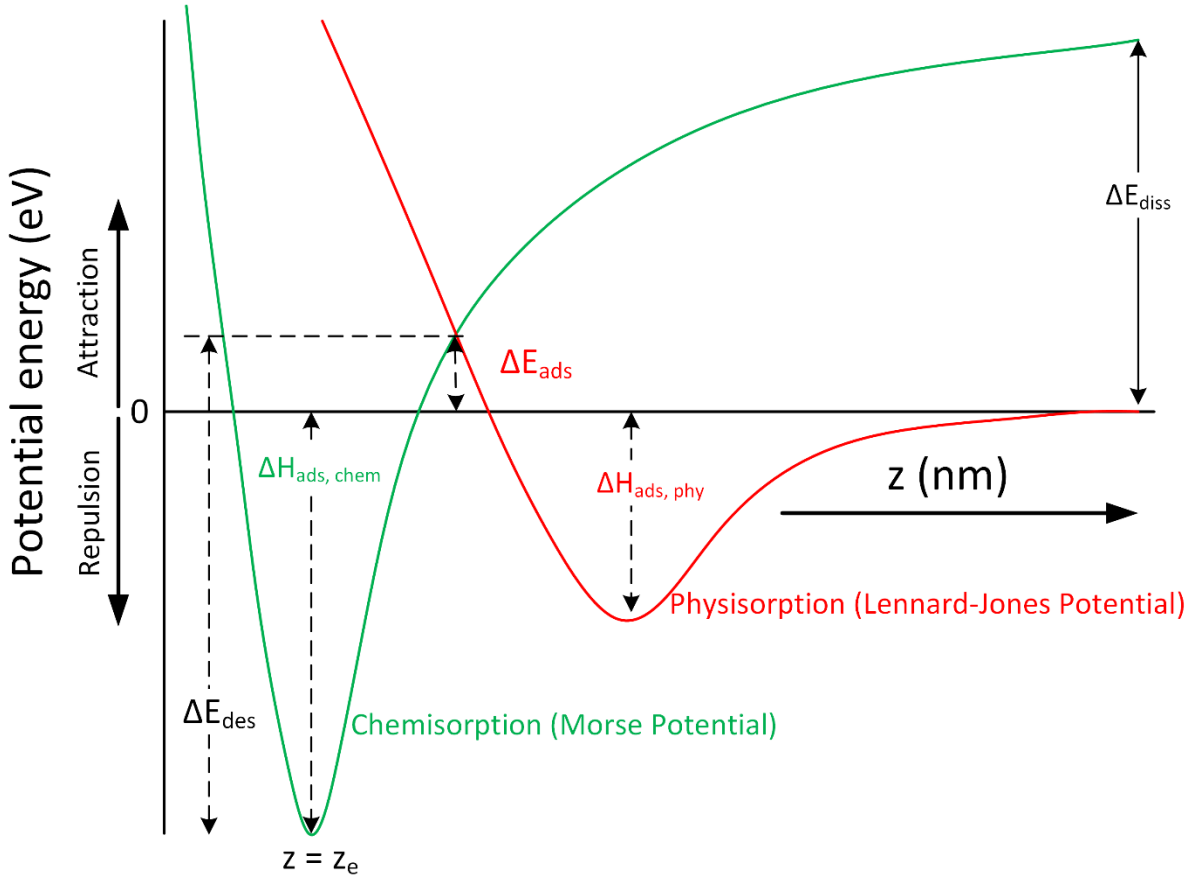

Fig. 3.3: The potential energy diagram showing adsorption and desorption energies.

3.7.3 Residence time:

The residence time of the adsorbate on the surface of the metal-oxide is an important property of the gas sensors. It is defined as the average time the adsorbate molecule will spend on the surface of the metal-oxide before been desorbed [40]. Residence time is given by the following equation:

$$t = t_0 * \exp(\frac{-\Delta H_{ads}}{RT}) \quad \text{(E3.6)}$$

Where, t = residence time in s, t_0 = 1/A = period of vibration of the bond between the adsorbate and the metal-oxide surface. The value for t_0 is ~10–13 s.

3.7.4 Debye length:

Debye length (λ_D) is defined as the radius of the imaginary sphere beyond which the charges are electrically screened. It is a property which depends upon the material. In a metal oxide, Debye length represents the distance over which band bending exists from the surface, as well as the thickness of depletion layer. The Debye length is determined by the following equation [43]:

$$\lambda_D = \sqrt{\frac{\varepsilon_0 \varepsilon_r k_B T}{q^2 n_c}} \quad \text{(E3.7)}$$

where ε_0 = Permittivity of free space = $8.854 * 10^{-12} \frac{\text{Farad}}{\text{m}}$,

ε_r = dielectric constant of the material

k_B = Boltzmann's constant = $1.38 * 10^{-23} \frac{\text{J}}{\text{K}}$, T = temperature

e = electron charge = $1.6 * 10^{-19}$ Coulombs, n_c = carrier concentration

Assuming *d* represents the diameter of a crystal grain and Λ represents the thickness of the electron depletion layer, ($\Lambda_{oxidizing}$ for oxidizing analyte, $\Lambda_{reducing}$ for reducing analyte, Λ_{air} for air), there are three conditions which are possible, which is shown in Fig. 3.4 and summarized below. It is also assumed that the grains are connected by necks or grain boundaries [44].

3.7.4.1 Grain boundary control:

When $d >> 2\Lambda$, the electron depletion layer only appears at the surface of the grain. In this case electrical resistance of the sensor is determined by the resistance of the grain boundary and the bulk has no contribution to the resistance [43]. This is because at the

grain boundary, two grains are present back to back and the thickness of the electron depletion layer is doubled.

3.7.4.2 Neck control:

When $d \geq 2\Lambda$, the neck contributes mostly to the resistance of the sensor. The bulk of the grain is still mostly unavailable.

3.7.4.3 Grain control:

When $d << 2\Lambda$, both the surface and bulk of the grain contributes to the resistance and yields the largest gas sensor response.

The thickness of electron depletion layer is related to the height of band bending (qV_s), and the Debye length by the following equation:

$$\Lambda = \lambda_D \left(\frac{2qV_s}{k_B T}\right)^{1/2} \quad \text{(E3.8)}$$

, the symbols defined previously.

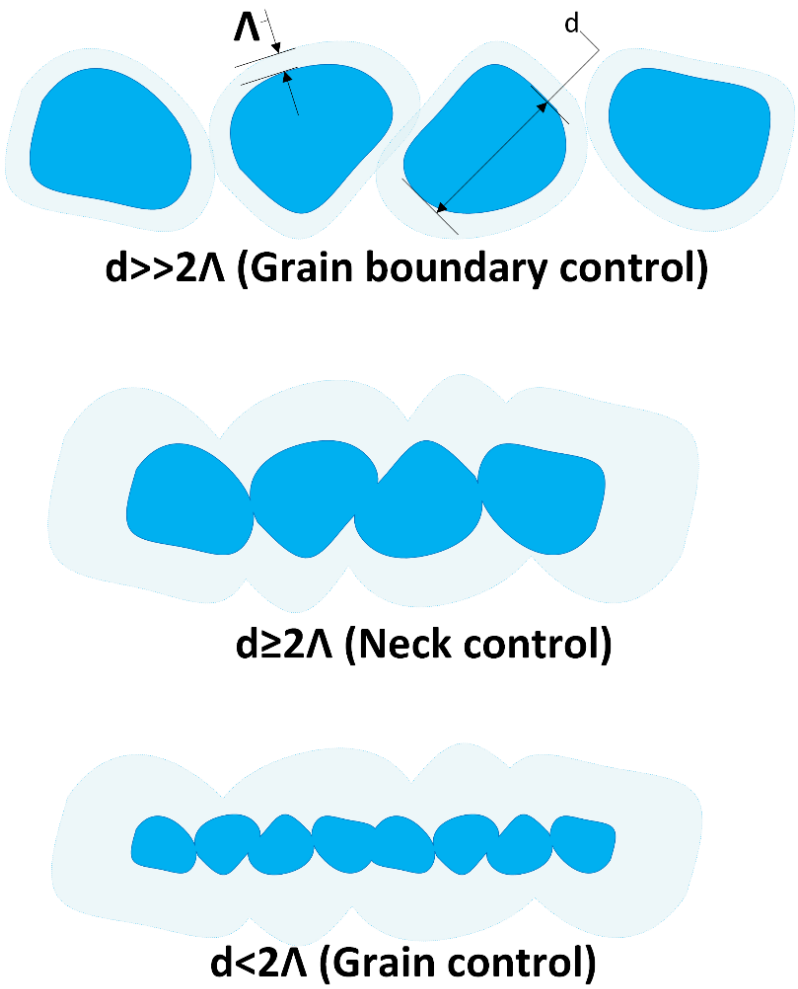

Fig. 3.4: Effect of grain size and necking in the electron depletion layer.

3.7.5 Film morphology:

Film morphology plays an important role in the sensitivity of the metal oxide film towards a particular analyte. Porous film allows an efficient diffusion of the analyte through the bulk of the film thereby creating a larger number of reaction sites. Three cases have been presented here:

3.7.5.1 Dense layer:

For a dense film the diffusion of the analyte only takes place on the surface. The active surface area is small. Even if the metal oxide layer is polycrystalline with $d<<2\Lambda$, they are not accessible by the gases, and they will not change when the ambient atmosphere composition changes. Conductivity of an ideal single crystal dense layer can be determined by the following equation [4]:

$$C = \text{constant} * \frac{q}{z_g} \int_0^{z_g} n(z) * \mu(z)\, dz, \qquad \text{(E3.9)}$$

Where the constant depends upon the sample geometry,

z_g = film thickness, n = charge concentration, and μ = electron mobility. The other symbols are as defined previously.

3.7.5.2 Porous layer:

For porous layers, the active surface area is much larger than the dense layers. The charge transport can take place by the either of the cases presented in section 3.7.4 and Fig. 3.4. Two different transport mechanism for the charge carriers was proposed for the porous layers by Barsan and Weimar [4]:

3.7.5.2.1 Diffusion theory:

According to the diffusion theory in porous layers, conductance is calculated by the following equation:

$$C_{diff} = area * \left(\frac{q^2 n_b \mu_b}{k_B T}\right) * \sqrt{\frac{q n_b V_s}{2\varepsilon}} * exp\left(\frac{-q v_s}{k_B T}\right) \qquad \text{(E3.10)}$$

Where “C” is the conductance and “area” has the dimensions in m^2 and represents the active area seen by the electrons while travelling from grain to grain. The subscript “b” represents bulk. The other symbols are as defined previously.

3.7.5.2.2 Thermoelectronic emission theory:

According to this theory, only the electrons which possess the kinetic energy greater than the band bending height can move across the boundary. The net current is the difference in the charge fluxes across the boundary from left to right and right to left respectively.

$$G_{thermo} = area * \left(\frac{q}{k_B T}\right) * q * \sqrt{\frac{8 * k_B * T}{\Pi * m'}} * exp\left(\frac{-q v_s}{k_B T}\right) \quad \text{(E3.11)}$$

Where, $\sqrt{\frac{8 * k_B * T}{\Pi * m'}}$ = mean thermal velocity of the carriers and m’ is the effective mass. The other symbols are as defined previously.

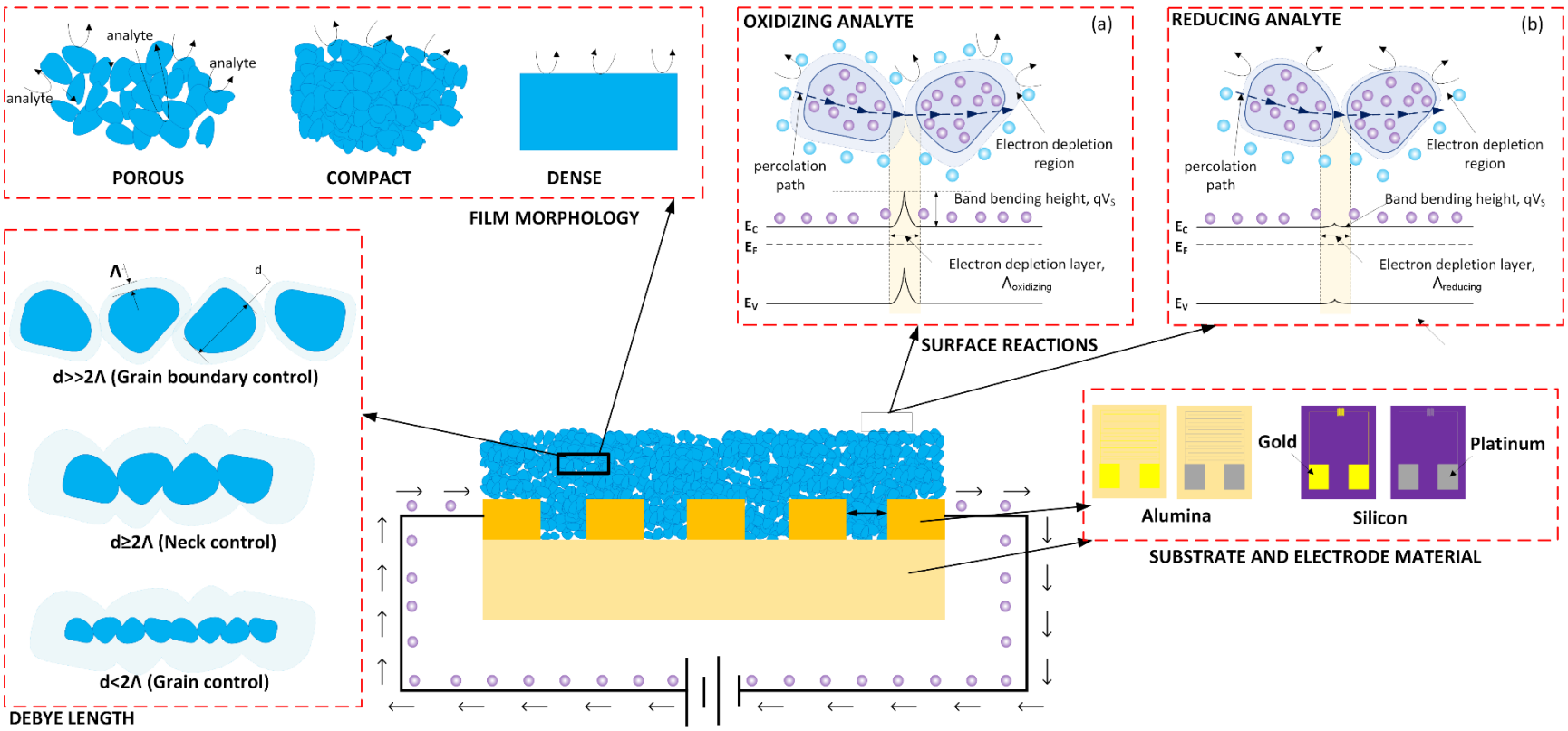

Fig. 3.5: Various factors responsible for the analyte sensing.

3.7.6 Metastable materials metal oxides:

Materials which are thermodynamically metastable at the given conditions of temperature and pressure are called metastable materials. Some of these materials possess unusual electronic properties. Synthesizing metastable materials require special synthesis conditions, such as extreme temperature, high pressure and/or rapid quenching. There are many metal oxides which are very good gas sensors in their metastable states as shown in the table below. The classical example is the ferroelectric ε-WO_3 which is metastable at room temperature and highly sensitive towards low concentration (<1 ppm) acetone. This is explained in more details in chapter 4 and chapter 10. A list of metastable metal oxides and the analytes which they sense are given in table 3.2.

Table 3.2: Metastable metal oxide based sensors along with the respective analyte.

Metal oxide	Metastable form	Sensing analyte	Reference
In_2O_3	Corundum-type hexagonal structure	Ethanol	[45]
WO_3	ε-WO_3 (Monoclinic)	Acetone	[14,46]
MoO_3	Monoclinic	Ammonia	[47]
SnO_2	$CaCl_2$-type orthorhombic phase	reducing gas: CO, H_2 and oxidizing gas: NO_2	[48]
ZrO_2	Tetragonal	reducing gas: CO, H_2 and oxidizing gas: NO_x.	[49]
TiO_2	Anatase	CO	[50]

3.8 References:

[1] S. Rajaram, Sensors: Technologies and Global Markets, Sensors: Technologies and Global Markets. IAS006D (Available at: http://www.bccresearch.com/market-research/instrumentation-and-sensors/sensors-technologies-markets-ias006d.html) (2011).

[2] L. Filipovic, S. Selberherr, Performance and Stress Analysis of Metal Oxide Films for CMOS-Integrated Gas Sensors, Sensors. 15 (4) (2015) 7206-7227.

[3] C.D. Kohl, Electronic Noses, in: R. Waser (Ed.), Nanoelectronics and Information Technology, Wiley-VCH, Berlin, 2005, pp. 835-864.

[4] N. Barsan, U. Weimar, Conduction Model of Metal Oxide Gas Sensors, Journal of Electroceramics. 7 (3) (2001) 143-167.

[5] S. Sharma, M. Madou, A new approach to gas sensing with nanotechnology, Philosophical Transactions of the Royal Society A. 370 (1967) (2012) 2448-2473.

[6] M.E. Franke, T.J. Koplin, U. Simon, Metal and metal oxide nanoparticles in chemiresistors: does the nanoscale matter? Small (Weinheim an der Bergstrasse, Germany). 2 (1) (2006) 36-50.

[7] M.J. Madou, S.R. Morrison, Chemical Sensing with Solid State Devices, 1st ed., Academic Press, New York, 1989.

[8] G. Korotcenkov, Metal oxides for solid-state gas sensors: What determines our choice? Materials Science and Engineering: B. 139 (1) (2007) 1-23.

[9] D. Barrettino, M. Graf, M. Zimmermann, C. Hagleitner, A. Hierlemann, H. Baltes, A Smart Single-Chip Micro-Hotplate-Based Gas Sensor System in CMOS-Technology, Analog Integrated Circuits and Signal Processing. 39 (3) (2004) 275-287.

[10] Y. Liu, J. Parisi, X. Sun, Y. Lei, Solid-state gas sensors for high temperature applications - a review, Journal of Materials Chemistry A. 2 (26) (2014) 9919-9943.

[11] G. Korotcenkov, Gas response control through structural and chemical modification of metal oxide films: state of the art and approaches, Sensors and Actuators B: Chemical. 107 (1) (2005) 209-232.

[12] M. Phillips, J. Herrera, S. Krishnan, M. Zain, J. Greenberg, R.N. Cataneo, Variation in volatile organic compounds in the breath of normal humans, Journal of Chromatography B: Biomedical Sciences and Applications. 729 (1–2) (1999) 75-88.

[13] C. Deng, J. Zhang, X. Yu, W. Zhang, X. Zhang, Determination of acetone in human breath by gas chromatography–mass spectrometry and solid-phase microextraction with on-fiber derivatization, Journal of Chromatography B. 810 (2) (2004) 269-275.

[14] L. Wang, A. Teleki, S.E. Pratsinis, P.I. Gouma, Ferroelectric WO_3 Nanoparticles for Acetone Selective Detection, Chemistry of Materials. 20 (15) (2008) 4794-4796.

[15] M. Righettoni, A. Tricoli, S. Gass, A. Schmid, A. Amann, S.E. Pratsinis, Breath acetone monitoring by portable Si: WO_3 gas sensors, Analytica Chimica Acta. 738 (2012) 69-75.

[16] P. Gao, H. Ji, Y. Zhou, X. Li, Selective acetone gas sensors using porous WO_3-Cr_2O_3 thin films prepared by sol-gel method, Thin Solid Films. 520 (7) (2012) 3100-3106.

[17] N.H. Al-Hardan, M.J. Abdullah, A. Abdul Aziz, H. Ahmad, L.Y. Low, ZnO thin films for VOC sensing applications, Vacuum. 85 (1) (2010) 101-106.

[18] S.V. Ryabtsev, A.V. Shaposhnick, A.N. Lukin, E.P. Domashevskaya, Application of semiconductor gas sensors for medical diagnostics, Sensors and Actuators B: Chemical. 59 (1) (1999) 26-29.

[19] K. Kim, P. Cho, S. Kim, J. Lee, C. Kang, J. Kim, S. Yoon, The selective detection of C_2H_5OH using SnO_2–ZnO thin film gas sensors prepared by combinatorial solution deposition, Sensors and Actuators B: Chemical. 123 (1) (2007) 318-324.

[20] Z. Jiang, Z. Guo, B. Sun, Y. Jia, M. Li, J. Liu, Highly sensitive and selective butanone sensors based on cerium-doped SnO_2 thin films, Sensors and Actuators B: Chemical. 145 (2) (2010) 667-673.

[21] J. Zhao, L. Huo, S. Gao, H. Zhao, J. Zhao, Alcohols and acetone sensing properties of SnO_2 thin films deposited by dip-coating, Sensors and Actuators B: Chemical. 115 (1) (2006) 460-464.

[22] S.S. Sehnert, L. Jiang, J.F. Burdick, T.H. Risby, Breath biomarkers for detection of human liver diseases: preliminary study, Biomarkers. 7 (2) (2002) 174-187.

[23] M. Phillips, R.N. Cataneo, R. Condos, G.A. Ring Erickson, J. Greenberg, V. La Bombardi, M.I. Munawar, O. Tietje, Volatile biomarkers of pulmonary tuberculosis in the breath, Tuberculosis (Edinburgh, Scotland). 87 (1) (2007) 44-52.

[24] M. Phillips, R.N. Cataneo, B.A. Ditkoff, P. Fisher, J. Greenberg, R. Gunawardena, C.S. Kwon, F. Rahbari-Oskoui, C. Wong, Volatile markers of breast cancer in the breath, Breast Journal. 9 (3) (2003) 184-191.

[25] M. Phillips, R.N. Cataneo, A.R. Cummin, A.J. Gagliardi, K. Gleeson, J. Greenberg, R.A. Maxfield, W.N. Rom, Detection of lung cancer with volatile markers in the breath, Chest. 123 (6) (2003) 2115-2123.

[26] S. Davies, P. Spanel, D. Smith, Quantitative analysis of ammonia on the breath of patients in end-stage renal failure, Kidney international. 52 (1) (1997) 223-228.

[27] M. Phillips, R.N. Cataneo, J. Greenberg, R. Grodman, M. Salazar, Breath markers of oxidative stress in patients with unstable angina, Heart disease (Hagerstown, Md.). 5 (2) (2003) 95-99.

[28] M. Phillips, J.P. Boehmer, R.N. Cataneo, T. Cheema, H.J. Eisen, J.T. Fallon, P.E. Fisher, A. Gass, J. Greenberg, J. Kobashigawa, D. Mancini, B. Rayburn, M.J. Zucker, Heart allograft rejection: detection with breath alkanes in low levels (the HARDBALL study), Journal of Heart and Lung Transplantation. 23 (6) (2004) 701-708.

[29] M. Phillips, M. Sabas, J. Greenberg, Increased pentane and carbon disulfide in the breath of patients with schizophrenia, Journal of Clinical Pathology. 46 (9) (1993) 861-864.

[30] Z.W. Weitz, A.J. Birnbaum, P.A. Sobotka, E.J. Zarling, J.L. Skosey, High breath pentane concentrations during acute myocardial infarction, Lancet (London, England). 337 (8747) (1991) 933-935.

[31] C.O. Olopade, M. Zakkar, W.I. Swedler, I. Rubinstein, Exhaled pentane levels in acute asthma, Chest. 111 (4) (1997) 862-865.

[32] S. Humad, E. Zarling, M. Clapper, J.L. Skosey, Breath pentane excretion as a marker of disease activity in rheumatoid arthritis, Free Radical Research Communications. 5 (2) (1988) 101-106.

[33] S. Sedghi, A. Keshavarzian, M. Klamut, D. Eiznhamer, E.J. Zarling, Elevated breath ethane levels in active ulcerative colitis: evidence for excessive lipid peroxidation, American Journal of Gastroenterology. 89 (12) (1994) 2217-2221.

[34] E. Baraldi, S. Carraro, Exhaled NO and breath condensate, Paediatric Respiratory Reviews. 7 Suppl 1 (2006) S20-2.

[35] S.A. Kharitonov, A.U. Wells, B.J. O'Connor, P.J. Cole, D.M. Hansell, R.B. Logan-Sinclair, P.J. Barnes, Elevated levels of exhaled nitric oxide in bronchiectasis, American Journal of Respiratory and Critical Care Medicine. 151 (6) (1995) 1889-1893.

[36] I. Horvath, S. Loukides, T. Wodehouse, S.A. Kharitonov, P.J. Cole, P.J. Barnes, Increased levels of exhaled carbon monoxide in bronchiectasis: a new marker of oxidative stress, Thorax. 53 (10) (1998) 867-870.

[37] W. Maziak, S. Loukides, S. Culpitt, P. Sullivan, S.A. Kharitonov, P.J. Barnes, Exhaled nitric oxide in chronic obstructive pulmonary disease, American Journal of Respiratory and Critical Care Medicine. 157 (3 Pt 1) (1998) 998-1002.

[38] M. Barker, M. Hengst, J. Schmid, H.J. Buers, B. Mittermaier, D. Klemp, R. Koppmann, Volatile organic compounds in the exhaled breath of young patients with cystic fibrosis, European Respiratory Journal. 27 (5) (2006) 929-936.

[39] P. Atkins, J. de Paula, R. Friedman, Physical Chemistry: Quanta, Matter, and Change, 2nd ed., Oxford University Press, United Kingdom, 2013.

[40] R.M. Nix, An Introduction to Surface Chemistry, Available at: http://www.chem.qmul.ac.uk/surfaces/scc/. 2015(11/21).

[41] S. Schauermann, T.L. Silbaugh, C.T. Campbell, Single-crystal adsorption calorimetry on well-defined surfaces: from single crystals to supported nanoparticles, Chemical record (New York, N.Y.). 14 (5) (2014) 759-774.

[42] B.B. Darwent, Bond Dissociation Energies in Simple Molecules, U.S. National Bureau of Standards, Washington DC, 1970.

[43] J. Tamaki, Z. Zhang, K. Fujimori, M. Akiyama, T. Harada, N. Miura, N. Yamazoe, Grain-Size Effects in Tungsten Oxide-Based Sensor for Nitrogen Oxides, Journal of Electroceramic Society. 141 (8) (1994) 2207-2210.

[44] C. Xu, J. Tamaki, N. Miura, N. Yamazoe, Grain size effects on gas sensitivity of porous SnO_2-based elements, Sensors and Actuators B: Chemical. 3 (2) (1991) 147-155.

[45] A. Gurlo, N. Barsan, U. Weimar, M. Ivanovskaya, A. Taurino, P. Siciliano, Polycrystalline Well-Shaped Blocks of Indium Oxide Obtained by the Sol−Gel Method and Their Gas-Sensing Properties, Chemistry of Materials. 15 (23) (2003) 4377-4383.

[46] M. Righettoni, A. Tricoli, S.E. Pratsinis, Si: WO_3 Sensors for Highly Selective Detection of Acetone for Easy Diagnosis of Diabetes by Breath Analysis, Analytical Chemistry. 82 (9) (2010) 3581-3587.

[47] A. K. Prasad. Study of gas specificity in molybdenum trioxide/tungsten oxide thin film sensors and their arrays (Doctoral dissertation). (2005).

[48] T. Sahm, L. Mädler, A. Gurlo, N. Barsan, S.E. Pratsinis, U. Weimar, Flame spray synthesis of tin dioxide nanoparticles for gas sensing, Sensors and Actuators B: Chemical. 98 (2–3) (2004) 148-153.

[49] E. Di Bartolomeo, M.L. Grilli, E. Traversa, Sensing Mechanism of Potentiometric Gas Sensors Based on Stabilized Zirconia with Oxide Electrodes: Is It Always Mixed Potential? Journal of the Electrochemical Society. 151 (5) (2004) H133-H139.

[50] M. Bendahan, J. Guerin, R. Boulmani, K. Aguir, WO_3 sensor response according to operating temperature: Experiment and modeling, Sensors and Actuators B: Chemical. 124 (1) (2007) 24-29.

CHAPTER 4:

Tungsten oxide nanoparticle thin films for gas and chemical sensors

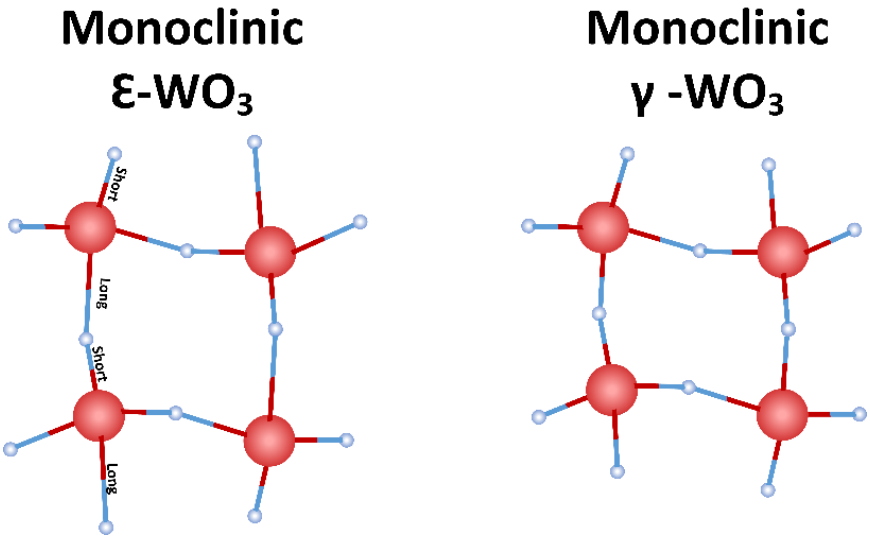

4.1 History of tungsten oxide:

Tungsten oxide also known as tungsten trioxide or tungsten (VI) oxide or tungstic anhydride with a chemical formula WO_3 is a semiconductor material which was discovered by Carl Wilhelm Scheele in late 1780's [1]. The word *tungsten* comes from the Swedish language *tung sten*, which directly translates to *heavy stone.* In 2012 China had a production capacity of 83% of the world's annual tungsten supply with the total world production estimated to be 74000 tonnes. The total US reserves are estimated to be 140,000 tonnes. It was Robert Oxland who described the procedure for preparing WO_3 and was granted a patent for his work in 1847 [2].

4.2 Structure of tungsten oxide:

WO_3 has a density of 7.16 g/cc, insoluble in water and melts at 1473°C [3]. WO_3 is an n-type semiconductor material with an indirect band gap of 3.3 eV in the amorphous form and 2.6 eV in the crystalline form [4]. It is known to exist in multiple polymorphs at different temperatures such as tetragonal (α) [5], orthorhombic (β) [6], monoclinic (ε and γ) [7, 8], triclinic (δ) [9, 10] and so called pseudo cubic [11] as shown in table 4.1. The structure of WO_3 is shown in Fig. 4.1. The main differences between the phases are shifts in the position of the W atoms within the octahedral, and variations in W-O bond lengths. The W ions occupy the corners of a primitive unit cell, and O ions bisect the unit cell edges. Each W ion is surrounded by six oxygen ions. The stable monoclinic γ-WO_3 can have a ReO_3-type structure (corner sharing arrangement of octahedra). An infinite array of corner-sharing WO_6 octahedra is formed. These octahedra are in planes perpendicular to the [001] hexagonal axis and they form four membered rings in the x-y or (001) plane. These layers are stacked in periodic arrangement and are held together by weak van de Waal´s forces. The stacking of such planes along the z axis leads to the formation of tunnels

between these octahedra as marked in Fig. 4.1. In the extended tunnel small ions can stay or move in response to an exterior force. This may present the possibility of ionic transport and intercalation in the structure, and a mechanism for the electron conducting materials [12].

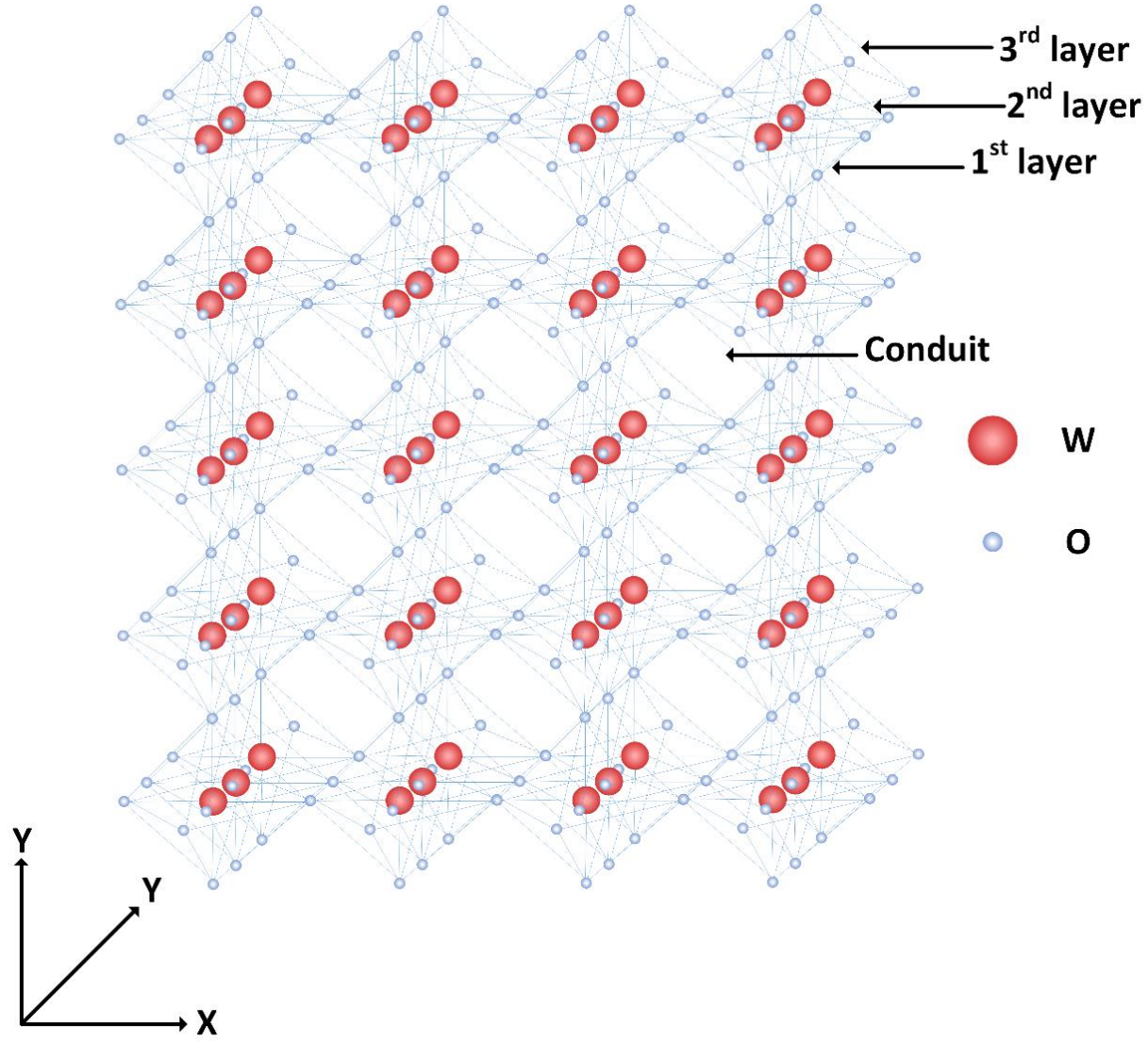

Fig. 4.1: Structure of WO_3 showing the existence of different layers of the octahedron and the formation of conduit.

Table 4.1: The unit cell parameters and temperature dependence for the existence of different phases of WO_3.

Phase	Symmetry	Space group	Z	Temperature (K)	Lattice parameters	Unit cell volume ($Å^3$)	Dipole moment	Reference
α	Tetragonal	P4/nmm	2	1010–1170	a = 5.3031 Å; c = 3.9348 Å	-	none	[5,13]
β	Orthorhombic	Pmnb	8	600–1170	a = 7.341 Å; b = 7.57 Å; c = 7.754 Å	-	none	[6]
γ	Monoclinic	$P2_1/n$	8	290–600	a = 7.306 Å; b = 7.54 Å; c = 7.692 Å; α = 90°; β = 90.88°; γ = 90°	423.7	none	[7,8]
δ	Triclinic	P1-	8	230–290	a = 7.3090 Å; b = 7.5165 Å; c = 7.6811 Å; α = 88.811°; β = 90.949°; γ = 90.985°	422.5	none	[9,10]
ε	Monoclinic	Pc	4	0–230	a = 7.378 Å; b = 7.378 Å; c = 7.664 Å; α = 88.73°; β = 91.27°; γ = 91.34°	417	2.5 ± 0.8 Debye	[7,8]

Table 4.2: The ICDD cards for ε-WO_3 and γ-WO_3.

ICDD# 01-087-2386 Structure: Monoclinic ε-WO_3 Space group: Pc				**ICDD# 01-043-1035 Structure: Monoclinic γ-WO_3 Space group: P21/n**			
2-theta (degrees)	**relative intensity (counts)**	**miller indices**	**d (Å)**	**2-theta (degrees)**	**relative intensity (counts)**	**miller indices**	**d (Å)**
23.20	46	002	3.83	23.12	100	002	3.84
24.12	100	110	3.69	23.59	97	020	3.77
29.01	10.4	012	3.08	24.38	99	200	3.65
33.34	23	-112	2.69	26.60	19	120	3.35
33.97	15.5	200	2.64	28.62	16	-112	3.12
34.08	24	112	2.63	28.94	17	112	3.08
34.76	10.8	020	2.58	33.27	39	022	2.69
49.39	12.7	220	1.84	33.58	27	-202	2.67
				34.16	62	220	2.62
				34.16	62	202	2.62
				41.44	14	-222	2.18
				41.91	14	222	2.15
				49.95	24	140	1.82
				49.95	24	400	1.82
				50.34	13	-114	1.81
				50.74	12	114	1.80
				53.49	12	-204	1.71
				53.49	12	024	1.71
				54.78	10	240	1.67
				55.81	10	142	1.65
				55.96	18	420	1.64
				56.11	15	402	1.64

WO_3 has mixed ionic and covalent bonding. The % ionic character can be calculated from the following equation [14]:

$$\% \text{ ionic character} = [1 - \exp\{-(0.25) * (X_A - X_B)^2\}] * 100 \quad \text{(E4.1)}$$

X_A and X_B are the Pauling's electro negativity of the element A and B respectively, the element A being more electronegative than element B. By putting A as oxygen (X_A = 3.5) and B as tungsten (X_B = 1.7) we calculate that WO_3 has a 55% ionic character. The structure of γ-WO_3 is given by the ICDD# 01-043-1035 and the structure of ε-WO_3 is given by the ICDD# 01-087-2386 as shown in table 4.2.

4.3 Properties and applications:

Each of the WO_3 crystal structure exhibits different electrical, optical and magnetic behaviors, which are favorable for particular applications. At room temperature, monoclinic and triclinic are the most common structures. In its defect free form it is transparent, however it appears colored because of defects in its structure [15]. The color changes at different temperatures and crystal structure forms. Color change can be explained by the change in band gap of WO_3 at various temperatures. Band gaps generally decrease with increases in temperature because of a reversible increase in atomic vibration with temperature [8]. The color of γ and δ WO_3 is light green—the mixture of light yellow and bluish white. The yellow component is due to the oxygen to tungsten charge transfer transition (valence band to conduction band transition) which is mainly in the UV but has a tail into the visible spectrum [8]. The bluish white component is due to the slight loss of oxygen which generates an additional valence state in the WO_3 parent structure, either W^{5+} or W^{4+} [16] . Exploitation of the many properties of WO_3 has evolved progressively over 3 centuries. Each of these properties is explained in brief with the purpose of directing the reader to the relevant literature. However this thesis will solely focus on the gas sensing nature of WO_3.

4.3.1 Chromogenic effect:

In 1969, SK Deb discovered the chromogenic effect of amorphous WO_3 [17]. He observed a reversible change in color of the WO_3 film on application of an electrical potential. In his paper Deb has described the construction of a solid state imaging device utilizing this electrochromic property. Deb's discovery paved the way for the development of products which benefit from this property such as smart windows for energy efficient infrastructures [12, 18], electronic information display devices [19], writing-reading-erasing devices, and flat panel displays. The smart windows utilize the principle of thermochromism in which the window glass is coated with a thin film of WO_3. This allows the passage of sun light but the infrared rays are reflected. Hence this provides heat protection. Other applications include high energy density microbatteries [20, 21], electro-catalysis, optoelectronics, microelectronics, and selective catalysis. Photo electrochemical and photo catalytic properties are enhanced when the WO_3 film is highly crystalline and preferentially oriented in the monoclinic phase because this structure will have fewer defects when acting as the recombination center and should suppress mutual e^--h^+ recombination [22, 23]. Polycrystalline WO_3 film has almost no photochromic sensitivity whereas amorphous WO_3 has high photochromic and electrochromic sensitivity due to high surface area [24, 25].

4.3.2 Photocatalytic property:

In 1976, Hodes et al. experimented with the photo catalytic property of WO_3 and its narrow optical band gap (2.8 eV) which allows for maximum absorption of the photons. They also argued that W is capable of reversibly changing its valence state to accommodate a hole without actually decomposing the semiconductor as opposed to having a single valence state in the semiconductor unlike Ti in TiO_2, Cd in CdS and Zn in ZnO [26].

4.3.3 Thermoelectric property:

Thermoelectric property of WO_3 is a recent discovery in the earlier part of this decade when Wang et al. [27] discovered that doping WO_3 with ceria improved the Seebeck coefficient. Since then many researchers have doped WO_3 with oxides bearing high thermopower and electrical conductivity such as ZnO [28], TiO_2 [29] and Co_2O_3 [30].

4.3.4 Sensing property:

Gas sensing property of WO_3 was discovered for the first time by Shaver, in 1967 when he observed a change in conductivity of Pt activated γ-WO_3 thin film in presence of low concentration of H_2. The d^0 configuration and strong catalytic effect of W cations enables WO_3 to be an excellent material for gas sensing.

Tungsten oxide (WO_3) thin films have been a subject of extensive scientific investigation following the discovery of WO_3's gas sensing properties in 1967 (H_2 [31], H_2S [32–38], NO_X [39–42], NH_3 [43–48], O_3 [49–52], CO [53–56]) and its suitability for use in breath acetone monitors as a tool for non-invasive blood glucose quantification[57–61]. For sensing functions, the WO_3 film needs to be porous and have a large surface area to enable the analytes to diffuse through the film [62]. The acentric nature and spontaneous electric dipole moment of ferroelectric ε-WO_3 leads to increased interaction with high dipole moment analytes such as acetone [8]. It is used for medical devices sensing the acetone level in human breath in concentrations of parts per billion (ppb) for non-invasive diabetes testing [59, 60]. However, some phases of WO_3 such as ε-monoclinic are metastable at room temperature and higher temperature, thereby making it challenging to obtain such phases by the traditional synthesis processes. The gas sensing property of WO_3 films strongly depends on the preparation method and the growing

conditions of the film itself. In order to have a high productivity, low resistance, and a low power consumption sensor, the current trend is to construct all sensing elements on a chip [63].

4.4 Gamma tungsten oxide for NO_2 sensors:

4.4.1 Requirement for NO_2 sensor:

NO_x (NO_2, NO) is a toxic air pollutant which is produced as a byproduct of gasoline combustion in an internal combustion engine [64]. Exposure to unsafe levels of NO_2 (>10 ppm) causes irritation in eyes, nose and throat, while higher exposure (>25 ppm) can cause severe reactions for people with underlying pulmonary diseases like Chronic Obstructive Pulmonary Disease (COPD) or asthma. NO_2 reacts with water droplets in the trachea and lungs and forms droplets of nitric acid. These tiny droplets of nitric acid penetrate deeply into the lungs and causes various respiratory diseases. NO_2 exposure has also being associated with Sudden Infant Death Syndrome (SIDS) [65]. A detailed report of the actual accidental release of NO_2 and its subsequent health effect on the population is provided by Bauer et al [66]. The United States Occupational Safety and Health Administration (OSHA) has set a 5 ppm workplace permissible exposure limit (PEL) for NO_2, time averaged over an 8 h. work shift. NO_2 also leads to the formation of ozone which is hazardous to both aquatic and terrestrial ecosystems. Current methods of quantification of NO_2 in the air includes gas chromatography equipped with mass spectroscopy (GC-MS) [67], chemiluminescence [68], differential optical absorption spectroscopy (DOAS) [69], laser induced fluorescence (LIF) [70], cavity ring down spectroscopy (CRDS) [71], and resonance enhanced multi photon ionization (REMPI) [72]. However, these analyses can be very expensive, requiring trained experts, and having complex, bulky and non-portable instrumentation. Metal-oxide semiconductor based gas sensors could be an effective solution to the underlying limitations faced by currently used methods for measuring NO_2. Metal oxide materials, such as

yttria stabilized zirconia (YSZ) [73], natrium superionic conductor (NASICON) [74], In_2O_3 [75], and WO_3 [76], have been used for NO_2 gas sensing. Among metal oxides, WO_3 is considered to be a good candidate for low concentration NO_2 sensing. Many synthesis procedures have been proposed for producing the WO_3 films for NO and NO_2 sensors. These include spray pyrolysis [77], drop coating [78], co-precipitation [79], sol-gel synthesis [80], plasma-enhance chemical vapor deposition (PECVD) [81], thermal evaporation [76, 82], and glancing angle DC magnetron sputtering [83]. NO_2 sensing by gamma tungsten oxide has been described in detail in chapter 9.

4.4.2 Mechanism of NO_2 sensing by γ-WO_3:

WO_3 film deposited interdigitated electrodes possesses both receptor and transducer functions, where the reaction of the NO_2 species takes place on the WO_3 film (receptor function) and the adsorbed NO_2 changes the resistance (transducer function) of the sensing film. This change in resistance can be correlated with the concentration of NO_2. The response (S) for NO_2 is calculated as the ratio of the resistance of the WO_3 film on gold interdigitated electrodes at different gas concentration and is given by the following equation [84]:

$$S = \frac{R_g}{R_a} \quad \text{(E4.2)}$$

Where, R_g is the resistance of the film in presence of NO_2 and R_a is the resistance of the film in air. Metal-oxide gas sensors based on this principle are one of the most studied gas sensor types because of its low cost of production, miniature size, low power consumption, and large number of applications [85]. The detailed mechanism of a n-type semiconductor thin film sensor is explained by Franke et al. [86] which can be used as a model to define the interaction between n-type WO_3 and NO_2. Fig. 4.2 depicts the mechanism. At elevated temperature, oxygen from the air is adsorbed on the WO_3 surface. Since a constant voltage is

applied externally on the WO_3 film, the electrons are exchanged from the conduction band of WO_3 to the adsorbed oxygen causing them to convert to ionosorbed species. Because of the presence of an unpaired electron in its outermost shell, NO_2 is a strong oxidizer, which supports the formation of ionosorbed oxygen [80] according to the following equations:

$$NO_2 + e^- = NO^+ + O_{ads}^{2-} \quad (<150°C) \tag{E4.3}$$

$$NO_2 + e^- = NO^+ + O_{ads}^{-} \quad (150–500°C) \quad [87] \tag{E4.4}$$

This causes the formation of an electron depletion region around the individual WO_3 particle, also known as space-charge layer, Λ_{gas} [88]. At the junction of two particles a larger electron depletion layer ($2 * \Lambda_{gas}$) is formed causing conduction band bending of WO_3 and the generation of a surface potential barrier (height of band bending qV_S). Since the electronic conduction occurs along a percolation path via particle to particle contact, presence of the large electron depletion region hampers the electron path causing an increase in overall WO_3 film resistance.

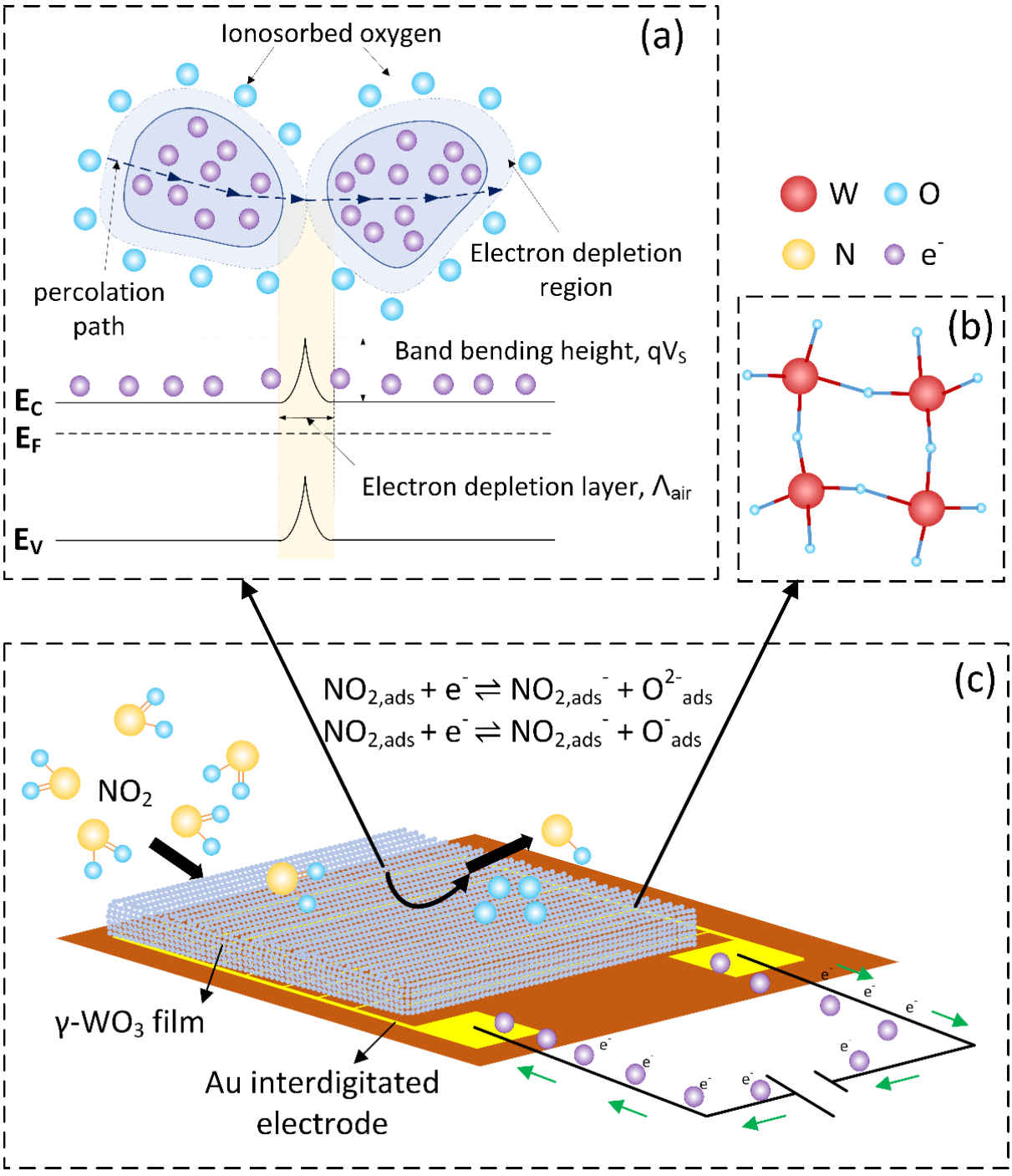

Fig. 4.2: Simplified model explaining the NO_2 sensing phenomenon by monoclinic γ-WO_3. (a) Band bending after ionosorption of oxygen. E_C, E_F and E_V denotes the energy of conduction band, Fermi level and valence band respectively. qV_S and $2\Lambda_{gas}$ denotes the band bending height and thickness respectively. (b) Structure of γ-WO_3. (c) γ-WO_3 thin film deposited on a gold interdigitated electrode.

4.5 Epsilon tungsten oxide for acetone sensing:

4.5.1 Requirement for acetone sensor:

Diabetes is a serious condition in which blood glucose level rises rapidly because of the inability of the body to produce and utilize enough insulin. There are hosts of other risks associated with diabetes including increased risk of heart stroke, kidney diseases, blindness and increased cholesterol level to name a few [89]. By the end of 2014 there were 387 million people world-wide suffering from diabetes and this statistic is expect to rise further to 592 Million by 2035 [89]. Diabetes was also responsible for 4.9 million deaths worldwide in 2014 [89]. An estimated $612 billion were spent worldwide on diabetes in 2014, roughly 11% of the total healthcare costs [90]. Presently, evaluation of blood by self-monitoring blood glucose (SMBG) devices is the predominant method for the detection of diabetes. SMBG is recognized by the American Diabetes Association as an essential part of effective diabetes self-management [91]. The American Diabetes Association recommends that the patients on multiple-dose insulin or insulin pump therapy should perform SMBG prior to meals and snacks, occasionally postprandially, at bedtime, prior to exercise, when they suspect low blood glucose, after treating low blood glucose until they are normoglycemic, and prior to critical tasks such as driving. This translates to SMBG device use frequency of 6–10 times per day [91]. However currently available SMBG devices are invasive and requires patients to prick their fingers to obtain a blood drop which is applied on a plastic test strip connected with a small electronic device. The test strip contains glucose oxidase, an enzyme which reacts with glucose in the blood. Glucose oxidase oxidizes glucose to gluconolactone ($C_6H_{10}O_6$) while reducing oxygen to H_2O_2. As the test strip is inserted into the device, the change in glucose oxidase is recorded which triggers an electrical signal calibrated with the amount of glucose and displayed on the device [92]. However this process is

very painstaking and expensive and the wounds are prone to infections. Moreover, the presence of other components in the blood such as ascorbic acid, uric acid, acetaminophen, and salicylic acid can oxidize the H_2O_2 thereby falsifying the results [93]. As of May 2015, the world wide SMBG business is dominated by four players- Abbot, Riche, J&J and Bayer, and the test strips market is expected to be valued at $10.9 billion by 2017 [94]. In 2009, the annual cost of test strip supplies for such SMBG devices was reported to be $772 per patient in the United States [95]. Generation of millions of pounds of used test strip as well as the needles used for pricking fingers, possess an additional threat to the environment since they are considered a biohazards and require proper disposal. Improper disposal of used test strips and needles can lead to needle-stick injuries (NSIs) among domestic waste handlers, rag pickers and the community. NSIs could lead to epidemics of blood-borne infections such as HIV/AIDS, hepatitis B and hepatitis C. The lancets used for SMBG are often loosely recapped and are vulnerable to be broken/detached when subjected to minimal force. According to the Centre for Disease Control, Atlanta, outbreaks of hepatitis B have been reported in non-hospital settings due to improper blood glucose monitoring practices [96]. It is also worth noting that there is a variability in blood sugar levels in finger tips (capillary blood) and forearms (arterial blood) caused by the diffusion of glucose from the plasma to the interstitial fluid as the blood circulates through the capillary system. This might indicate falsely low or high glucose levels [93]. Because of increasing costs and inconvenience to the patients, an alternative non-invasive route to detect diabetes has become indispensable.

4.5.2 Source of acetone in human body:

Acetone (CH_3-CO-CH_3) is one of the components present in trace quantity (0.5–10 ppm) in human breath. Acetone in breath is related to the glucose concentration in blood. In the human body, insulin is produced by the pancreas, which is responsible for the glucose

metabolism. In diabetic patients, the function of the pancreas to produce insulin is seriously hampered which causes an increase in blood glucose concentration. When it is unable to utilize glucose as an energy source, the body releases ketones to tap the body fat for energy. The partial oxidation of free fatty acids in the liver generates β-hydroxy- β-methylglutaryl-CoA (HMGCoA) and hydronium (H^+). HMGCoA converts into acetoacetate (AcAc) ($CH_3OCH_2OO^-$). Acetone is produced by decarboxylation of acetoacetate and the dehydrogenation of isopropanol in the liver [67, 97, 98] both of these reactions occurring because of the increased level of blood glucose.

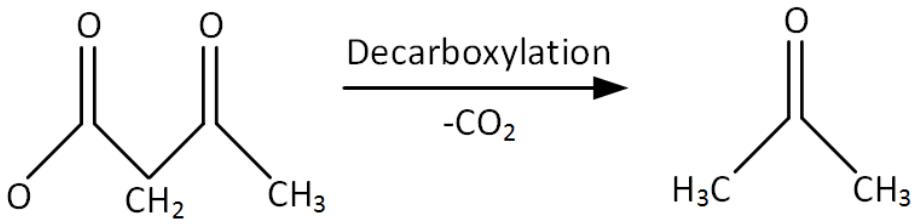

(E4.5)

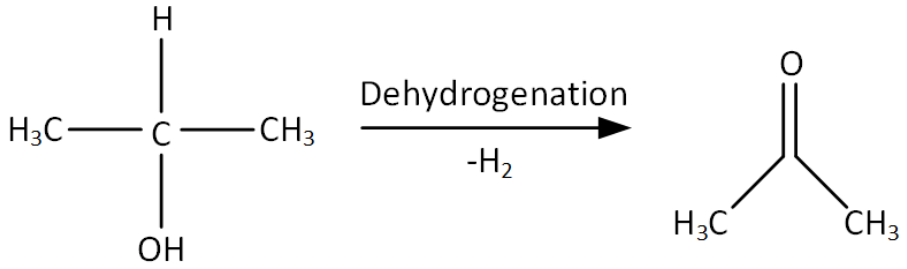

(E4.6)

This acetone in the blood is carried towards the lungs and eventually excreted with the exhaled breath [99]. Measurement of this acetone level can be used as a non-invasive tool to check the severity of type-I diabetes. Acetone concentration in human breath ranges from 0.5 ppm for healthy individuals and greater than 1.8 ppm for individuals with diabetes [100–102]. Quantifying such a low concentration of acetone with high selectivity and without cross sensitivity with other gases can prove challenging for available conductometric sensing capabilities.

4.5.2 Current technology for acetone and non-invasive diabetes monitoring:

Current methods of quantification of acetone includes bulky, non-portable and expensive measurements such as gas chromatography equipped with mass spectroscopy (GC-MS) [67], or proton transfer reaction-mass spectrometry (PTR-MS) [103] etc. and requires the patients to visit the laboratory to be tested. Since the time of writing this thesis in December 2015, there has been reports on the "internet" about many innovative non-invasive or minimally invasive routes for determining blood glucose concentration. These technologies, if successful has a high potential for eliminating the invasive blood glucose monitors and dramatically improve the quality of life for diabetes patients. Some of these technologies are: (1) Smart contact lens developed by Google, Inc. embedded with sensors to monitor blood glucose through tears [104], (2) Glucowizzard^{TM} developed by Biorasis, Inc. which consists of an ultra-small (0.5 mm by 0.5 mm by 5 mm) sensor implantable under the skin for continuous glucose monitoring (CGM) [105], (3) Continuous glucose monitoring system developed by Dexcom, Inc. [106], (4) Sweat meters for measuring glucose in sweat and correlating with blood glucose [107], and (5) urine strips to measure glucose in urine (the extra sugar in the bloodstream is usually only removed via the kidneys at blood sugar concentrations of 180 mg/dL or above) [108].

Metal oxide based gas sensors is one such device which has been used since 1960 for gas monitoring and can be utilized for breath acetone measurements. This device consists of Au or Pt interdigitated line electrodes on a silicon or alumina base [84]. A metal oxide semiconductor film with narrow band gap is deposited on the interdigitated lines and resistance across them is measured externally. The resistance increases in presence of oxidizing analytes and reduces in presence of reducing analytes (for n-type semiconductor metal oxide film).

4.5.2 Structure of acetone:

Acetone (CH_3-CO-CH_3) molecule has a triangular planar or AX3 geometry ("A" is the cation and "X" is the anion) since the carbon atom at the center is attached with three other atoms as shown in Fig. 4.3. The bond angles are 120°. In the acetone molecule, there is a double bond between the central carbon and the oxygen. The oxygen has two unshared electron pairs which make that end of the molecule highly negative. The bonds between the carbon-carbon atoms are single which are connected with three hydrogen atoms each, having positive charges. The uneven distribution of charges throughout the molecule makes it polar. The dipole moment of an acetone molecule is around 2.9 Debye (1 Debye = $3.34*10^{-30}$ coulomb meter = 0.20819434 eÅ = 10^{-18} esu) [109,110]. Because of its polarity, it is preferentially attracted by other polar molecules [8] such as monoclinic ε-WO_3.

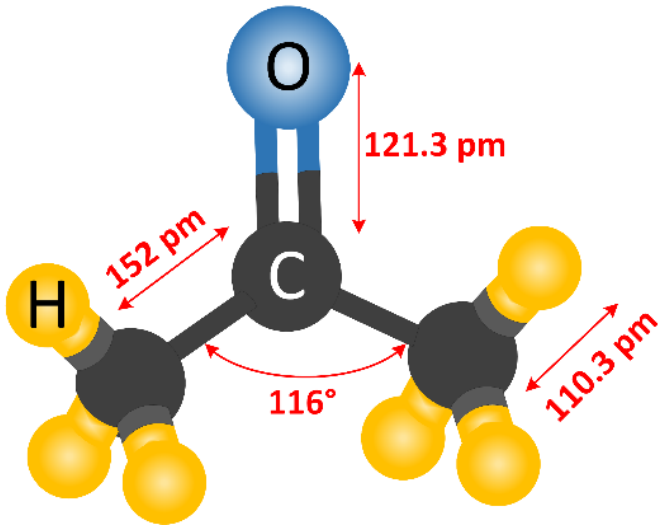

Fig. 4.3: The AX3 structure of acetone showing the bond lengths and the angles.

4.5.3 Structure of ε-WO_3:

The monoclinic ε-WO_3 is the only structure of WO_3 which is polar because of its acentricity [8]. The crystal structure of ε-WO_3 is shown in Fig. 4.4 as calculated by Salje et al., which highlights the distortions of the WO_6 octahedra caused by the displacements of the W atoms away from the center of the octahedra. It can be seen that there is an alternating pattern of long and short W-O bonds along z direction. This acentric structure causes a net electric dipole moment primary along the z direction which was calculated by neutron diffraction study conducted by Salje et al. in reference [7]. The final moment summed over the four W sites is 0:52 ± 0.16 e Å (2.5 ± 0.8 Debye). The alternative long and short bonds can be clearly seen in ε-WO_3 and absent in γ-WO_3 phase.

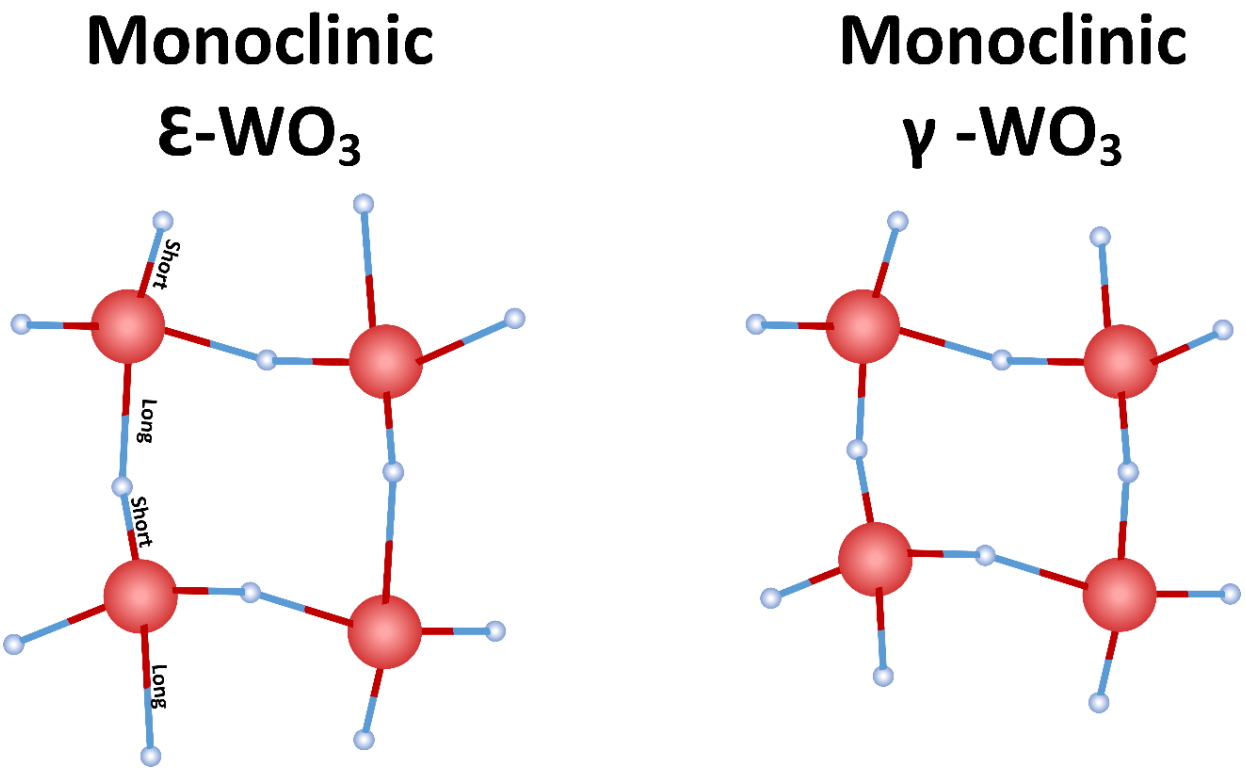

Fig. 4.4: The comparison of the structure of monoclinic ε-WO_3 and γ-WO_3 showing the origin of polarity in ε-WO_3 due to the shift of central W atom.

However ε-WO_3 is stable only at temperature below -40°C [7] which is far below the sensor operating temperature (400–500°C), and metastable at room temperature and higher temperature, thereby making it challenging to obtain such phases by the traditional synthesis processes. There have been various reports in literature which suggests various formulations to obtain this phase in metastable form at room temperature and temperature up to 735°C. Levine et al. (1956) formulated the metastable ε-WO_3 at room temperature by adding 2–4% Ta_2O_5 in WO_3 [111]. Roth and Waring (1966) conducted a series of experiments by changing the composition of niobia (Nb_2O_5) in a solid solution with WO_3 and found that WO_3 can only accept a maximum of 3 mol% of Nb_2O_5 in the solid solution. They also determined that, by varying the concentration of Nb_2O_5, all the available polymorphs could be obtained at room temperature. They obtained ε-WO_3 at a concentration of 2 mol% Nb_2O_5 and 98 mol% WO_3 after rapidly quenching the sample in a beaker of water from 1230–1385°C to room temperature. The structure was stable up to 735°C after which it experienced a reversible transformation directly to tetragonal α-WO_3 [112]. More recently, Wang et al. (2008) obtained 80% ε-WO_3 after doping 10 atomic % Cr_2O_3 to WO_3 and after rapidly quenching in a flame spray pyrolysis system. The structure was stable till 700°C after which it transformed directly to tetragonal α-WO_3 [60, 61]. In a similar study, Righettoni et al. (2010) obtained 70% ε-WO_3 by rapidly quenching the undoped WO_3 particles in flame spray pyrolysis and 100% ε-WO_3 by doping 10 mol% amorphous SiO_2 to WO_3. However the ε-WO_3 structure was stable only till 400°C for undoped WO_3 and till 500°C for SiO_2 doped WO_3 [113]. Gao et al. (2012) obtained ε-WO_3 at room temperature by a sol-gel technique after rapidly cooling the sample from 700°C to room temperature [114]. Since ε-WO_3 is acentric, the only reason for its existence at room temperature could be that the tungsten atoms are shifted from their thermodynamically stable positions in the WO_6 octahedra, resulting in the formation of net

polarity in the molecule. From all the cases above it is clear that quenching plays an important role for obtaining ε-WO_3 at room temperature. During rapid quenching, the tungsten atoms may not have enough time to settle in their stable positions and it also causes the formation of internal stress in the structure. It should be also noted that in all the above mentioned cases the WO_3 particles were in the nano regime with grain size less than 30 nm. Nanometer size particles tends to contain a higher concentration of defects and deformation during the crystal growth than micron sized particles [115]. Doping with foreign particles like Nb_2O_5, Cr_2O_3 and SiO_2 causes the preservation of this stress in the structure at high temperature, and reduces the driving force for this phase transformation. For example, Cr atoms favor attachment on the particle surface to form chromates which form a layer around each WO_3 particle and prevent phase transformation till 400°C [60]. Doping with SiO_2 leads to the formation of amorphous SiO_2 domain around WO_3 particles which inhibit the growth of WO_3 grain boundaries due to the large difference in thermal expansion coefficient (α) between SiO_2 ($\alpha = 0.55–0.75*10^{-6}/°C$) and WO_3 ($\alpha = 12*10^{-6}/°C$). [59]. This has been explained in details in chapter 8.

4.6 Mechanism of acetone sensing by ε-WO_3:

Fig. 4.5 explains the mechanism of interaction between acetone and ε-WO_3 as supported by Barsan and Weimar [87,116,117]. Both acetone and ε-WO_3 are polar ($\mu_{acetone}$ = 2.9 Debye; $\mu_{\varepsilon\text{-}WO3} = 2.5 \pm 0.8$ Debye). Hence acetone is preferentially attracted to the ε-WO_3. Moreover, since W^{6+} in WO_3 is a Lewis acid site, it readily adsorbs acetone which is a Lewis base [118]. On applying a constant electric potential across a sensing electrode coated with WO_3, and on exposing it to air at a temperature about 350–400°C, there is a constant flow of oxygen ions (O^{2-}, O^-) and the oxygen is ionosorbed on the WO_3 surface. This also fills the oxygen vacancies in

WO_3. The ionosorbed oxygen removes the electron from the conduction band of WO_3 as described in the equations below:

$$O_2(\text{gas}) \Leftrightarrow O_2(\text{absorbed}) \quad \text{(E4.7)}$$

$$O_2(\text{absorbed}) + e^- \Leftrightarrow O_2^- \quad \text{(E4.8)}$$

$$O_2^- + e^- \Leftrightarrow 2O^- \quad \text{(E4.9)}$$

The ionosorbed oxygen also forms a layer around individual WO_3 crystallites. This results in the formation of an electron depletion layer, also known as space-charge layer, (Λ_{gas}) [88]. At the junction of two particles a larger electron depletion layer ($2 * \Lambda_{gas}$) is formed causing conduction band bending of WO_3 and the generation of a surface potential barrier (height of band bending qV_S). Since the electronic conduction occurs along a percolation path via particle to particle contact, presence of the large electron depletion region hampers the electron path causing an increase in overall WO_3 film resistance. Acetone vapor is a strong reducing agent. When the air supply to the electrode is replaced with a mixture of acetone/air, and the acetone is readily oxidized, thereby reducing the ionosorbed oxygen concentration on the WO_3 surface. This causes the release of the electron back to the conduction band of WO_3 and a reduction in the size of the electron depletion layer, resulting in the reduction in the film resistance. Following equations describe the reaction pathways between acetone and WO_3 as suggested by Khadayate et al. [119]:

$$CH_3COCH_3(\text{gas}) + O^-_{\text{adsorbed}} \rightarrow CH_3COC^+H_2 + OH^- + e^- \quad \text{(E4.10)}$$

$$CH_3COCH_3\ (\text{gas}) + OH^- \rightarrow CH_3CHO + CH_3O^- \quad \text{(E4.11)}$$

$$CH_3CHO + O_{\text{bulk}} \rightarrow CH_3COOH + O_{\text{vacancies}} \quad \text{(E4.12)}$$

OR

$$CH_3COCH_3\ (gas) + O^- \rightarrow CH_3C^+O + e^- \quad \text{(E4.13)}$$

$$CH_3C^+O \rightarrow C^+H_3 + CO \quad \text{(E4.14)}$$

$$CO + O^- \rightarrow CO_2 + e^- \quad \text{(E4.15)}$$

It is clear from the above that the most important element for these reactions is the oxygen, either from the air or the lattice oxygen from WO_3. An interesting study by Labidi et al. on replacing oxygen with nitrogen attests to this fact [120].

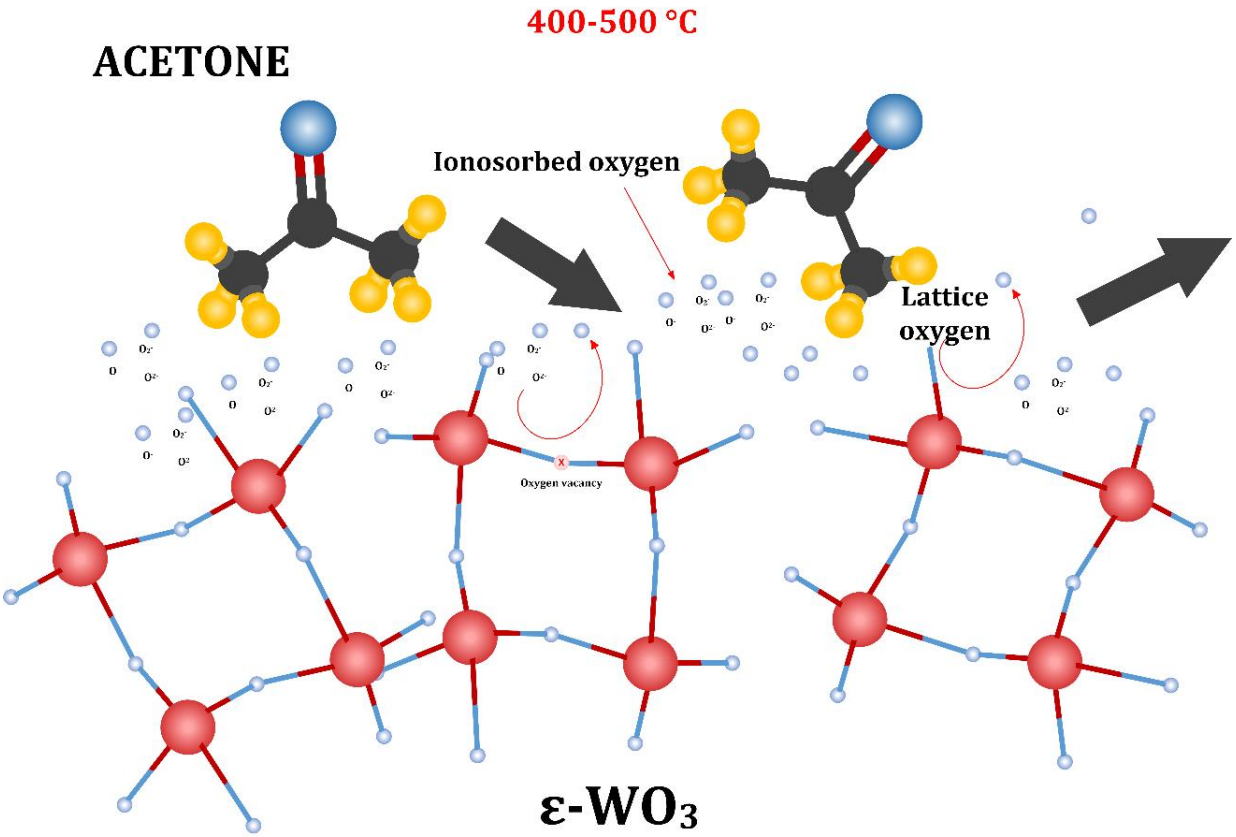

Fig. 4.5: Mechanism of the interaction between acetone and ε-WO_3.

4.7 References:

[1] P. Patnaik, Tungsten, McGraw Hill, New York, 2003.

[2] R. Oxland, Improvements partly applicable to the manufacture of metallic alloys, British Patent. (11848) (1847).

[3] 8 - Thermochemical data, in: W.F. Gale, T.C. Totemeier (Eds.), Smithells Metals Reference Book (Eighth Edition), Butterworth-Heinemann, Oxford, 2004, pp. 1-58.

[4] A. Doménch-Carbó, Michael A. Carpenter, Sanjay Mathur and Andrei Kolmakov (Eds.): Metal oxide nanomaterials for chemical sensors, Analytical and Bioanalytical Chemistry. 405 (12) (2013) 3917-3918.

[5] W.L. Kehl, R.G. Hay, D. Wahl, The Structure of Tetragonal Tungsten Trioxide, Journal of Applied Physics. 23 (2) (1952) 212-215.

[6] E.K.H. Salje, The orthorhombic phase of WO_3, Acta Crystallographica: B. 33 (1977) 574.

[7] E.K.H. Salje, S. Rehmann, F. Pobell, D. Morris, K.S. Knight, T. Herrmannsdörfer, M.T. Dove, Crystal structure and paramagnetic behaviour of ε–WO_{3-x}, Journal of Physics: Condensed Matter. 9 (31) (1997) 6563.

[8] P.M. Woodward, A.W. Sleight, T. Vogt, Ferroelectric Tungsten Trioxide, Journal of Solid State Chemistry. 131 (1) (1997) 9-17.

[9] P.M. Woodward, A.W. Sleight, T. Vogt, Structure refinement of triclinic tungsten trioxide, Journal of Physics and Chemistry of Solids. 56 (10) (1995) 1305-1315.

[10] R. Diehl, G. Brandt, E. Salje, The crystal structure of triclinic WO_3, Acta Crystallographica: B. 34 (1978) 1105-1111.

[11] I. Jiménez, J. Arbiol, G. Dezanneau, A. Cornet, J.R. Morante, Crystalline structure, defects and gas sensor response to NO_2 and H_2S of tungsten trioxide nanopowders, Sensors and Actuators B: Chemical. 93 (1–3) (2003) 475-485.

[12] H. N. Cui. Preparation and characterization of optical multilayered coatings for smart windows applications (Doctoral dissertation). University of Minho. Retrieved from: http://www.rcaap.pt/detail.jsp?id=oai:repositorium.sdum.uminho.pt:1822/3341 (2005).

[13] K.R. Locherer, I.P. Swainson, E.K.H. Salje, Transition to a new tetragonal phase of WO_3: crystal structure and distortion parameters, Journal of Physics: Condensed Matter. 11 (21) (1999) 4143.

[14] W.D. Callister, D.G. Rethwisch, Atomic Structure and Interatomic Bonding, in: Anonymous Materials Science and Enginering an Introduction, 8th ed., John Wiley and Sons, Inc., USA, 2010, pp. 33.

[15] M. Weil, W. Schubert, The Beautiful Colours of Tungsten Oxides, International Tungsten Industry Association. June (2013).

[16] R. Tilley, Colour and the Optical Properties of Materials, 1st ed., John Wiley & Sons, Ltd., England, Colour and the optical properties of Materials.

[17] S.K. Deb, A Novel Electrophotographic System, Applied Optics. 8 (1969) 192-195.

[18] J.S.E.M. Svensson, C.G. Granqvist, Electrochromic coatings for smart windows: Crystalline and amorphous WO_3 films, Thin Solid Films. 126 (1–2) (1985) 31-36.

[19] B.W. Faughnan, R.S. Crandall, Electrochromic displays based on WO_3, in: J.I. Pankove (Ed.), Springer Berlin Heidelberg, 1980, pp. 181-211.

[20] H. Varella, F. Huguenin, M. Malta, R.M. Torresi, Quimica Nova. 25 (2002) 287.

[21] B.C. Trasferetti, F.P. Rouxinol, R.V. Gelamo, d.M. Bica, C.U. Davanzo, de Faria, Dalva L. A., Berreman Effect in Amorphous and Crystalline WO_3 Thin Films, Journal of Physical Chemistry B. 108 (33) (2004) 12333-12338.

[22] J. Liu, X. Dong, X. Liu, F. Shi, S. Yin, T. Sato, Solvothermal synthesis and characterization of tungsten oxides with controllable morphology and crystal phase, Journal of Alloys and Compounds. 509 (5) (2011) 1482-1488.

[23] H. Kominami, J. Kato, S. Murakami, Y. Ishii, M. Kohno, K. Yabutani, T. Yamamoto, Y. Kera, M. Inoue, T. Inui, B. Ohtani, Solvothermal syntheses of semiconductor photocatalysts of ultra-high activities, Catalysis Today. 84 (3–4) (2003) 181-189.

[24] A.I. Gavrilyuk, Photochromism in WO_3 thin films, Electrochimica Acta. 44 (18) (1999) 3027-3037.

[25] S. Lee, H.M. Cheong, J. Zhang, A. Mascarenhas, D.K. Benson, S.K. Deb, Electrochromic mechanism in a-WO_{3-y} thin films, Applied Physics Letters. 74 (2) (1999) 242-244.

[26] G. Hodes, D. Cahen, J. Manassen, Tungsten trioxide as a photoanode for a photoelectrochemical cell (PEC), Nature. 260 (5549) (1976) 312-313.

[27] H. Wang, Z. Hua, S. Peng, X. Dong, L. Dong, Y. Wang, Effect of CeO_2 on the thermoelectric properties of WO_3-based ceramics, Ceramics International. 38 (2) (2012) 1133-1137.

[28] H. Wang, X. Dong, S. Peng, L. Dong, Y. Wang, Improvement of thermoelectric properties of WO_3 ceramics by ZnO addition, Journal of Alloys and Compounds. 527 (2012) 204-209.

[29] H. Wang, Y. Gan, X. Dong, S. Peng, L. Dong, Y. Wang, Thermoelectric properties of Ti-doped WO_3 ceramics, Journal of Materials Science-Materials in Electronics. 23 (12) (2012) 2229-2234.

[30] X. Dong, H. Wang, Z. Hua, S. Peng, L. Dong, Y. Wang, Thermoelectric properties of WO_3-based ceramics doped with Co_2O_3, Journal of Materials Science: Materials in Electronics. 23 (6) (2012) 1210-1214.

[31] M.Z. Ahmad, J.H. Kang, A.Z. Sadek, A. Moafi, G. Sberveglieri, W. Wlodarski, Synthesis of WO_3 Nanorod based Thin Films for Ethanol and H_2 Sensing, Procedia Engineering. 47 (0) (2012) 358-361.

[32] Z.Y. Sun, H.Q. Yuan, Z.M. Liu, B.X. Han, X.R. Zhang, A highly efficient chemical sensor material for H_2S: alpha-Fe_2O_3 nanotubes fabricated using carbon nanotube templates, Advanced Materials. 17 (24) (2005) 2993-2997.

[33] L.M. Kuo, Y. Shih, C. Wu, Y. Lin, S. Chao, A new hybrid method for H_2S-sensitive devices using WO_3-based film and ACF interconnect, Measurement Science & Technology. 24 (7) (2013) 075105.

[34] C.M. Ghimbeu, M. Lumbreras, M. Siadat, J. Schoonman, Detection of H_2S, SO_2, and NO_2 using electrostatic sprayed tungsten oxide films, Materials Science in Semiconductor Processing. 13 (1) (2010) 1-8.

[35] R. Ionescu, A. Hoel, C.G. Granqvist, E. Llobet, P. Heszler, Ethanol and H_2S gas detection in air and in reducing and oxidising ambience: application of pattern recognition to analyse the output from temperature-modulated nanoparticulate WO_3 gas sensors, Sensors and Actuators B: Chemical. 104 (1) (2005) 124-131.

[36] I.M. Szilagyi, S. Saukko, J. Mizsei, A.L. Toth, J. Madarasz, G. Pokol, Gas sensing selectivity of hexagonal and monoclinic WO_3 to H_2S, Solid State Sciences. 12 (11) (2010) 1857-1860.

[37] L. Geng, Gas sensitivity study of polypyrrole/WO_3 hybrid materials to H_2S, Synthetic Metals. 160 (15-16) (2010) 1708-1711.

[38] S.D. Han, I. Singh, H.S. Kim, S.T. Kim, Y.H. Jung, B.K. Kim, H_2S gas sensing characteristics of WO_3 thick-films, Indian Journal of Chemistry Section A-Inorganic Bio-Inorganic Physical Theoretical & Analytical Chemistry. 41 (9) (2002) 1832-1836.

[39] M. Ono, K. Shimanoe, N. Miura, N. Yamazoe, Amperometric sensor based on NASICON and NO oxidation catalysts for detection of total NOx in atmospheric environment, Solid State Ionics. 136 (2000) 583-588.

[40] K. Shimizu, K. Kashiwagi, H. Nishiyama, S. Kakimoto, S. Sugaya, H. Yokoi, A. Satsuma, Impedancemetric gas sensor based on Pt and WO_3 co-loaded TiO_2 and ZrO_2 as total NO_x sensing materials, Sensors and Actuators B: Chemical. 130 (2) (2008) 707-712.

[41] S.P. Mondal, P.K. Dutta, G.W. Hunter, B.J. Ward, D. Laskowski, R.A. Dweik, Development of high sensitivity potentiometric NO_x sensor and its application to breath analysis, Sensors and Actuators B: Chemical. 158 (1) (2011) 292-298.

[42] J.J. Ho, Novel nitrogen monoxides (NO) gas sensors integrated with tungsten trioxide (WO_3)/pin structure for room temperature operation, Solid-State Electronics. 47 (5) (2003) 827-830.

[43] N.V. Hieu, D. Le, N.D. Khoang, N.V. Quy, N.D. Hoa, P.D. Tam, A. Le, T. Trung, A comparative study on the NH_3 gas-sensing properties of ZnO, SnO_2, and WO_3 nanowires, International Journal of Nanotechnology. 8 (3-5) (2011) 174-187.

[44] B.T. Marquis, J.F. Vetelino, A semiconducting metal oxide sensor array for the detection of NO_x and NH_3, Sensors and Actuators B: Chemical. 77 (1-2) (2001) 100-110.

[45] E. Maciak, Z. Opilski, T. Pustelny, M. Bednorz, An optical detection NH_3 gas by means of a-WO_3 thin films based on SPR technique, Journal De Physique IV (Proceedings). 129 (2005) 131-136.

[46] I. Jimenez, A.M. Vila, A.C. Calveras, J.R. Morante, Gas-sensing properties of catalytically modified WO_3 with copper and vanadium for NH_3 detection, IEEE Sensors Journal. 5 (3) (2005) 385-391.

[47] V. Srivastava, K. Jain, Highly sensitive NH_3 sensor using Pt catalyzed silica coating over WO_3 thick films, Sensors and Actuators B: Chemical. 133 (1) (2008) 46-52.

[48] M. D'Arienzo, L. Armelao, C.M. Mari, S. Polizzi, R. Ruffo, R. Scotti, F. Morazzoni, Macroporous WO_3 Thin Films Active in NH_3 Sensing: Role of the Hosted Cr Isolated Centers and Pt Nanoclusters, Journal of the American Chemical Society. 133 (14) (2011) 5296-5304.

[49] J. Guerin, A. Bendahan, K. Aguir, A dynamic response model for the WO_3-based ozone sensors, Sensors and Actuators B: Chemical. 128 (2) (2008) 462-467.

[50] W.M. Qu, W. Wlodarski, A thin-film sensing element for ozone, humidity and temperature, Sensors and Actuators B: Chemical. 64 (1-3) (2000) 42-48.

[51] A. Labidi, M. Gaidi, J. Guerin, A. Bejaoui, M. Maaref, K. Aguir, Alternating current investigation and modeling of the temperature and ozone effects on the grains and the grain boundary contributions to the WO_3 sensor responses, Thin Solid Films. 518 (1) (2009) 355-361.

[52] M. Bendahan, R. Boulmani, J.L. Seguin, K. Aguir, Characterization of ozone sensors based on WO_3 reactively sputtered films: influence of O_2 concentration in the sputtering gas and working temperature, Sensors and Actuators B: Chemical. 100 (3) (2004) 320-324.

[53] M.F. Al-Kuhaili, S.M.A. Durrani, I.A. Bakhtiari, Carbon monoxide gas-sensing properties of CeO_2-WO_3 thin films, Materials Science and Technology. 26 (6) (2010) 726-731.

[54] H. Fukuda, R. Zohnishi, S. Nomura, Highly sensitive metal-insulator-semiconductor field-effect transistor sensors for detecting carbon monoxide gas using porous platinum and tungsten

oxide thin films, Japanese Journal of Applied Physics Part 1-Regular Papers Short Notes & Review Papers. 40 (4B) (2001) 2782-2786.

[55] M.I. Baraton, L. Merhari, H. Ferkel, J.F. Castagnet, Comparison of the gas sensing properties of tin, indium and tungsten oxides nanopowders: carbon monoxide and oxygen detection, Materials Science & Engineering C-Biomimetic and Supramolecular Systems. 19 (1-2) (2002) 315-321.

[56] G.E. Buono-Core, A.H. Klahn, G. Cabello, E. Munoz, M.J. Bustamante, C. Castillo, B. Chornik, Pt/WO_3 thin films prepared by photochemical metal-organic deposition (PMOD) and its evaluation as carbon monoxide sensor, Polyhedron. 41 (1) (2012) 134-139.

[57] M. Righettoni, A. Tricoli, S. Gass, A. Schmid, A. Amann, S.E. Pratsinis, Breath acetone monitoring by portable Si: WO_3 gas sensors, Analytica Chimica Acta. 738 (2012) 69-75.

[58] M. Righettoni, A. Schmid, A. Amann, S.E. Pratsinis, Correlations between blood glucose and breath components from portable gas sensors and PTR-TOF-MS, Journal of Breath Research. 7 (3) (2013) 037110.

[59] M. Righettoni, A. Tricoli, S.E. Pratsinis, Thermally Stable, Silica-Doped ε-WO_3 for Sensing of Acetone in the Human Breath, Chemistry of Materials. 22 (10) (2010) 3152-3157.

[60] L. Wang, A. Teleki, S.E. Pratsinis, P.I. Gouma, Ferroelectric WO_3 Nanoparticles for Acetone Selective Detection, Chemistry of Materials. 20 (15) (2008) 4794-4796.

[61] L. Wang, K. Kalyanasundaram, M. Stanacevic, P. Gouma, Nanosensor Device for Breath Acetone Detection, Sensor Letters. 8 (1-4) (2010) 709-712.

[62] Z. Liu, T. Yamazaki, Y. Shen, T. Kikuta, N. Nakatani, Influence of annealing on microstructure and NO_2-sensing properties of sputtered WO_3 thin films, Sensors and Actuators B: Chemical. 128 (1) (2007) 173-178.

[63] G. García J., C.A. Jara, J. Pomares, A. Alabdo, L.M. Poggi, F. Torres, A Survey on FPGA-Based Sensor Systems: Towards Intelligent and Reconfigurable Low-Power Sensors for Computer Vision, Control and Signal Processing, Sensors (Basel, Switzerland). 14 (4) (2014) 6247-6278.

[64] G.A. Bishop, D.H. Stedman, Measuring the Emissions of Passing Cars, Accounts of Chemical Research. 29 (10) (1996) 489-495.

[65] H. Klonoff-Cohen, P.K. Lam, A. Lewis, Outdoor carbon monoxide, nitrogen dioxide, and sudden infant death syndrome, Archives of Disease in Childhood. 90 (7) (2005) 750-753.

[66] U. Bauer, D. Berg, M.A. Kohn, R.A. Meriwether, R.A. Nickle, Acute effects of nitrogen dioxide after accidental release, Public health reports. 113 (1) (1998) 62-70.

[67] O. B. Crofford, R. E. Mallard, R. E. Winton, N. L. Rogers, J. C. Jackson, and U. Keller, Acetone in breath and blood, Transactions of the American Clinical and Climatological Association. 88 (1977) 128-139.

[68] K.L. Demerjian, A review of national monitoring networks in North America, Atmospheric Environment. 34 (12–14) (2000) 1861-1884.

[69] H. Edner, P. Ragnarson, S. Spännare, S. Svanberg, Differential optical absorption spectroscopy (DOAS) system for urban atmospheric pollution monitoring, Applied Optics. 32 (3) (1993) 327-333.

[70] J.A. Thornton, P.J. Wooldridge, R.C. Cohen, Atmospheric NO_2: In Situ Laser-Induced Fluorescence Detection at Parts per Trillion Mixing Ratios, Analytical Chemistry. 72 (3) (2000) 528-539.

[71] T. Stacewicz, J. Wojtas, Z. Bielecki, M. Nowakowski, J. Mikołajczyk, R. Mędrzycki, B. Rutecka, Cavity ring down spectroscopy: detection of trace amounts of substance, Opto-Electronics Review. 20 (1) (2012) 53-60.

[72] G. Villena, I. Bejan, R. Kurtenbach, P. Wiesen, J. Kleffmann, Development of a new Long Path Absorption Photometer (LOPAP) instrument for the sensitive detection of NO_2 in the atmosphere, Atmospheric Measurement Techniques. 4 (2011) 1663-1676.

[73] Y. Guan, C. Li, X. Cheng, B. Wang, R. Sun, X. Liang, J. Zhao, H. Chen, G. Lu, Highly sensitive mixed-potential-type NO_2 sensor with YSZ processed using femtosecond laser direct writing technology, Sensors and Actuators B: Chemical. 198 (2014) 110-113.

[74] S. Yao, J.R. Stetter, Modification of NASICON Solid Electrolyte for NO_x Measurements, Journal of Electroceramic Society. 151 (4) (2004) H75-H80.

[75] L. Gao, Z. Cheng, Q. Xiang, Y. Zhang, J. Xu, Porous corundum-type In_2O_3 nanosheets: Synthesis and NO_2 sensing properties, Sensors and Actuators B: Chemical. 208 (2015) 436-443.

[76] T. Siciliano, A. Tepore, G. Micocci, A. Serra, D. Manno, E. Filippo, WO_3 gas sensors prepared by thermal oxidization of tungsten, Sensors and Actuators B: Chemical. 133 (1) (2008) 321-326.

[77] V.V. Ganbavle, S.V. Mohite, G.L. Agawane, J.H. Kim, K.Y. Rajpure, Nitrogen dioxide sensing properties of sprayed tungsten oxide thin film sensor: Effect of film thickness, Journal of Colloid and Interface Science. 451 (2015) 245-254.

[78] T. Akamatsu, T. Itoh, N. Izu, W. Shin, NO and NO_2 Sensing Properties of WO_3 and Co_3O_4 Based Gas Sensors, Sensors (Basel, Switzerland). 13 (9) (2013) 12467-12481.

[79] D.S. Lee, S.D. Han, S.M. Lee, J.S. Huh, D.D. Lee, The TiO_2-adding effects in WO_3-based NO_2 sensors prepared by coprecipitation and precipitation method, Sensors and Actuators B: Chemical. 65 (1-3) (2000) 331-335.

[80] P.I. Gouma, K. Kalyanasundaram, A selective nanosensing probe for nitric oxide, Applied Physics Letters. 93 (24) (2008) 244102.

[81] M.S. Tong, G.R. Dai, Y.D. Wu, X.L. He, D.S. Gao, WO_3 thin film prepared by PECVD technique and its gas sensing properties to NO_2, Journal of Materials Science. 36 (10) (2001) 2535-2538.

[82] W. Gao, Y. Ling, X. Liu, J. Sun, Simple point contact WO_3 sensor for NO_2 sensing and relevant impedance analysis, International Journal of Minerals, Metallurgy and Materials. 19 (12) (2012) 1142-1148.

[83] M. Horprathum, K. Limwichean, A. Wisitsoraat, P. Eiamchai, K. Aiempanakit, P. Limnonthakul, N. Nuntawong, V. Pattantsetakul, A. Tuantranont, P. Chindaudom, NO_2-sensing properties of WO_3 nanorods prepared by glancing angle DC magnetron sputtering, Sensors and Actuators B: Chemical. 176 (2013) 685-691.

[84] C.D. Kohl, Electronic Noses, in: R. Waser (Ed.), Nanoelectronics and Information Technology, Wiley-VCH, Berlin, 2005, pp. 835-864.

[85] C. Wang, L. Yin, L. Zhang, D. Xiang, R. Gao, Metal Oxide Gas Sensors: Sensitivity and Influencing Factors, Sensors (Basel, Switzerland). 10 (3) (2010) 2088-2106.

[86] M.E. Franke, T.J. Koplin, U. Simon, Metal and metal oxide nanoparticles in chemiresistors: does the nanoscale matter? Small (Weinheim an der Bergstrasse, Germany). 2 (1) (2006) 36-50.

[87] N. Barsan, U. Weimar, Conduction Model of Metal Oxide Gas Sensors, Journal of Electroceramics. 7 (3) (2001) 143-167.

[88] S. Sharma, M. Madou, A new approach to gas sensing with nanotechnology, Philosophical Transactions of the Royal Society A. 370 (1967) (2012) 2448-2473.

[89] Centers for Disease Control and Prevention, National Diabetes Statistics Report: Estimates of Diabetes and Its Burden in the United States, (2014).

[90] International Diabetes Federation, Diabetes: Facts and Figures, (http://www.idf.org/node/2294) (2014).

[91] American Diabetes Association, Standards of Medical Care in Diabetes—2015, Journal of Clinical and Applied Research and Education. 38 (2015) S1-S93.

[92] J. Hönes, P. Müller, N. Surridge, The technology behind glucose meters: test strips, Diabetes Technology & Therapeutics. 10 (S1) (2008) S10-S26.

[93] E. Cengiz, W.V. Tamborlane, A Tale of Two Compartments: Interstitial Versus Blood Glucose Monitoring, Diabetes Technology & Therapeutics. 11 (2009) S11-S16.

[94] Blood Glucose Meters - Pipeline Review, 2015, GlobalData. 3165401(http://www.rnrmarketresearch.com/blood-glucose-meters-pipeline-review-2015-market-report.html.) (February 2015) 1-259.

[95] J. Yeaw, W.C. Lee, M. Aagren, T. Christensen, Cost of self-monitoring of blood glucose in the United States among patients on an insulin regimen for diabetes, Journal of Managed Care Pharmacy. 18 (1) (2012) 21-32.

[96] Center for Disease Control, Atlanta, Healthcare-Associated Hepatitis B and C Outbreaks Reported to the Centers for Disease Control and Prevention (CDC), (2008-2013) Available from: http://www.cdc.gov/hepatitis/Outbreaks/PDFs/HealthcareInvestigationTable.pdf.

[97] Z. Wang, C. Wang, Is breath acetone a biomarker of diabetes? A historical review on breath acetone measurements. Journal of Breath Research. 7 (3) (2013) 037109.

[98] O.E. Owen, V.E. Trapp, C.L. Skutches, M.A. Mozzoli, R.D. Hoeldtke, G. Boden, G.A. Reichard Jr, Acetone metabolism during diabetic ketoacidosis, Diabetes. 31 (3) (1982) 242-248.

[99] G.E. Umpierrez, M.B. Murphy, A.E. Kitabchi, Diabetic Ketoacidosis and Hyperglycemic Hyperosmolar Syndrome, Diabetes Spectrum. 15 (1) (2002) 28-36.

[100] A.M. Diskin, P. Španěl, D. Smith, Time variation of ammonia, acetone, isoprene and ethanol in breath: a quantitative SIFT-MS study over 30 days, Physiological Measurement. 24 (1) (2003) 107.

[101] C. Deng, J. Zhang, X. Yu, W. Zhang, X. Zhang, Determination of acetone in human breath by gas chromatography–mass spectrometry and solid-phase microextraction with on-fiber derivatization, Journal of Chromatography B. 810 (2) (2004) 269-275.

[102] American Diabetes Association, Management of dyslipidemia in children and adolescents with diabetes, Diabetes care JID - 7805975. (0330).

[103] J. King, A. Kupferthaler, K. Unterkofler, H. Koc, S. Teschl, G. Teschl, W. Miekisch, J. Schubert, H. Hinterhuber, A. Amann, Isoprene and acetone concentration profiles during exercise on an ergometer, Journal of Breath Research. 3 (2) (2009) 027006.

[104] F. Honoré, B. Otis, A. Nelson, Reader Communication with Contact Lens Sensors and Display Device, US Patent. US 14/536,856 (US20150061837 A1) (2015).

[105] R.A. Croce Jr, S. Vaddiraju, J. Kondo, Y. Wang, L. Zuo, K. Zhu, S.K. Islam, D.J. Burgess, F. Papadimitrakopoulos, F.C. Jain, A miniaturized transcutaneous system for continuous glucose monitoring, Biomedical Microdevices. 15 (1) (2013) 151-160.

[106] M.C. Shults, S.J. Updike, R.K. Rhodes, Device and method for determining analyte levels, (2011).

[107] J. Moyer, D. Wilson, I. Finkelshtein, B. Wong, R. Potts, Correlation between sweat glucose and blood glucose in subjects with diabetes, Diabetes technology & therapeutics. 14 (5) (2012) 398-402.

[108] S.H. Golden, T. Brown, H.C. Yeh, N. Maruthur, P. Ranasinghe, Z. Berger, Y. Suh, L.M. Wilson, E.B. Haberl, E.B. Bass, Methods for Insulin Delivery and Glucose Monitoring:

Comparative Effectiveness, AHRQ Comparative Effectiveness Reviews. 12-EHC036-EF (Number 57) (2012).

[109] R.D. Nelson, Selected Values of Electric Dipole Moments for Molecules in the Gas Phase Electronic Resource] / Ralph D. Nelson, Jr., and David R. Lide, Jr., and Arthur A. Maryott, U.S. Dept. of Commerce, National Bureau of Standards : For sale by the Supt. of Docs., U.S. G.P.O, Washington, D.C, 1967.

[110] O. Dorosh, Z. Kisiel, Electric Dipole Moments of Acetone and of Acetic Acid Measured in Supersonic Expansion, Acta Physica Polonica A. 112 (2007) S-95-S-106.

[111] S. Levine, R. Corwin, L.H. Blood, Polarization and Electromechanical Activity in Sintered WO_3, Bulletin of the American Physical Society Series II. 1(55) (1956) 255.

[112] R.S. Roth, J.L. Waring, Phase equilibria as related to crystal structure in the system niobium pentoxide-tungsten trioxide, Journal of Research of the National Bureau of Standards, Section A: Physics and Chemistry. 70A (4) (1966) 281-304.

[113] M. Righettoni, A. Tricoli, S.E. Pratsinis, Si: WO_3 Sensors for Highly Selective Detection of Acetone for Easy Diagnosis of Diabetes by Breath Analysis, Analytical Chemistry. 82 (9) (2010) 3581-3587.

[114] P. Gao, H. Ji, Y. Zhou, X. Li, Selective acetone gas sensors using porous WO_3-Cr_2O_3 thin films prepared by sol-gel method, Thin Solid Films. 520 (7) (2012) 3100-3106.

[115] M. Arai, S. Hayashi, K. Yamamoto, S.S. Kim, Raman Studies of Phase-Transitions in Gas-Evaporated WO_3 Microcrystals, Solid State Communications. 75 (7) (1990) 613-616.

[116] N. Barsan, D. Koziej, U. Weimar, Metal oxide-based gas sensor research: How to? Sensors and Actuators B: Chemical. 121 (1) (2007) 18-35.

[117] M. Huebner, C.E. Simion, A. Haensch, N. Barsan, U. Weimar, CO sensing mechanism with WO_3 based gas sensors, Sensors and Actuators B: Chemical. 151 (1) (2010) 103-106.

[118] D.M. Griffiths, C.H. Rochester, Infrared study of the adsorption of acetone on rutile, Journal of the Chemical Society, Faraday Transactions 1: Physical Chemistry in Condensed Phases. 74 (1978) 403-417.

[119] R.S. Khadayate, V. Sali, P.P. Patil, Acetone vapor sensing properties of screen printed WO_3 thick films, Talanta. 72 (3) (2007) 1077-1081.

[120] A. Labidi, C. Lambert-Mauriat, C. Jacolin, M. Bendahan, M. Maaref, K. Aguir, dc and ac characterizations of WO_3 sensors under ethanol vapors, Sensors and Actuators B: Chemical. 119 (2) (2006) 374-379.

SECTION II:

Pt/CERIA CATALYSTS FOR LOW TEMPERATURE WATER-GAS SHIFT REACTION

CHAPTER 5:

Synthesis of Pt nanoparticles onto Ceria Support as Catalyst for Water-Gas Shift Reaction by Reactive Spray Deposition Technology

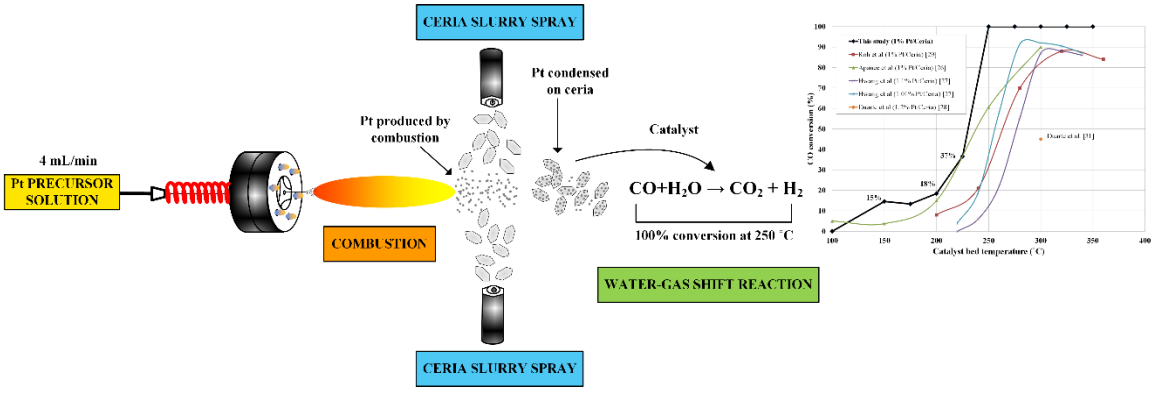

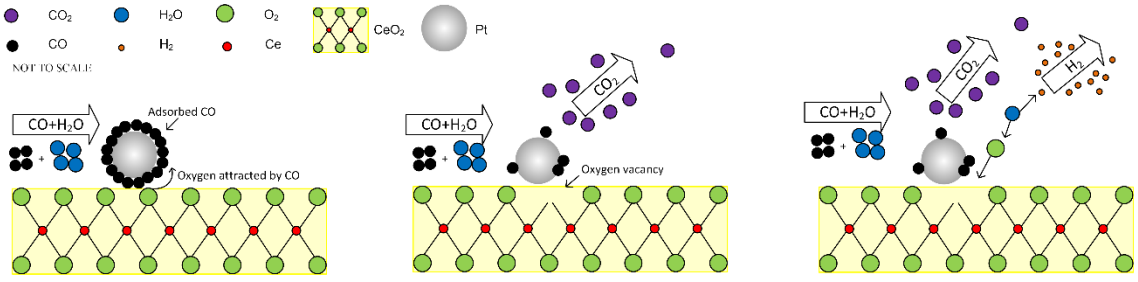

(a) Step 1: CO is adsorbed on the Pt surface.

(b) Step 2: Oxygen vacancy is formed with the formation of 2 Ce^{3+} and release of CO_2

(c) Step 3: Oxygen vacancy is filled by an oxygen provided by H_2O molecule with the release of H_2. Ce^{3+} is re-oxidized to Ce^{4+}

5.1 Highlights:

1. 1 wt% Pt nanoparticles on ceria were synthesized using RSDT for water-gas shift reaction.

2. Catalyst was tested with 1 vol% CO, 3 vol% H_2O in the range 100–400°C.

3. No sintering or agglomerations of Pt nanoparticles was evident from HRTEM.

4. Complete CO conversion was obtained at 250°C at GHSV of 8622 h^{-1}.

5. RSDT prepared catalyst showed a 40% activity boost over conventional catalysts.

5.2 Abstract:

Reactive Spray Deposition Technology (RSDT) was employed to synthesize 1 wt% Pt of 0.5–2 nm onto ceria of 8–30 nm. The catalyst was evaluated for water-gas shift (WGS) reaction with 1 vol% CO & 3 vol% H_2O, atmospheric pressure, temperature range (100–350°C) and gas hourly space velocity (GHSV) of 8622 h^{-1}. CO conversion of 15% (150°C), 18% (200°C), 37% (225°C) and 100% (250°C) was observed. Comparison with conventionally prepared catalysts (sol-gel, co-precipitation, and incipient wetness impregnation) from literature revealed superior activity with RSDT synthesized catalysts. Catalyst morphology was investigated with TGA, ICP-OES, XRD, TPR, HRTEM, and SEM with XEDS. No evidence of sintering or agglomeration of Pt nanoparticles was observed in HRTEM which could account for the dramatic improvement in activity.

5.3 Keywords:

Water-Gas Shift Reaction; Ceria Supported Platinum Catalyst; CO Conversion; Reactive Spray Deposition Technology; High resolution transmission electron microscopy

5.4 Introduction:

The RSDT for Pt based electro catalyst clearly have shown that the process can be adjusted to give precise control (<1 nm) metallic nanoparticle diameter. The studies also showed that specific activity for O_2 reduction varied non-monotonically with particle size showing a relatively sharp peak in specific Pt activity at 2.2 nm diameter [1–3]. Here we report the comparison of the WGS activity of nanocrystalline Pt/ceria catalyst prepared by RSDT with the results reported in literature by conventional wet chemistry processes: sol-gel, co-precipitation, and incipient wetness impregnation. Microstructure and morphology of the catalyst was characterized for thermogravimetric analysis (TGA), inductively coupled plasma optical emission spectroscopy (ICP-OES), X-ray diffraction (XRD), temperature programmed reduction (TPR) with hydrogen, scanning electron microscopy (SEM), and high resolution transmission electron microscopy (HRTEM) with X-ray energy dispersive spectroscopy (XEDS). The work presented in this chapter was presented at the Microscopy and Microanalysis (M&M) 2013 meeting at, Indianapolis, Indiana at symposium P04.P1: Deriving Fundamental Catalyst Properties from Electron Microscopy as a poster# 198. This work is also published in *Applied Catalysis A: General* [4].

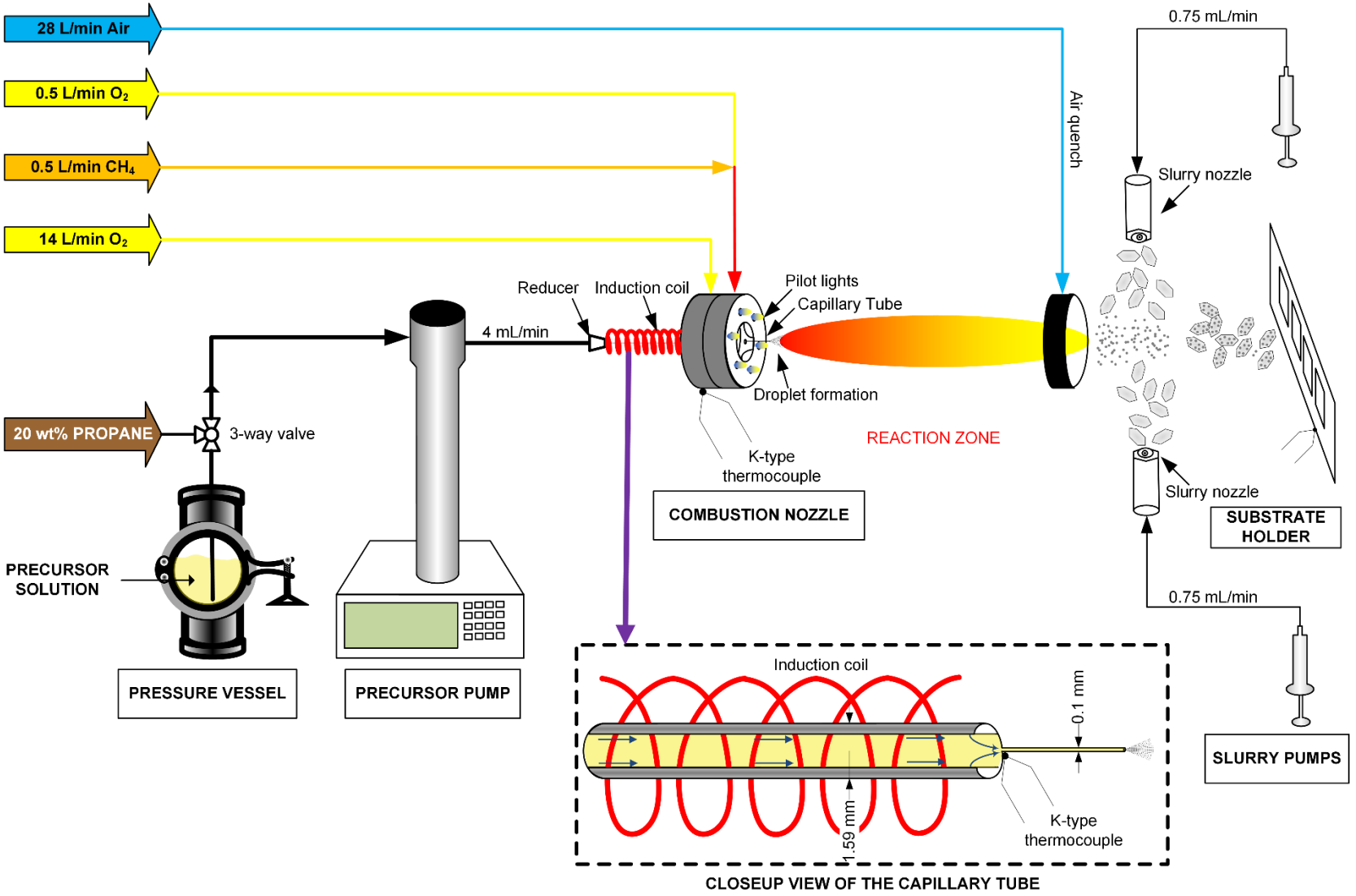

Fig. 5.1: Arrangement of the Reactive Spray Deposition Technology equipment for the synthesis of Pt on ceria catalysts for water-gas shift reaction.

5.5 Experimental:

5.5.1 Catalyst synthesis:

The ceria was obtained from Sigma Aldrich (Catalogue (# 544841). Pt nanoparticles were deposited on to the ceria using RSDT. A detailed explanation of the equipment and the process is given in chapter 1. The schematic for RSDT is shown in Fig. 5.1. The precursor used was platinum (II) 2, 4-pentanedionate ["platinum acetylacetonate" or "Pt acac"] obtained from Colonial Metals, Inc. (# 6039) which was dissolved in a solvent blend consisting of xylene and acetone (Fisher Scientific # X5-20 and A18-4 respectively) in the weight ratio of 3:1. In order to support the atomization, 20 wt% sulfur free liquefied propane (Airgas catalogue # PRCP350S) was added to the precursor solution resulting in a final concentration of 0.6 mmol/L Pt acac, 62.5 wt% xylene, 21 wt% acetone, and 16.5 wt% propane. The flow rate of the precursor solution was set at 4 mL/min and the temperature at 60°C based on our previous design of experiments to create nano sized Pt particles of 1–3 nm [1]. The precursor solution was atomized by a gas-assisted external mixing nozzle (combustion nozzle) by oxygen (14 L/min). Six methane-oxygen flamelets (methane and oxygen at 0.5 L/min each) surrounds the capillary end which ignites the combustible precursor mist. Since the droplets produced by this process are mostly sub-micron due to energetic inputs of heat, pressure, and a supercritical propane diluent—the metal-organic precursor is confined to the nanoscale regime during particle formation. During the particle formation process the precursor heats up, decomposes, and then undergoes a phase transition to vapor followed by concurrent reduction of the Pt^{2+} to Pt metal. At around 6 inches from the flame, a circular air quench (Exair, Super Air Wipe^{TM}) was placed with an air flow rate of 28 L/min. The air quench cools the Pt nanoparticles instantly and eliminates further growth, agglomeration, and sintering,

thereby keeping the particle size small and increasing active surface area which is an essential requirement for the high catalytic activity.

The ceria slurry was prepared by suspending 1 wt% ceria in deionized water and maintaining the pH at 5 by adding concentrated nitric acid. The acidity helps deaggregation of the ceria particles [5]. The slurry was subjected to stirring and ultra-sonication for 1 h. with an energy input of 200–250 kJ. The slurry was sprayed using a pair of Nordson EFD 781 spray valves (slurry nozzles) which were positioned at 180° to each other and perpendicularly to the flame, the total flow rate of which was maintained at 1.5 mL/min. The Pt nanoparticles from the flame were condensed on the ceria sprayed from the slurry nozzles during time of flight and the Pt/ceria catalyst was collected on the glass fiber filter (GFF) substrate. In addition to this, few more substrates were used for deposition as shown in Fig. 5.2.

5.5.2 Characterization:

The decomposition profile of Pt acac was obtained using TGA Q5000 IR thermogravimetric analyzer from TA instruments. It is a required parameter which is useful to set the flame conditions to ensure that no residual Pt acac remained in the prepared catalyst. To simulate the conditions of the reaction in the flame, TGA was performed in air from 30–550°C at the ramp rate of 5°C /min. Elemental analysis of the deposited catalyst film was determined by ICP-OES using a Perkin Elmer Optima 7300DV. XRD patterns were recorded on a Bruker D8 advanced powder diffractometer using CuKα radiation with a zero background quartz disc on which the catalyst was deposited. HRTEM micrographs of Pt on ceria particles were obtained on a 200kV JEOL 2010 FasTEM with a LaB_6 source equipped with an EDAX XEDS system. Lacey formvar/carbon, 200 mesh Cu grids (Ted Pella, Inc.) were mounted on a custom built multiple grid holder. The holder was introduced directly in front of the flame. The grids were removed after 150

s and introduced directly in the TEM chamber without any further sample preparation steps. SEM micrographs were collected on an FEI ESEM Quanta 250 with a field emission gun with an EDAX XEDS system. The glass fiber filter (GFF) substrate was sputter coated with gold prior to imaging. The catalyst film was also deposited on conductive glassy carbon for further SEM studies. TPR studies were performed in 1 vol% H_2 and balance Ar with a flow rate of 100 sccm in the temperature range (30–600°C) with a ramp rate of 2°C/min.

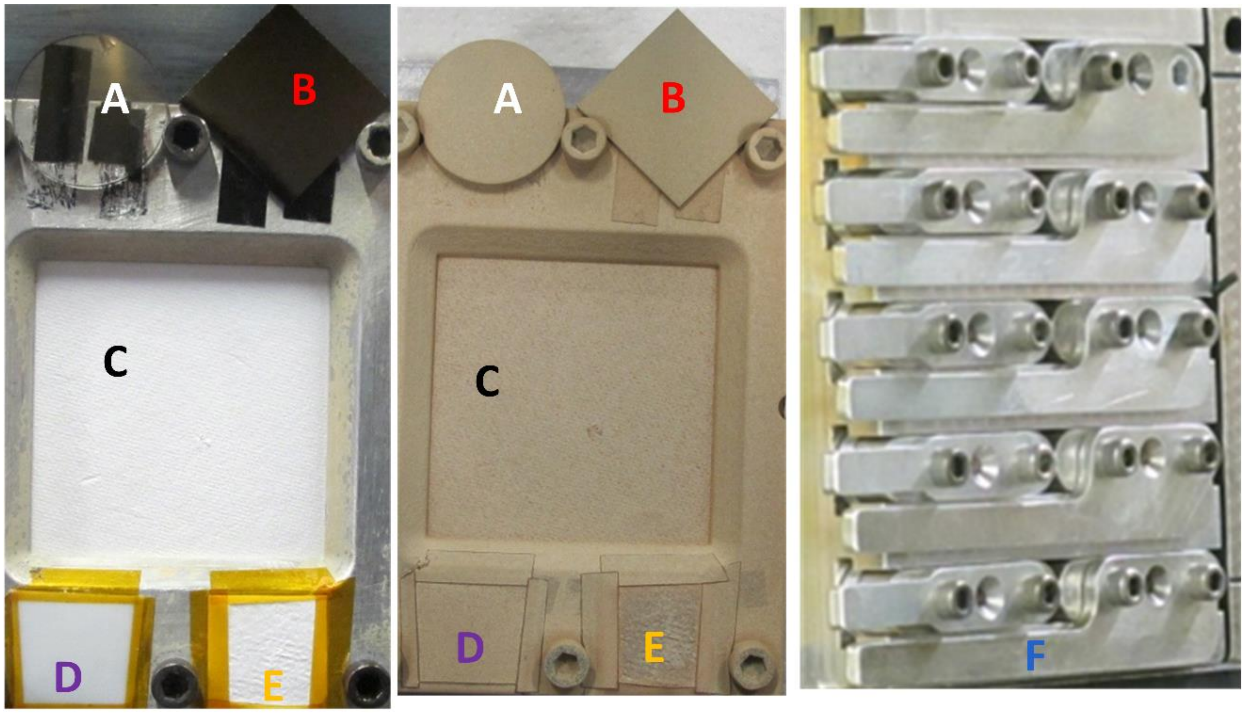

Fig. 5.2: Arrangement of the substrates for the deposition of Pt on ceria catalysts for water-gas shift reaction.

5.5.3 Catalytic Reaction:

The catalyst was tested for WGS activity at atmospheric pressure and temperature range (100–350°C) with a ramp rate of 5°C/min in Altamira Instrument's BenchCAT™ 1000R HP equipped with a fixed bed reactor, furnace, and mass flow controllers for precise gas flow. A schematic of the arrangement of the WGS test is shown in Fig. 5.3. The reactor was a 1 in. OD and 7 in. long quartz tube. The gas flow with a composition of 1 vol% CO and 99 vol% Ar was set at 100 sccm and humidified by bubbling through water maintained at 25°C. The catalyst bed was monitored with an Omega standard k-type thermocouple. An Agilent Micro gas chromatography (GC) with a thermal conductivity detector (TCD) was used for the identification of the products from the reactor. The GC was calibrated for CO, CO_2, and H_2 by flowing known standards. The product gas stream was directed through a Peltier cooled chiller to remove any residual moisture before it was sent to GC. The catalyst was also tested with the conditions (pretreatment and reaction) similar to references [6–9] as described in table 5.1.

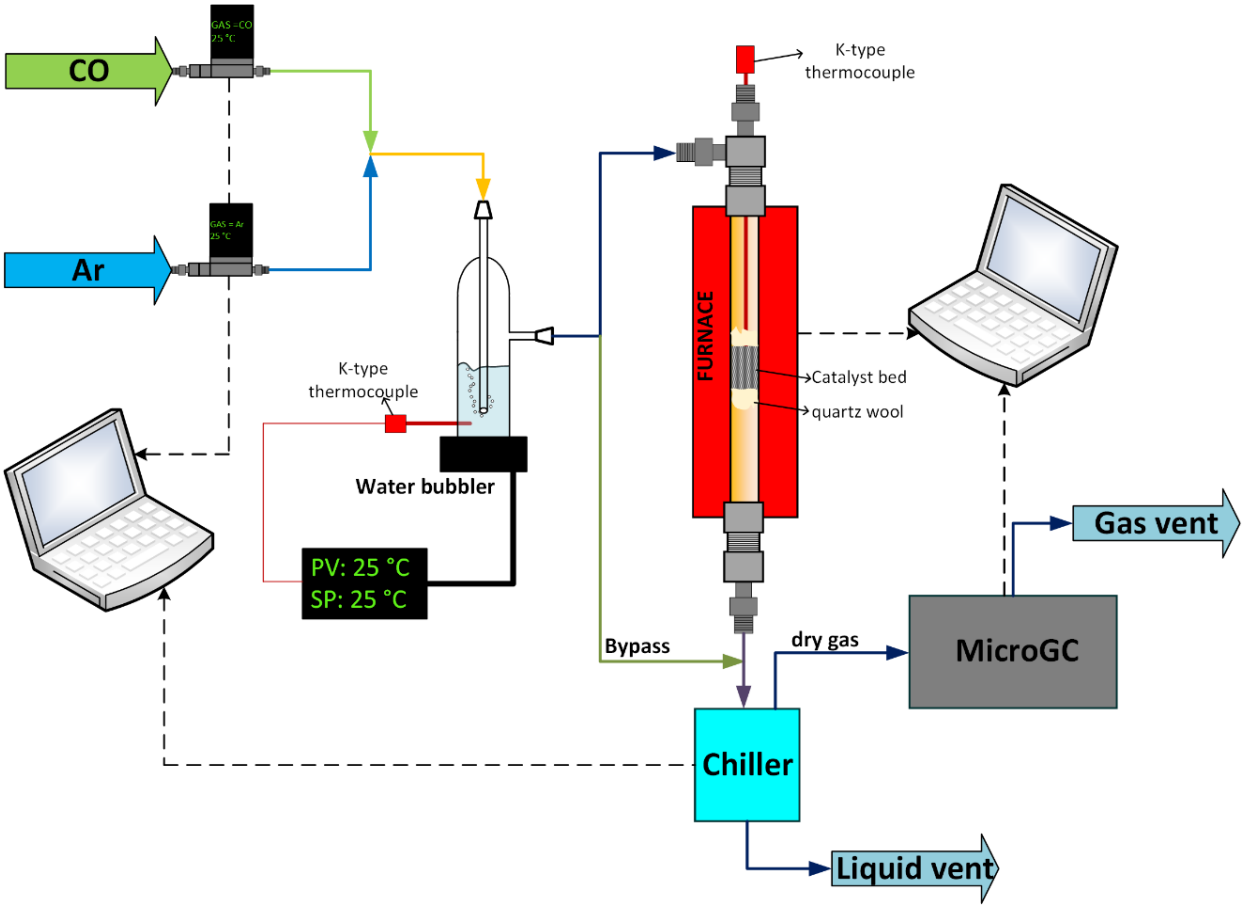

Fig. 5.3: Schematic of the BenchCAT used for testing the Pt/ceria catalysts for water-gas shift reaction.

5.6 Results and discussion:

5.6.1 Catalyst Characterization:

Fig. 5.4 shows the TGA profile of Pt acac in air. The initial weight was 22.39 mg. The weight loss process began at 173°C and leveled off at 257°C with the final weight loss of 59 wt%. This shows that the precursor can be easily decomposed to metallic Pt in the flame. A Pt doping value of 0.91 wt% was confirmed by ICP-OES.

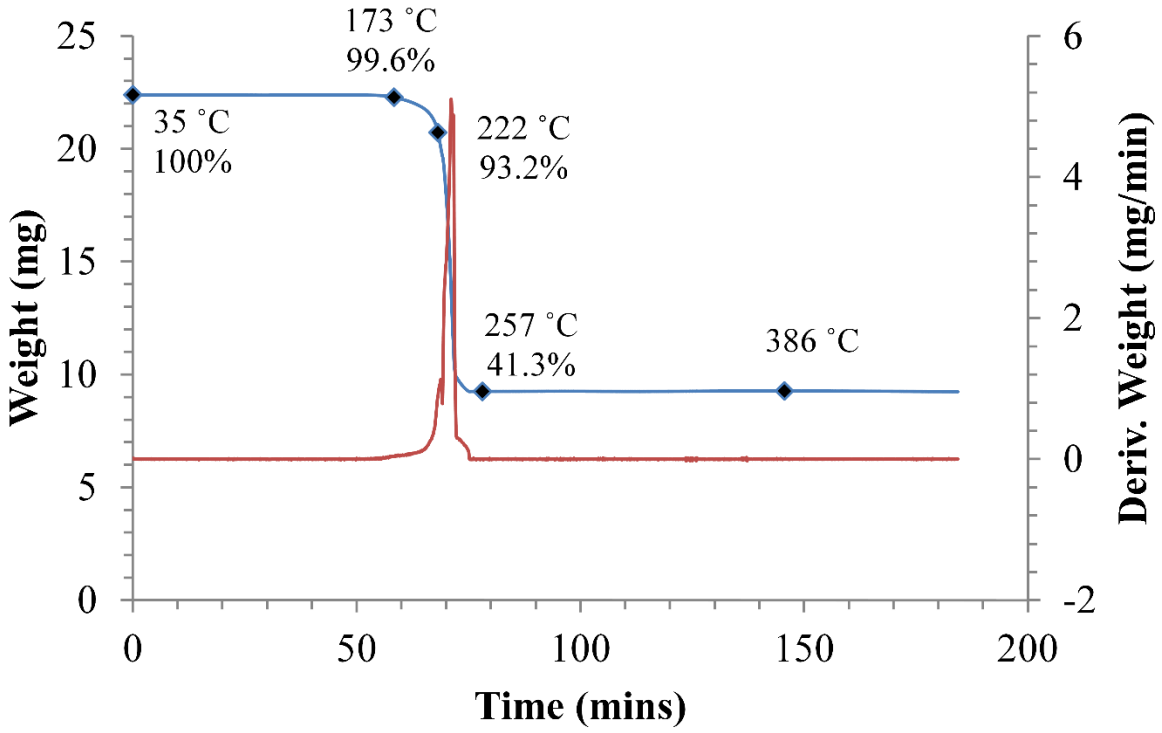

Fig. 5.4: Thermogravimetric analysis (TGA) of platinum acetylacetonate in air from 30–550°C shows the decomposition at 257°C.

Fig. 5.5 shows the XRD pattern of the ceria support and Pt on ceria catalyst. The ceria shows the fluorite cubic structure and is associated with the ICDD# 01-075-9470. The crystallite size of the support was measured to be 27.0 nm by the Debye Scherrer's method:

$$\tau = \frac{k\lambda}{\beta Cos\theta} \qquad \text{(E5.1)}$$

Where, τ is the crystallite size, k is the shape factor which is generally 1, β is the line broadening at half the maximum intensity (FWHM), θ is half the Bragg angle. However, this method of crystallite size calculation does not take into account the distribution of sizes and only considers the mean size of the particles. No visible Pt peaks were observed, possibly due to the interference

with ceria and the low Pt loading value [10]. The crystallite size of ceria remained unchanged after Pt doping inferring that the cubic structure of ceria is retained and was not influenced by high temperature conditions which may have caused sintering. The substrate temperature in the RSDT was in the range of 90–110°C. There was no significant position shift of the prepared catalysts as compared with the bare ceria which implies that the Pt atom was not incorporated into the ceria structure [11].

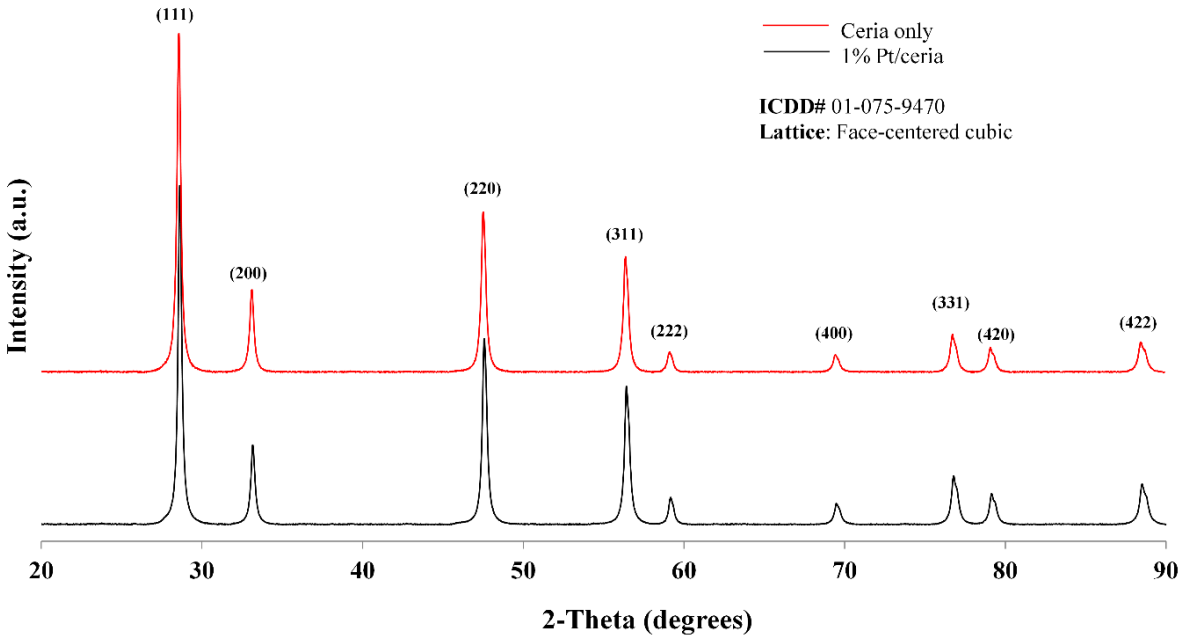

Fig. 5.5: XRD pattern of 1 wt% Pt/ceria prepared by RSDT as compared with bare ceria.

The microstructure and film morphology were characterized by SEM. The SEM micrographs of the non-coated GFF substrate and catalyst film are shown in Fig. 5.6 (a) and (b) respectively. From Fig. 5.6 (a) it can be noticed that the fibers are 0.5–2 μm in diameter. Fig. 5.6 (b) illustrates non uniformity in the catalyst film on the GFF substrate. Three insets are shown in Fig. 5.6 (b). Left inset shows the edge of the catalyst coated substrate. The middle inset is the

image of the film on conductive glassy carbon substrate and it shows the part of the film which is peeling off from the substrate. This shows that the film thickness is around 12.6 μm. The right inset is a magnified view of the film coated on fibers and it shows that the resultant conformal film of Pt/ceria nanoparticles covered the individual fibers on the upper-side of the membrane completely, without inducing any fiber aggregation.

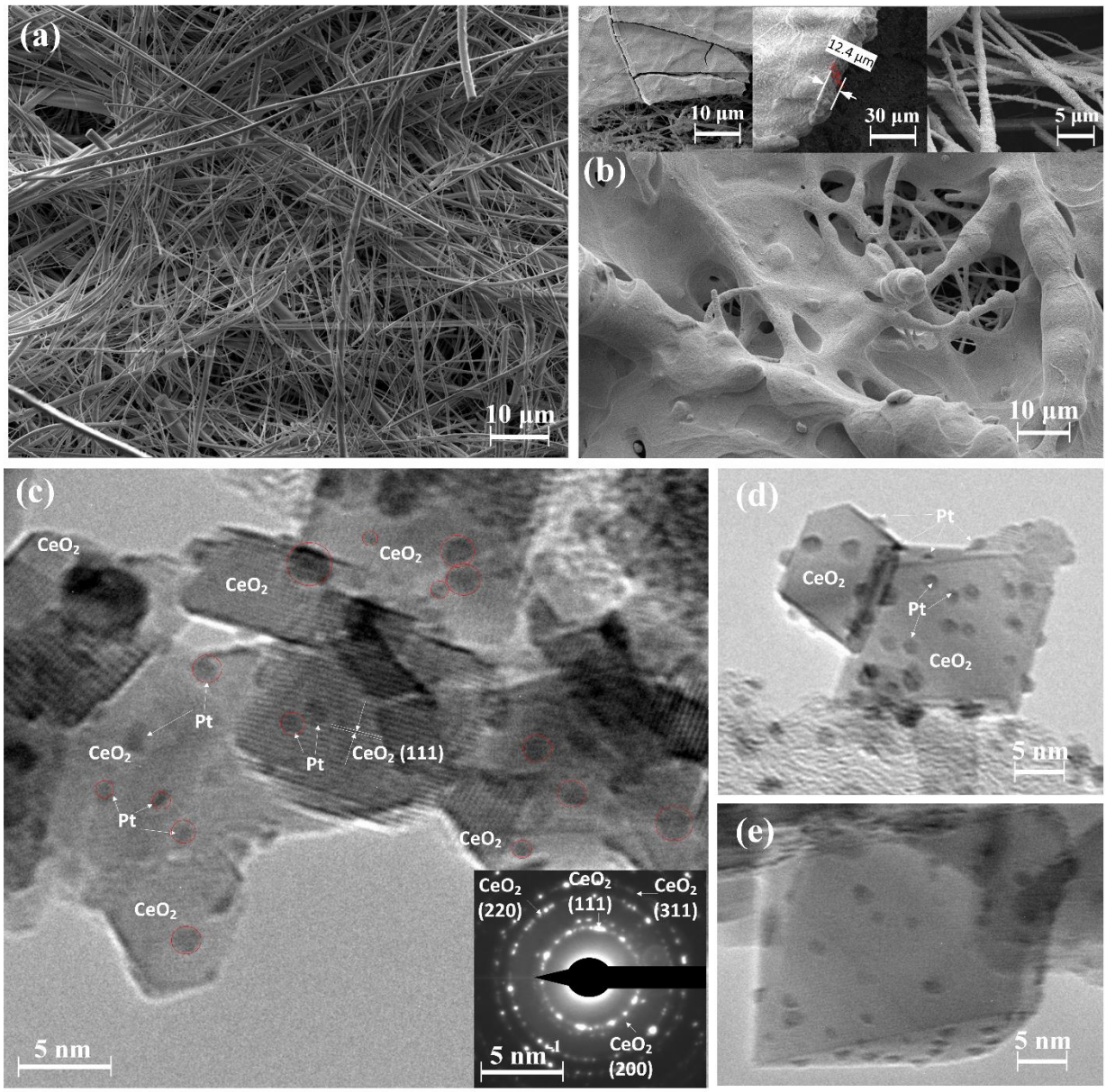

Fig. 5.6: (a) SEM micrograph of non-coated glass fiber filter. (b) Pt/ceria catalyst on glass fiber filter (c) HRTEM micrograph of Pt/ceria as deposited on lacey carbon grid; (d) and (e) higher magnification micrograph showing Pt nanoparticles on ceria.

In order to identify the metal-support interaction, HRTEM micrographs were taken as shown in Fig. 5.6 (c), (d), and (e). The TEM micrograph shows the size distribution of Pt nanoparticles to be in the range of 0.5–2 nm. Nanoparticles of Pt are evenly distributed on the surface of ceria nanoparticles that are 10–30 nm in diameter. No evidence of agglomeration or

sintering of Pt nanoparticles can be seen. The bottom right inset of Fig. 5.6 (c) shows the selected area diffraction pattern which mainly corresponds to the ceria lattice. XEDS also confirmed the Pt loading to be around 1 wt% (data not shown here). Ceria has a variety of geometries including rectangular, polygon, and facet and has a size distribution in the range of 8–30 nm. TPR measurement of the catalysts was performed in H_2 from 100–600°C (plot not shown here). Three distinct peaks were obtained at 100°C, 175°C, and 425°C which were assigned to the reduction of surface PtO_x, PtO_x interacting with ceria, and bulk ceria respectively [12].

5.6.2 Water Gas Shift Catalytic Activity:

The activity of the ceria supported 1 wt% Pt catalyst is shown in Fig. 5.7. No methanation activity was observed in the reaction as evident from the absence of methane peak in the micro GC. The catalyst was active at 150°C and gave a CO conversion of 15% at 150°C, 18% at 200°C, 37% at 225°C, and 100% at 250°C. The activity is compared with the catalysts prepared by the conventional wet chemistry processes with similar Pt doping: sol-gel, co-precipitation, and incipient wetness impregnation [6–9] and the comparison is shown in table 5.1. In order to do a fair comparison, our catalysts were also tested with the conditions of reference [6–9] as shown in Fig. 5.7 (A–D). It can be seen that the catalyst performed better than the catalyst of Apanee et al., Duarte et al. and Hwang et al. and poorly with Roh et al. There can be a number of factors responsible for the catalyst activity. Preparation methods and catalyst pre-treatment play a significant role in the performance. Hwang et al. [7] and Dwarte et al. [8] subjected their catalysts (each with a Pt doping around 1–1.2 wt% on ceria) to 350°C for 1 h. in a reducing environment which could have led to sintering of Pt nanoparticles thereby reducing the active surface area. It is interesting to see in Fig. 5.7 that after pretreating the catalyst at 110°C with O_2 for 2 h., the catalyst performed better than the untreated one. CO concentration in the reactor feed also had a significant

role. WGS rate is proportional to the CO partial pressure to the zero order observed over the Pt-based catalysts, which implies that reducing the CO concentration from 2 vol% to 1 vol% requires twice as much catalyst [13]. However, increase in CO causes poisoning of Pt thereby making it inactive. A typical value for CO concentration for an LTS reactor is 1 vol %. Apanee et al. measured the highest CO conversion around 17% at 320°C by using 4% CO in the feed [6]. However, on reducing the CO concentration to 1%, activity improved dramatically giving 90% CO conversion at 300°C. Further reduction of CO to 0.5% concentration improved activity to 95% CO conversion at 250°C. Catalysts are also prone to sulfur poisoning which significantly hampers the performance. It can be seen that the amount of Pt doping has a direct influence on the activity. The amount of Pt doping and the synthesis method needed to be optimized for a maximum activity. Yeung et al. reported a Pt doping of 2 wt% and resulted in reduced CO conversion of only 16.5% at 450°C [14]. This could be due to the fact that higher Pt doping results in the formation of clusters and agglomeration leading to a reduced Pt dispersion and decreased support-metal contact area [15]. In order to better understand the influence of Pt doping on the activity of ceria the density functional theory (DFT) was employed [16–19]. It was found that the structural relaxation is the main factor responsible for decrease of the oxygen vacancy formation energy, i.e. the Pt doping makes structural distortion much more exothermic for the reduced ceria. The mechanism for the large reduction in vacancy formation energy can partly be explained by simple electrostatic arguments. The Pt^{2+} dopants are lower in formal charge than Ce^{4+}, and it is easier to form an oxygen vacancy from next to Pt^{2+} than next to Ce^{4+}. Lastly, enhancement in the WGS reaction activity of Pt/ceria catalysts has also been explained by the electronic perturbation of the Pt by the ceria support [20]. Electronic interaction between Pt and ceria greatly reduces the activation barrier for water splitting and stabilizes the adsorbed OH and H products as shown by DFT [21].

Table 5.1: Comparison of the catalysts synthesized by RSDT with conventionally prepared catalysts from literature.

Catalyst	Synthesis method	Pretreatment	Reactor feed	Reaction conditions	Crystallite size (nm)		GHSV (h^{-1})	TPR with H_2 (°C)			Maximum CO conversion	Ref.
					CeO_2	Pt		Surface PtO_x	Bulk PtO_x	Bulk CeO_2		
1% Pt/Ceria	RSDT	None	1% CO/Ar bubbled through water at 25°C. Flow rate 100 sccm.	100–400°C, atm. pressure	8–30	1.5–2	8622	100	175	425	100% at 250°C	[4]
1% Pt/Ceria	Ceria-precipitation process using $Ce(NO_3)_3 \cdot 6H_2O$. Pt doping-incipient wetness impregnation using $Pt(NH_3)_4(NO_3)_2$.	Reduced in 5% H_2/N_2 from room temperature to 400°C at the ramp rate of 3.3°C/min and the temperature was maintained for 1 h.	6.4 vol.% CO, 7.1 vol.% CO_2, 0.7 vol.% CH_4, 43.0 vol.% H_2, 28.4 vol.% H_2O, and 14.4 vol.% N_2. The feed $H_2O/(CH_4 + CO + CO_2)$ ratio was fixed at 2.	200–360°C, atm. pressure	11	3	45515	70	160	600	88% at 320°C	[9]
1% Pt/Ceria	Single step sol-gel using Ce acetate and $H_2PtCl_6.6H_2O$ with NH_4OH.	Oxidized in pure O_2 at 110°C for 2 h.	1% CO in He, saturated with water vapor by bubbler.	120–360°C, atm. pressure	34.8	>5	30000	NM	NM	NM	90% at 300°C	[6]

Catalyst	Synthesis method	Pretreatment	Reactor feed	Reaction conditions	Crystallite size (nm)		GHSV (h^{-1})	TPR with H_2 (°C)			Maximum CO conversion	Ref.
					CeO_2	Pt		Surface PtO_x	Bulk PtO_x	Bulk CeO_2		
1.1% Pt/Ceria	Ceria-precipitation process using $Ce(NO_3)_3 \cdot 6H_2O$ and NH_4OH. Pt doping-incipient wetness impregnation using $H_2PtCl_6 \cdot 6H_2O$.	Reduced *in-situ* by 10% H_2/N_2 at 350°C for 1 h.	7.0 % CO, 8.5 % CO_2, 22.0 % H_2O, 37 % H_2 and 25.5 % N_2. Flow rate 40 sccm.	200–360°C, atm. pressure	15	1–1.3	14000	NM	185	230	88% at 320°C	[7]
1.01% Pt/Ceria	Ceria-precipitation process using $Ce(NO_3)_3 \cdot 6H_2O$ and NaOH. Pt doping-incipient wetness impregnation using $H_2PtCl_6 \cdot 6H_2O$.	Reduced *in-situ* by 10% H_2/N_2 at 350°C for 1 h.	7.0 % CO, 8.5 % CO_2, 22.0 % H_2O, 37 % H_2 and 25.5 % N_2. Flow rate 40 sccm.	220–360°C, atm. pressure	14.2	1–1.4	14000	NM	260	310	92% at 300°C	[7]
1.2% Pt/Ceria	Ceria-precipitation process using $(NH_4)Ce(NO_3)_6$ $6H_2O$. Pt doping-incipient wetness impregnation using $Pt(NH_3)_4(NO_3)_2$	Reduced in H_2 (30 mL/min) from room temperature to 350°C at the ramp rate of 10°C/min and the temperature was maintained for 1 h.	5.49 % CO, 4.10 % CO_2, 9.71 % H_2, 30.75 % H_2O (H_2O:CO molar ratio = 5.6:1) and N_2 (balance). Flow rate 90 sccm.	300°C, atm. pressure	7.7	NM	NM	NM	NM	NM	45% at 300°C (Initial conversion. Max not measured.)	[8]

Catalyst	Synthesis method	Pretreatment	Reactor feed	Reaction conditions	Crystallite size (nm)		GHSV (h^{-1})	TPR with H_2 (°C)			Maximum CO conversion	Ref.
					CeO_2	Pt		Surface PtO_x	Bulk PtO_x	Bulk CeO_2		
		Afterwards, the atmosphere was purged with N_2 (30 mL/min) while the temperature was lowered to 300°C.										
NM: Not measured												

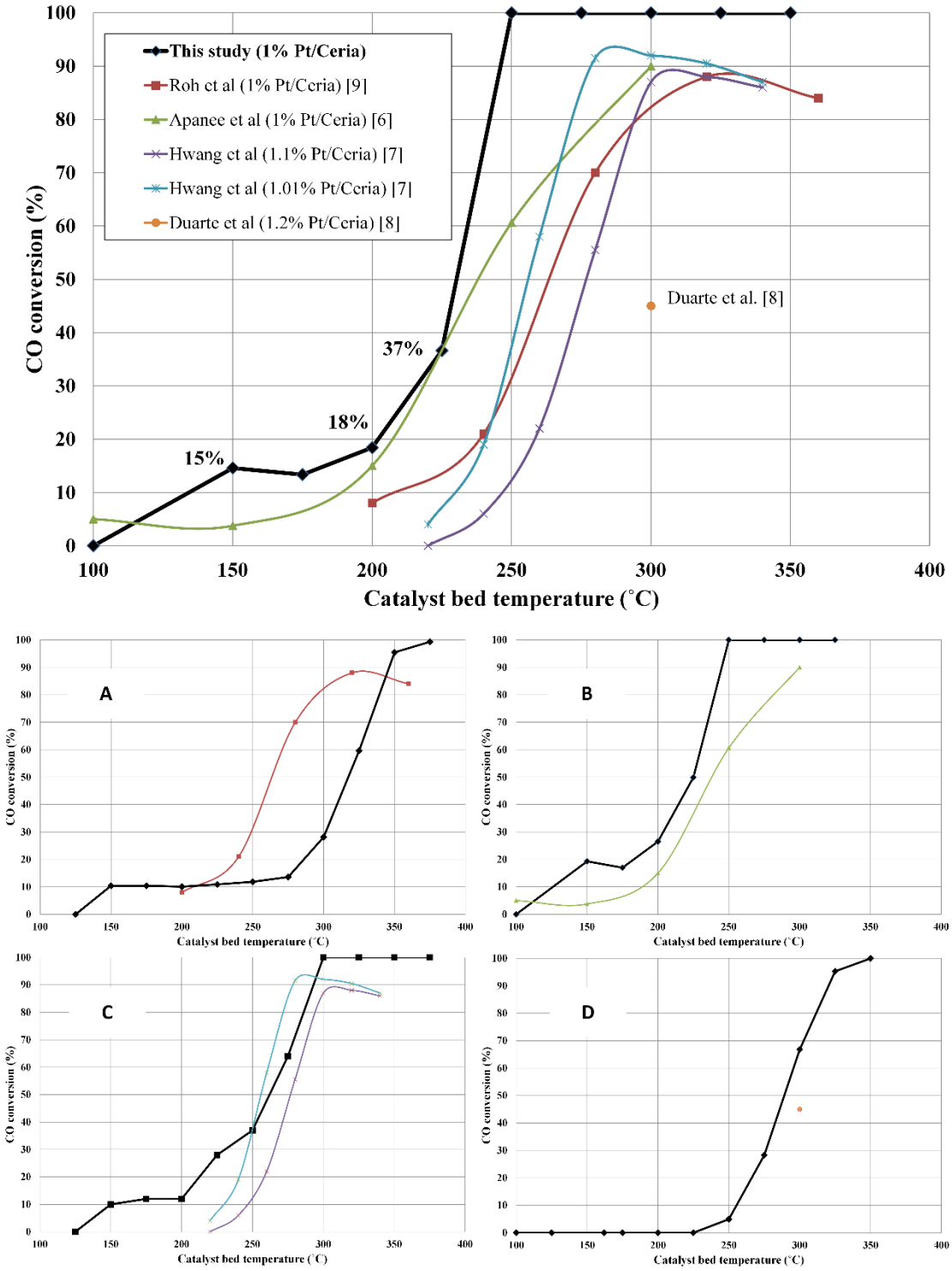

Fig. 5.7: Water-gas shift reaction activity of RSDT made catalysts as compared with literature (conventional wet chemistry based catalysts). A, B, C and D: WGS reaction activity tested with similar conditions as references [9], [6], [7] and [8] respectively.

5.7 Conclusions:

1 wt% Pt on ceria catalyst was synthesized using RSDT where solid nanoparticles were grown from the vapor phase and collected on glass fiber filter substrates. The catalyst was tested for WGS reaction at various pretreatment and operating conditions. The activity was compared with the literature for the catalysts prepared by conventional processes. It was found that the RSDT produced catalyst performed better than most of the other catalysts. This is due to uniform distribution of Pt nanoparticles on the ceria surface and no agglomeration between particles. The catalyst activity depends strongly on the particle size of Pt, CO feed concentration, GHSV, water/CO ratio, ceria-Pt interaction, availability of surface oxygen vacancies in ceria, and catalyst poisoning by excess CO or sulfur. Chapter 6 will elaborate further the influence of the ceria size, synthesis technique, morphology and surface activation in the Pt/ceria catalyst for WGS reaction.

5.8 References:

[1] J.M. Roller, R. Neagu, F. Orfino, R. Maric, Supported and unsupported platinum catalysts prepared by a one-step dry deposition method and their oxygen reduction reactivity in acidic media, Journal of Materials Science. 47 (11) (2012) 4604-4611.

[2] J.M. Roller, M.J. Arellano-Jiménez, H. Yu, R. Jain, C.B. Carter, R. Maric, Catalyst nanoscale assembly from the vapor phase on corrosion resistant supports, Electrochimica Acta. 107 (0) (2013) 632-655.

[3] J.M. Roller, M. Josefina Arellano-Jiménez, R. Jain, H. Yu, C. Barry Carter, R. Maric, Oxygen Evolution during Water Electrolysis from Thin Films Using Bimetallic Oxides of Ir-Pt and Ir-Ru, Journal of Electroceramic Society. 160 (6) (2013) F716-F730.

[4] R. Jain, R. Maric, Synthesis of nano-Pt onto ceria support as catalyst for water-gas shift reaction by Reactive Spray Deposition Technology, Applied Catalysis A: General. 475 (2014) 461-468.

[5] J.H. Woodhead, Process for preparing aqueous dispersion of ceria and resulting product, United States Patent. 05/954,658(4231893) (1980).

[6] A. Luengnaruemitchai, S. Osuwan, E. Gulari, Comparative studies of low-temperature water-gas shift reaction over Pt/CeO_2, Au/CeO_2, and Au/Fe_2O_3 catalysts, Catalysis Communications. 4 (5) (2003) 215-221.

[7] K. Hwang, S. Ihm, J. Park, Enhanced CeO_2-supported Pt catalyst for water-gas shift reaction, Fuel Processing Technology. 91 (7) (2010) 729-736.

[8] A.M. Duarte de Farias, D. Nguyen-Thanh, M.A. Fraga, Discussing the use of modified ceria as support for Pt catalysts on water-gas shift reaction, Applied Catalysis B: Environmental. 93 (3–4) (2010) 250-258.

[9] H. Roh, D. Jeong, K. Kim, I. Eum, K. Koo, W. Yoon, Single Stage Water-Gas Shift Reaction Over Supported Pt Catalysts, Catalysis Letters. 141 (1) (2011) 95-99.

[10] T. Hyde, Crystallite Size Analysis of Supported Platinum Catalysts by XRD, Platinum Metals Review. 52 (2) (2008) 129.

[11] J. F. Bozeman III and H. Huang, Structural Characteristics of Bimetallic Catalysts Supported on Nano-Ceria, Journal of Nanomaterials. 2011 (2011) 329757.

[12] L. Pino, A. Vita, M. Cordaro, V. Recupero, M.S. Hegde, A comparative study of Pt/CeO_2 catalysts for catalytic partial oxidation of methane to syngas for application in fuel cell electric vehicles, Applied Catalysis A: General. 243 (1) (2003) 135-146.

[13] C. Ratnasamy, J.P. Wagner, Water Gas Shift Catalysis, Catalysis Reviews. 51 (3) (2009) 325-440.

[14] C. Yeung, S. Tsang, Microemulsion Prepared Pt in Ceria: Catalytically Active for Water Gas Shift Reaction but Totally Inert for Methanation, Catalysis Letters. 128 (3-4) (2009) 349-355.

[15] C.M. Kalamaras, D.D. Dionysiou, A.M. Efstathiou, Mechanistic Studies of the Water-Gas Shift Reaction over $Pt/Ce_xZr_{1-x}O_2$ Catalysts: The Effect of Pt Particle Size and Zr Dopant, ACS Catalysis. 2 (12) (2012) 2729-2742.

[16] C. Spiel, P. Blaha, Y. Suchorski, K. Schwarz, G. Rupprechter, CeO_2/Pt(111) interface studied using first-principles density functional theory calculations, Physical Review B. 84 (4) (2011) 045412.

[17] R.T. Kinch, C.R. Cabrera, Y. Ishikawa, A Density-Functional Theory Study of the Water-Gas Shift Mechanism on Pt/Ceria(111), Journal of Physical Chemistry C. 113 (21) (2009) 9239-9250.

[18] D. Loffreda, F. Delbecq, Growth of a Pt film on non-reduced ceria: A density functional theory study, Journal of Chemical Physics. 136 (4) (2012) 044705-1-044705-10.

[19] Y. Zongxian, L. Gaixia, L. Zhansheng, K. Tom Woo., H. Kersti, Structural and electronic properties of NM-doped ceria (NM = Pt, Rh): a first-principles study, Journal of Physics: Condensed Matter. 20 (3) (2008) 035210.

[20] A. Bruix, J.A. Rodriguez, P.J. Ramirez, S.D. Senanayake, J. Evans, J.B. Park, D. Stacchiola, P. Liu, J. Hrbek, F. Illas, A new type of strong metal-support interaction and the production of H_2 through the transformation of water on Pt/CeO_2 (111) and $Pt/CeO_x/TiO_2$ (110) catalysts, Journal of the American Chemical Society. 134 (21) (2012) 8968-8974.

[21] C.T. Campbell, Catalyst-support interactions: Electronic perturbations, Nature Chemistry. 4(8) (2012) 597-598.

CHAPTER 6:

Comparative study for low temperature water-gas shift reaction on Pt/ceria catalysts: Role of different ceria supports

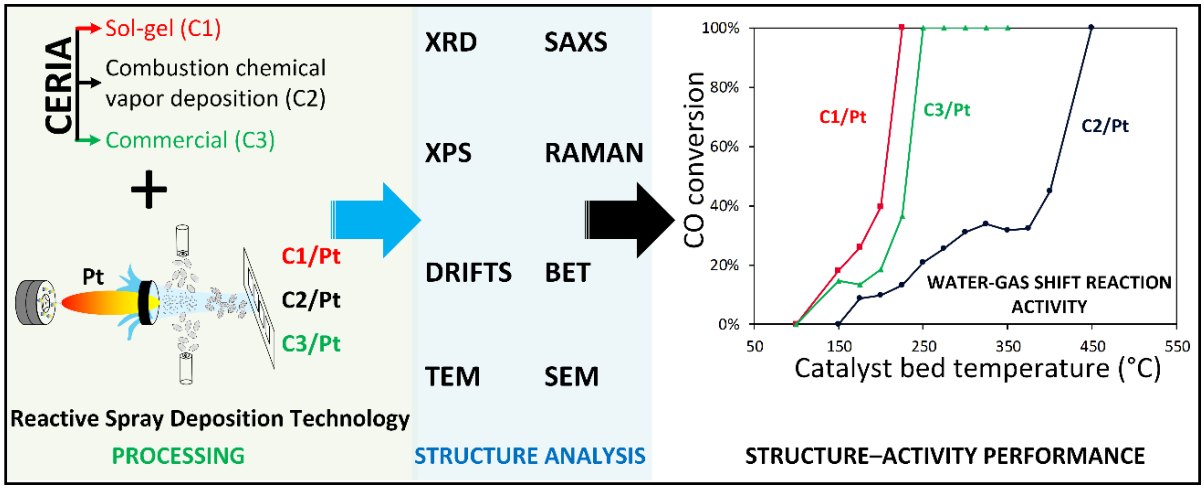

6.1 Highlights:

1. Processing-structure-property relationship of Pt/ceria catalysts were evaluated for the water-gas shift reaction using three different ceria nanopowder synthesized with different techniques.

2. Physical and microstructural properties of the ceria and Pt/ceria catalysts were compared.

3. The structural properties of the support were correlated with the activity for the water-gas shift reaction.

4. Tests data suggest that performance improvements that approach 100% CO conversion can be achieved.

6.2 Abstract:

Pt on ceria catalysts for water-gas shift (WGS) reaction were prepared by employing three ceria nanopowder synthesized with different processing techniques and having different surface area and porosities. Pt nanoparticles (~0.5–2 nm) were deposited in the vapor phase onto each of the three ceria supports by Reactive Spray Deposition Technology (RSDT). The catalysts were performance tested for the WGS reaction in the temperature range of 150–450°C at a gas hourly space velocity (GHSV) of 13,360 h^{-1}. The structure-activity relationship for the ceria-based materials was studied. The most promising catalyst was Pt supported on mesoporous ceria with crystallite size of 5.8 nm and Brunauer-Emmett-Teller (BET) surface area of 187 m^2/g. This configuration demonstrated complete CO conversion at 225°C. The CO adsorption strength and the ability to dissociate H_2O are the two main factors that determine the activity of a particular catalyst site for the water-gas shift (WGS) reaction. This study leads to the conclusion that the highest water-gas shift reaction activity was obtained with Pt supported on the

mesoporous ceria, with low crystallite size and high surface area, with well dispersed Pt, leading to enhanced Pt-ceria interaction.

6.3 Keywords:

Water-gas shift reaction; Flame spray pyrolysis; Pt-ceria interface; Mesoporous ceria; Processing-structure-property relationship.

6.4 Introduction:

In chapter 5, Reactive Spray Deposition Technology (RSDT) has been evaluated as a single step option for the synthesis of ceria supported Pt catalysts [1]. In this study, RSDT has been evaluated for Pt nanoparticles applied on three different ceria supports to determine the ceria morphology that is the most suitable as a Pt support material for the for low temperature WGS reaction. The ceria supports differ by their syntheses: sol-gel, combustion chemical vapor deposition, and the one obtained by a commercial process of firing high purity cerium carbonate to ceria. Each process gave unique properties: mesoporosity, particle size and surface area. The syntheses of each of these ceria support materials were compared, and the processing-structure-properties relationship of the catalysts were established by the following tests: the microstructural properties of the ceria supported Pt catalysts were investigated by X-ray diffraction (XRD), small angle X-ray scattering (SAXS), X-ray photoelectron spectroscopy (XPS), Raman spectroscopy, N_2 sorption experiments using Brunauer-Emmett-Teller (BET) method, transmission electron microscopy (TEM), and scanning electron microscopy (SEM). The catalysts were performance tested for the WGS reaction. In this work, our objective was to determine the influence of the crystallite size, surface area, and mesoporosity of the ceria support on the WGS reaction rate. We have also determined, the reaction mechanism and the possible reaction pathways for each of

these Pt/ceria catalysts using *in-situ* diffuse reflectance infrared Fourier transform spectroscopy (DRIFTS). This work was presented at the 2013 Materials Research Society (MRS) fall meeting and exhibit, Boston, MA, symposium AA: Catalytic Nanomaterials for Energy and Environment, December 1–6 (2013). This work was published in *Applied Catalysis A: General* [2].

6.5 Experimental:

6.5.1 Syntheses of ceria:

The ceria supports used in this study were chosen based on their individual synthesis processes: sol-gel method, combustion chemical vapor deposition, and commercially obtained ceria from Sigma Aldrich (catalogue# 202975). These materials are denoted by C1, C2 and C3 respectively in this text. Corresponding ceria supported Pt catalysts are denoted by C1/Pt, C2/Pt and C3/Pt. C1 was the mesoporous ceria (UCT-16) prepared at University of Connecticut by Poyraz et al. using a sol-gel based inverse micelle method [3]. C2 was prepared by combustion chemical vapor deposition (CCVD) using cerium (III) 2-ethylhexanoate, 49% in 2-ethylhexanoic acid (Alfa Aesar product# 40451) as the ceria precursor. The precursor concentration was maintained at 0.1 (M) in a solvent blend of toluene and liquefied propane. The description of the setup is explained elsewhere [4, 5]. C3 is the commercial ceria obtained from Sigma Aldrich (lot # 202975) which was mass produced by a proprietary process of firing high purity cerium carbonate. For the three ceria supports, Pt nanoparticles were deposited under the same deposition conditions by RSDT.

6.5.2 Syntheses of ceria supported Pt:

The detailed explanation of RSDT equipment is given in chapter 1. Fig. 6.1 shows the schematic of RSDT. The platinum precursor was platinum (II) 2, 4-pentanedionate [“platinum acetylacetonate” or “Pt acac”] obtained from Colonial Metals, Inc. (# 6039) which has

a Pt content of 49.6%. The precursor was chosen based on its low decomposition temperature of 257°C which was determined by thermogravimetric analysis (TGA) [1]. The precursor was dissolved in a solvent mixture consisting of xylene ($\Delta H^{\circ}_{c,\ 298K}$ = -4309 kJ/mol) and acetone ($\Delta H^{\circ}_{c,\ 298K}$ = -1658 kJ/mol) (Fisher Scientific # X5-20 and A18-4 respectively) in the weight ratio of 3:1. Xylene and acetone has a dual role of solvent and fuel for the combustion of Pt acac. Xylene helps in maintaining the solubility of Pt acac and also aids in the decomposition of Pt acac to Pt. Although acetone has a relatively low enthalpy ($\Delta H^{\circ}_{c,\ 298K}$ = -1658 kJ/mol), it is added to further enhance the solubility and prevent the settling of any undissolved Pt acac. This mixture was filled in a sealed high pressure stainless steel chamber (120 psi) and sulfur free liquefied propane ($\Delta H^{\circ}_{c,\ 298K}$ = -2202 kJ/mol) (Airgas catalogue # PRCP350S) was added to the precursor solution resulting in a final concentration of 0.6 mmol/L Pt acac, 62 wt% xylene, 21 wt% acetone, and 17 wt% propane. Propane helps in atomization by increasing the pressure drop between the needle and the point of exit of the solution, thereby splitting the solution into tiny droplets approximately 15 μm in diameter as measured by Malvern Instrument's Spraytec laser diffraction system [6]. The increase in surface area of the overall droplets helps in efficient combustion of the precursor. This solution was filled in a syringe pump (Teledyne Isco 500D, Lincoln NE) and directed to a series of stainless steel tubes of varying diameters: 0.025 cm inner diameter 316 stainless steel tube which is brazed to a capillary of diameter 100 μm (Vita Needle company) to assist in the pressure drop. The flow rate of the precursor was set at 4 mL/min. An Omega k type thermocouple was placed at the junction of the tube and capillary, the temperature of which is maintained at 190°C by means of an induction coil wrapped upstream of the flow of precursor solution based on our previous design of experiments to create nanometer sized Pt particles of 1–3 nm [7]. This caused the temperature of the precursor solution at the exit point to be 60°C and a pressure drop of 110–120

psi. The combined effect of liquefied propane, temperature, and reduction of diameter of the tube, causes the solution to shift into the supercritical regime and formation of sub-micron size droplets [6]. The precursor solution was atomized by a gas-assisted external mixing nozzle (combustion nozzle) by oxygen (14 L/min). The ratio of fuel/oxygen for stoichiometric conditions ($\acute{\eta}_{Oxygen/}\ \acute{\eta}_{Fuel})_{stoic}$ and the actual value $(\acute{\eta}_{Oxygen/}\ \acute{\eta}_{Fuel})_{actual}$ is also known as the equivalence ratio [8] defined as follows:

$$\varphi = (\frac{\dot{n}_{oxidant}}{\dot{n}_{fuel}})_{stoichiometric} / (\frac{\dot{n}_{oxidant}}{\dot{n}_{fuel}})_{real} \quad \text{(E6.1)}$$

Where $\dot{n}_{oxidant}$ and $\dot{n}_{fuel}$ are the molar flow rate of oxygen and precursor solution (fuel) respectively. Equivalence ratio can be utilized to determine the oxidation or reduction condition of the flame since φ >1 (reducing flame), φ = 1 (stoichiometric flame), φ <1 (oxidizing flame). For the synthesis of Pt/ceria catalysts, Φ was set below 1 or oxidizing combustion. Six methane-oxygen flamelets at 1 L/min (4:5 methane to oxygen volumetric ratio) surround the capillary end which ignites the combustible precursor mist. During the particle formation process the precursor heats up, decomposes, and then undergoes a phase transition to vapor followed by concurrent reduction of the Pt^{2+} to Pt metal. At about 10 cm from the flame, a circular air quench (Exair, Super Air Wipe^{TM}) was placed with an air flow rate of 70 L/min. The distance between the combustion nozzle and the air quench is the reaction zone and the length of the reaction zone is proportional to the residence time of the nanoparticles in the zone. Independent adjustment of the length of the reaction zone and the flow rate of compressed air through the air quench provides unique conditions for obtaining an assortment of phases and structures of nanoparticles synthesized by RSDT [9]. The air quench rapidly cools the Pt nanoparticles and prevents growth, agglomeration, and sintering, thereby keeping the particle size small maintaining high active surface area which is an essential requirement for the high catalytic activity.

The ceria slurry was prepared by suspending 1 wt% ceria in deionized water and maintaining the pH at 5 by adding concentrated nitric acid. The acidity helps the deaggregation of the ceria particles [10]. The slurry was subjected to stirring and ultra-sonication for 1 h. with an energy input of 200–250 kJ. In order to test any precipitation of ceria, a small slurry sample was allowed to stand undisturbed for 72 h. and no significant ceria precipitate was observed. The slurry was introduced onto a pair of stainless steel syringe pumps (Harvard apparatus catalogue# 702259) with the capacity of 100 mL each which were connected with a pair of Nordson EFD 781 spray valves (slurry nozzles) used for spraying the slurry. The slurry nozzle was connected with an air supply line of pressure 70 psi and it operating by the principle of pressure drop and the atomization of the slurry by air. The slurry nozzle end is shown in Fig. 6.1 has three main parts: needle, needle seat and annulus. As the air is turned on, the air pressure retracts the needle from its nozzle seat allowing the liquid to flow around the annulus. This creates a pressure drop around the annulus and causes the liquid to atomize into fine droplets. The slurry nozzles were positioned at 180° to each other and perpendicularly to the flame, the total flow rate of which was maintained at 1.5 mL/min. The Pt nanoparticles from the flame were condensed on the ceria sprayed from the slurry nozzles during time of flight. Pt/ceria catalyst was directly deposited as a film on glass fiber filter coupon (Proweigh filters catalogue # F93476mm) which was mounted on a stainless steel block placed on an x-y-z motion system as shown in Fig. 6.2. The substrates were placed 15 cm from the flame. The deposition area on the glass fiber filter was 25 cm^2. The substrate temperature was measured using an Omega standard k-type thermocouple and was in the 110–120°C range.

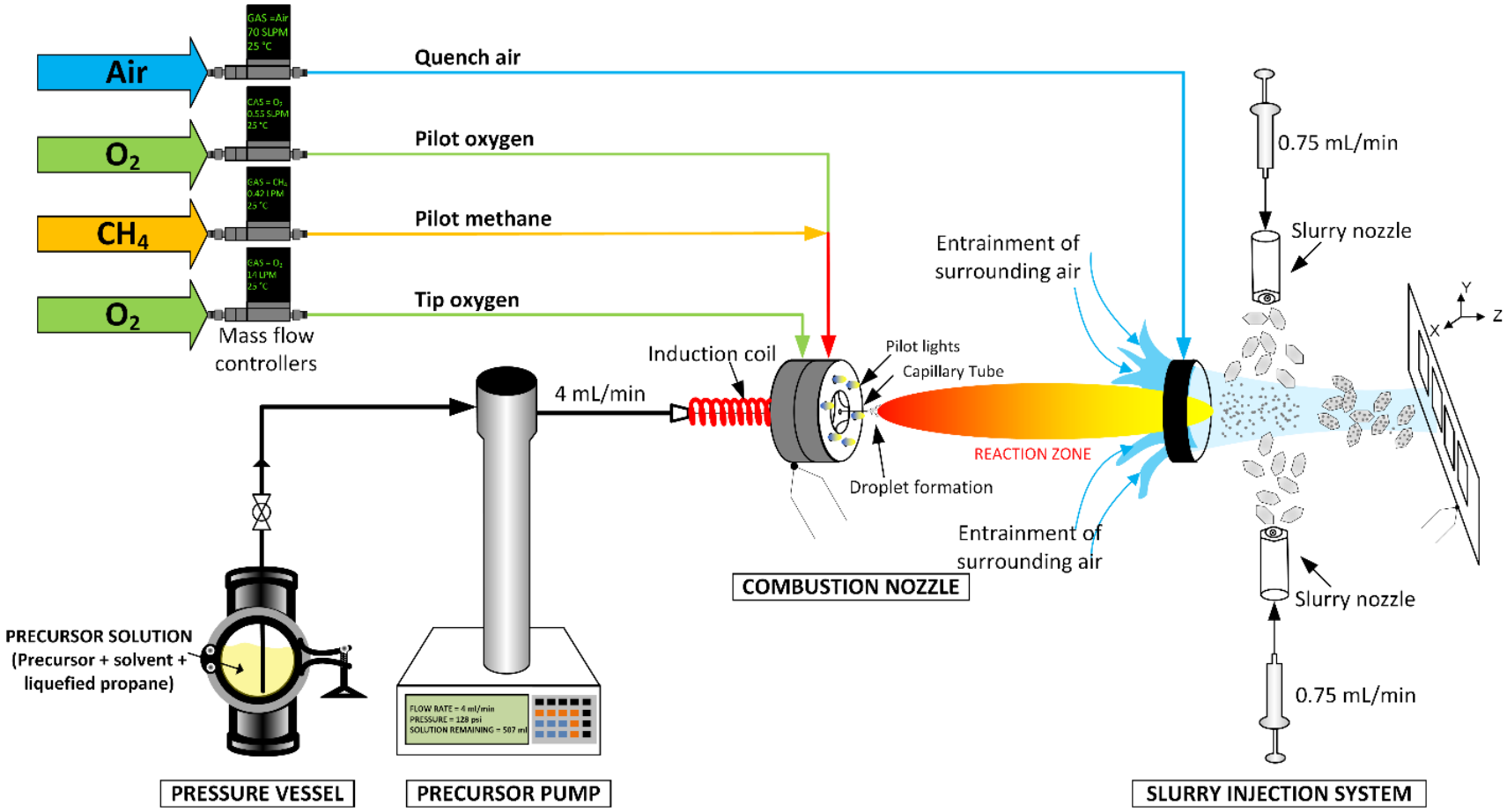

Fig. 6.1: Schematic of RSDT for the synthesis of Pt/ceria catalysts.

6.5.3 Characterization:

XRD patterns were obtained on a Bruker D8 advanced powder diffractometer using Cu Kα radiation. Small angle X-ray scattering (SAXS) was performed on a Rigaku Ultima IV diffractometer with CuKα radiation in the 2θ range of (0.6–5) with a step size of 0.05. Raman spectroscopy measurements were obtained with a Renishaw Ramascope micro-Raman spectrometer fitted with a reflected light microscope using a 50 mW laser (514.5 nm) and exposure time of 10 s at ambient conditions. Instrument alignment was optimized using a 520 cm^{-1} signal of a silicon wafer. Raman spectroscopy measurements were performed since this technique is well known to provide the concentration of active oxygen species and non-stoichiometry of the oxide supports [11, 12]. The spectra were obtained at room temperature in ambient atmosphere in the spectral range between 200 and 1200 cm^{-1}. XPS measurements were obtained on a PHI 595 Multiprobe system. The X-ray source was Al Kα (1486.6 eV) with 170 W power. The pass energy, step size and time per step was set at (100 eV/1 eV per step/50 ms) and (50 eV/0.1 eV per step/50 ms) for the survey scan and high resolution multiplex scan respectively. A pressure of 4 X 10^{-8} torr was maintained in the ultra-high vacuum (UHV) chamber. Data analysis and deconvolution of peaks were done using the CasaXPS software package. Nitrogen sorption experiments were performed on a Quantachrome Autosorb-1-1C automated adsorption system. The surface area was calculated by the BET method. SEM micrographs were obtained at 10 kV accelerating voltage and 10 mm working distance on an FEI ESEM Quanta 250. TEM micrographs of Pt on ceria particles were taken on a 200 kV JEOL 2010 FasTEM and also on a 120 kV FEI Tecnai T12 S/TEM, both fitted with LaB_6 source. To obtain the composition of the catalytic films, elemental analysis of the deposited films was determined by X-ray energy dispersive spectroscopy (XEDS) on an EDAX system and

inductively coupled plasma optical emission spectroscopy (ICP-OES) using a Perkin Elmer Optima 7300DV ICP-OES. *In-situ* diffuse reflectance infrared Fourier transform spectroscopy (DRIFTS) was used to monitor adsorption and reaction of CO and water on the Pt/ceria catalysts. DRIFTS spectra were recorded using a Thermo Nicolet 6700 FTIR (MCT detector) with a Harrick Praying Mantis DRIFTS accessory and reaction chamber fitted with a ZnSe window. 64 scans at 4 cm^{-1} resolution and 6.33 cm/s velocity were taken for each measurement, and fresh supported catalyst was used as the background. All experiments were performed using 1 vol% CO and 99 vol% Ar which was bubbled through a water bubbler maintained at 25°C for humidifying the reactant gases. This gave a final reactant gas composition of 0.94 vol% CO, 93 vol% Ar and 6 vol% water vapor at 25°C. Each catalyst was equilibrated under an inert Ar atmosphere at 100°C. The reactant gas stream was then introduced to the cell, and was exposed to the catalyst at 100°C for at least 20 min. The temperature was then ramped in 25°C increments followed by equilibration for at least 20 min, until no difference was observed in consecutive spectra. All data were analyzed using Thermo OMNIC software.

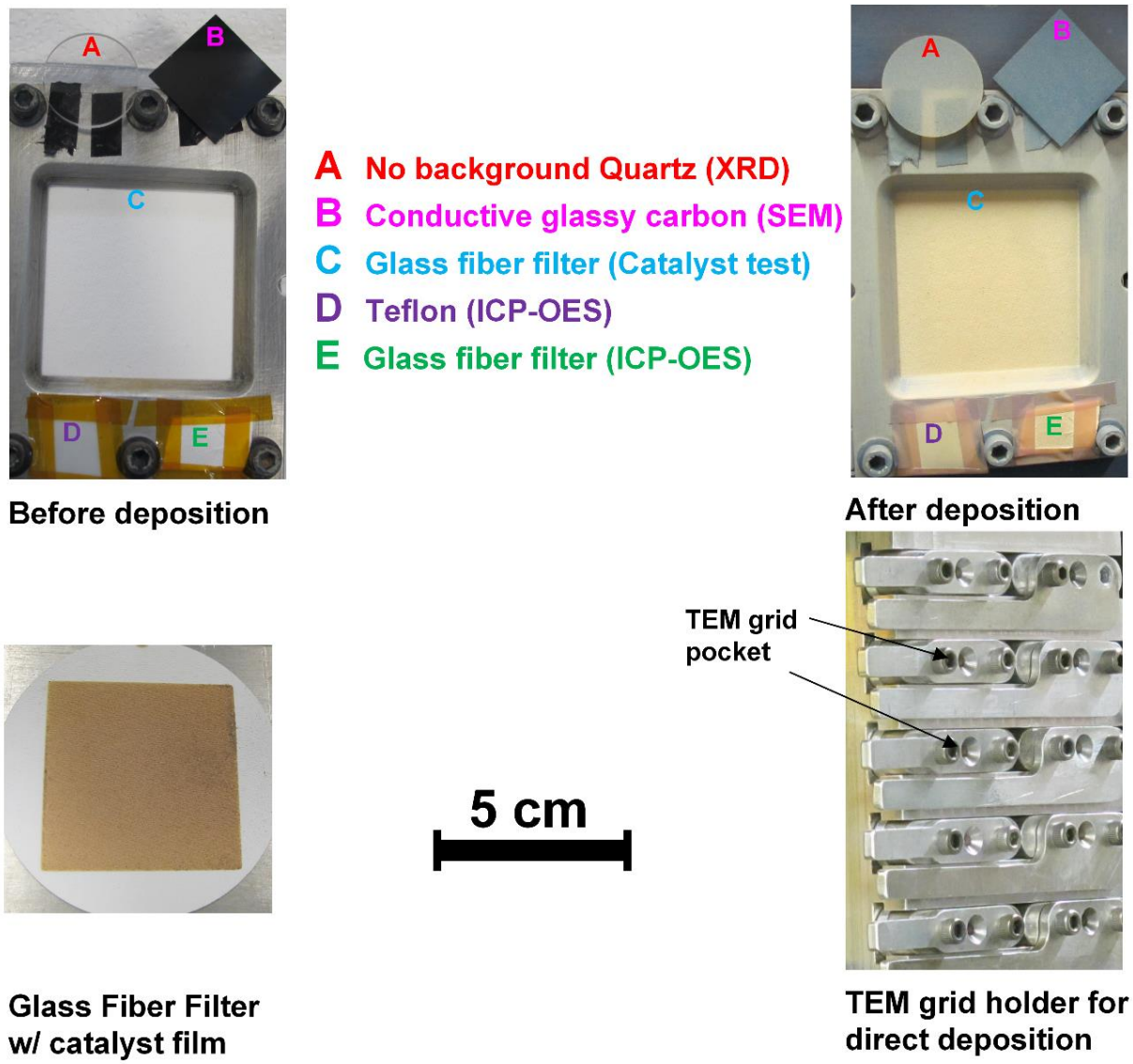

Fig. 6.2: Various substrates used during the deposition of Pt/ceria catalysts.

6.5.4 Catalytic testing:

Catalysts were tested for WGS activity, CO_2 & H_2 selectivity, in the temperature range of (150–450°C) with a ramp rate of 5°C/min. in Altamira Instrument's BenchCAT™ 1000R HP equipped with a fixed bed reactor, furnace and mass flow controllers for precise gas flow. The glass fiber filter substrates deposited with Pt/ceria catalysts were

crushed to a powder using a mortar and pestle and packed in the center of a quartz tube (18 cm long, and 3.9 mm ID) to a packing length of 4 cm. The packed bed reactor volume was approximately 0.48 cm^3 and length/diameter (L/D) ratio was 10.3. The gas flow with a composition of 1 vol% CO and 99 vol% Ar was set at 100 sccm and bubbled through a water bubbler maintained at 25°C for humidifying the reactant gases. This gave a final reactant gas composition of 0.94 vol% CO, 93 vol% Ar and 6 vol% water vapor at 25°C. The water bubbler was previously calibrated by bubbling Ar for a set period of time and collecting the water at the outlet using an ethanol cold trap to capture all the moisture picked up by Ar. Gas hourly space velocity (GHSV) of 13360 h^{-1} was used for the tests. An Agilent Micro gas chromatography (GC) with a thermal conductivity detector (TCD) was used for the identification of the products from the reactor. The GC was calibrated for CO, CO_2 and H_2 in the range (0.1–1 vol% in Ar) by flowing known standards. The concentration of the reactants and products were determined by comparing the GC peak area with the calibrated values. Complete CO conversion was concluded when the CO peak disappeared in the chromatogram. Glass fiber filter substrate was separately tested for WGS reaction to confirm that it does not participate in the reaction. In order to obtain a fair comparison between the catalysts, all the conditions of testing and characterization were kept exactly the same.

6.6 Results:

6.6.1 Structural properties:

6.6.1.1 X-ray diffraction (XRD):

Fig. 6.3 shows the XRD pattern of the ceria supported Pt catalysts. All three ceria materials show the fluorite cubic structure and were indexed with ICDD# 01-075-

9470. The difference in crystallite size is clearly evident from the peak width of the three catalysts. The mean crystallite size was calculated from X-ray line broadening by Debye Scherrer's method and was 5.6 nm (C1/Pt), 5.7 nm (C2/Pt) and 27.0 nm (C3/Pt). Lower crystallite size tends to have a higher Pt dispersion which may lead to better catalyst activity [13]. No significant Pt peaks were observed in the XRD possibly due to the small size of Pt (0.5–2 nm) [67] in spite of having a high Pt loading of 5 wt% [66] as measured by XEDS and ICP–OES. However, for C2/Pt a very small peak from Pt (111) was observed around the 2θ value of 40°. No significant peak shift of the prepared catalysts as compared with the non-doped ceria was observed which implied that the Pt was not incorporated into the ceria structure [14]. SAXS measurement for the catalysts revealed mesoporosity for C1/Pt catalysts.

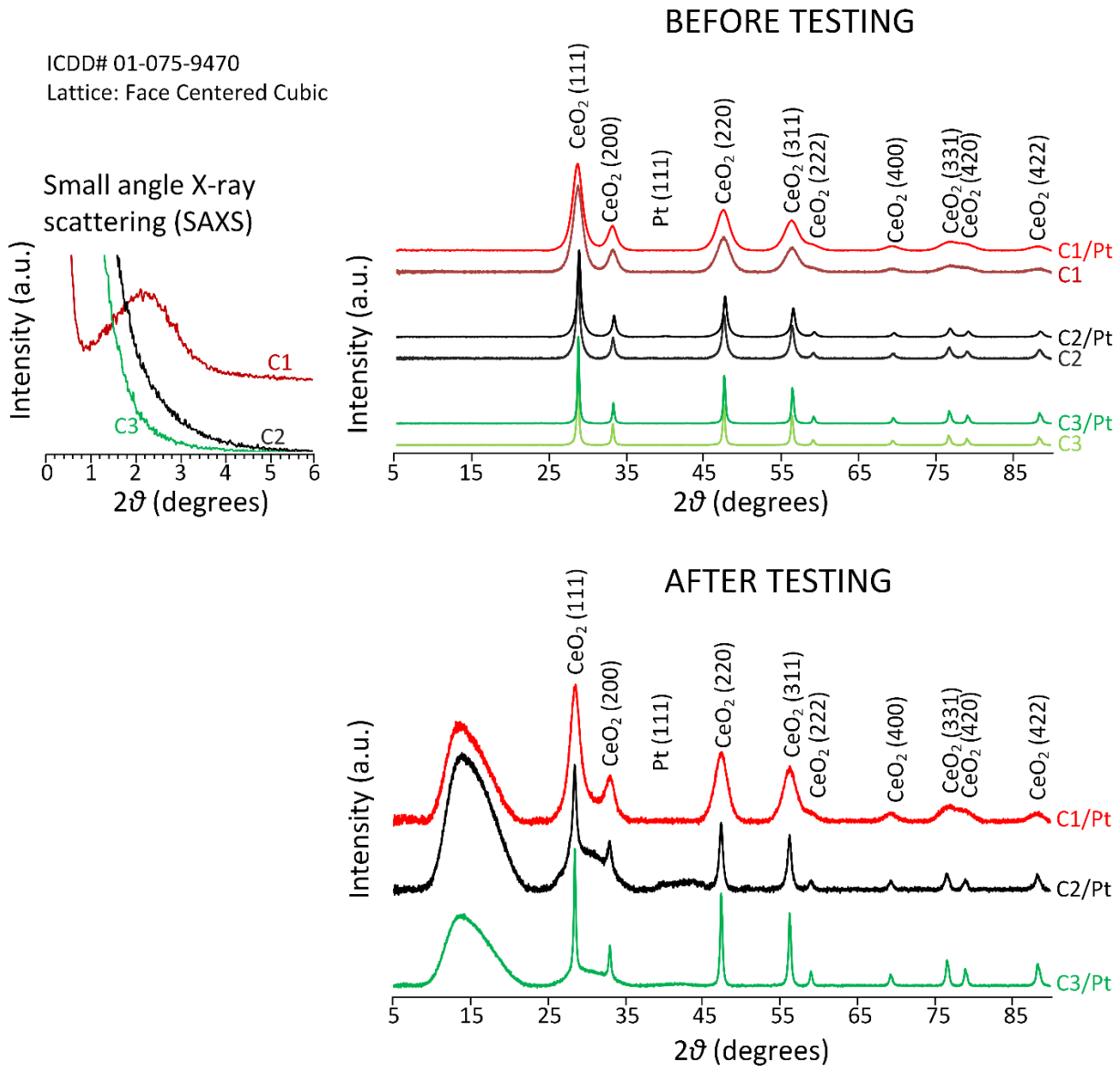

Fig. 6.3: X-ray diffraction (XRD) pattern of ceria (C1, C2, C3) support and of Pt/ceria (Pt/C1, Pt/C2, Pt/C3) catalysts before and after testing for water-gas shift (WGS) reaction showing the difference in crystallite size and small angle XRD (SAXS) showing the difference in crystallite size and small angle XRD (SAXS) showing the mesoporosity in ceria (C1) support.

6.6.1.2 Raman Spectroscopy:

Since the defect formation in nanocrystalline materials is controlled by the microstructure, Raman spectroscopy was used to obtain information about the interaction

between the ions and was very useful in studying the microscopic nature of the nanocrystalline ceria [15]. Fig. 6.4 shows the Raman spectroscopy results of the as prepared Pt/ceria samples before the WGS reaction tests. The strongest intensity mode at around 457 cm^{-1} as seen in C1/Pt and C2/Pt represents the first order Raman F2g mode, which originates from Ce-8O stretching vibrations. However this peak is shifted to 464 cm^{-1} for C3/Pt. The full width at half maximum (FWHM) of the ceria peak is of the order C1/Pt>C2/Pt>C3/Pt. High FWHM and lower energy for this first order Raman peak is associated with smaller crystallite size [16, 17], consistent with the crystallite size calculation from XRD data. Several second order peaks can be seen. A peak is seen in C1/Pt near 260 cm^{-1} which can be assigned to the 2TA or doubly degenerated TO mode [18, 19] which is present only in ceria lattice with high defect concentration. A weak and broad peak at about 600 cm^{-1} can be seen in C1/Pt and C3/Pt which can be assigned to the intrinsic oxygen vacancies due to the non-stoichiometry of the sample [11]. Non-stoichiometric ceria (CeO_{2-x} where $x \leq 0.28$ [20]) possesses a high concentration of defects, reduced grain boundary impedance, and heat of reduction around 2.4 eV lower per oxygen vacancy compared to stoichiometric ceria [21]. In C1/Pt, mesoporous ceria, additional secondary peaks were seen near 841 cm^{-1} and 1055 cm^{-1} which can be denoted by peroxides (O_2^{2-}) and superoxide (O_2^-) respectively, caused by adsorbed surface oxygen [22]. No such peaks can be observed in C2/Pt, and only the superoxide peak is observed in C3/Pt. These active oxygen species are formed at one-electron defect sites at the metal-support interface which oxidize adsorbed CO to CO_2 and increase catalytic activity [22]. Similar results were also witnessed by Hua et al. on mesoporous ceria nanotubes [23].

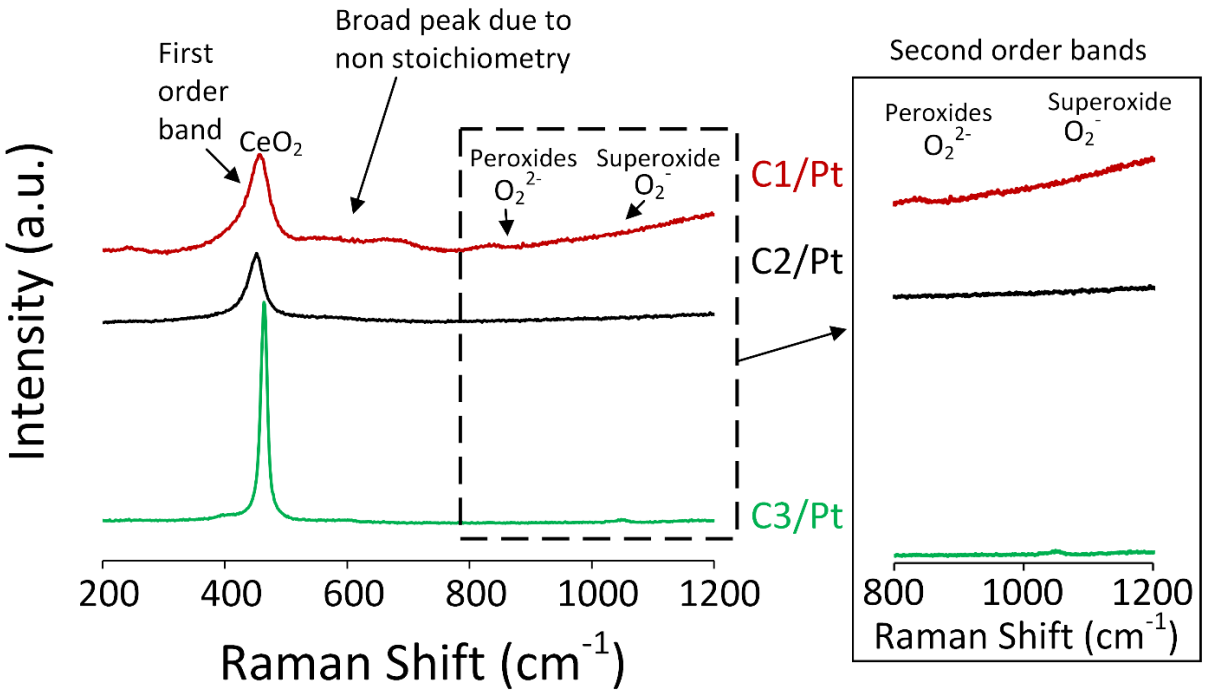

Fig. 6.4: Raman spectroscopy of Pt/ceria catalysts showing the presence of active oxygen species and non-stoichiometry in ceria for C1/Pt and C3/Pt.

6.6.1.3 BET surface area:

N_2 sorption measurements were performed for the fresh catalysts as well as spent catalyst after 100 h. of operation, and surface area was calculated by the BET method which is shown in table 6.1. The surface area of the catalysts reduced by 38% (C1/Pt), 75% (C2/Pt) and 44% (C3/Pt) after 100 h. of operation. This reduction in surface area can be attributed to the catalyst sintering at high temperature.

Table 6.1: Comparison of the catalyst properties and performance.

Sample (powder)	Syntheses method	BET surface area (m^2/g)	Crystallite size from XRD (nm)		
			As synthesized	After Pt deposition by RSDT	After WGS tests
C1	Sol-gel-based inverse micelle method	187	5.8	5.4	6.0
C2	Combustion chemical vapor deposition	78	15.5	15.8	15.8
C3	Commercially obtained (firing high purity cerium oxalate)	183	24.6	27.5	29.0

Sample (on glass fiber filter)	Syntheses method	BET surface area (m^2/g)		100%CO conversion temperature (°C)
		Before testing	After 100 h. testing	
C1/Pt	RSDT	56	35	225
C2/Pt	RSDT	40	10	450
C3/Pt	RSDT	36	20	250

6.6.1.4 X-ray photoelectron spectroscopy (XPS):

A high resolution spectra for Pt(4f), O(1s), and Ce(3d) is shown in Fig. 6.5 for the as prepared samples before WGS reaction tests. For the Pt(4f) spectra in the binding energy range 65–85 eV, the peaks were deconvoluted into two sets of photoemission doublets- Pt($4f_{7/2}$) and Pt($4f_{5/2}$). The reference binding energy for Pt($4f_{7/2}$) and Pt($4f_{5/2}$) is 70.9 eV and 74.25 eV respectively with a spin-orbital splitting energy of 3.35 eV [24]. This data show, that the doublets for Pt($4f_{7/2}$) and Pt($4f_{5/2}$) represents a Pt^{2+} & Pt^{4+} on the ceria surface, which are the most

stable oxidation states of Pt. The corresponding coverage area of Pt^{2+} & Pt^{4+} on the ceria surface for as prepared C1/Pt, C2/Pt and C3/Pt were (80% & 20%), (75% & 25%) and (91% & 9%) respectively. Ce($3d_{5/2,3/2}$) spectra was shown at 882.9 eV and 901.3 eV respectively along with the characteristic satellite peaks at 917.3 eV, 907.8 eV, 899 eV, and 890 eV. Both Ce^{3+} and Ce^{4+} oxidation states can be seen in C1/Pt and C3/Pt which demonstrates that the corresponding ceria are non-stoichiometric, and the ceria lattice has oxygen vacancies [25]. Only a minor Ce^{3+} peak can be seen at 907.8 eV binding energy for C2/Pt. O(1s) spectra in the binding energy range 525–540 eV, were deconvoluted into 4–5 peaks to determine the surface concentration of oxygen ions and were compared with the reference binding energy of peroxides [O_2^{2-} (530.5 eV)], superoxides [O^{2-} (529.5 eV)], PtO_2 (531.4–531.9 eV), CeO_2 (528.7 eV), Ce_2O_3 (529 eV), C=O (533 eV), and C-O (531.5–532 eV)] [26]. It is difficult to determine the exact concentration of each species due to relatively close binding energy value between the species, however the presence of peroxides and superoxides cannot be ruled out for C1/Pt in conjunction with the Raman spectroscopy measurements.

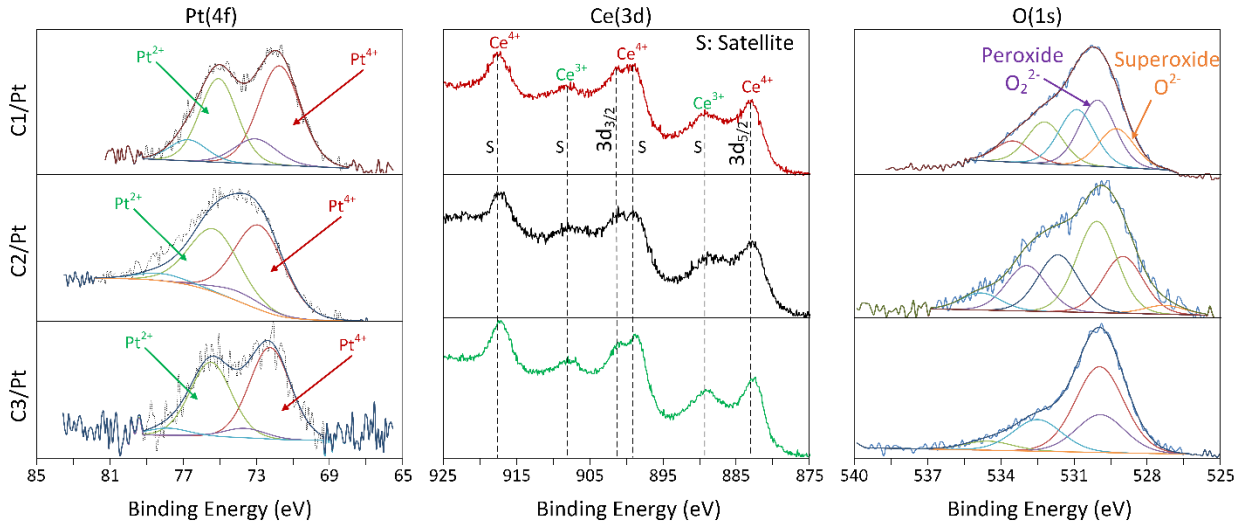

Fig. 6.5: XPS of core level region of Pt(4f), Ce(3d) and O(1s) for Pt/ceria catalysts.

6.6.1.5 Electron microscopy (SEM and TEM):

The SEM micrographs of the as prepared catalyst films are shown in Fig. 6.6 (a), (b) and (c) for C1/Pt, C2/Pt and C3/Pt respectively. From Fig. 6.6 (a) and (b) the surfaces of the catalyst films are very rough, and show the formation of some agglomerated particles around 5–10 μm wide. Fig. 6.6 (a) shows that the glass fiber filter is evenly coated and the Pt/ceria particles have coated the fibers uniformly on the front as well as the back. Fig. 6.6 (c) for shows a smooth and uniform film for C3/Pt catalysts. Fig. 6.6 (d)–(i) shows the TEM micrographs of the as prepared catalysts. Mesoporosity is evident from the TEM micrograph of C1/Pt catalyst in Fig. 6.6 (g). The spherical agglomerates for the mesoporous ceria (C1) as shown in Fig. 6.6 (d) are formed during their synthesis by the sol-gel based inverse micelle method, inside the inverse spherical surfactant micelles. The initial size is controlled by the size of the inverse micelle, it can expand later based on the heat treatment. The monodispersed nanoparticles aggregate to form the porous network as shown in Fig. S12 of reference [3]. These materials, in general, produce these types of aggregates and the behavior is typical for the materials synthesized using the inverse micelle method. The diameter of spherical agglomerates do not change after deposition of Pt onto them. C1/Pt sample range from 60–180 nm. However the individual crystallites in the agglomerates are always in the range 4–5 nm. HRTEM micrographs in Fig. 6.6 (g), (h) and (i) clearly shows 0.5–2 nm size Pt particles on ceria. No evidence of Pt sintering is observed during its formation in RSDT which could be due to the use of air quench in RSDT. Selected area diffraction patterns (SADP) are shown in the insets in Fig. 6.6 (g), (h) and (i). The diffraction rings corresponds to cubic fluorite ceria. Reflection from the Pt (111) plane could not be seen from the SADP possibly due to strong interference from ceria.

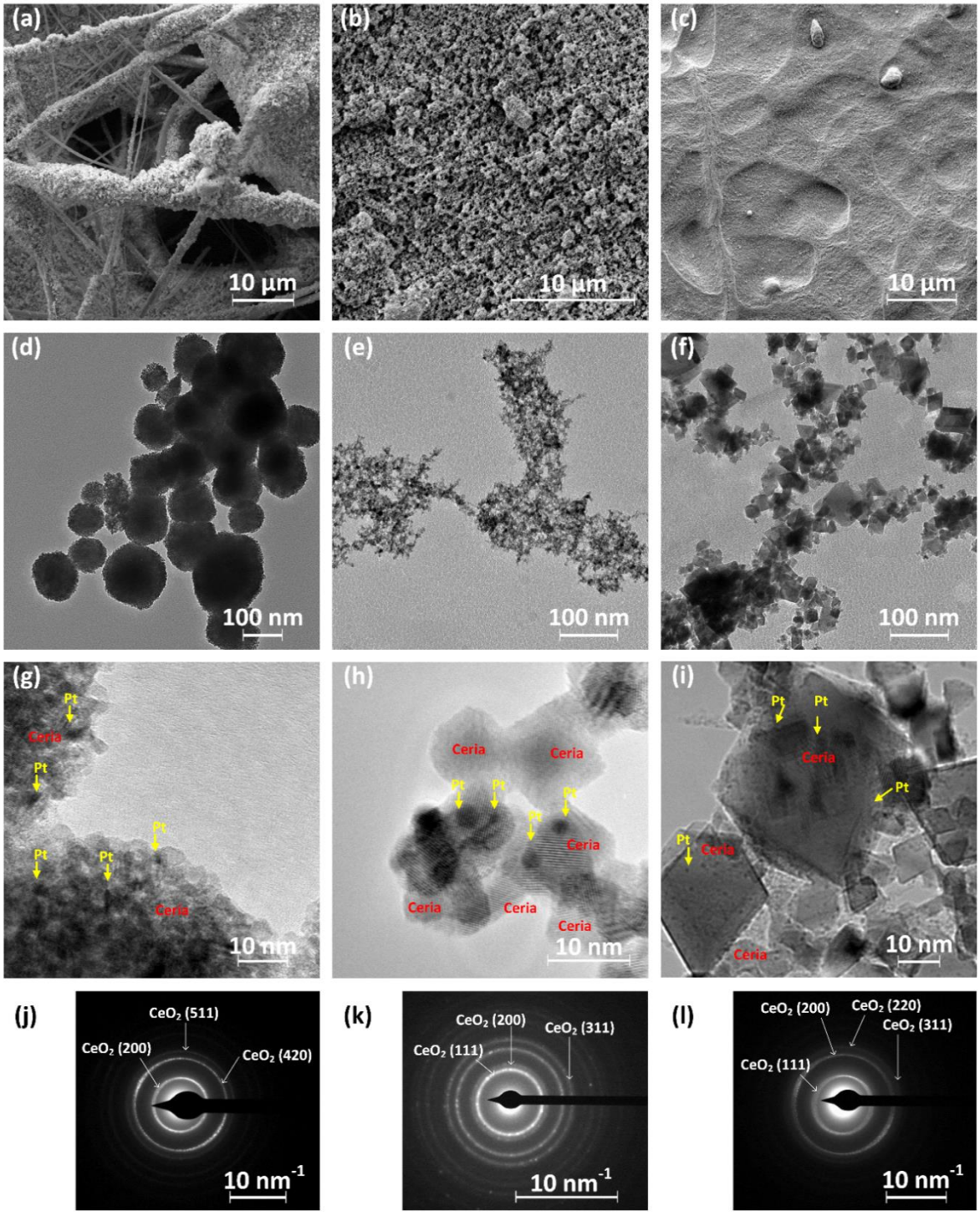

Fig. 6.6: Electron microscopy study for Pt/ceria catalysts after water-gas shift reaction testing: (a), (d), (g): C1/Pt, (b), (e), (h): C2/Pt, (c), (f), (i): C3/Pt. (a), (b) and (c): SEM on glass fiber filter with catalyst coating. (d), (e) and (f): TEM micrographs using 120 kV FEI Tecnai T12. (g), (h) and (i): HRTEM micrographs using 200 kV JEOL 2010 FasTEM. (j), (k) and (l) SADP taken for the area shown in (g), (h) and (i).

6.6.1.6 Diffuse reflectance infrared Fourier transform spectroscopy (DRIFTS):

In order to confirm the mechanism involved in the WGS reaction, *in-situ*-DRIFTS studies were performed at 100–300°C (C1/Pt), 100–450°C (C2/Pt), and 100–350°C (C3/Pt). The species obtained are monitored as shown in Fig. 6.7. The peak assignments for various species are provided in detail in table 6.2, as confirmed from literature [27]. The DRIFTS spectra can be divided into three main groups based on the position of the IR bands: OH groups (3800–3600 cm^{-1}), formate groups (3000–2800 cm^{-1}), and carbonate groups (1700–1000 cm^{-1}). There are very distinct differences in the three catalysts based on the evolution of various groups at different temperatures and band intensity. OH groups started evolving at 200°C for C1/Pt, 250°C for C2/Pt, and 250°C for C3/Pt and is much lower in intensity for C3/Pt than C1/Pt and C2/Pt. Formate bands at 2951–2947 cm^{-1} (bridged C-H) and 2858–2845 cm^{-1} (bidentate C-H) were seen in all the catalysts due to the C-H stretching vibrations and the reaction of CO with hydroxyl groups [28]. The CO_2 bands at 2359 and 2349 cm^{-1} produced from CO oxidation in the WGS reaction [29] can be seen starting at 100°C for C1/Pt and C3/Pt, however not until 225°C for C2/Pt. Bands around 2170 cm^{-1} for CO-Ce^{4+} interaction were not detected for C2/Pt. An interesting observation was seen in C3/Pt between 2100 cm^{-1} and 2050 cm^{-1}, the region where the interaction between CO and Pt can be observed. A band started evolving at 150°C which continued to shift towards lower wavelengths: 2090 cm^{-1} (150–175°C), 2077 cm^{-1} (175–225°C), 2073 cm^{-1} (250°C), 2070 cm^{-1} (275–300°C), 2067 cm^{-1} (325°C), and 2063 cm^{-1} (350°C). This could indicate the interaction between CO and oxidized Pt at low temperature (150–175°C) which ultimately ended up with the interaction between CO and Pt nanoclusters [30]. Such a peak shift was not noticeable in C1/Pt. A very weak CO-Pt band can be observed in C2/Pt. This could be because the CO adsorption on Pt is not significant for C2/Pt. A weak band was observed at 1963 cm^{-1} (275–350°C)

in C3/Pt which could be due to electronic effects, surface energetics or formation of Pt-carbonyls. From the DRIFTS studies of the three catalysts it can be concluded that the formate mechanisms dominate the WGS reaction for C1/Pt and C3/Pt. However, the ceria mediated redox mechanisms cannot be ruled out based on these studies. The presence of only weak formate bands for C2/Pt strongly indicate the ceria mediated redox mechanism for this material. There is a strong bias and disagreement in literature on the formate and redox mechanism and it is imperative that a suitable agreement is reached to enable better design and development of WGS reaction catalysts [31]. The role of the Pt is the extraction of oxygen from the ceria and water splitting to form OH groups. These OH groups are the basis of the WGS reaction. The reaction steps for the redox and formate mechanisms are explained in details in Fig. 6.8.

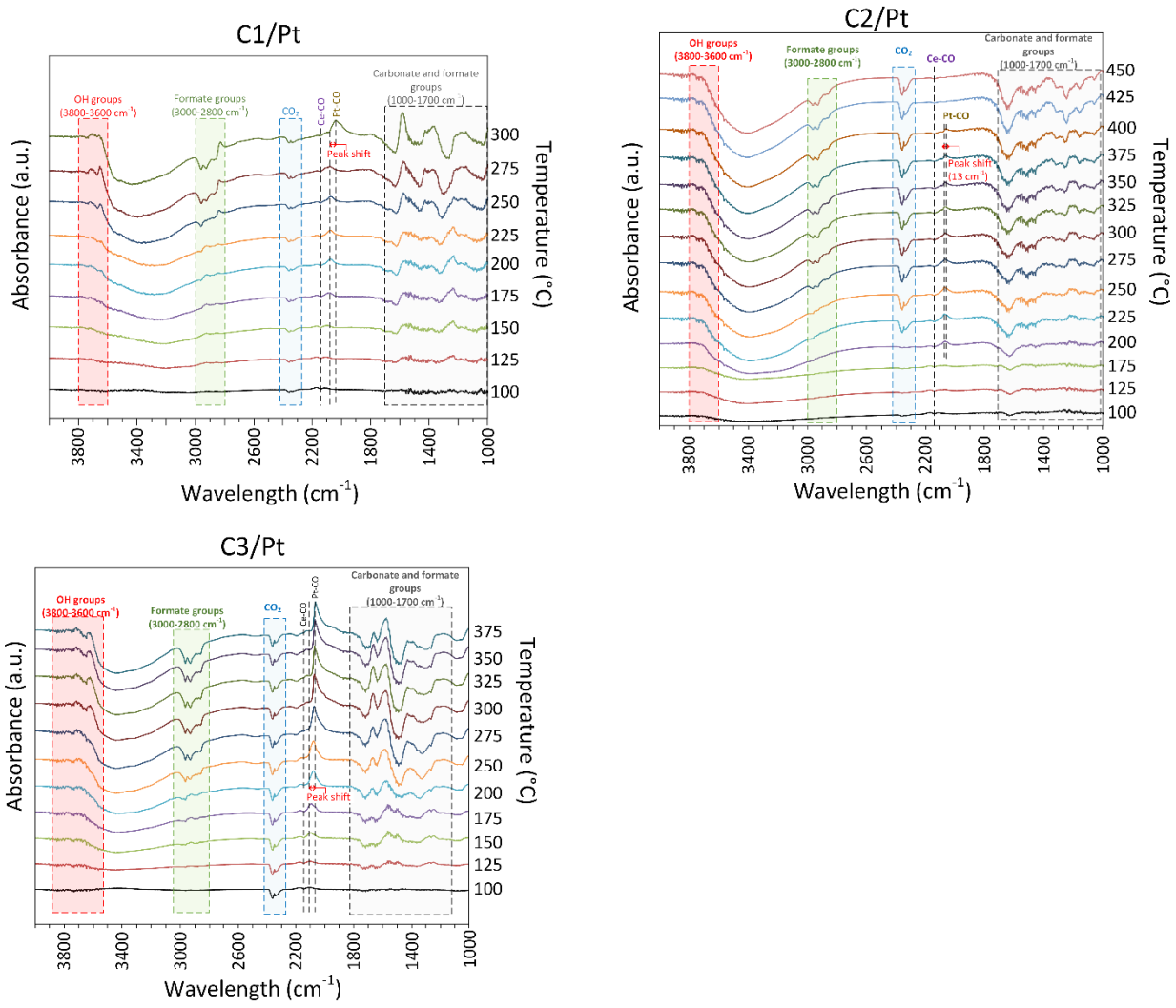

Fig. 6.7: Comparison of the DRIFTS spectra of Pt/ceria catalysts conducted *in-situ* in presence of 0.94 vol% CO, 93 vol% Ar and 6 vol% water vapor at various temperatures.

Table 6.2: DRIFTS bands assignment for the Pt/ceria catalysts.

Species		Wavelength (cm^{-1})		
		C1/Pt	**C2/Pt**	**C3/Pt**
OH	unidentate	3710	3716	3716
	bidentate	3660	3635	3635
	tridentate	3508	3508	3508
Formates	bidentate C−H	2845	2858	2858
	bridged C−H	2947	2951	2951
	asymmetric OCO	1585	1579	1572
	symmetric OCO	1379	1381	1383
Carbonates	unidentate, bidentate, and bridged	1000−1400	1000−1400	1000−1400
	carboxylic acid	1635	1635	1659
CO_2	asymmetric stretching vibrations	2359	2359	2359
		2349	2349	2349
CO−Pt		2070	2073−2060	2090−2063
Ce−CO	Ce^{4+}	2173	not detected	2170−2158
	Ce^{3+}	2143	2143	2123

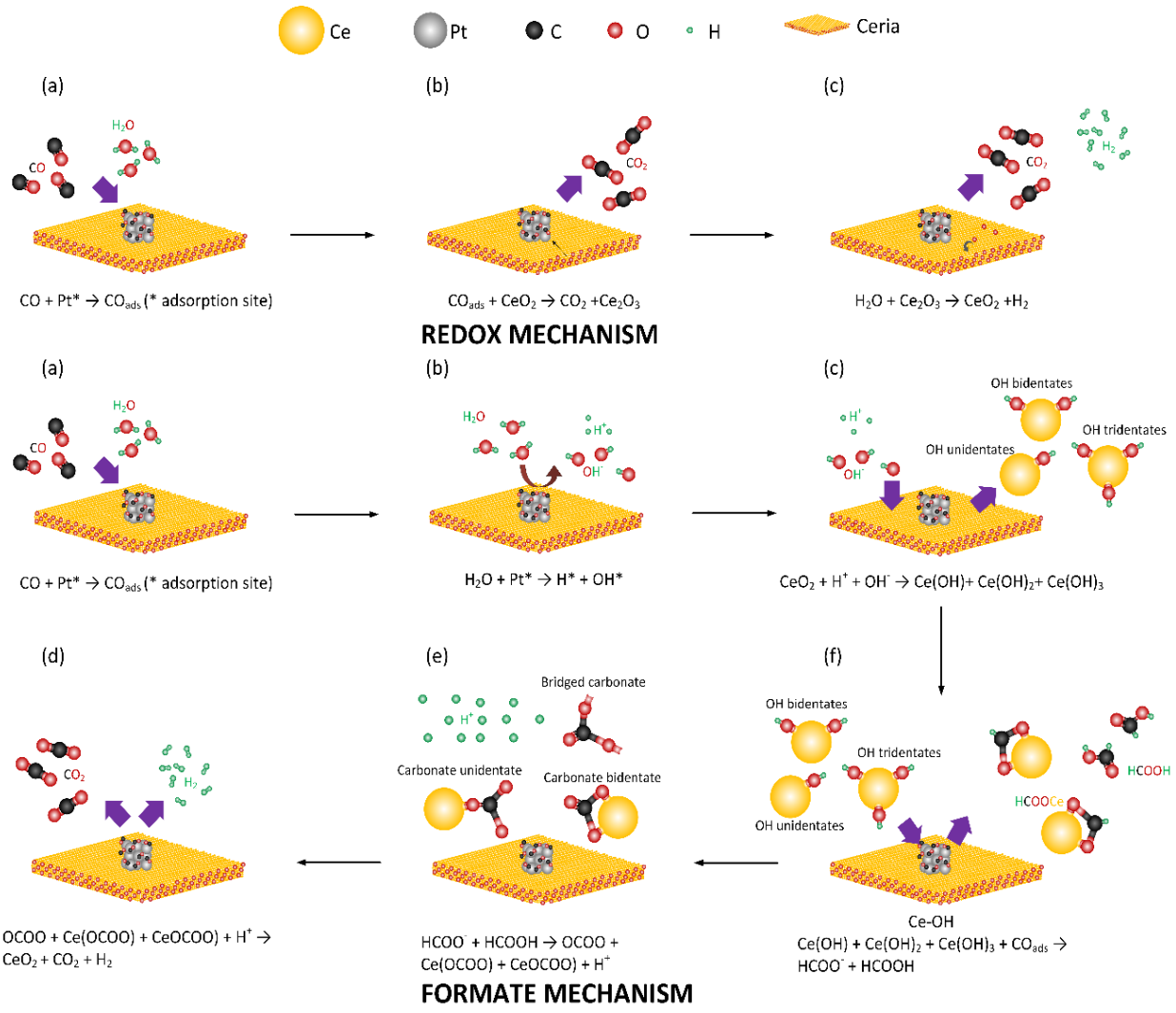

Fig. 6.8: Redox and formate mechanisms for the water-gas shift (WGS) reaction on Pt/ceria catalysts shown in atomic scale.

6.6.2 Water gas shift (WGS) reaction activity:

The activity of the three ceria supported Pt catalysts is shown in Fig. 6.9 as tested from 150–450°C with a feed flow rate of 100 sccm (composition of 0.94 vol% CO, 93 vol% Ar and 6 vol% water vapor). CO concentration in the products of the WGS reaction was checked in GC by comparing the area under the curve for the output, and calibrated CO. Complete CO

conversion was concluded if no peak was obtained for CO. The C1/Pt performed best in this range with a complete CO conversion to CO_2 at 225°C followed very closely by C3/Pt at 250°C and C2/Pt at 450°C. No methanation activity was observed in the reaction. All the three catalysts were active at 175°C.

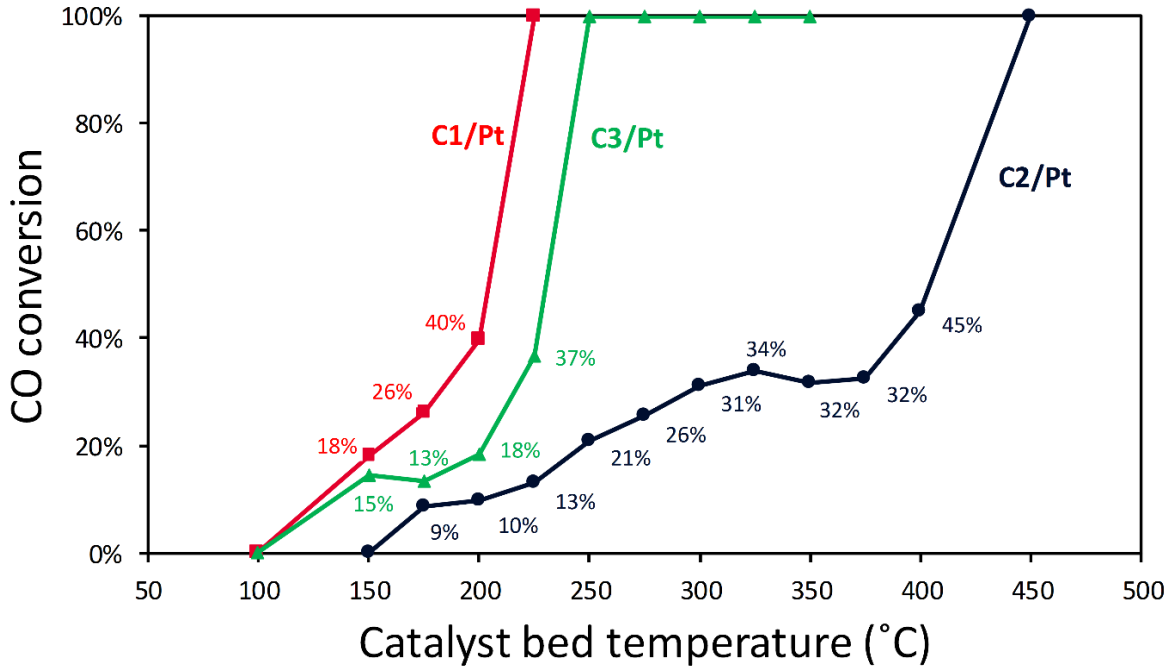

Fig. 6.9: Water-gas shift reaction activity comparison for Pt/ceria catalysts.

6.7 Discussion:

On the basis of the WGS reaction testing of the three ceria supported Pt catalysts, it was found that the catalyst with sol-gel produced ceria (C1/Pt) had performance superior to the catalyst employing commercial ceria (C3/Pt). Both C1/Pt and C3/Pt performed better than the catalyst employing CCVD produced ceria (C2/Pt). Our previous work [1] and a review of the literature has shown that the characteristics of the catalysts support that are most important for

good performance are: (1) high surface area of the ceria and Pt [32], (2) higher Pt dispersion [33], (3) presence of ionic Pt rather than metallic Pt [33], (4) CO adsorption strength at Pt-ceria interface [34], (5) smaller crystallite size of ceria and Pt [21, 32, 35], (6) non-stoichiometry of ceria [21], (7) presence of active oxygen species on the surface of the catalysts [12, 22], (8) better resistance to deactivation [36], and (9) mesoporosity in the ceria support [37]. In this discussion we will identify the reasons for the importance of these characteristics for catalyst performance and show that the WGS reaction test data presented in this work explains the related catalyst activity as a function of these supports.

WGS kinetics is strongly dependent upon the morphology of ceria support. Bunluesin et al. measured the steady-state, WGS kinetics on Pd supported low temperature sintered (570K) ceria and high temperature sintered (1670K) ceria. They found that with similar Pd dispersions, the low temperature sintered ceria catalysts had a 50 times higher reaction rate and 50% lower activation energy than high temperature sintered ceria catalyst [32]. This could be due to the decrease in the surface area of the ceria support at high temperature sintering. The larger crystallite size of ceria produced by high-temperature calcination prior to noble metal addition (as in commercial ceria, C3) decreases its reducibility and eliminates the ceria mediated process step for CO oxidation [32, 38]. The defect site concentration in ceria is strongly dependent on the surface area. High surface area may correspond to smaller crystallite size which causes an increase in strain at the edges of the particles as reported by Schimming et al. [39]. Similarly, low energy grain boundary formed in smaller ceria particles also facilitates the formation of defects [21]. Higher concentration of defects corresponds to greater non-stoichiometry in ceria which has lower oxygen vacancy formation energy (E_{vac}) than ordered ceria. Hence non-stoichiometric ceria can be easily reduced at low temperature [21]. This results in reduced activation energy. On the basis

of the WGS reactions results in this study and the findings in literature [32, 39, 40] we can presume that, there can be an indirect relationship between the activation energy and the BET surface area of the ceria support and the lower BET surface area C2 (78 m^2/g) required higher activation energy than C1 (187 m^2/g) and C3 (183 m^2/g).

In regards to Pt loading comparison with our previous work on WGS reaction activity with 1% nanoparticles Pt loading onto ceria support [1], we see a remarkable similarity in the results. This showed that increasing the Pt metal loading did not improve the WGS reaction activity of catalysts. This can be explained as follows: The role of Pt is to catalyze the partial reduction of ceria and the generation of active OH groups. Relatively few Pt atoms at the Pt-ceria-CO triple phase boundary are available for catalysis in Pt/ceria catalyst [34]. After a threshold loading, no further improvement in catalytic activity can be observed [30, 33, 41]. At low Pt loading (<1%), highly dispersed Pt can be present on the surface in the ionic state and metallic state. However at high loading, only a small fraction is present in ionic state and most of it is in metallic state. Fu et al. has proposed that the key catalytic sites for the WGS reaction is highly dispersed Pt-O and the metallic Pt does not participate in the WGS reaction and most of it remains unutilized. Preferential diffusion of ionic Pt in the subsurface of ceria has been considered as an explanation [33]. Similar studies have also been confirmed, both experimentally and by using DFT modelling by Zhai et al. [42]. These observations in literature are consistent with our XPS study that at 5% Pt loading, Pt is available in mostly metallic form consistent with the findings in literature [43].

From the comparison of the DRIFTS band for the CO-Pt at around 2070 cm^{-1}, it can be concluded that the CO adsorption strength was highest in C3/Pt followed by C1/Pt and C2/Pt. DFT and micro kinetic modelling has shown that strongly adsorbed CO molecules on Pt-

ceria interface could enhance the WGS reaction at the neighboring sites by reducing the CO adsorption strength at those sites [34]. Another reason for the better activity can be attributed to the CO uptake of ceria which is linearly dependent on the surface area [27]. High surface/grain-boundary area enhances the electron-transport properties between the ceria and Pt. This leads to faster CO_2 conversion.

Enhanced activity of C1/Pt could also be explained by the small crystallite size of C1 (5.8 nm). Ceria particles with crystallite size <10 nm shows remarkable catalytic properties and lower heat of reduction per oxygen vacancy as compared to coarser ceria [21] which could be due to the presence of low energy grain boundary, which facilitates the formation of defects. Size dependency of ceria has also been elaborated by Cargnello et al. [35]. Bunluesin et al. has suggested that the activation energy of the WGS reaction is strongly dependent upon the crystal structure of ceria and tends to decrease with the decrease in its crystallite size [44]. This is because the larger crystallite size of ceria produced by high-temperature calcination prior to noble metal addition (as in commercial ceria, C3) decreases its reducibility and eliminates the ceria mediated process step for CO oxidation [32, 38]. The surface areas for C1 and C3 (before Pt was deposited) are nearly identical (table 6.1), but the crystallite sizes are very different. We believe that this difference occurred because the BET surface area takes into account the particle size. Fig. 6.10 shows a hypothetical case when this situation (similar BET surface area but different crystallite size) is possible. It should be also noted that the crystallite size determination from XRD (Debye Scherrer's equation) and BET surface area determination from N_2 sorption does not take into account the distribution. It only considers the average throughout the sample in consideration. HRTEM micrographs of C1 [Fig. 6.6 (g)] and C2 [Fig. 6.6 (i)] do show the crystallites of size around 5 nm for C1 and around (10–100 nm) for C3.

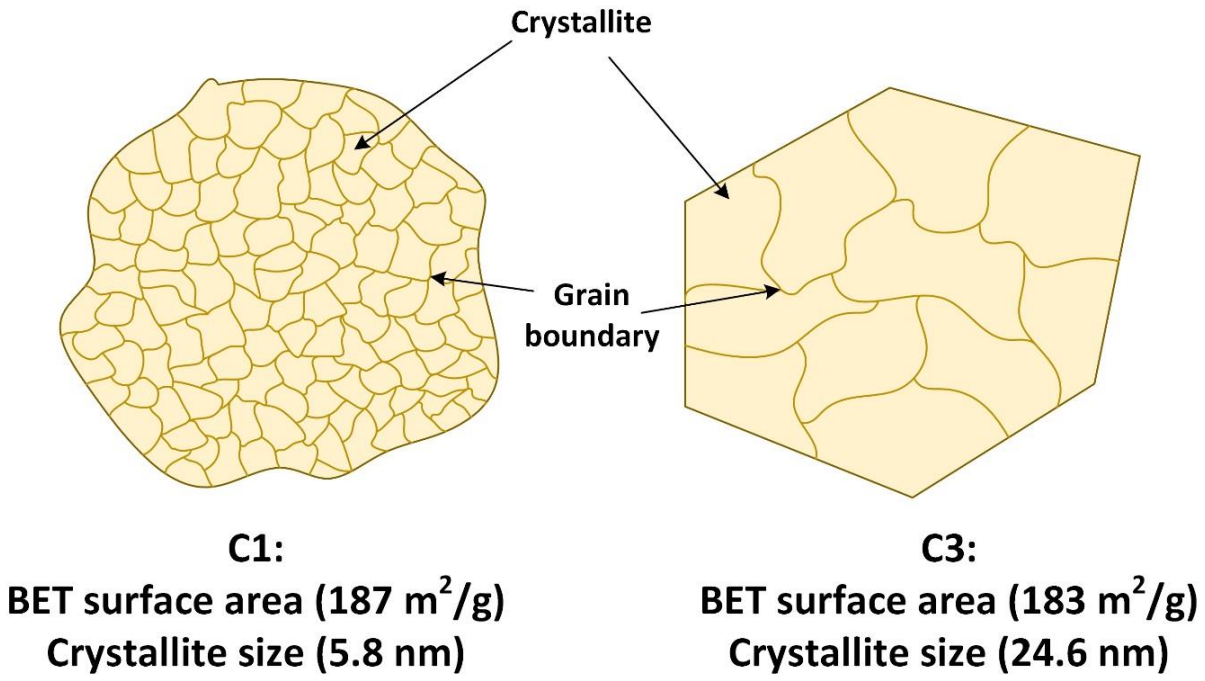

Fig. 6.10: A hypothetical situation when similar surface area particles can have varying crystallite sizes.

The WGS reaction rate is directly dependent on the synthesis conditions of ceria [30, 31]. From DFT modelling, two types of interactions between Pt and ceria have been defined: transfer of electrons from the Pt nanoparticle to ceria, which is independent of the morphology of ceria, and the oxygen transfer from ceria to Pt, which is strongly dependent on the ceria support and occurs only when the ceria is nanostructured, oxygen deficient, and non-stoichiometric (CeO_{2-x}) [45]. Non-stoichiometric "ceria" has lower oxygen vacancy formation energy (E_{vac}) than ordered "ceria". Hence non-stoichiometric ceria can be easily reduced at low temperature [21]. XPS results indicate the non-stoichiometric characteristics of C1/Pt and C3/Pt due to the presence of Ce^{3+} and Ce^{4+} peaks [25]. Raman spectroscopy results in this work also indicate that the ceria in C1/Pt and C3/Pt is non-stoichiometric as evident from the weak and broad peaks at the Raman shift at 600

cm^{-1} [11]. The 600 cm^{-1} peak intensity is greater in C1/Pt than C3/Pt and C2/Pt. This means that C1/Pt has a higher concentration of defects than C3/Pt and C2/Pt. These results are consistent with the performance of WGS reaction tests in Fig. 6.9.

Raman spectroscopy also showed the existence of dioxygen such as peroxides and superoxides subspecies at the surface of the catalyst with mesoporous ceria (C1/Pt) and catalyst with commercial ceria (C3/Pt). Formation of these species could also be explained by the following: peroxides are diamagnetic and could be formed as a result of the interaction of O_2 with the oxygen vacancies at the ceria surface because these are two-electron-donor centers. It was shown by DFT calculations that superoxides are formed by direct interaction of O_2 with low-coordinated Ce^{3+} ions on reduced ceria surface [46]. These active oxygen species are formed at one-electron defect sites at the metal-support interface and are preferentially stabilized by ceria which oxidize adsorbed CO to CO_2 and increase catalytic activity [12]. Superoxides are also responsible for the re-oxidation of the partially reduced ceria.

Deactivation of the catalysts are a major issue in WGS reactions. Deactivation of the catalysts can also be a cause of different reaction rates which can be caused by: (1) Pt deactivation due to CO poisoning caused by excess CO in the feed which blocks the sites for H_2O dissociation [43,47], (2) sintering of Pt to form large clusters [48], (3) formation of highly stable carbonates over the Pt-ceria active sites on the catalyst [49], thereby rendering them unavailable, (4) growth in the crystallite size of ceria under extended operation at high temperature which compromises its reducibility [50], (5) loss of faceted surface of ceria [51] and (6) reduction of the Pt dispersion on ceria [52]. From the BET surface area analysis we found that the surface area of the catalysts reduced by 38% (C1/Pt), 75% (C2/Pt) and 44% (C3/Pt) after 100 hours of operation. It was also found that the surface area of C2/Pt reduced by 55% at 225°C (13% CO conversion).

Mesoporosity of ceria also plays a major role in improving the WGS activity. In addition to the high surface area, the activation energy of WGS reaction is lower in mesoporous ceria supported Pt catalysts as compared with microporous ceria because mesoporous ceria provides more accessible and higher number of active sites for the reaction intermediates. This also delays the catalysts deactivation by coke formation [36].

Another reason for enhanced catalytic activity by mesoporous ceria could be derived from the pore geometry. The internal concave surface of the pores of the mesoporous ceria possess higher concentration of oxygen vacancies than the surface. This is attributed to the low adsorption energy of OH groups in the pores due to the enhanced inter adsorbate repulsion in the curved walls of the pores, formed during the WGS reaction [37]. The meso-pore expansion on heat treatment of mesoporous ceria as shown by Poyraz et al. certainly contributes to the enhanced activity of the WGS catalyst [3].

Strong metal-support interaction (SMSI) has been recently proposed to describe the chemisorption properties of nanometer sized Pt clusters as they are dispersed on the ceria support. The support has a strong influence on the catalysts because WGS activity is greatly effected in spite of having the same size and dispersion of Pt as also proved in this work. Bruix et al. has demonstrated, on the basis of theory and experimentation, that the chemical bonding and charge transfer at the metal-support interface could be used to tune the electronic and chemical properties of the WGS active sites. Electronic perturbation of the Pt by the ceria support has been shown to enhance the water splitting at the Pt surface causing upto 20 fold increase in WGS activity [53, 54].

Addition of catalyst promotors and dopants can prevent the sintering of noble metals and support. Thermodynamically stable Cu/Pt near surface alloy (NSA) with Cu monolayer preferentially deposited on Pt (111) the has shown to be tolerant for CO poisoning than pure Pt [55]. Addition of zirconium in varying concentration in Pt/ceria catalysts has shown to inhibit the sintering of ceria as well as Pt crystallites by the formation of Zr-Ce metastable phases [56]. It has been shown that the incorporation of basic oxides such as MgO in the catalyst could prevent the formation of carbonates and boost the formic acid dehydrogenation [28]. Similarly, sintering of ceria can be prevented at a temperature as high as 800°C by doping it with La. This results in the formation of several intermediate Ce-La-O phases [57] which inhibit sintering. With the recent advances in techniques such as *in-situ* environmental transmission electron microscopy (ETEM), it will be easier to design catalysts with better thermal stability [58].

6.8 Conclusions:

We investigated the role of three different ceria materials for water-gas shift reaction studies for Pt/ceria catalysts. Reasons for the better catalytic activity of mesoporous Pt/ceria catalysts could be attributed to many factors such as noble metal loading, particle size of support and metal, porosity, pore size, concentration of defects, and presence of active species. Here our main objective was to correlate the influence of the synthesis process, and the resultant structural properties of the ceria support with the performance of the Pt/ceria catalyst for the activity of low temperature water-gas shift reaction. We highlighted these properties and their influence on the WGS reaction which will provide a platform for generating catalyst with improved performance compared to the currently used catalysts. Three different ceria supports were chosen based on various syntheses techniques and 5 wt% Pt nanoparticles were applied onto them in the vapor phase using RSDT. The structure and crystallite size were determined using

various characterization techniques. The catalysts were tested for WGS reaction in the temperature range of 150–450°C. Following conclusions can be made from this work:

1. C1/Pt mesoporous ceria had superior activity with complete CO conversion seen at 175°C followed by C2/Pt (225°C) and C3/Pt (450°C).
2. Increasing the Pt metal loading from 1% to 5% did not improve the WGS reaction activity of catalysts.
3. Catalytically active oxygen species [peroxides (O_2^{2-}) and superoxide (O_2^{-})] exist on the one-electron defect sites at the metal-support interface as observed from Raman spectroscopy.
4. Formation of OH, surface formate, surface carbonates, CO-Ce^{4+} and CO-Ce^{3+} species were seen by *in-situ* DRIFTS studies, which infers the occurrence of both ceria mediated redox and formate mechanism in the WGS reaction.
5. Weak CO-Pt interaction was observed in C2/Pt by *in-situ* DRIFTS studies which could explain the poor WGS reaction activity.
6. Non-stoichiometry of ceria was noticed by Raman spectroscopy in C1/Pt and C3/Pt.
7. Crystallite size of <10 nm attributes to higher surface areas and lower activation rates for the WGS reaction.

6.9 References:

[1] R. Jain, R. Maric, Synthesis of nano-Pt onto ceria support as catalyst for water-gas shift reaction by Reactive Spray Deposition Technology, Applied Catalysis A: General. 475 (2014) 461-468.

[2] R. Jain, A.S. Poyraz, D.P. Gamliel, J. Valla, S.L. Suib, R. Maric, Comparative study for low temperature water-gas shift reaction on Pt/ceria catalysts: Role of different ceria supports, Applied Catalysis A: General. 507 (2015) 1-13.

[3] A.S. Poyraz, C. Kuo, S. Biswas, C.K. King'ondu, S.L. Suib, A general approach to crystalline and monomodal pore size mesoporous materials, Nature Communications. 4 (2013) 2952.

[4] M. Oljaca, Y. Xing, C. Lovelace, S. Shanmugham, A. Hunt, Flame synthesis of nanopowders via combustion chemical vapor deposition, Journal of Materials Science Letters. 21 (8) (2002) 621-626.

[5] R. Maric, S. Seward, P.W. Faguy, M. Oljaca, Electrolyte Materials for Intermediate Temperature Fuel Cells Produced via Combustion Chemical Vapor Condensation, Electrochemical and Solid-State Letters. 6 (5) (2003) A91-A95.

[6] J. M. Roller. Flame Synthesis of Nanomaterials for Alternative Energy Applications (Doctoral dissertation). University of Connecticut. Retrieved from: http://digitalcommons.uconn.edu/dissertations/432/ (2014).

[7] R. Maric, J.M. Roller, R. Neagu, K. Fatih, A. Tuck, Low Pt Thin Cathode Layer Catalyst Layer by Reactive Spray Deposition Technology, ECS Transactions. 12 (1) (2008) 59-63.

[8] S.R. Turns, An Introduction to Combustion: Concepts and Applications, 3rd ed., McGraw-Hill, New York, 2012.

[9] R. Jain, Y. Wang, R. Maric, Tuning of WO_3 Phase Transformation and Structural Modification by Reactive Spray Deposition Technology, Journal of Nanotechnology and Smart Materials. 1 (2014) 1-7.

[10] J.H. Woodhead, Process for preparing aqueous dispersion of ceria and resulting product, United States Patent. 05/954,658(4231893) (1980).

[11] Z.V. Popović, Z. Dohčević-Mitrović, M. Šćepanović, M. Grujić-Brojčin, S. Aškrabić, Raman scattering on nanomaterials and nanostructures, Annals of Physics. 523 (1-2) (2011) 62-74.

[12] J. Guzman, S. Carrettin, J.C. Fierro-Gonzalez, Y. Hao, B.C. Gates, A. Corma, CO Oxidation Catalyzed by Supported Gold: Cooperation between Gold and Nanocrystalline Rare-Earth Supports Forms Reactive Surface Superoxide and Peroxide Species, Angewandte Chemie International Edition. 44 (30) (2005) 4778-4781.

[13] A. Trovarelli, C. Deleitenburg, G. Dolcetti, J.L. Lorca, CO_2 Methanation Under Transient and Steady-State Conditions over Rh/CeO_2 and CeO_2-Promoted Rh/SiO_2: The Role of Surface and Bulk Ceria, Journal of Catalysis. 151 (1) (1995) 111-124.

[14] J. F. Bozeman III and H. Huang, Structural Characteristics of Bimetallic Catalysts Supported on Nano-Ceria, Journal of Nanomaterials. 2011 (2011) 329757.

[15] I. Kosacki, V. Petrovsky, H.U. Anderson, P. Colomban, Raman Spectroscopy of Nanocrystalline Ceria and Zirconia Thin Films, Journal of the American Ceramic Society. 85 (11) (2002) 2646-2650.

[16] G.W. Graham, W.H. Weber, C.R. Peters, R. Usmen, Empirical method for determining CeO_2-particle size in catalysts by raman spectroscopy, Journal of Catalysis. 130 (1) (1991) 310-313.

[17] J.E. Spanier, R.D. Robinson, F. Zhang, S. Chan, I.P. Herman, Size-dependent properties of CeO_{2-y} nanoparticles as studied by Raman scattering, Physical Review B. 64 (24) (2001) 245407.

[18] W.H. Weber, K.C. Hass, J.R. McBride, Raman study of CeO_2: Second-order scattering, lattice dynamics, and particle-size effects, Physical Review B. 48 (1) (1993) 178-185.

[19] Y. Lee, G. He, A.J. Akey, R. Si, M. Flytzani-Stephanopoulos, I.P. Herman, Raman Analysis of Mode Softening in Nanoparticle $CeO_{2-\delta}$ and Au-$CeO_{2-\delta}$ during CO Oxidation, Journal of the American Chemical Society. 133 (33) (2011) 12952-12955.

[20] H.L. Tuller, A.S. Nowick, Doped Ceria as a Solid Oxide Electrolyte, Journal of Electroceramic Society. 122 (2) (1975) 255-259.

[21] E.B. Lavik, I. Kosacki, H.L. Tuller, Y. Chiang, J.Y. Ying, Nonstoichiometry and Electrical Conductivity of Nanocrystalline $CeO_{\{2-x\}}$, Journal of Electroceramics. 1 (1) (1997) 7-14.

[22] J. Guzman, S. Carrettin, A. Corma, Spectroscopic Evidence for the Supply of Reactive Oxygen during CO Oxidation Catalyzed by Gold Supported on Nanocrystalline CeO_2, Journal of the American Chemical Society. 127 (10) (2005) 3286-3287.

[23] G. Hua, L. Zhang, G. Fei, M. Fang, Enhanced catalytic activity induced by defects in mesoporous ceria nanotubes, Journal of Materials Chemistry. 22 (14) (2012) 6851-6855.

[24] C.D. Wanger, W.M. Riggs, L.E. Davis, J.F. Moulder, G.E. Muilenberg, Handbook of X-Ray Photoelectron Spectroscopy, Physical Electronics Division, Perkin-Elmer Corp, Eden Prairie, Minnesota, USA, 1979.

[25] R.D. Robinson, J.E. Spanier, F. Zhang, S. Chan, I.P. Herman, Visible thermal emission from sub-band-gap laser excited cerium dioxide particles, Journal of Applied Physics. 92 (4) (2002) 1936-1941.

[26] Measurement Services Division of the National Institute of Standards and Technology (NIST) Material Measurement Laboratory (MML), Version 4.1 (National Institute of Standards and Technology, Gaithersburg, 2012), 2015 (2012).

[27] A. Holmgren, B. Andersson, D. Duprez, Interactions of CO with Pt/ceria catalysts, Applied Catalysis B: Environmental. 22 (3) (1999) 215-230.

[28] A.M. Duarte de Farias, A.P.M.G. Barandas, R.F. Perez, M.A. Fraga, Water-gas shift reaction over magnesia-modified Pt/CeO_2 catalysts, Journal of Power Sources. 165 (2) (2007) 854-860.

[29] J.C.S. Wu, Y. Cheng, In situ FTIR study of photocatalytic NO reaction on photocatalysts under UV irradiation, Journal of Catalysis. 237 (2) (2006) 393-404.

[30] G. Jacobs, L. Williams, U. Graham, G.A. Thomas, D.E. Sparks, B.H. Davis, Low temperature water-gas shift: in situ DRIFTS-reaction study of ceria surface area on the evolution of formates on Pt/CeO_2 fuel processing catalysts for fuel cell applications, Applied Catalysis A: General. 252 (1) (2003) 107-118.

[31] R. Si, J. Raitano, N. Yi, L. Zhang, S. Chan, M. Flytzani-Stephanopoulos, Structure sensitivity of the low-temperature water-gas shift reaction on Cu–CeO_2 catalysts, Catalysis Today. 180 (1) (2012) 68-80.

[32] T. Bunluesin, R.J. Gorte, G.W. Graham, CO oxidation for the characterization of reducibility in oxygen storage components of three-way automotive catalysts, Applied Catalysis B: Environmental. 14 (1-2) (1997) 105-115.

[33] Q. Fu, H. Saltsburg, M. Flytzani-Stephanopoulos, Active Nonmetallic Au and Pt Species on Ceria-Based Water-Gas Shift Catalysts, Science. 301 (5635) (2003) 935-938.

[34] S. Aranifard, S.C. Ammal, A. Heyden, On the importance of metal–oxide interface sites for the water-gas shift reaction over Pt/CeO_2 catalysts, Journal of Catalysis. 309 (0) (2014) 314-324.

[35] M. Cargnello, V.V.T. Doan-Nguyen, T.R. Gordon, R.E. Diaz, E.A. Stach, R.J. Gorte, P. Fornasiero, C.B. Murray, Control of Metal Nanocrystal Size Reveals Metal-Support Interface Role for Ceria Catalysts, Science. 341 (6147) (2013) 771-773.

[36] T. Li, L. Sun, L. Gong, X. Liu, X. Liu, In situ generation of superbasic sites on mesoporous ceria and their application in transesterification, Journal of Molecular Catalysis A: Chemical. 352 (0) (2012) 38-44.

[37] C. Wen, Y. Zhu, Y. Ye, S. Zhang, F. Cheng, Y. Liu, P. Wang, F. Tao, Water-Gas Shift Reaction on Metal Nanoclusters Encapsulated in Mesoporous Ceria Studied with Ambient-Pressure X-ray Photoelectron Spectroscopy, ACS Nano. 6 (10) (2012) 9305-9313.

[38] H. Cordatos, T. Bunluesin, J. Stubenrauch, J.M. Vohs, R.J. Gorte, Effect of Ceria Structure on Oxygen Migration for Rh/Ceria Catalysts, Journal of Physical Chemistry. 100 (2) (1996) 785-789.

[39] S.M. Schimming, G.S. Foo, O.D. LaMont, A.K. Rogers, M.M. Yung, A.D. D'Amico, C. Sievers, Kinetics of hydrogen activation on ceria–zirconia, Journal of Catalysis. 329 (2015) 335-347.

[40] R. Leppelt, B. Schumacher, V. Plzak, M. Kinne, R.J. Behm, Kinetics and mechanism of the low-temperature water-gas shift reaction on Au/CeO_2 catalysts in an idealized reaction atmosphere, Journal of Catalysis. 244 (2) (2006) 137-152.

[41] Y. Li, Q. Fu, M. Flytzani-Stephanopoulos, Low-temperature water-gas shift reaction over Cu- and Ni-loaded cerium oxide catalysts, Applied Catalysis B: Environmental. 27 (3) (2000) 179-191.

[42] Y. Zhai, D. Pierre, R. Si, W. Deng, P. Ferrin, A.U. Nilekar, G. Peng, J.A. Herron, D.C. Bell, H. Saltsburg, M. Mavrikakis, M. Flytzani-Stephanopoulos, Alkali-Stabilized Pt-OH_x Species Catalyze Low-Temperature Water-Gas Shift Reactions, Science. 329 (5999) (2010) 1633-1636.

[43] J. Zarraga-Colina, R.M. Nix, Fabrication of model Pt-ceria catalysts and an analysis of their performance for CO oxidation, Surface Science. 600 (15) (2006) 3058-3071.

[44] T. Bunluesin, R.J. Gorte, G.W. Graham, Studies of the water-gas-shift reaction on ceria-supported Pt, Pd, and Rh: Implications for oxygen-storage properties, Applied Catalysis B: Environmental. 15 (1–2) (1998) 107-114.

[45] G.N. Vayssilov, Y. Lykhach, A. Migani, T. Staudt, G.P. Petrova, N. Tsud, T. Skála, A. Bruix, F. Illas, K.C. Prince, V. Matolı´n, K.M. Neyman, J. Libuda, Support nanostructure boosts oxygen transfer to catalytically active platinum nanoparticles, Nature Materials. 10 (4) (2011) 310-315.

[46] G. Preda, A. Migani, K.M. Neyman, S.T. Bromley, F. Illas, G. Pacchioni, Formation of Superoxide Anions on Ceria Nanoparticles by Interaction of Molecular Oxygen with Ce^{3+} Sites, Journal of Physical Chemistry C. 115 (13) (2011) 5817-5822.

[47] D.Y. Chung, H. Kim, Y. Chung, M.J. Lee, S.J. Yoo, A.D. Bokare, W. Choi, Y. Sung, Inhibition of CO poisoning on Pt catalyst coupled with the reduction of toxic hexavalent chromium in a dual-functional fuel cell, Scientific Reports. 4 (2014) 7450.

[48] X. Zhu, T. Hoang, L. Lobban, R. Mallinson, Significant Improvement in Activity and Stability of Pt/TiO_2 Catalyst for Water Gas Shift Reaction Via Controlling the Amount of Na Addition, Catalysis Letters. 129 (1-2) (2009) 135-141.

[49] X. Liu, W. Ruettinger, X. Xu, R. Farrauto, Deactivation of Pt/CeO_2 water-gas shift catalysts due to shutdown/startup modes for fuel cell applications, Applied Catalysis B: Environmental. 56 (1–2) (2005) 69-75.

[50] T. Bunluesin, R.J. Gorte, G.W. Graham, Studies of the water-gas-shift reaction on ceria-supported Pt, Pd, and Rh: Implications for oxygen-storage properties, Applied Catalysis B: Environmental. 15 (1–2) (1998) 107-114.

[51] W. Han, One-Dimensional Oxygen-Deficient Metal Oxides, in: J. Wu, J. Cao, W. Han, A. Janotti, H. Kim (Eds.), Functional Metal Oxide Nanostructures, 1st ed., Springer-Verlag, New York, 2012, pp. 241-268.

[52] X. Wang, R.J. Gorte, J.P. Wagner, Deactivation Mechanisms for Pd/Ceria during the Water-Gas-Shift Reaction, Journal of Catalysis. 212 (2) (2002) 225-230.

[53] C.T. Campbell, Catalyst-support interactions: Electronic perturbations, Nature Chemistry. 4(8) (2012) 597-598.

[54] A. Bruix, J.A. Rodriguez, P.J. Ramirez, S.D. Senanayake, J. Evans, J.B. Park, D. Stacchiola, P. Liu, J. Hrbek, F. Illas, A new type of strong metal-support interaction and the production of H_2 through the transformation of water on Pt/CeO_2 (111) and $Pt/CeO_x/TiO_2$ (110) catalysts, Journal of the American Chemical Society. 134 (21) (2012) 8968-8974.

[55] J. Knudsen, A.U. Nilekar, R.T. Vang, J. Schnadt, E.L. Kunkes, J.A. Dumesic, M. Mavrikakis, F. Besenbacher, A Cu/Pt near-surface alloy for water-gas shift catalysis, Journal of the American Chemical Society. 129 (20) (2007) 6485-6490.

[56] C. Ratnasamy, J.P. Wagner, Water Gas Shift Catalysis, Catalysis Reviews. 51 (3) (2009) 325-440.

[57] J. Kašpar, M. Graziani, P. Fornasiero, Chapter 184 Ceria-containing three-way catalysts, in: J.G. Bünzli, V.K. Pecharsky (Eds.), Handbook on the Physics and Chemistry of Rare Earths, Elsevier, pp. 159-267.

[58] A.T. DeLaRiva, T.W. Hansen, S.R. Challa, A.K. Datye, In situ Transmission Electron Microscopy of catalyst sintering, Journal of Catalysis. 308 (0) (2013) 291-305.

SECTION III:

TUNGSTEN OXIDE FOR GAS AND CHEMICAL SENSORS

CHAPTER 7:

Tuning of WO_3 phase transformation and structural modification by Reactive Spray Deposition Technology

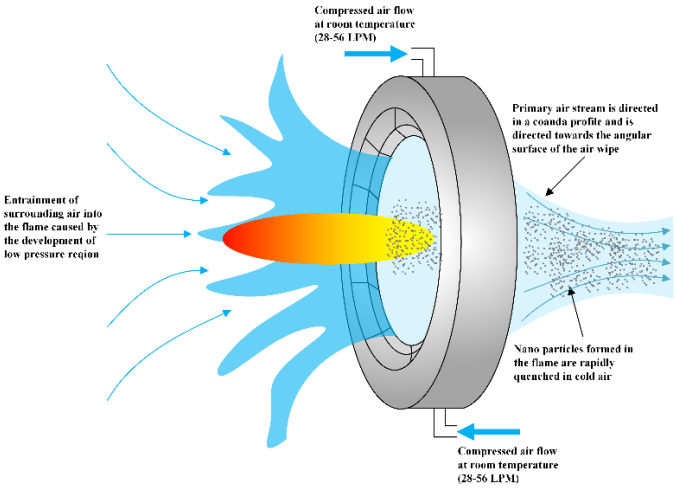

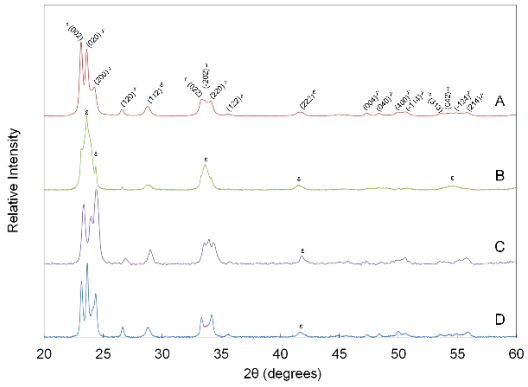

7.1 Abstract:

WO_3 nanoparticle thin films were synthesized by Reactive Spray Deposition Technology (RSDT) by varying the length of the reaction zone (9–14 cm), flow rate of quench air (0–57 L/min) and substrate temperature (80–400°C). The resulting samples were subjected to different annealing conditions (no annealing–500°C). Distinct metastable phases of WO_3 such as ferroelectric ε-WO_3 and the preferential orientation of the three major lattice planes (002), (020) and (200) can be obtained using this synthesis technique and the morphology. The microstructure of the films are a decisive function of the synthesis process. RSDT has a strong potential to allow the properties of WO_3 to be tailored to its desired structure and application. The morphology, structure, and size of WO_3 nanoparticles were probed using, X-ray diffraction (XRD), Raman spectroscopy, transmission electron microscopy (TEM) with selected area diffraction pattern (SADP), and scanning electron microscopy (SEM) with X-ray energy dispersive spectroscopy (XEDS).

7.2 Keywords:

WO_3 thin film; X-ray diffraction; Phase transformation; Preferential orientation; Reactive Spray Deposition Technology

7.3 Introduction:

In this chapter we have demonstrated a one-step flame-based direct deposition technique to engineer a particular required phase by changing the length of the reaction zone in the flame, flow rate of quench air, and the substrate temperature. RSDT is a type of flame spray pyrolysis system which is a one-step open atmosphere process for synthesizing nanometer scale materials with high efficiency and reduced solvent waste. Here we will give a brief description of the RSDT process

and, the conditions required to achieve a particular phase, and we will provide characterization results obtained by Raman spectroscopy, SEM, TEM, and XRD that prove the existence of these phases. The motivation of this research was to study the particle size, crystallinity, and crystal structure of the WO_3 films grown by RSDT by varying the conditions of the experiments. It is assumed that the results from this study can be used to obtain the configuration of WO_3 film demanded by its application. This work was published in the *Journal of Nanotechnology and Smart Materials* [1].

7.4 Experimental:

7.4.1 Synthesis of WO_3:

An explanation of the RSDT equipment and process is described in detail in chapter 1. Tungsten hexacarbonyl ($W(CO)_6$) was obtained from Sigma Aldrich (Catalogue #AC221040100) and was dissolved in a tetrahydrofuran (THF) ($\Delta H^{\circ}_{c,\ 298K}$ = -2501 kJ/mol) (Fisher Scientific # SHBD3901V). 20 wt% sulfur free liquefied propane ($\Delta H^{\circ}_{c,\ 298K}$ = -2202 kJ/mol) (Airgas catalogue # PRCP350S) was added to the above to form a precursor solution resulting in a final concentration of 5 mmol/L $W(CO)_6$, and 16.5 wt% propane. Propane assists in the atomization of the precursors by increasing the enthalpy of the solution mixture and reducing the droplet size due to supercritical expansion. The flow rate of 4 mL/min was maintained by using a syringe pump. The precursor solution was atomized by a gas-assisted external mixing nozzle (combustion nozzle) using oxygen (5 L/min). Six methane-oxygen flamelets (methane and oxygen at 0.5 L/min each) which ignites the combustible precursor mist, surround the capillary end. Prior to atomization, the precursor solution was heated to approximately 50–60°C by enclosing the capillary by a heating coil. The precursor mist was ignited with a propane torch to obtain a bluish-white flame. At approximately 9–14 cm from the flame, a circular air quench (Exair, Super Air Wipe®) with a compressed air flow

rate of 28–56 L/min at room temperature was positioned. A stainless steel substrate holder mounted on an x-y-z platform and having the option of water cooling was used for collection of WO_3 particles. On the substrate holder was mounted a zero diffraction background quartz plate (MTI®) on which the film was grown. Quartz was selected for various reasons: it can withstand the high temperature required during *in-situ* XRD, it can be imaged in a SEM, it does not have an interfering background in a Raman spectrometer, and the film can be scraped off for TEM analysis.

7.4.2 Characterization:

In-situ X-ray diffraction patterns of WO_3 film were recorded in air at 30°C, 150°C, 250°C, 300°C, 350°C, 400°C and 500°C on a Bruker D8 advanced powder diffractometer using CuKα radiation. Heating rate of 5°C /min was used with a hold time of 1 h. at the temperature of the scan. Crystallite size was measured by using the Debye Scherrer method. Raman spectra were obtained with a Renishaw Ramascope micro-Raman spectrometer fitted with a reflected light microscope using a 50 mW laser (514.5 nm) and exposure time of 30 s at ambient conditions. Instrument alignment was optimized using a 519 cm^{-1} signal of a silicon wafer. Raman measurements were performed since this technique is well known to give the "fingerprint" of WO_3 material [2, 3]. The spectra were obtained at room temperature in ambient atmosphere in the spectral range between 100 and 1000 cm^{-1}. SEM micrographs were collected on an FEI ESEM Quanta 250 with a field emission gun with an EDAX XEDS system. TEM micrographs and selected area diffraction pattern (SADP) of WO_3 particles were obtained on a 120 kV FEI Technai T12 S/TEM with a LaB_6 source equipped with an EDAX XEDS system. 300 mesh Cu grids coated with holey/thin carbon films (Pacific Grid Tech Cu-300HD) were used. A small portion of the film was scraped off of the quartz plate and was sonicated with ethanol. Few drops of the resulting solution were dropped on the grids and air dried before they were placed in the UHV chamber of the TEM.

7.5 Results and discussion:

7.5.1 X-ray diffraction:

γ and ε WO_3 with different phase ratios were synthesized in four different sets of conditions in the RSDT as described in table 7.1 by altering the length of the reaction zone, flow rate of quench air, and the temperature of substrate. Fig. 7.1 shows the X-ray diffraction spectra for the samples A, B, C and D. It can be clearly interpreted that very different structures of WO_3 were obtained by changing the conditions of the flame. All four samples were monoclinic, the most dominant structure of WO_3 and which can be indexed to ICDD#00-043-1035 (space group P21/n). Sample A is the as prepared sample with no post annealing, and it shows a well crystalline structure with (002) preferential plane oriented at $2\theta = 23.1°$. This could be due to the high temperature of the particles in the absence of quench air which can cause the migration of WO_3 atoms towards the lower energy nucleation sites [4]. All the other samples were found to be amorphous in nature because the quench was close to the nucleation site. This amorphous structure could arise because the particles are air quenched as soon as they are produced from the flame and the residence time of the particles in the hot zone is too short. The amorphous samples were thermally annealed in the high temperature stage of the XRD—the crystallization steps and the corresponding XRD patterns can be found in the supplementary figures (Fig. 7.5–7.8) at the end of this chapter. Thermal annealing of amorphous WO_3 causes the particles to become crystalline, and it also changes the phase ration, grain size, porosity, density of adsorption sites and pore volume [5]. It is clear from *in-situ* XRD that the crystallization of the WO_3 particles started at 350°C. Sample B was prepared with no air quench; however the substrate temperature was maintained at 200°C by the water cooled substrate holder and the sample thereby retained an amorphous structure. By comparing the XRD spectra of sample B with that of Wang et al. [6] and Righettoni et al. [7] it can be concluded that the sample is mostly

ε-WO_3, the metastable phase at room temperature. Sample C is oriented preferentially along the (200) direction. This preferentially-oriented crystallization was also observed by Sun et al. [8] and Zhifu et al. [5] who prepared their films by physical vapor deposition (PVD). Sun et al. suggested that preferential orientation along the (200) direction happened to reduce the lattice mismatch with the sapphire lattice on which the film was grown. According to Zhifu et al. the cause of this behavior was the column-like accumulation of the WO_3 species during the sputtering process at the operating pressure (20 Pa). The (200) orientation could also form *in-situ* during the annealing process. Sample D is oriented along the (020) plane direction, and sample A is oriented along the (002) direction, as was also reported by Garavand et al. [9], Guo et al. [10] and Jing et al. [11]. Guo et al. evaluated the photoelectrochemical activity and photoconversion efficiency of self-assembled nanoporous WO_3 and WO_3 film with preferential orientations at (002) and (020), respectively. They found that the photocurrent of the (002) plane-oriented nanoporous WO_3 was nine times the value of that of the WO_3 film and the photoconversion efficiency was 4.57 times higher than those of (020) plane-oriented WO_3. Furthermore, (002) WO_3 was more favorable in absorption and redox of pollutants than (020) WO_3. Jing et al. found that the (002) preferential orientation of WO_3 resulted in higher photocatalytic degradation of NO [11].

Table 7.1. Synthesis conditions of WO_3 in Reactive Spray Deposition Technology

Sample	Substrate temperature (°C)	Quench air flow rate (L/min)	Length of reaction zone (nozzle to substrate) (cm)	Preferential plane orientation	Crystallite size (nm)
A	350–400	0	17.1	002	33.1
B	200	0	13.3	NONE	61.6
C	100–130	28.3	20.6	200	29.0
D	80	56.6	12.6	020	42.3

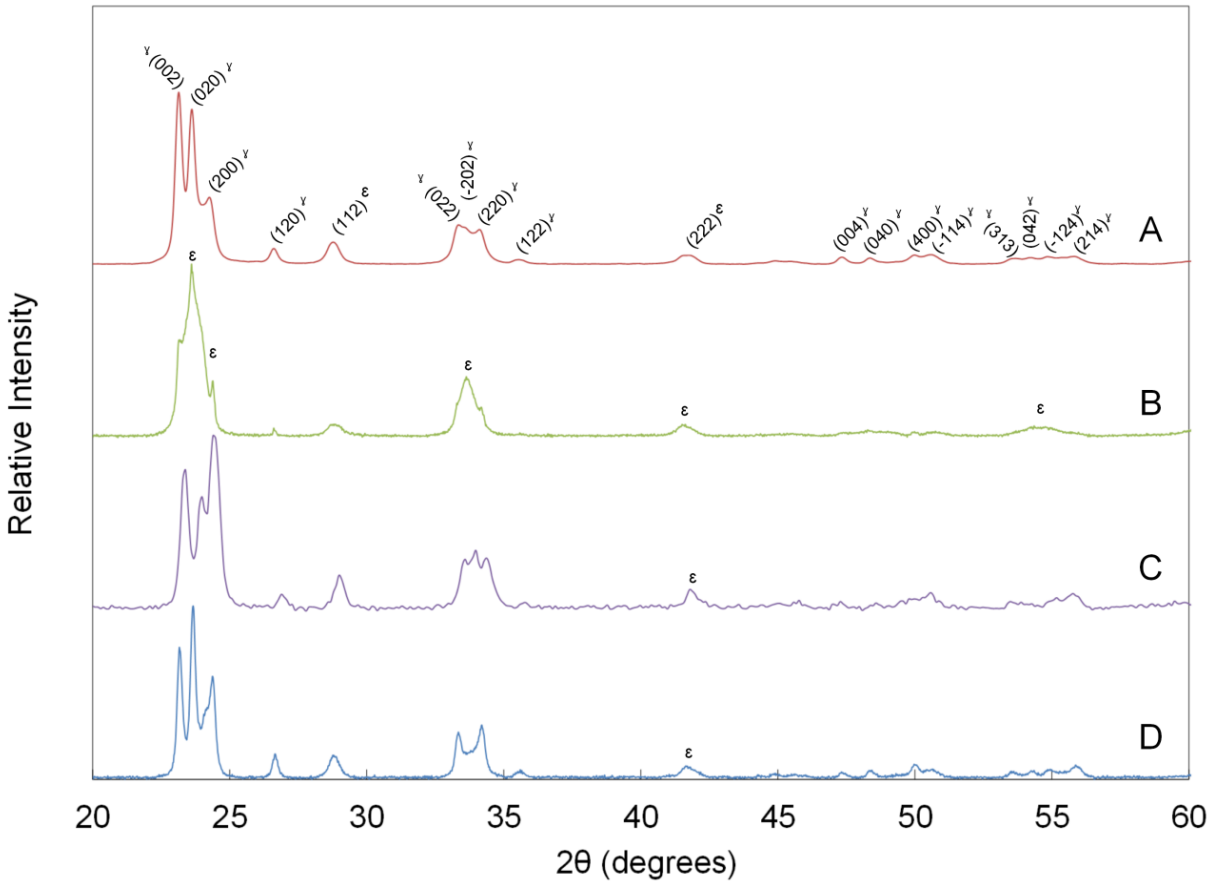

Fig. 7.1: X-ray diffraction of samples A, B, C, and D showing different crystallographic orientations and phase ratio.

7.5.2 Raman Spectroscopy:

Fig. 7.2 shows the Raman scattering measurements of untreated sample A and the post-annealed samples B, C and D (since the Raman signal of WO_3 cannot be obtained for amorphous structure).

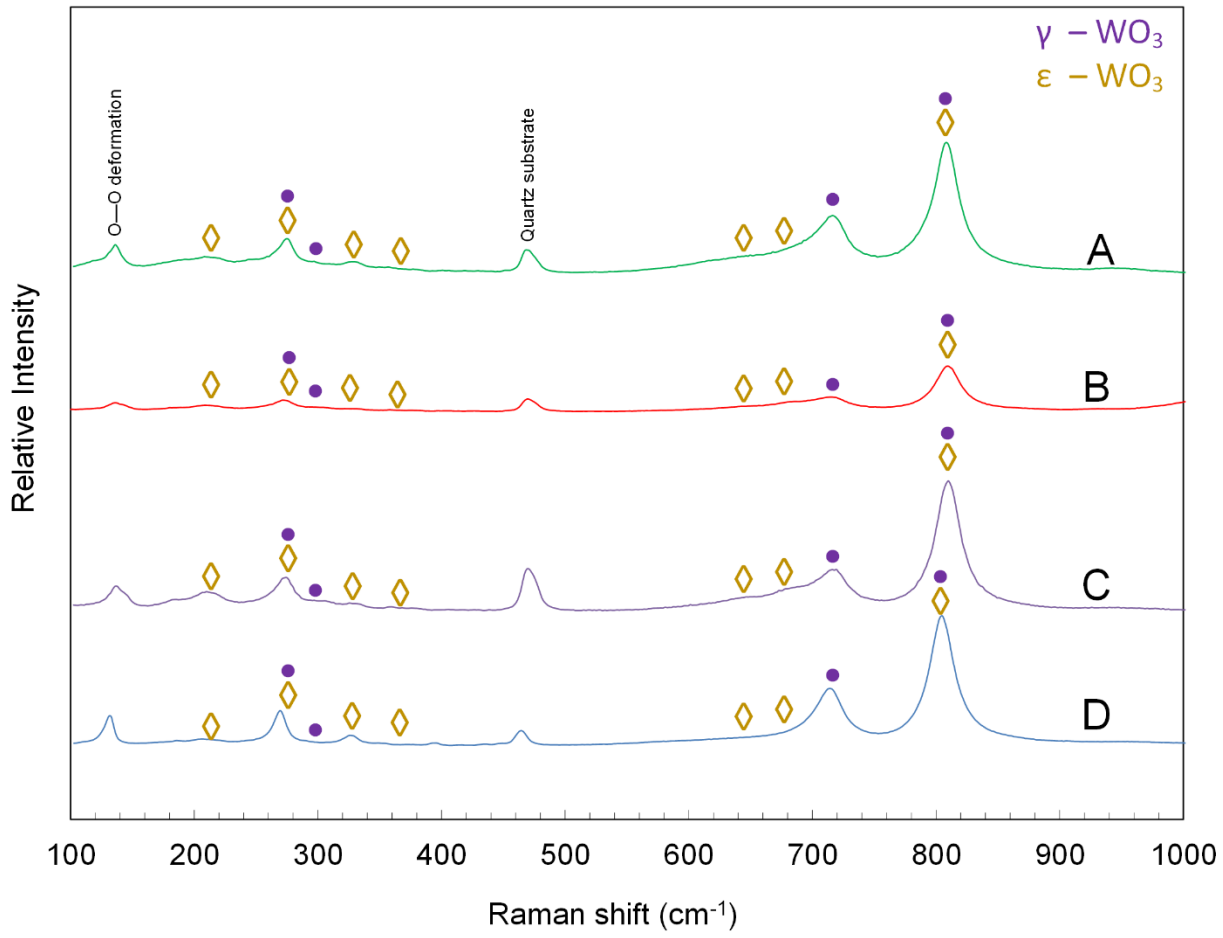

Fig. 7.2: Raman spectroscopy for samples A, B, C, and D showing mostly monoclinic structure.

The spectra are similar to those of the monoclinic WO_3 as apparent from the strong peaks at 808 and 715 cm^{-1}. The peak at 450 cm^{-1} can be assigned to the quartz substrate. The intensity of the substrate peak is different for the samples because of the difference in the thickness of the film. A relatively strong peak is obtained at below 150 cm^{-1} for all the samples which can indicate the O-O deformation mode [12]. Salje et al. has obtained the Raman spectra of the monoclinic (γ and ε) WO_3 and is reported in reference [13-15]. After comparing with Salje et al. it can be assumed that the peaks at 205, 310, 372, 394, 427, 645, 680, 697cm^{-1} can be assigned to

ferroelectric ε-WO_3 while peaks at 327, and 716 cm^{-1} are for γ-WO_3 only. There is clearly an overlap between γ and ε WO_3 as evident from the spectra.

7.5.3 Electron Microscopy:

Fig. 7.3 shows the SEM micrographs of the WO_3 film as deposited (top) and after annealing at 500°C. Films A and D are very homogeneous while B and C shows particle agglomeration. As is clear from the Fig. 7.3, the size of the grains are in the order B>D>A>C. Pores and cracks can be seen in samples A and D while samples B and C show uniform morphology. It is interesting to see that in samples A and D, the pores and cracks have grown in size after annealing at 500°C. This same phenomenon was observed by Santato et al. and could be due to the elimination of organics from the film surface after heat treatment [16]. The increase in porosity of the films is advantageous to the sensing function of WO_3 since this favors diffusion of analytes into the bulk of the film. The images indicate high quality of WO_3 films deposited by RSDT.

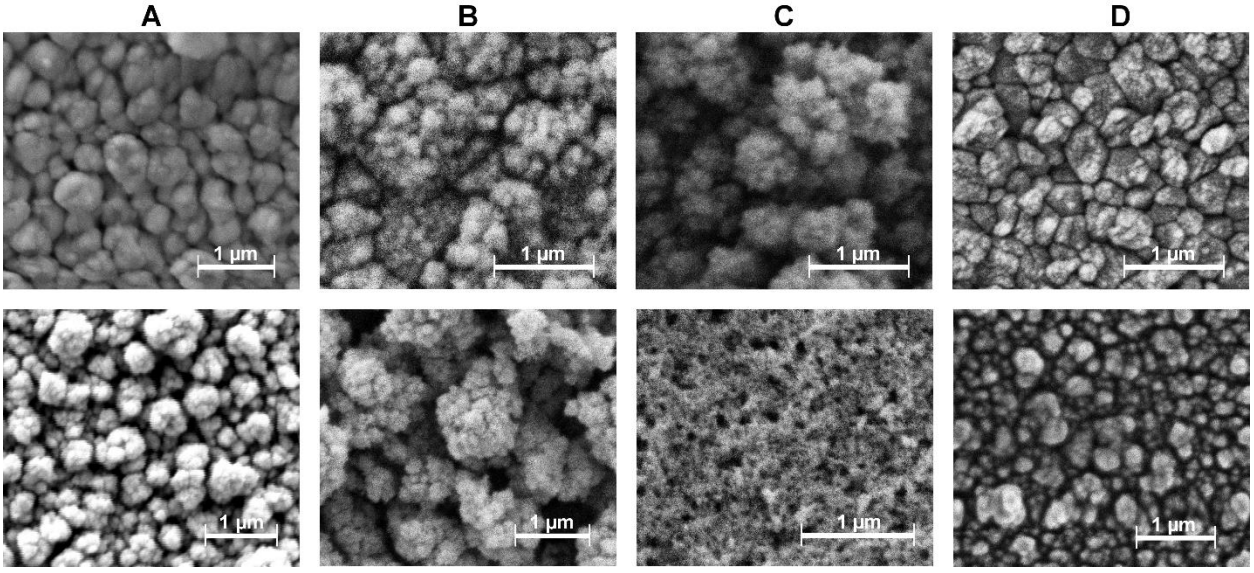

Fig. 7.3: Scanning Electron Microscopy micrographs of WO_3 films deposited by RSDT under condition A, B, C and D. (Top: as deposited, Bottom: after annealing at 500°C).

Fig. 7.4 shows the bright field TEM micrographs along with the SADP of samples A-D after post annealing. All samples were polycrystalline, as evident from the SADP and were indexed to monoclinic WO_3. As measured from the micrographs the size of the WO_3 particles were 15–40 nm for sample A, 30–50 nm for sample B, 20–25 nm for sample C, and 20–30 nm for sample D. Different shapes and sizes of particles were seen from the micrographs, as labelled. Sample A shows faceted particles with edges and corners. Samples B and D show circular particles, whereas circular, oval, elliptical, and dumb bell shaped particles can be seen in sample D. Only sample B depicts the formation of necks between individual WO_3 particles.

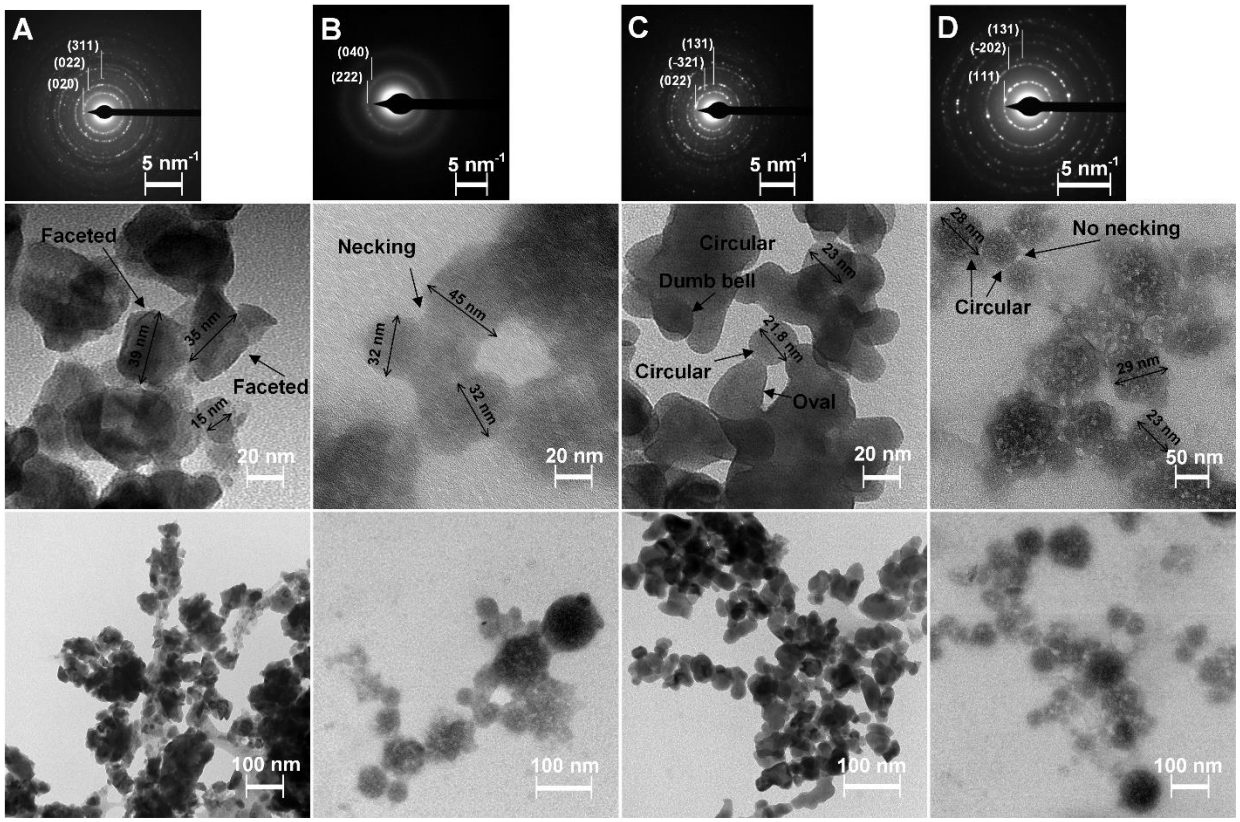

Fig. 7.4: Transmission Electron Microscopy micrographs of WO_3 films deposited by RSDT under conditions A, B, C, and D along with their selected area diffraction pattern (SADP).

7.6 Conclusions

Reactive Spray Deposition Technology was employed to synthesize WO_3 (γ and ε phase) thin films of from the vapor phase. The morphology, structure and preferential lattice plane orientation was tuned by changing the parameters of the flame setup including substrate temperature, quench air flow rate, and length of reaction zone. It was determined that the particular structure and properties of WO_3 are a function of the synthesis process. By employing the RSDT, the properties of WO_3 can be tuned to be favorable towards a particular application. Chapter 9 and 10 will elaborate upon this technique for exploring the sensing function of WO_3 by changing the synthesis conditions.

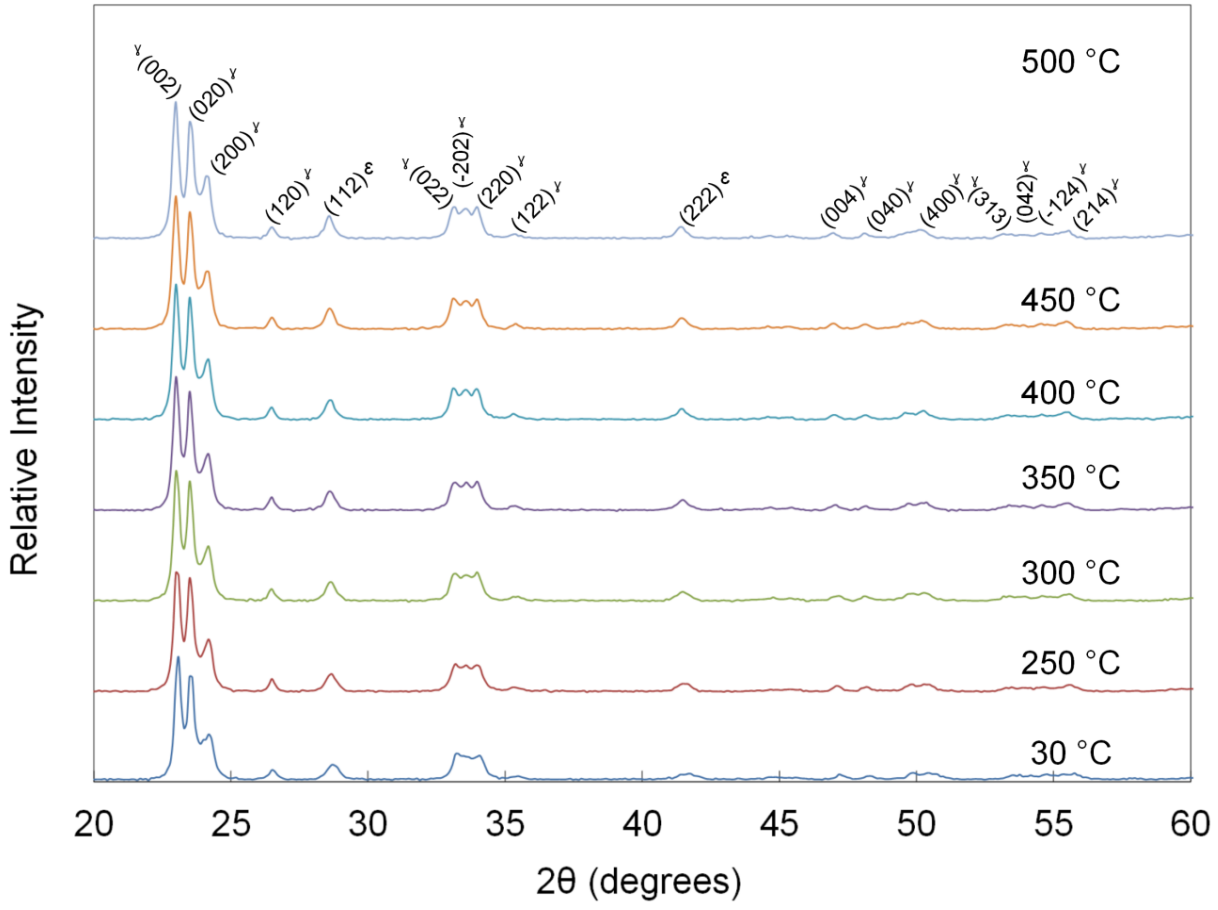

Fig. 7.5: XRD spectra of sample A during annealing from 30–500°C. No change in crystallinity is evident.

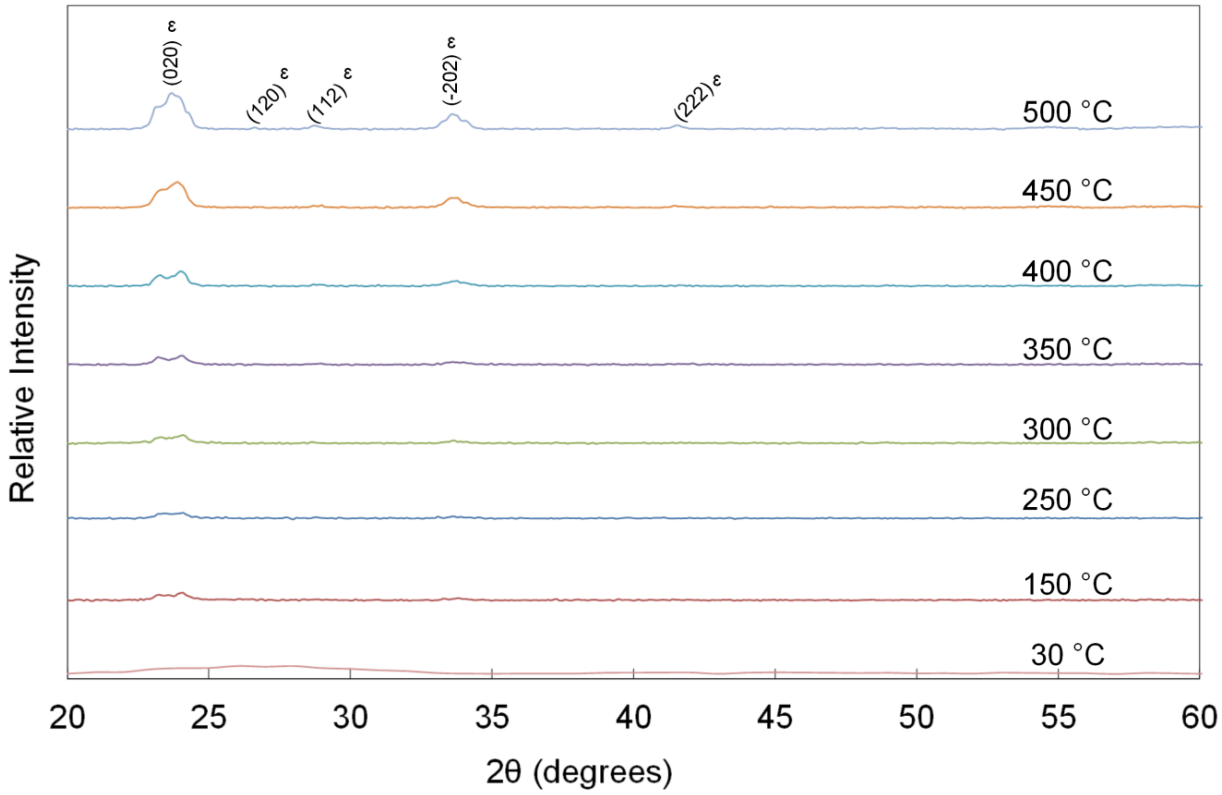

Fig. 7.6: XRD spectra of sample B during annealing from 30–500°C.

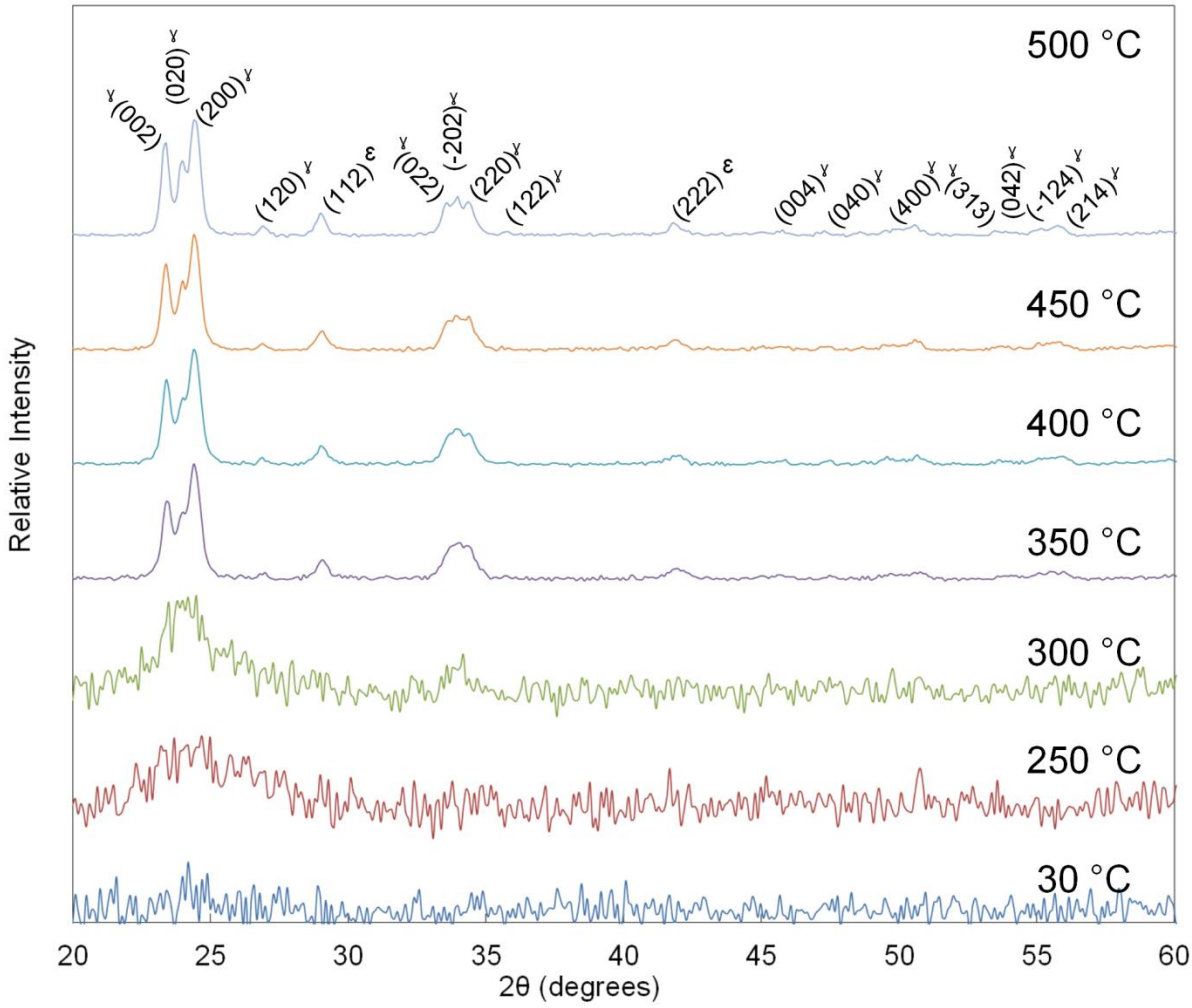

Fig. 7.7: XRD spectra of sample C during annealing from 30–500°C.

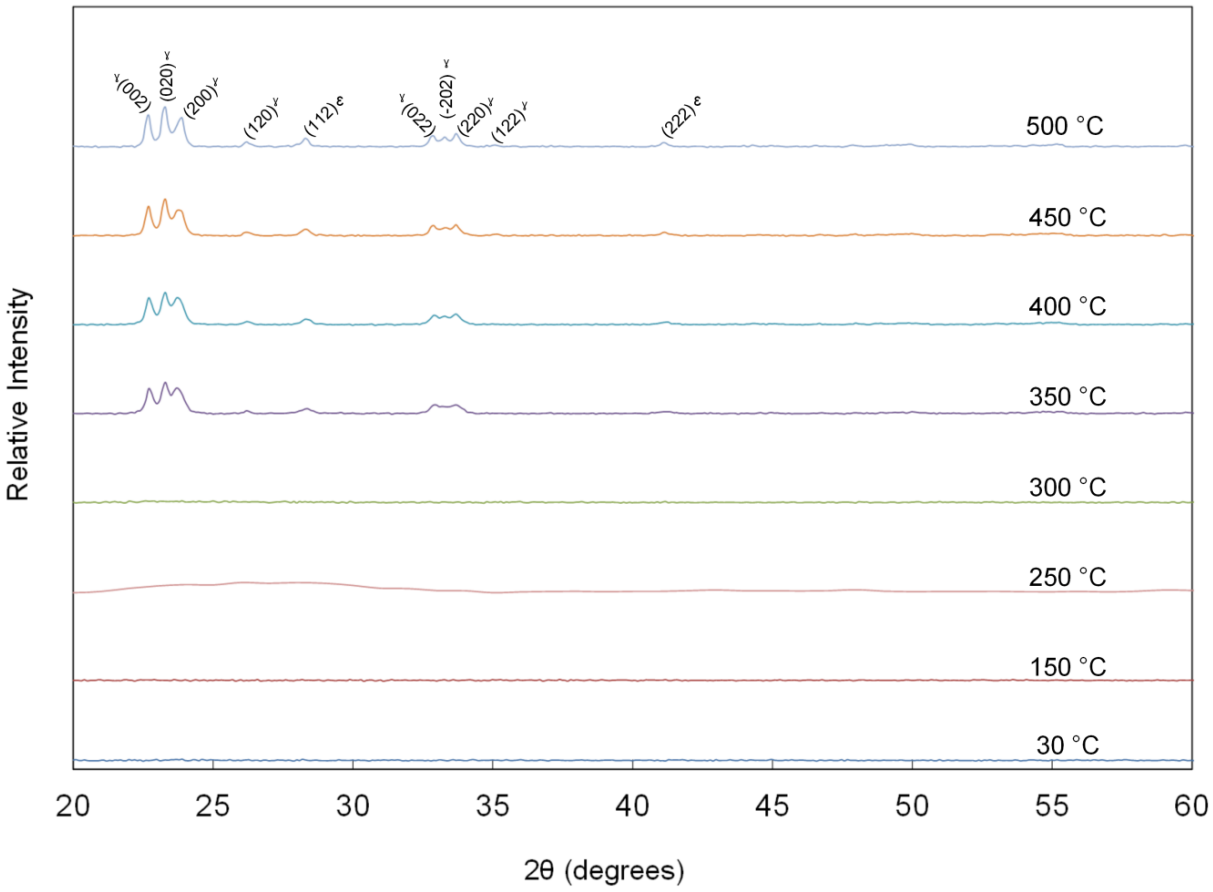

Fig. 7.8: XRD spectra of sample D during annealing from 30–500°C.

7.7 References

[1] R. Jain, Y. Wang, R. Maric, Tuning of WO_3 Phase Transformation and Structural Modification by Reactive Spray Deposition Technology, Journal of Nanotechnology and Smart Materials. 1 (2014) 1-7.

[2] C. Bittencourt, E. Llobet, P. Ivanov, X. Vilanova, X. Correig, M.A.P. Silva, L.A.O. Nunes, J.J. Pireaux, Ag induced modifications on WO_3 films studied by AFM, Raman and x-ray photoelectron spectroscopy, Journal of Physics D-Applied Physics. 37 (24) (2004) 3383-3391.

[3] R. Garcia-Sanchez, T. Ahmido, D. Casimir, S. Baliga, P. Misra, Thermal Effects Associated with the Raman Spectroscopy of WO_3 Gas-Sensor Materials, Journal of Physical Chemistry A. 117 (50) (2013) 13825-13831.

[4] Y.S. Zou, Y.C. Zhang, D. Lou, H.P. Wang, L. Gu, Y.H. Dong, K. Dou, X.F. Song, H.B. Zeng, Structural and optical properties of WO_3 films deposited by pulsed laser deposition, Journal of Alloys and Compounds. 583 (2014) 465-470.

[5] Z. Liu, T. Yamazaki, Y. Shen, T. Kikuta, N. Nakatani, Influence of annealing on microstructure and NO_2-sensing properties of sputtered WO_3 thin films, Sensors and Actuators B: Chemical. 128 (1) (2007) 173-178.

[6] L. Wang, A. Teleki, S.E. Pratsinis, P.I. Gouma, Ferroelectric WO_3 Nanoparticles for Acetone Selective Detection, Chemistry of Materials. 20 (15) (2008) 4794-4796.

[7] M. Righettoni, A. Tricoli, S.E. Pratsinis, Thermally Stable, Silica-Doped ε-WO_3 for Sensing of Acetone in the Human Breath, Chemistry of Materials. 22 (10) (2010) 3152-3157.

[8] H.T. Sun, C. Cantalini, L. Lozzi, M. Passacantando, S. Santucci, M. Pelino, Microstructural effect on NO_2 sensitivity of WO_3 thin film gas sensors Part 1. Thin film devices, sensors and actuators, Thin Solid Films. 287 (1-2) (1996) 258-265.

[9] N.T. Garavand, S.M. Mahdavi, A.I. Zad, M. Ranjbar, The effect of operating temperature on gasochromic properties of amorphous and polycrystalline pulsed laser deposited WO_3 films, Sensors and Actuators B: Chemical. 169 (2012) 284-290.

[10] Y. Guo, X. Quan, N. Lu, H. Zhao, S. Chen, High photocatalytic capability of self-assembled nanoporous WO_3 with preferential orientation of (002) planes, Environmental Science & Technology. 41 (12) (2007) 4422-4427.

[11] J. Liu, X. Dong, X. Liu, F. Shi, S. Yin, T. Sato, Solvothermal synthesis and characterization of tungsten oxides with controllable morphology and crystal phase, Journal of Alloys and Compounds. 509 (5) (2011) 1482-1488.

[12] M. Arai, S. Hayashi, K. Yamamoto, S.S. Kim, Raman Studies of Phase-Transitions in Gas-Evaporated WO_3 Microcrystals, Solid State Communications. 75 (7) (1990) 613-616.

[13] E.K.H. Salje, S. Rehmann, F. Pobell, D. Morris, K.S. Knight, T. Herrmannsdörfer, M.T. Dove, Crystal structure and paramagnetic behaviour of ε–WO_{3-x}, Journal of Physics: Condensed Matter. 9 (31) (1997) 6563.

[14] E.K.H. Salje, The orthorhombic phase of WO_3, Acta Crystallographica: B. 33 (1977) 574.

[15] R. Diehl, G. Brandt, E. Salje, The crystal structure of triclinic WO_3, Acta Crystallographica: B. 34 (1978) 1105-1111.

[16] C. Santato, M. Odziemkowski, M. Ulmann, J. Augustynski, Crystallographically oriented Mesoporous WO_3 films: Synthesis, characterization, and applications, Journal of the American Chemical Society. 123 (43) (2001) 10639-10649.

CHAPTER 8:

Phase transformation study for WO_3 and Si doped WO_3 under various heat treatment

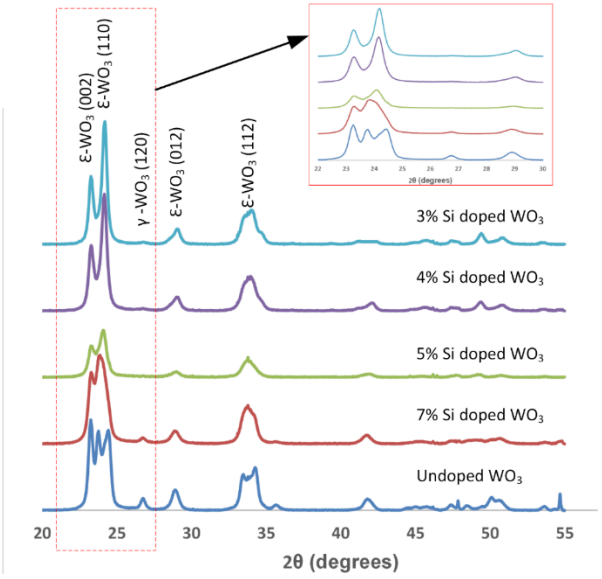

8.1 Highlights:

1. Non-doped and SiO_2 doped WO_3 films were synthesized by a single step flame based process.

2. The films were subjected to different annealing treatment.

3. The structural properties of the WO_3 was determined by various characterization techniques.

4. Presence of amorphous SiO_2 domains around the WO_3 grains were confirmed by HRTEM.

5. Data presented in this work shows that metastable ε-WO_3 phase can be obtained from 30–600°C.

8.2 Abstract:

SiO_2 doped WO_3 nanoparticle thin films were synthesized directly on silicon substrate by Reactive Spray Deposition Technology (RSDT). The doping concentration was set at 0, 3, 4, 5, and 7 wt% by adjusting the concentration of the SiO_2 precursor. The air quench rate was 10 L/min, tip oxygen was 7 L/min and the substrate temperature was 400°C. Four samples were prepared for each deposition with the deposition time set at 30, 60, 90 and 120 mins. The resulting samples were subjected to different annealing conditions (no annealing–600°C). The purpose of this work was to adjust the SiO_2 doping to obtain metastable monoclinic ferroelectric ε-WO_3 and preserving it from 30–600°C. The morphology, structure and size of WO_3 nanoparticles were probed using, X-ray diffraction (XRD), Raman spectroscopy, transmission electron microscopy (TEM) with selected area diffraction pattern (SADP), and scanning electron microscopy (SEM) with X-ray energy dispersive spectroscopy (XEDS).

8.3 Keywords:

WO_3 thin film; Metastable phase; Phase transformation; SiO_2 doping; Reactive Spray Deposition Technology

8.4 Introduction:

This chapter is focused on the synthesis by non-doped and SiO_2 doped WO_3 by Reactive Spray Deposition Technology (RSDT). Here we will give a brief description of the experimental method, and the characterization techniques utilized. The purpose here is to show that by varying the concentration of the dopants in the WO_3 film and by employing the RSDT, metastable monoclinic ε-WO_3 can be obtained which can be preserved at temperatures up to 600°C. In order to support this claim we will provide characterization results obtained by Raman spectroscopy, SEM, HRTEM, and XRD that prove the existence of the ε-WO_3 phase. We will also report the effect of the WO_3 particle size on annealing. It is assumed that the results from this study can be used to obtain ε-WO_3 film for human breath acetone sensing. This work was presented as a talk at the 2014 Materials Research Society (MRS) fall meeting and exhibit in the symposium HH titled "Flame and High-Temperature Synthesis of Functional Nanomaterials-Fundamentals and Applications" as a paper #HH3.05 on tuesday, December 02, 2014.

8.5 Experimental:

8.5.1 Synthesis of WO_3:

An explanation of the RSDT equipment and process is described in detail in chapter 1. Tungsten hexacarbonyl [$W(CO)_6$] was obtained from Sigma Aldrich (Catalogue #AC221040100) and was dissolved in a solvent blend consisting of tetrahydrofuran (THF) (ΔH°_c,

$_{298K}$ = -2501 kJ/mol) (Fisher Scientific # SHBD3901V) and diethylene glycol monobutyl ether (DEGME) ($\Delta H^{\circ}_{c,\ 298K}$ = -5234 kJ/mol) (Fisher Scientific # E182-4) mixed in equal volume. For doping SiO_2 in WO_3, various RSDT depositions were performed with the SiO_2 doping ranging from 0–7 wt% by adding hexamethyene disiloxane (HMDSO) (Fisher Scientific #A0326266) to the above precursor solution. This mixture was filled in a sealed high pressure stainless steel chamber (120 psi) and sulfur free liquefied propane ($\Delta H^{\circ}_{c,\ 298K}$ = -2202 kJ/mol) (Airgas catalogue # PRCP350S) was added to the precursor solution resulting in a final concentration of 8 mmol/L $W(CO)_6$, and 18.3 wt% propane. The precursor solution was filled in a syringe pump (Teledyne Isco 500D, Lincoln NE) and directed to a series of stainless steel tubes of varying diameters: 0.025 cm inner diameter 316 stainless steel tube which is brazed to a capillary of diameter 100 μm (Vita Needle Company). The flow rate of the precursor was set at 4 mL/min. The combined effect of liquefied propane, and reduction of diameter of the tube, caused the solution to shift into the supercritical regime with the formation of tiny droplets approximately 15 μm in diameter as measured by Malvern Instrument's Spraytec laser diffraction system [1].The precursor solution was atomized by a gas-assisted external mixing nozzle (combustion nozzle) by oxygen (7 L/min). Six methane-oxygen flamelets (methane 0.42 L/min and oxygen at 0.55 L/min each) surround the capillary end, which ignites the combustible precursor mist. The precursor mist was ignited with a propane torch to obtain a bluish-white flame. At approximately 10 cm from the flame, a circular air quench (Exair, Super Air Wipe®) with a compressed air flow rate of 10 L/min at room temperature was positioned. A round silicon plate (2" diameter, p-type, cut to (100) orientation, 280 μm thickness) (Nova electronic materials item#8289) was used as substrate. The silicon plate was cut into 4 equal size quadrants and affixed on a stainless steel block by means of a high temperature kapton tape as shown in Fig. 8.1. The stainless steel holder with the silicon substrates was placed approximately 19.6 cm from the combustion nozzle

(standoff distance) to obtain a substrate temperature of 400°C as measured with an Omega k-type thermocouple. The deposition time was set at 30 min, 60 min, 90 min and 120 min for the silicon plates. After the WO_3 deposition, the four silicon plates were annealed separately for 5 h. in an electric oven. The temperature of annealing was at 400°C, 450°C, 500°C and 600°C for the 30 min, 60 min, 90 min and 120 min deposition sample respectively The heating and cooling rate was set at 5°C/min.

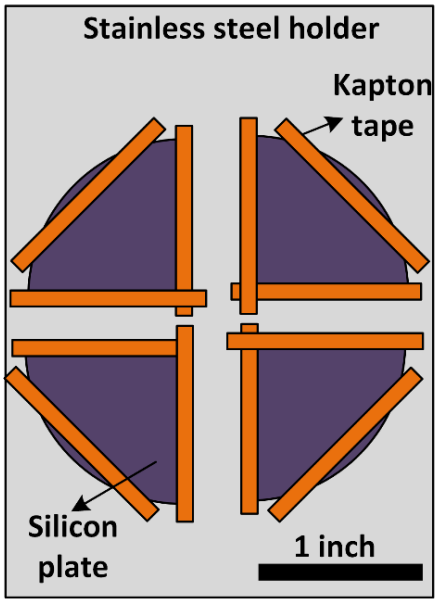

Fig. 8.1: Arrangement of the substrates for the RSDT deposition of WO_3 films.

8.5.2 Xylene flame impingement:

A desirable property for the ceramic films such as WO_3 synthesized by RSDT is the adhesion of such a film on smooth surfaces such as silicon. These complementary metal oxide semiconductor (CMOS) films when deposited on microelectromechanical systems (MEMS) substrates undergo rigorous post treatment such as setting, dicing, patterning, micromachining etc. Hence it is necessary that the deposited films are adhesive enough to

withstand the shock and stress during such processes [2]. In order to improve the adhesion of the films, the prepared samples were impinged with a blank particle free xylene flame for 60 s as shown in Fig. 8.2. This method has been shown to effectivity increase the adhesiveness of the CMOS films deposited by flame spray pyrolysis [3].

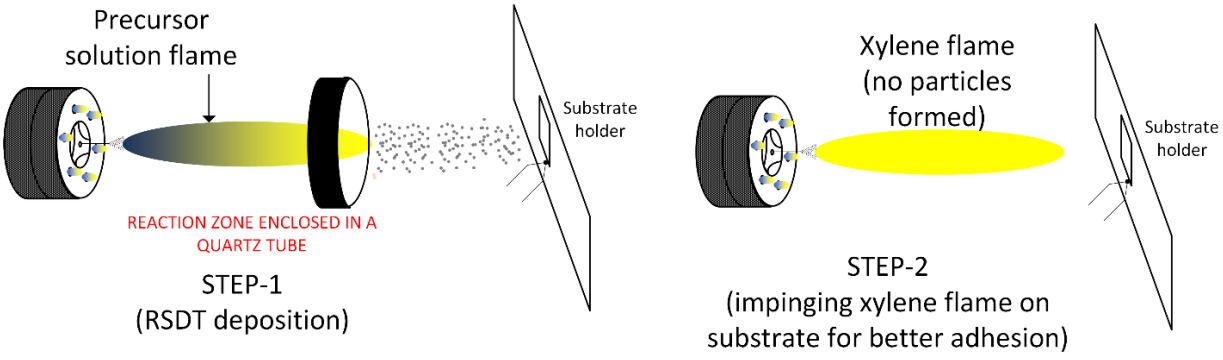

Fig. 8.2: Improvement of the CMOS films by xylene flame impingement method [3].

8.5.3 Characterization:

X-ray diffraction patterns of WO_3 film were recorded in air on a Bruker D8 advanced powder diffractometer using CuKα radiation. The scans were taken in the 2θ range of 20–55° with a step size of 0.02° and time per step of 5 s. Raman spectra were obtained in air in the spectral range between 100 and 1200 cm^{-1} with a Renishaw Ramascope micro-Raman spectrometer fitted with a reflected light microscope using a 50 mW laser (514.5 nm) and exposure time of 10 s. Laser power delivered to the sample was set at 20% (10 mW) to avoid sample damage. Instrument alignment was optimized using a 521 cm^{-1} signal of a silicon wafer. Raman measurements for WO_3 is well known to provide structural and phase information of WO_3 material [4, 5]. SEM micrographs were obtained at 5 kV accelerating voltage and 10 mm working distance on an FEI ESEM Quanta 250. For determining the cross-sectional thickness of the film, the silicon substrate with WO_3 film was fractured, and mounted on a 90° aluminum stub. The sample was gold sputter coated prior to

imaging under SEM. To obtain the composition of the films, elemental analysis of the deposited films was determined by X-ray energy dispersive spectroscopy (XEDS) on an EDAX system. TEM micrographs and selected area diffraction pattern (SADP) of WO_3 particles were obtained on a 120 kV FEI Tecnai T12 S/TEM with a LaB_6 source equipped with an EDAX XEDS system. HRTEM micrographs were obtained on a 200 kV FEI Metrios TEM with an X-FEG source and SuperX-EDS. XEDS elemental maps of the films were acquired using the SuperX silicon drift detector (SDD). The TEM grids used were 300 mesh Cu, which were coated with holey/thin carbon films (Pacific Grid Tech Cu-300HD). A small portion of the film was scraped off from silicon plate and was sonicated with ethanol. Few drops of the resulting solution was dropped on the grids and air dried before it was placed in the UHV chamber of the TEM.

8.5.4 N_2 jet impingement test:

In order to test the adhesiveness of the films, a N_2 jet impingement test was performed as suggested by Russ and Talbot [6]. This test is the most suitable for the nanopowder films. A comparison of the adhesion tests available for different kinds of coatings is given in table 8.1. The schematic of this test is shown in Fig. 8.3. In this test, pure N_2 was directed at 10 L/min at a pressure of 40 psia to a stainless steel tube of 0.1 cm inner diameter. The silicon substrate with WO_3 film was placed at a distance of 0.5 cm from N_2 jet. The N_2 was allowed to flow for 10 s. Photographs of the WO_3 film were taken before and after the test and inspected visually to determine any damage to the film.

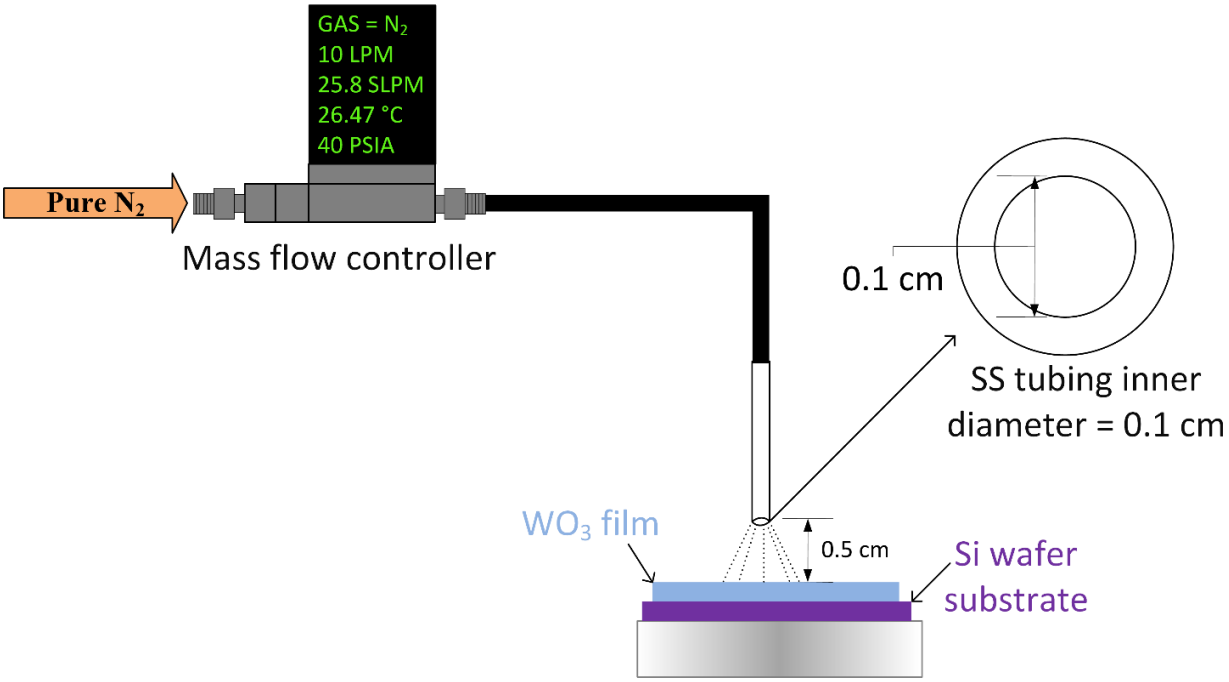

Fig. 8.3: Schematic of the arrangement for the N_2 gas jet impingement method suggested by Russ and Talbot [6].

Table 8.1. Different adhesion tests available in literature.

Test name	Adhesion force	Description	Comments	Ref.
Pull-off the thin film	10^7 Pa	The film is pulled directly from the substrate. The force required to pull the film from the substrate is the adhesion strength.	adhesion force too strong for powder coatings	[6,7]
Ultra-centrifugal	10^{-8}–10^{-5} N ~ 3 µm particles	The coating is placed in an ultracentrifuge in air facing away from the center.	adhesion force too weak for powder coatings	[8]
Ultrasonic	10^{-7} N	The film is placed in front of an ultrasonic horn.	adhesion force too weak for powder coatings	[8]
Adhesive Tape	50 N	A piece of adhesive tape is attached to top side of the film and then pulled, perpendicularly away from the substrate	adhesion force too strong for powder coatings	[6,7]
Tangential Shear	10 N	In this method a tangential shear is applied to the film either by passing a fluid over the film or attaching a grip	adhesion force too strong for powder coatings	[6,7]

Test name	Adhesion force	Description	Comments	Ref.
		to the top of the film and mechanically shearing the deposit.		
Tension Test	10–100 N	The film is pulled apart until it fractures. The force applied at the fracture point is a measure of adhesion.	adhesion force too strong for powder coatings	[6,7]
Knife or Scribe Test	10^7–10^9 Pa	A knife or other sharp device is placed on the substrate. The force required to scrape away the film is a measure of adhesion.	adhesion force too strong for powder coatings	[6,7]
N_2 gas jet impingement method	100 Pa	A N_2 jet is applied on a film for 10 s through a 1 mm inner diameter tube at a pressure of 40 psi. The jet should be placed perpendicularly and 0.5 cm above the film.	designed specifically for powder coatings as described by Russ and Talbot.	[6,9]

8.6 Results and discussions:

8.6.1 X-ray diffraction (XRD):

Fig. 8.4 and Fig. 8.5 shows the XRD pattern of the non-doped and SiO_2 doped WO_3 film coated on silicon substrates. Fig. 8.4 (a)-(e) shows the XRD of the post annealed WO_3 film with 0%, 3%, 4%, 5%, and 7% SiO_2 respectively. Fig 8.5 (a)-(e) shows the XRD of the post annealed WO_3 film arranged according to the post annealing temperature. The WO_3 film showed the monoclinic structure and was indexed to ICDD#01-043-1035 for the γ-WO_3 and to ICDD#01-043-1035 for the ε-WO_3. The characteristic main peaks for ε-WO_3 were seen at the 2θ value of 23.2°, 24.1°, 29°, 33.3°, 34°, and 49.4° and can be associated with the (002), (110), (012), (-112), (200) and (220) reflections respectively while the characteristic main peaks for γ-WO_3 were seen at the 2θ

value of 23.1°, 23.6°, 24.4°,26.6°,and 42° and can be associated with the (002), (020), (200), (120), and (222) reflections respectively. From Fig. 8.4 (a) it can be seen that the as prepared non-doped WO_3 without annealing is mostly ferroelectric ε-WO_3. The phase is maintained till 400°C after which it transforms back to the thermodynamically stable γ-WO_3. Fig. 8.4 (b)-(c) shows the structural behavior of the 3 wt% and 4 wt% SiO_2 doped WO_3 respectively, and it can be seen that the ε-WO_3 is stable till 500°C. From Fig. 8.4 (d)-(e) for the 5 wt% and 7 wt% SiO_2 doped WO_3 respectively, it is clear that the ε-WO_3 is stable till 600°C. From these studies it can be clearly interpreted that, increasing the SiO_2 doping increased the ε-WO_3 content of the films. To better understand the phase transformation, the XRD data for also presented by keeping the annealing and deposition time constant and varying the SiO_2 doping. This is shown in Fig 8.5 (a)-(e).

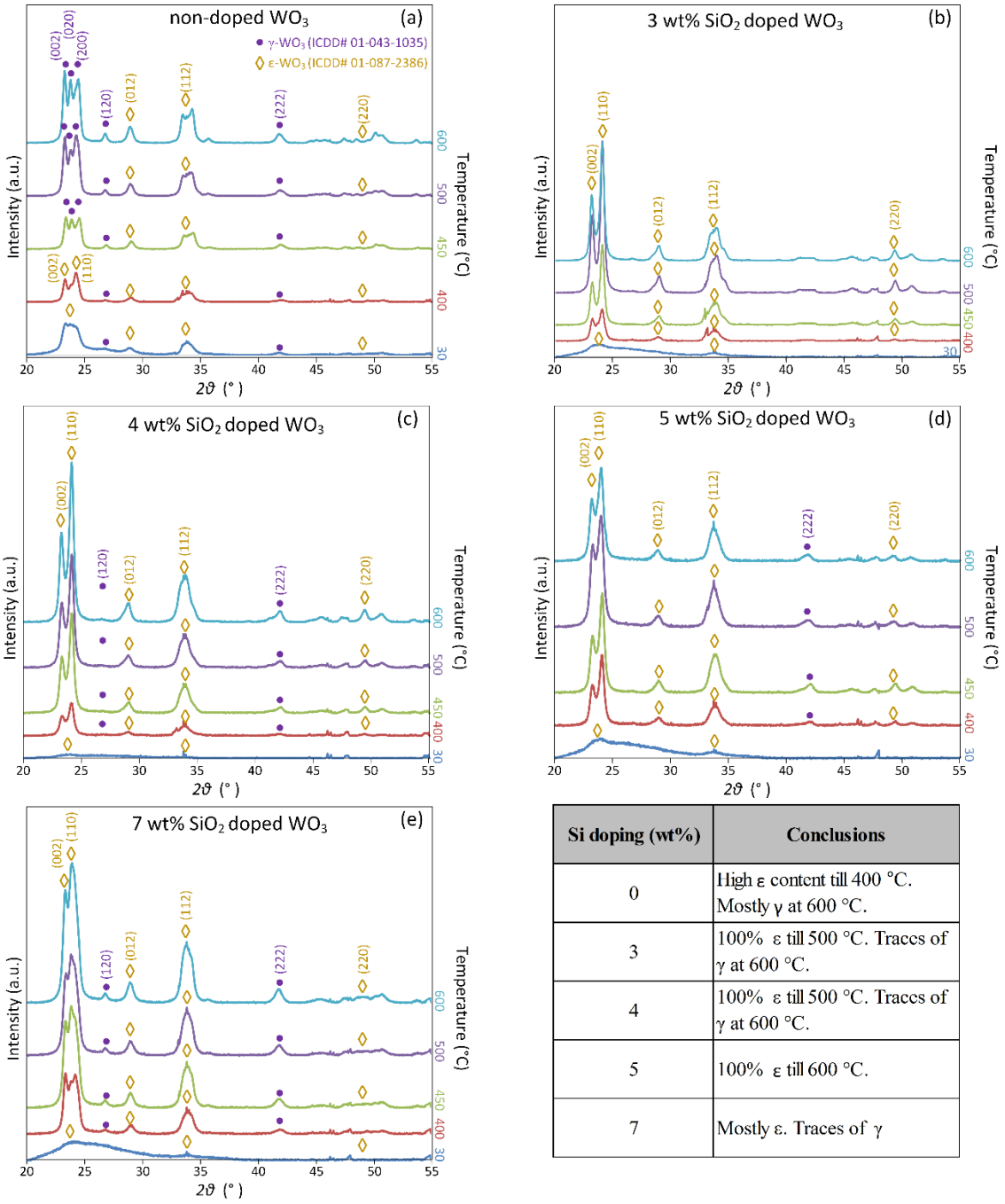

Si doping (wt%)	Conclusions
0	High ε content till 400 °C. Mostly γ at 600 °C.
3	100% ε till 500 °C. Traces of γ at 600 °C.
4	100% ε till 500 °C. Traces of γ at 600 °C.
5	100% ε till 600 °C.
7	Mostly ε. Traces of γ

Fig. 8.4: (a)-(e) The X-ray diffraction of the post annealed WO_3 film with 0%, 3%, 4%, 5%, and 7% SiO_2 respectively.

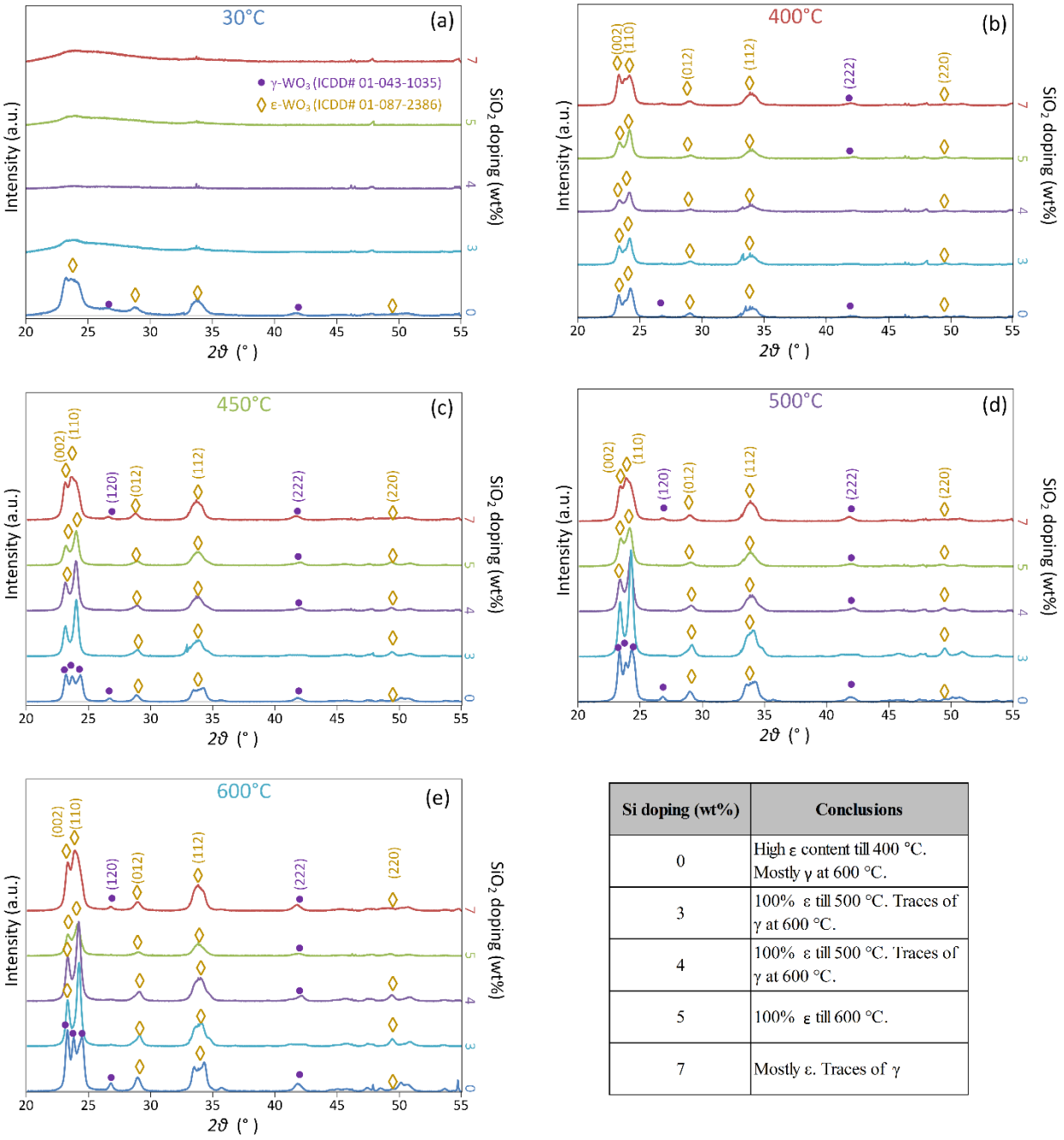

Si doping (wt%)	Conclusions
0	High ε content till 400 °C. Mostly γ at 600 °C.
3	100% ε till 500 °C. Traces of γ at 600 °C.
4	100% ε till 500 °C. Traces of γ at 600 °C.
5	100% ε till 600 °C.
7	Mostly ε. Traces of γ

Fig. 8.5: (a)-(e) The X-ray diffraction of the post annealed WO_3 film arranged according to the post annealing temperature.

8.6.2 Raman spectroscopy:

Raman spectroscopy technique was used for identifying the phases in the WO_3 film since this technique is well known to give the "fingerprint "of WO_3 material [4, 5]. Raman spectroscopy along with the XRD can be effectively used to determine the phase composition of WO_3. Fig. 8.6 and Fig. 8.7 shows the Raman spectroscopy of the non-doped and SiO_2 doped WO_3 film coated on silicon substrates. Fig. 8.6 (a)-(e) shows the Raman spectroscopy of the post annealed WO_3 film with 0%, 3%, 4%, 5%, and 7% SiO_2 respectively. Fig. 8.7 (a)-(e) shows the Raman spectroscopy of the post annealed WO_3 film arranged according to the post annealing temperature. The strongest peaks were seen at 808 and 715 cm^{-1} which are similar to those of the monoclinic γ-WO_3. A relatively strong peak was observed below 150 cm^{-1} for all the samples which indicates the O-O deformation mode [10]. The peaks were matched with the standards in references [4, 10]. The peaks for γ-WO_3 are at the Raman shift value of 808, 716, 328 and 275 cm^{-1} while the peaks for ε-WO_3 are at 808, 686, 646, 423, 373, 275 and 208 cm^{-1}. Raman spectroscopy results justifies the conclusions which were made on the basis of the XRD.

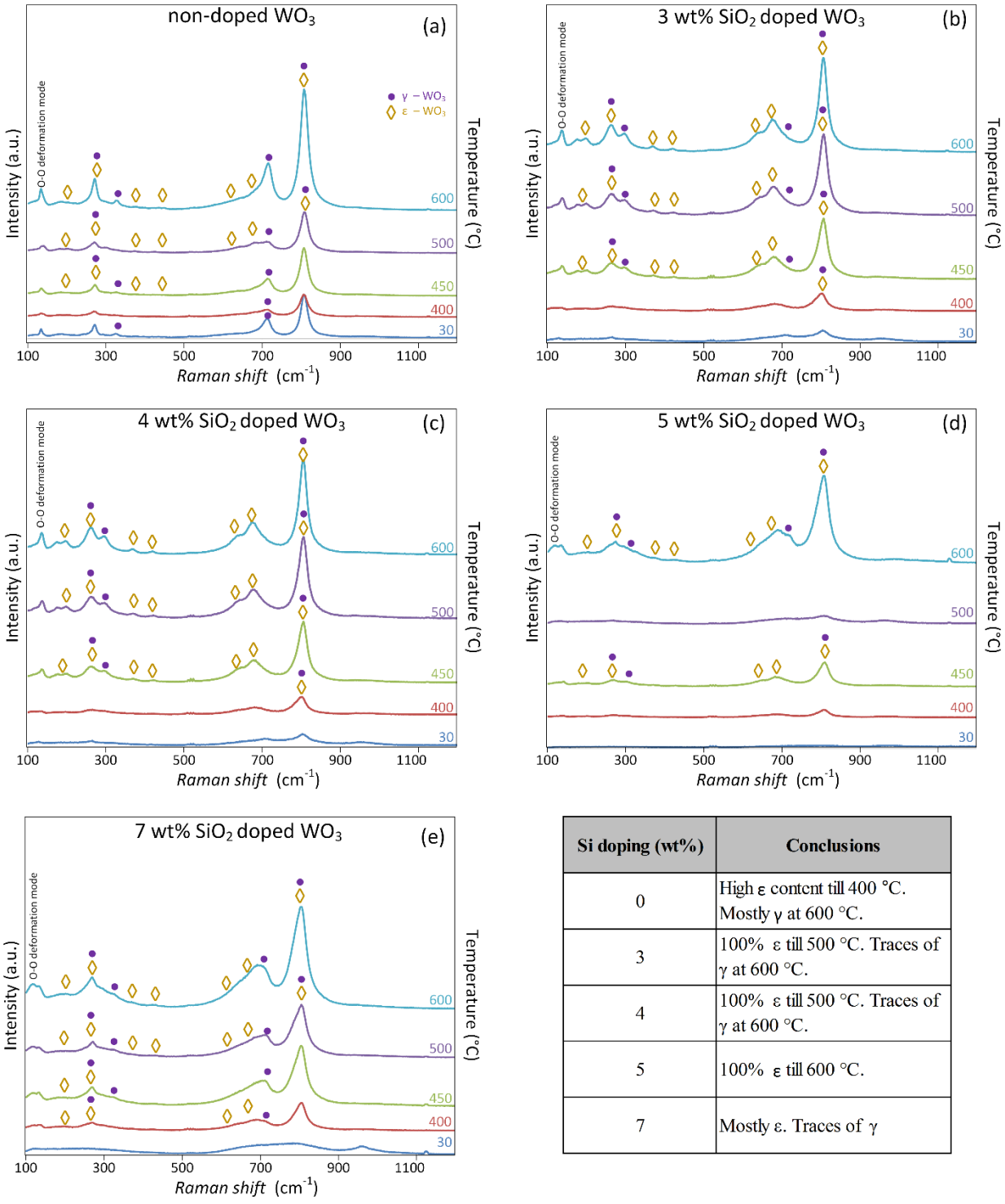

Si doping (wt%)	Conclusions
0	High ε content till 400 °C. Mostly γ at 600 °C.
3	100% ε till 500 °C. Traces of γ at 600 °C.
4	100% ε till 500 °C. Traces of γ at 600 °C.
5	100% ε till 600 °C.
7	Mostly ε. Traces of γ

Fig. 8.6: (a)-(e) The Raman spectroscopy of the post annealed WO_3 film with 0%, 3%, 4%, 5%, and 7% SiO_2 respectively.

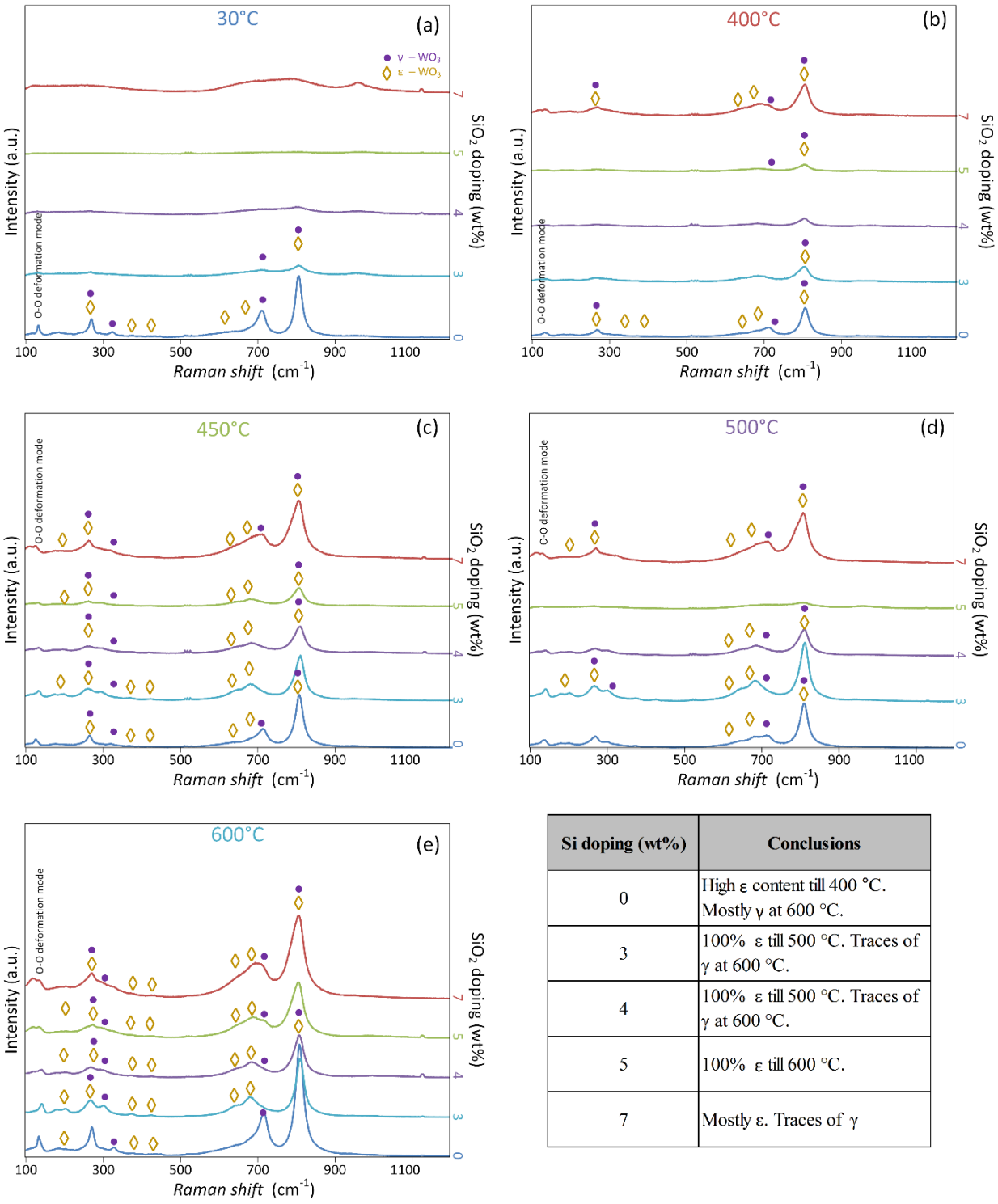

Si doping (wt%)	Conclusions
0	High ε content till 400 °C. Mostly γ at 600 °C.
3	100% ε till 500 °C. Traces of γ at 600 °C.
4	100% ε till 500 °C. Traces of γ at 600 °C.
5	100% ε till 600 °C.
7	Mostly ε. Traces of γ

Fig. 8.7: (a)-(e) The Raman spectroscopy of the post annealed WO_3 film arranged according to the post annealing temperature.

8.6.3 Transmission electron microscopy:

Fig. 8.8 shows the bright field TEM micrographs and the SADP of the non-doped and SiO_2 doped WO_3, both pre annealing and post annealing (600°C). All samples were polycrystalline, as evident from the SADP and were indexed to monoclinic WO_3. Grain size was measured by TEM point analysis. The initial grain size was in the range of 10–15 nm for non-doped doped WO_3, 7–16 nm for 3 wt% SiO_2 doped WO_3, 7–16 nm for 4 wt% SiO_2 doped WO_3, 7–13 nm for 5 wt% SiO_2 doped WO_3, 5–13 nm for 7 wt% SiO_2 doped WO_3, and 10-15 nm for non-doped doped WO_3. The grain size for the post annealed samples was in the range of 30-50 nm for the non-doped WO_3, 15–35 nm for 3 wt% SiO_2 doped WO_3, 10–20 nm for 4 wt% SiO_2 doped WO_3, 7–17 nm for 5 wt% SiO_2 doped WO_3, and 10–20 nm for 7 wt% SiO_2 doped WO_3. Different shapes and sizes of particles were seen from the images. None of the samples shows necking, a property which is desirable for the sensing applications [11, 12]. Fig. 8.9 (a)-(f) shows the high resolution TEM images of the post annealed (600°C) WO_3. Fig. 8.9 (a-b) shows the non-doped WO_3 while Fig. 8.9 (c-f) shows the 5 wt% SiO_2 doped WO_3. Amorphous domains can be clearly seen around the individual grains. It is interesting to observe the amorphous domains in the non-doped WO_3. This could be due to the presence of amorphous WO_3 which did not crystallized even after post annealing process. Lattice fringes can be clearly seen in the WO_3 grains. Fig. 8.10 shows the XEDS elemental map for the 5 wt% SiO_2 doped WO_3 proving that the amorphous domains in the doped WO_3 are SiO_2.

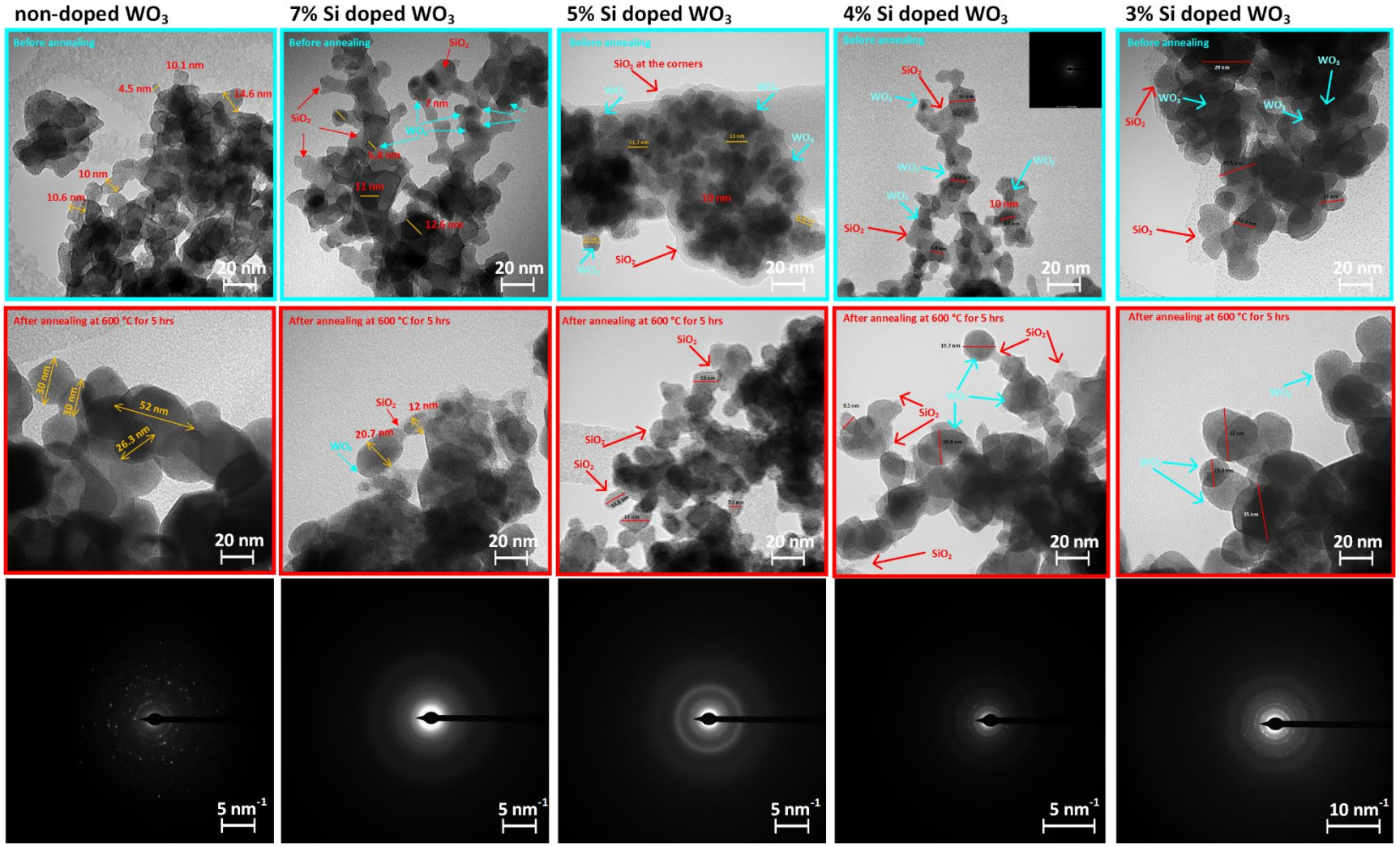

Fig. 8.8: (a)-(e) Transmission electron microscopy of the pre annealed and post annealed WO_3 film and the corresponding selected area diffraction pattern (SADP).

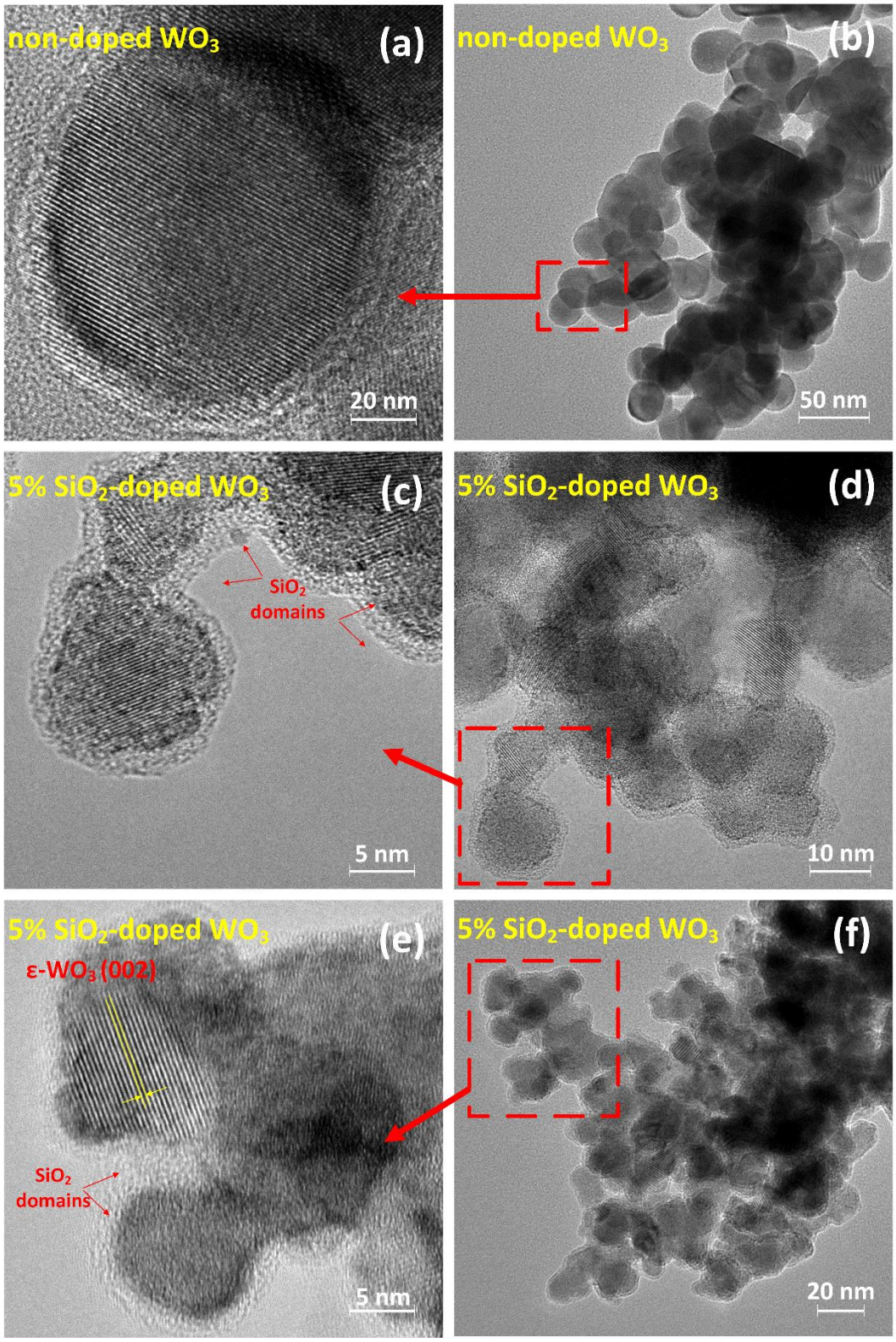

Fig. 8.9: High resolution transmission electron microscopy of the post annealed WO_3 film. (a)-(b) non-doped WO_3, (c)-(f) 5 wt% SiO_2 doped WO_3.

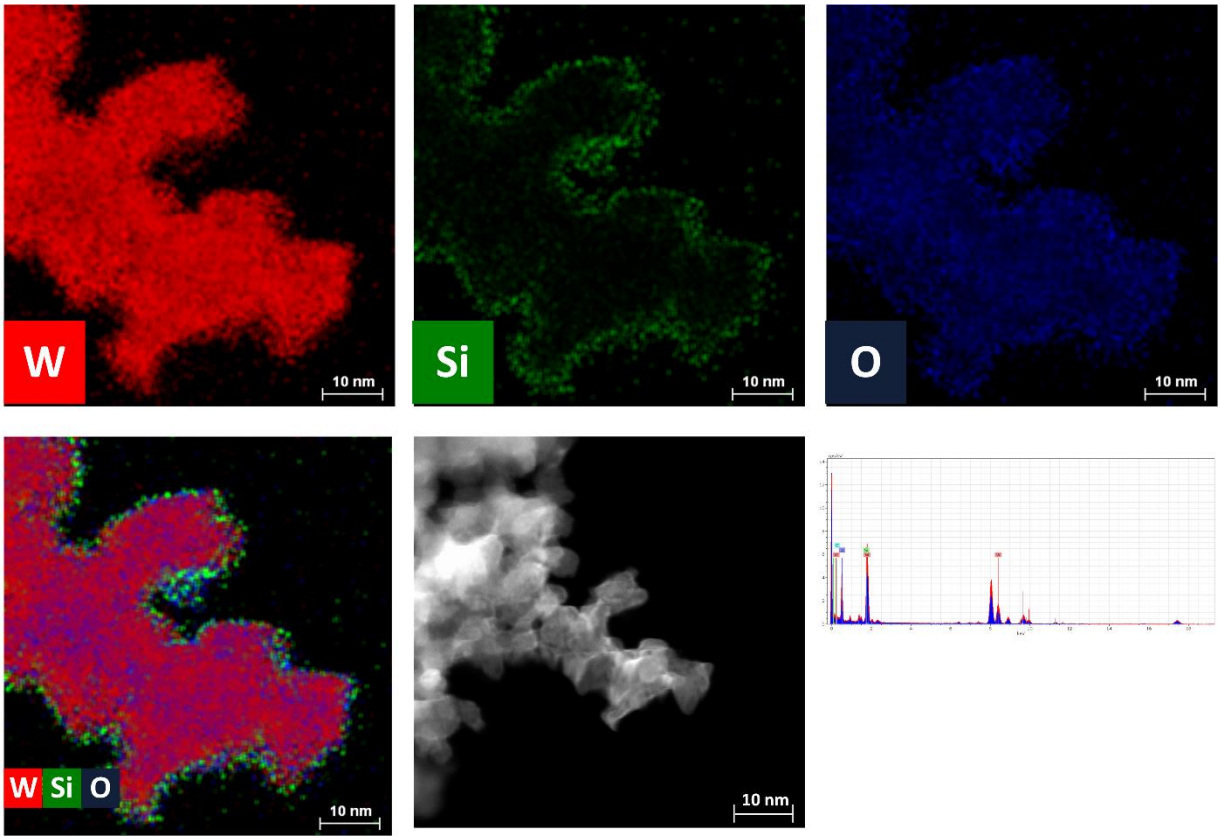

Fig. 8.10: X-ray energy dispersive spectroscopy (XEDS) elemental maps for 5 wt% SiO_2 doped WO_3 along with the scanning transmission electron microscopy (STEM) image.

8.6.3 Scanning electron microscopy:

Fig. 8.11 (a)- (c) shows the scanning electron microscopy images of the cross -section of the post annealed 5 wt% SiO_2 doped WO_3 films directly deposited in silicon substrates for (a) 30 min deposition and annealed at 400°C, (b) 90 min deposition and annealed at 500°C, and (c) 120 min deposition and annealed at 600°C. The film thickness was measured to be 4 μm, 5.6 μm and 6.4 μm respectively. Columnar growth (tree like) of the particle agglomerates can be seen. It can be inferred that the film is highly porous. The non-linearity of the deposition time and the film growth rate could be because of various reasons. Firstly the annealing temperature was different

which could cause the change in the porosity and overall structure of the film. Secondly, it is possible that after reaching a threshold thickness, it will become difficult for the particles to contribute to the growth of the columns.

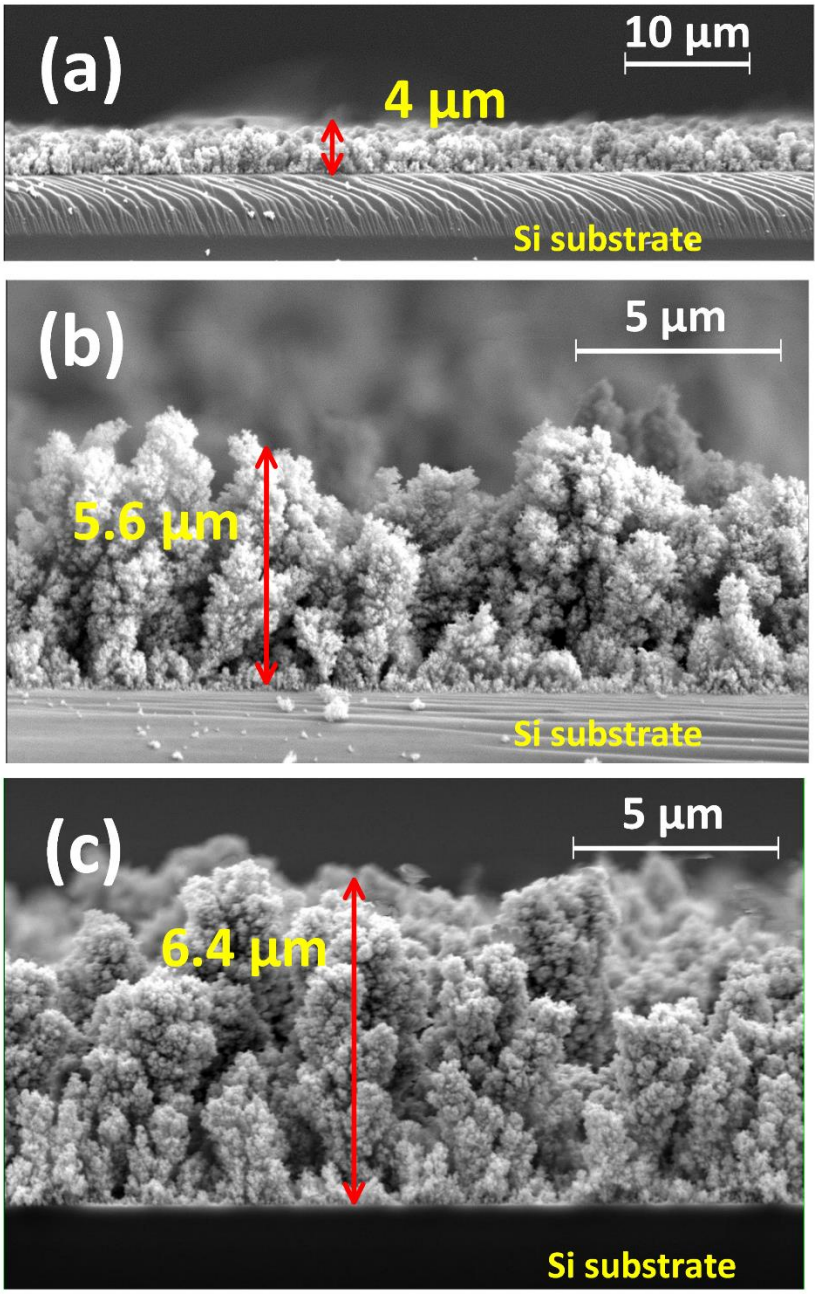

Fig. 8.11: Scanning electron microscopy (SEM) of the cross-section of post annealed 5 wt% SiO_2 doped WO_3 on a silicon substrate (a) 30 min deposition and annealed at 400°C, (b) 90 min deposition and annealed at 500°C, and (c) 120 min deposition and annealed at 600°C.

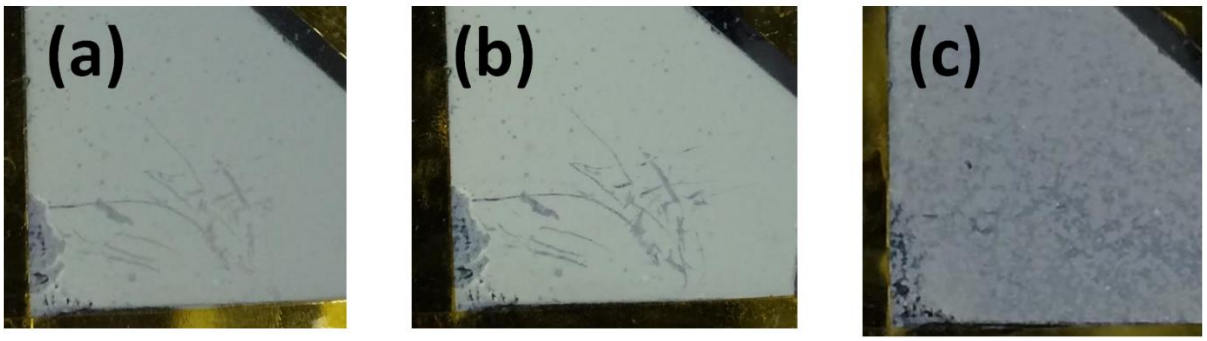

Fig. 8.12: 4 wt% SiO_2 doped WO_3 on a silicon substrate after annealing at 600°C. (a) initial film-(b) after impinging xylene based particle free frame for 60 s in RSDT, (c) after N_2 gas jet impingement test.

8.6.4 N_2 gas jet impingement test:

Fig. 8.12 (a)- (c) shows the 4 wt% SiO_2 doped WO_3 films directly deposited in silicon substrates where (a) is the initial film, (b) after impinging xylene based particle free frame for 60 s in RSDT, and (c) after N_2 gas jet impingement test. There is a marked difference between the three images. However from Fig. 8.12 (c) it can be interpreted that a large amount of the film was blown away by the N_2 jet. The adhesiveness of the films are large compromised because of the presence of the amorphous SiO_2.

8.7 Conclusions:

Reactive Spray Deposition Technology was employed to synthesize ε-WO_3 thin films from the vapor phase. The morphology, and structure was tuned by varying the SiO_2 doping from 0–7 wt%. This work was performed with the motivation to preserve the metastable ε-WO_3 over an extended temperature range desirable for acetone sensors. As discussed in Chapter 4, ε-WO_3 phase is polar and preferentially attracts acetone molecules. It was found that the 5 wt% SiO_2 doped WO_3 performed best in this class with the formation of ε-WO_3 in the temperature range 30–600°C. It was

determined that the particular structure and properties of WO_3 are a function of the synthesis process and doping concentration. However in spite of obtaining the WO_3 phase favorable towards acetone sensing, there was no acetone sensitivity. This could be caused due to the absence of necking between the individual WO_3 grains and also due to the possibility that the active sites were blocked by amorphous SiO_2 domains. Chapter 9 and 10 will elaborate upon exploring the sensing function of WO_3 by changing the synthesis conditions.

8.8 Acknowledgements:

Dr. Justin Roller at FEI Company, Hillsboro, OR is cheerfully acknowledged for the HRTEM images and the discussions thereafter.

8.9 References:

[1] J. M. Roller. Flame Synthesis of Nanomaterials for Alternative Energy Applications (Doctoral dissertation). University of Connecticut. Retrieved from: http://digitalcommons.uconn.edu/dissertations/432/ (2014).

[2] M. Graf, A. Gurlo, N. Bârsan, U. Weimar, A. Hierlemann, Microfabricated gas sensor systems with sensitive nanocrystalline metal-oxide films, Journal of Nanoparticle Research. 8 (6) (2006) 823-839.

[3] A. Tricoli, M. Graf, F. Mayer, S. Kuühne, A. Hierlemann, S.E. Pratsinis, Micropatterning Layers by Flame Aerosol Deposition-Annealing, Advanced Materials. 20 (16) (2008) 3005-3010.

[4] C. Bittencourt, E. Llobet, P. Ivanov, X. Vilanova, X. Correig, M.A.P. Silva, L.A.O. Nunes, J.J. Pireaux, Ag induced modifications on WO_3 films studied by AFM, Raman and x-ray photoelectron spectroscopy, Journal of Physics D-Applied Physics. 37 (24) (2004) 3383-3391.

[5] R. Garcia-Sanchez, T. Ahmido, D. Casimir, S. Baliga, P. Misra, Thermal Effects Associated with the Raman Spectroscopy of WO_3 Gas-Sensor Materials, Journal of Physical Chemistry A. 117 (50) (2013) 13825-13831.

[6] B.E. Russ, J.B. Talbot, A Method for Measuring the Adhesion Strength of Powder Coatings, Journal of Adhesion. 68 (3-4) (1998) 257-268.

[7] K.L. Mittal, Adhesion Measurement of Thin Films, Thick Films and Bulk Coatings, Adhesion. Philadelphia, PA, Nov 2-4, 1976 (1978) 408.

[8] M. J. Shane. An Analysis of the Electrophoretic Deposition of Phosphors (Doctoral dissertation). University of California, San Diego. Retrieved from: http://ezproxy.lib.uconn.edu/login?url=http://search.proquest.com/docview/304090742?accountid=14518 (1994).

[9] K. Iinoya, J.K. Beddow, G. Jimbo, Powder Technology, 1st ed., Hemisphere Publishing Corp., Washington, D.C., 1984.

[10] M. Arai, S. Hayashi, K. Yamamoto, S.S. Kim, Raman Studies of Phase-Transitions in Gas-Evaporated WO_3 Microcrystals, Solid State Communications. 75 (7) (1990) 613-616.

[11] S. Sharma, M. Madou, A new approach to gas sensing with nanotechnology, Philosophical Transactions of the Royal Society A. 370 (1967) (2012) 2448-2473.

[12] N. Barsan, U. Weimar, Conduction Model of Metal Oxide Gas Sensors, Journal of Electroceramics. 7 (3) (2001) 143-167.

CHAPTER 9:

Ultra-low NO_2 detection by gamma WO_3 synthesized by Reactive Spray Deposition Technology

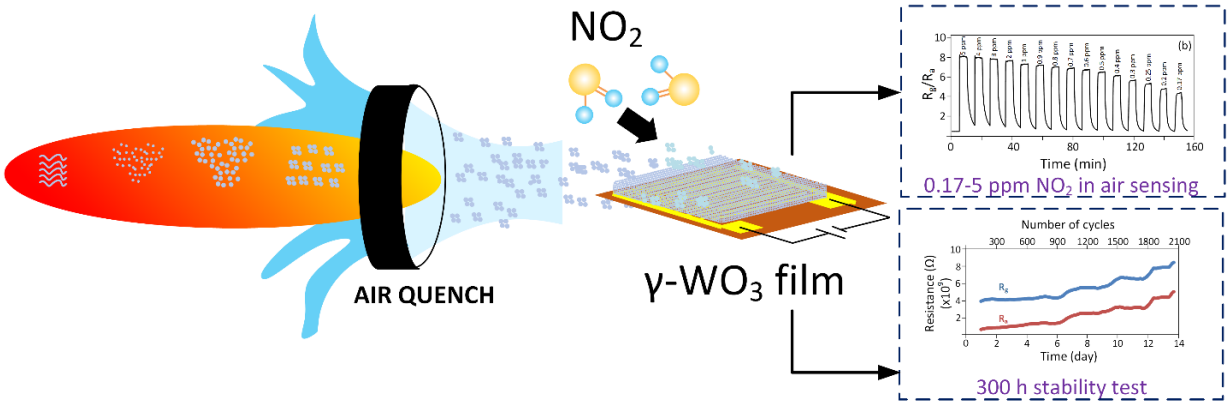

9.1 Highlights:

1. Monoclinic gamma WO_3 thin film was synthesized by a single step flame based process.

2. The WO_3 film was tested for 0.17–5 ppm NO_2 in air at 300°C and 100% relative humidity.

3. The structural properties of the WO_3 was correlated with the gas sensing data.

4. The WO_3 film showed quicker response time than the similar films synthesized by traditional processes.

5. Test and stability data shows that performance improvements that approach 100% efficiency can be made.

9.2 Abstract:

A porous tungsten oxide (WO_3) film based NO_2 sensor was developed by a one-step flame based process called Reactive Spray Deposition Technology (RSDT). This nano-crystalline WO_3 film was deposited directly on gold interdigitated electrodes. The sensitivity of this NO_2 sensor was measured at the parts per million (ppm) level, (0.17–5 ppm in air) at 300°C and 100% relative humidity. The sensors showed a relatively fast response time (~7s) and recovery time (~5 min), respectively. The stability of the sensor was evaluated for 300 h. in 0.5 ppm NO_2 in air at 100% relative humidity (2000 response-recovery cycles). The sensor was stable up to 6 days (~150 h.) of continuous operation and degraded between 150 to 300 h. The morphology and surface properties of the WO_3 film were investigated with XRD, Raman spectroscopy, BET, SEM, TEM, and HRTEM.

9.3 Keywords:

Gas sensor; Combustion; NO_2 sensing; Flame spray pyrolysis; Tungsten oxide nanoparticles; Reactive Spray Deposition Technology

9.4 Introduction:

In this chapter we have proposed Reactive Spray Deposition Technology (RSDT) for the synthesis of γ-WO_3 films directly on gold interdigitated electrodes. The RSDT process allows the flexibility to create γ-WO_3 with control of the particle size, porosity and thickness of the film. The sensitivity of porous WO_3 increases when the particle size is below its Debye length (λ_D) which is 25 nm [1]. In chapter 7, it had been shown that RSDT can be employed for the synthesis of WO_3 films with precise control of particle size, film morphology, and crystal structure [2]. In this study, we have employed RSDT for the deposition of nano crystalline WO_3 thin films directly on a gold interdigitated electrode which is to be assembled into an NO_2 sensing device. Here we provide a brief description of the synthesis, fabrication and testing procedure of the NO_2 sensor. The microstructure of the tungsten oxide films, and the effect of the film structure, grain size, and the sensor response to the ppm level concentration of NO_2 will be described. NO_2 response behavior on the tungsten oxide surface at various operating temperatures will also be presented. The properties of the WO_3 film was investigated by X-ray diffraction (XRD), Raman spectroscopy, the Brunauer-Emmett-Teller (BET) method, high resolution transmission electron microscopy (HRTEM), and scanning electron microscopy (SEM). The sensor response was tested from 0.17–5 ppm at different operating temperatures (250–350°C) to determine the optimum working temperature. The sensor film was ultimately performance tested for NO_2 sensitivity in the 0.17–5 ppm range at 300°C. The sensor was further tested for stability for 300 h. in 0.5 ppm NO_2

in the air which is 10 times lower than the workplace permissible exposure limit (PEL) as per the Occupational Safety and Health Administration (OSHA) specification. The sensor was tested below the PEL because it is desirable for the workplace atmosphere to remain below the PEL of NO_2. In order to check the selectivity, the sensor was also tested for 10 ppm acetone, 100 ppm ethanol, 10-100 ppm H_2, and 10 ppm isoprene. We have also compared the test data of WO_3 based NO_2 sensors prepared by RSDT with the results reported in the literature. This work was presented at the 225th Electrochemical Society (ECS) meeting, Orlando, Florida at symposium: B1: Sensors, Actuators, and Microsystems General Session (Chemical and Biological Sensors), May 11-16 (2014). This work was submitted for publication in Sensors and Actuators B: Chemical on October 28th, 2015.

9.5 Experimental:

9.5.1 Synthesis of WO_3:

An explanation of the RSDT equipment and process has been described in detail by Jain and Roller et al. [3, 4]. Fig. 9.1 shows the schematic of RSDT along with the cross-sectional view of the combustion nozzle. Tungsten hexacarbonyl [$W(CO)_6$] was obtained from Sigma Aldrich (Catalogue #AC221040100) and was dissolved in a tetrahydrofuran (THF) (enthalpy of combustion: 2501 kJ/mol) (Fisher Scientific # SHBD3901V). The precursor was chosen based on its low decomposition temperature of 170°C. 20 wt% sulfur free liquefied propane (Airgas catalogue # PRCP350S) was added to the above to form a precursor solution resulting in a final concentration of 5 mmol/L $W(CO)_6$, and 18 wt% propane. THF has a dual role of an inexpensive solvent and fuel for the combustion of the [$W(CO)_6$]. The precursor solution was filled in a syringe pump (Teledyne Isco 500D) and after heating to 50–60°C it was directed at 4 mL/min through a stainless steel capillary tube of 100 μm inner diameter to the combustion nozzle. Six

methane-oxygen flamelets (methane and oxygen at 0.5 L/min each) surround the capillary end, which ignites the combustible precursor mist. The precursor solution was atomized by oxygen (5 L/min) and a pressure drop of 125 psi was maintained at the exit point of the nozzle. A circular air quench ring (Exair, Super Air Wipe®) with a compressed air flow rate of 70 L/min was positioned at 10 cm from the combustion nozzle. The distance between the combustion nozzle and the air quench is considered the reaction zone and the length of the reaction zone is proportional to the residence time of the nano-particles in that zone. Adjusting the length of the reaction zone and the flow rate of compressed air gives unique conditions to obtain an assortment of crystalline structures and phases of the material [5]. This also enables "nano quenching" thereby limiting the particle size growth in the flame. Two silicon plates (Nova electronic materials item#8289) and two gold interdigitated electrodes on alumina base (Electronic design center-Case Western Reserve University item#102) were used as substrates. Silicon plates were used only to evaluate the film thickness since they can be easily fractured and can be mounted at 90° on a SEM stub. Gold interdigitated electrodes on alumina base (Electronic design center-Case Western Reserve University item#102) were used as substrates for the gas sensing. This thick film printed electrode consists of interdigitated gold deposits on a 0.6 mm thick alumina substrate. The dimensions of the alumina base is 15 mm by 15 mm. The gold thick film screen printed electrode digits are 250 μm wide with 250 μm spacing between them. The gold digits are connected with a pair of gold bonding pads which allow wires to be threaded through them as an aid for electrical connection. Prior to WO_3 deposition, the electrode was cleaned with acetone, methanol and deionized water, in order and dried in an air oven operating at 80°C for 1 h. The four substrates were mounted on a stainless steel substrate holder, which was placed on an x-y-z platform. This enabled the substrates to move along a serpentine path in front of the flame to ensure even coating of WO_3 on the

substrates. The total deposition area was 25 cm^2. All the samples were annealed in the air at 500°C for 5 h. in an oven to stabilize the WO_3 film. The characterization and gas sensing measurements were performed on the post annealed samples.

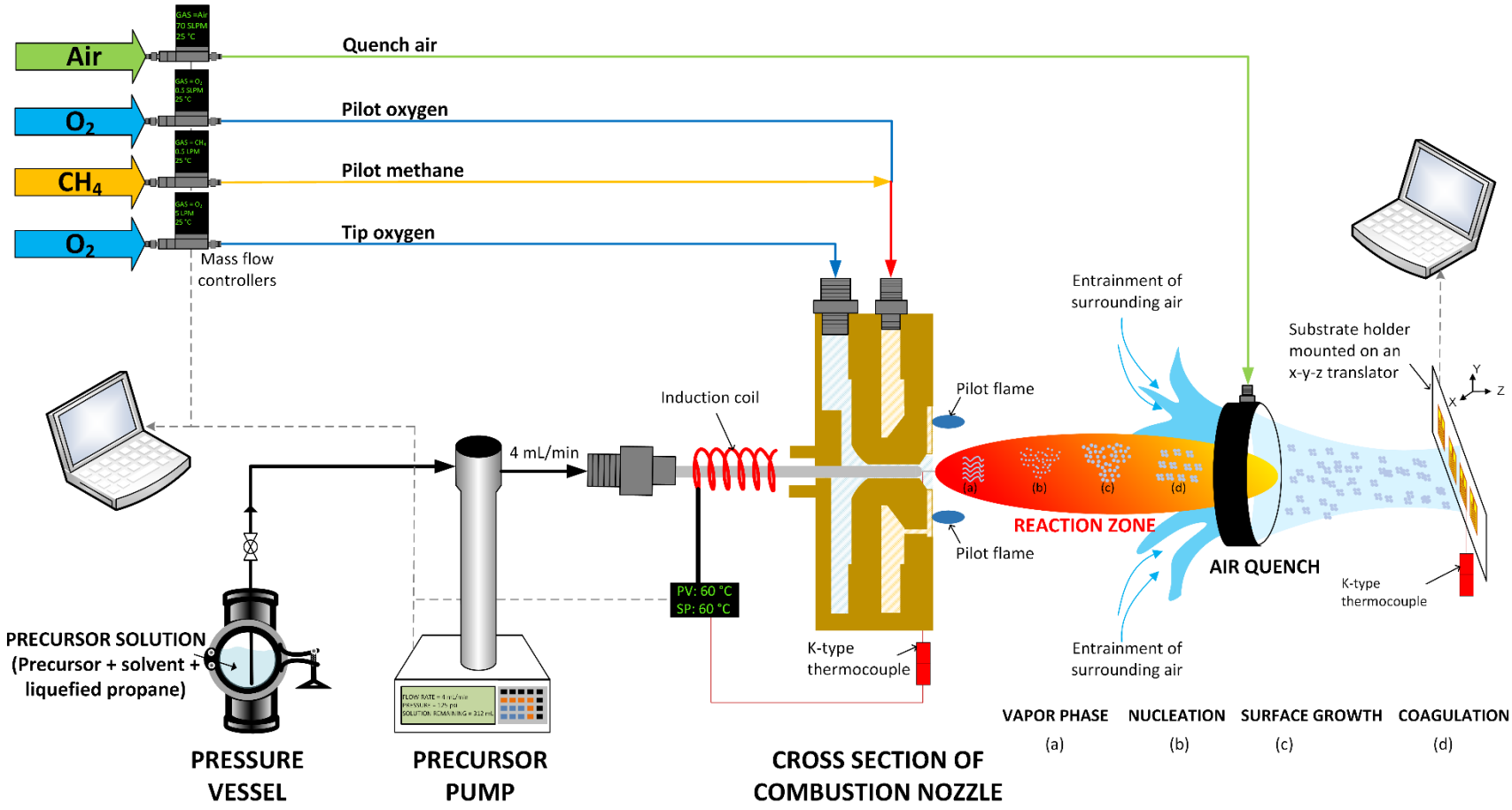

Fig. 9.1: Arrangement of the Reactive Spray Deposition Technology for direct deposition of WO_3 on gold interdigitated electrodes.

9.5.2 Characterization:

XRD patterns of WO_3 films directly deposited on gold interdigitated electrodes were recorded in the air at 25°C on a Bruker D8 advanced powder diffractometer using CuKα radiation. The scans were taken in the 2θ range of 20–55° with a step size of 0.02° and time per step of 5 s. Raman spectra were obtained in air at 25°C in the spectral range between 100 and 1200 cm^{-1} with a Renishaw Ramascope micro-Raman spectrometer fitted with a reflected light microscope using a 50 mW laser (514.5 nm) and exposure time of 10 s. Laser power delivered to the sample was set at 20% (10 mW) to avoid sample damage. Instrument alignment was optimized using a 521 cm^{-1} signal of a silicon wafer. Raman measurements for WO_3 is well known to provide structural and phase information of WO_3 material [6]. The surface area of WO_3 particles was calculated by the Brunauer-Emmett-Teller (BET) method using N_2 sorption experiments on a Micromeritics ASAP 2020 BET system. Samples were degassed for 12 h. prior to N_2 sorption measurements. For obtaining the samples for BET, a separate experiment was performed in which, WO_3 nanoparticles powder was directly collected on a stainless steel substrate holder. The deposit was scrapped off using a plastic spatula and analyzed for N_2 sorption experiments. SEM micrographs were collected on an FEI ESEM Quanta 250 with a field emission gun at 5 kV accelerating voltage and 8 mm working distance. For determining the cross-sectional thickness of the film, the silicon substrate with WO_3 film was fractured, and mounted on a 90° aluminum stub. The sample was gold sputter coated prior to imaging under SEM. TEM micrographs and selected area diffraction pattern (SADP) of WO_3 particles were obtained on a 120kV FEI Tecnai T12 S/TEM with a LaB_6 source. HRTEM micrographs were obtained on a 200kV FEI Metrios TEM with an X-FEG source. 300 mesh Cu grids coated with holey/thin carbon films (Pacific Grid Tech Cu-300HD) were used. A small portion of the film was scraped off from the gold interdigitated

electrodes and was sonicated with ethanol. Few drops of the resulting solution were dropped on the grids and air dried before they were placed in the ultra-high vacuum (UHV) chamber of the TEM.

9.5.3 Gas sensing test:

Gas sensing tests were performed in a dynamic flow system, implemented in the laboratory as shown in Fig. 9.2. Prior to gas sensing, the electrode was annealed in the air at 500°C for 5 h. in an electric oven to stabilize the WO_3 film. A WO_3 coated gold interdigitated electrode was introduced in a quartz cylindrical test chamber (10 cm length and 3.2 cm inner diameter) which was wrapped by a high temperature nozzle band heater (McMaster Carr item# 3594K981). The ends of the test chamber were sealed by stainless steel fittings. Several ports were introduced in the test chamber for (1) gas inlet, (2) 2 gas outlets, and (3) standard k-type thermocouple to monitor temperature. Gas flow to the furnace was controlled by Environics Series 4040 Computerized Gas Dilution System with an option for precise humidification control (0-100% relative humidity). Presence of 2 gas outlets in the test chamber allows a precisely controlled change in the atmosphere of the test chamber, as soon as the gas concentration is changed from NO_2 to pure air and vice versa. Dry synthetic air (Airgas #AI UZ300) was used as a diluent gas and 10 ppm NO_2 in the air (Airgas #X02AI99C15A2520) was used for adjusting the NO_2 concentration. Relative humidity level of 100% was maintained throughout the tests as measured by a calibrated hygrometer (Vaisala HMT 337). Flow rate of 1.5 L/min was maintained in the test chamber, because it is same as the human expiratory flow rate [7] and it is expected that the results of this study could lead us to develop a sensor for human breath analysis. For the two probe amperiometric measurements, the WO_3 coated electrode was connected with two Pt wires (99.9% metals basis) (0.127 mm diameter) (Alfa Aesar#F20X038) and connected with a

CHI instrument's electrochemical analyzer (CHI6116E). Current (I) was measured as a function of time and gas flow concentration at a constant 1 V DC power supply. Resistance (R) was calculated by applying Ohm's law (R = V/I). The data was collected every 100 ms.

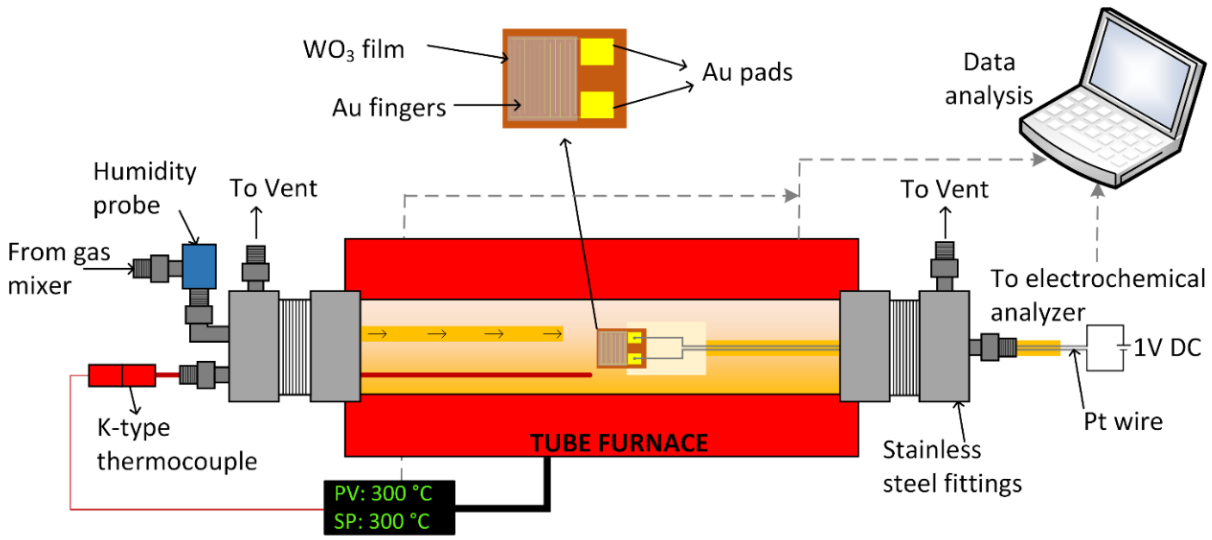

Fig. 9.2: Schematic of the gas sensing test setup.

9.6 Results:

9.6.1 X-ray diffraction (XRD):

Fig. 9.3 shows the XRD pattern of the WO_3 film coated on gold interdigitated electrodes pre and post NO_2 tests. The WO_3 film showed the monoclinic structure and was indexed to ICDD#01-043-1035. The characteristic main peaks for γ-WO_3 were seen at the 2θ value of 23.2°, 23.6° and 24.4° and can be associated with the (002), (020) and (200) reflections respectively. Average crystallite size of WO_3 was calculated from X-ray line broadening by Debye Scherrer's method and was 21 nm on the as prepared sample, and 27 nm on the post NO_2 test samples. As seen from the XRD pattern, there was an increase in the intensity of

the WO_3 film post NO_2 tests. This could be due to the increase in crystallinity of the WO_3 particles under the high temperature of testing. However no change in the overall structure of the film was observed verifying that the film was stable under the NO_2 test conditions.

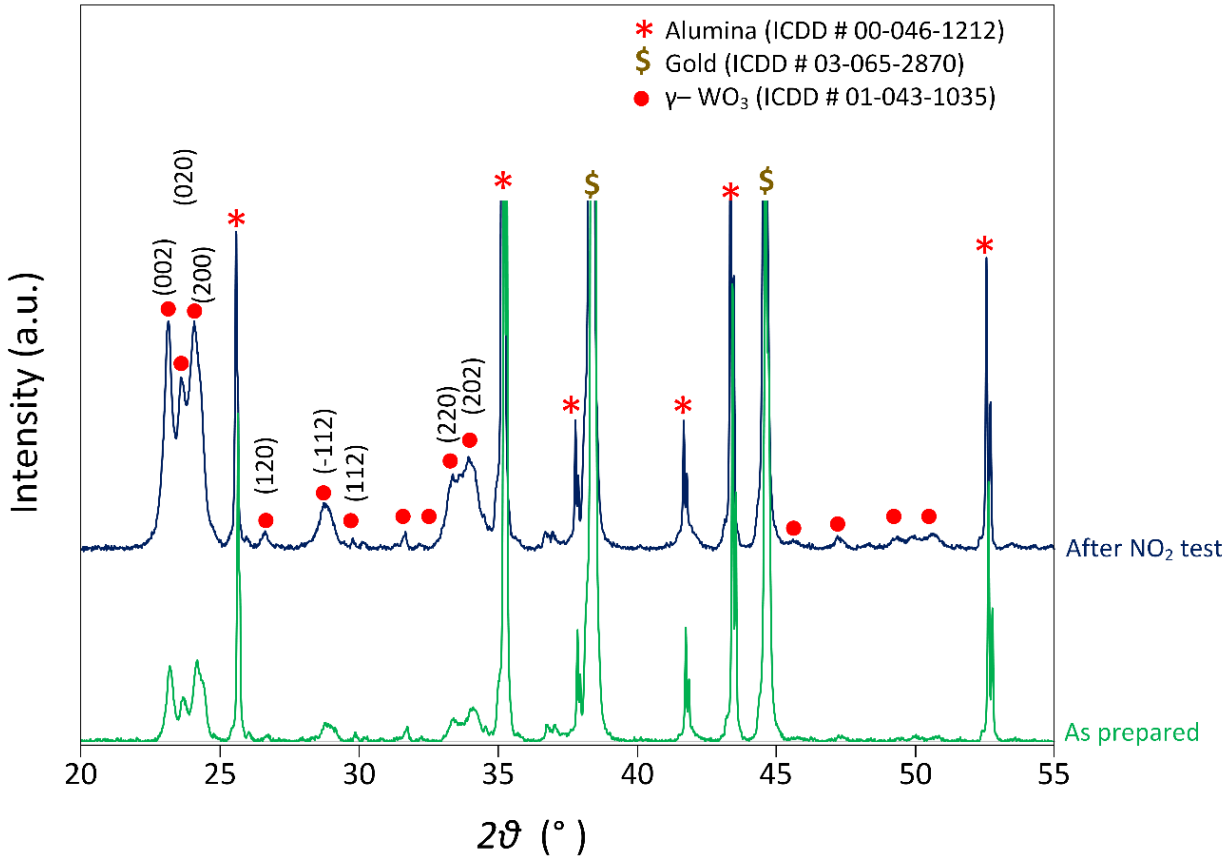

Fig. 9.3: X-ray diffraction of WO_3 film directly deposited on gold interdigitated electrodes, both pre and post NO_2 test showing that there is no change in the structure of the film.

9.6.2 Raman spectroscopy:

Raman spectroscopy technique was used for identifying the phases in the WO_3 film since this technique is well known to give the "fingerprint "of WO_3 material [6]. Fig. 9.4 shows the Raman spectroscopy results of the WO_3 film directly deposited on gold interdigitated electrodes, both pre and post NO_2 tests. The strongest peaks were seen at 808 and 715 cm^{-1} which

are similar to those of the monoclinic γ-WO_3. A relatively strong peak was observed below 150 cm^{-1} for all the samples which indicates the O-O deformation mode [8]. Intensity of the WO_3 film after NO_2 sensing has increased, consistent with the XRD results. On the basis of XRD and Raman spectroscopy results, it can be safely concluded that the structure of the WO_3 film in this study is monoclinic γ phase.

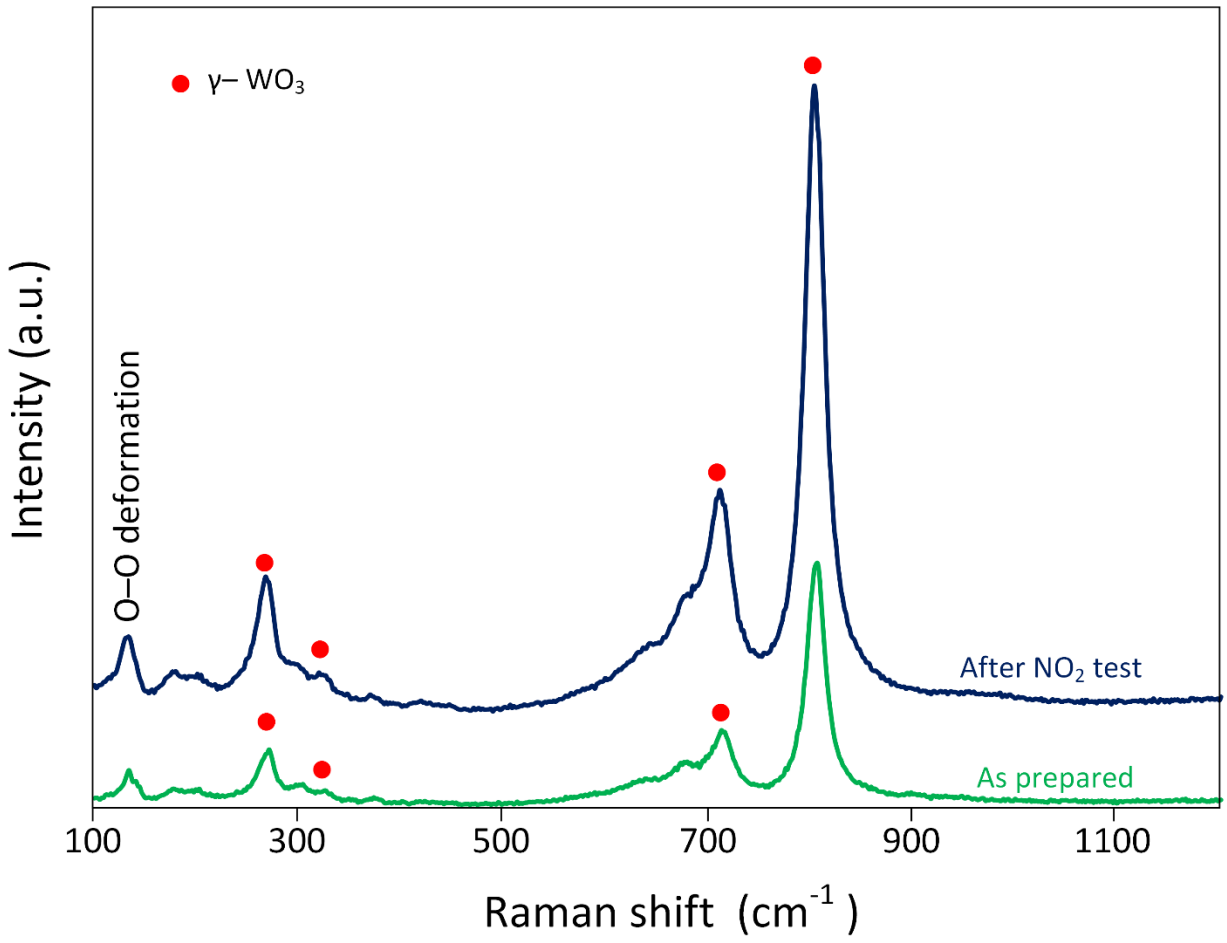

Fig. 9.4: Raman spectroscopy of WO_3 film directly deposited on gold interdigitated electrodes, both pre and post NO_2 test showing that there is no change in the structure of the film.

9.6.3 X-ray photoelectron spectroscopy (XPS):

Fig. 9.5 shows the high resolution spectra for W(4f) and O(1s). The W(4f) spectra was obtained in the binding energy range 30–45 eV, and the peaks were deconvoluted into two sets of photoemission doublets—W($4f_{7/2}$) and W($4f_{5/2}$). The reference binding energy for W($4f_{7/2}$) and W($4f_{5/2}$) is 31 eV and 33.15 eV respectively with a spin-orbital splitting energy of 2.15 eV [9]. The O(1s) spectra was obtained in the binding energy range 520–540 eV, which was deconvoluted into 4 peaks to determine the surface concentration of oxygen ions and were compared with the reference binding energy of peroxides [O_2^{2-} (530.5 eV)], superoxides [O^{2-} (529.5 eV)], [O^- (eV)], WO_3 (529.9–530.8 eV), WO_2 (530.4–531 eV), C=O (533 eV) and C-O (531.5–532 eV)] [10]. It is difficult to determine the exact concentration of each species due to relatively close binding energy value between the species.

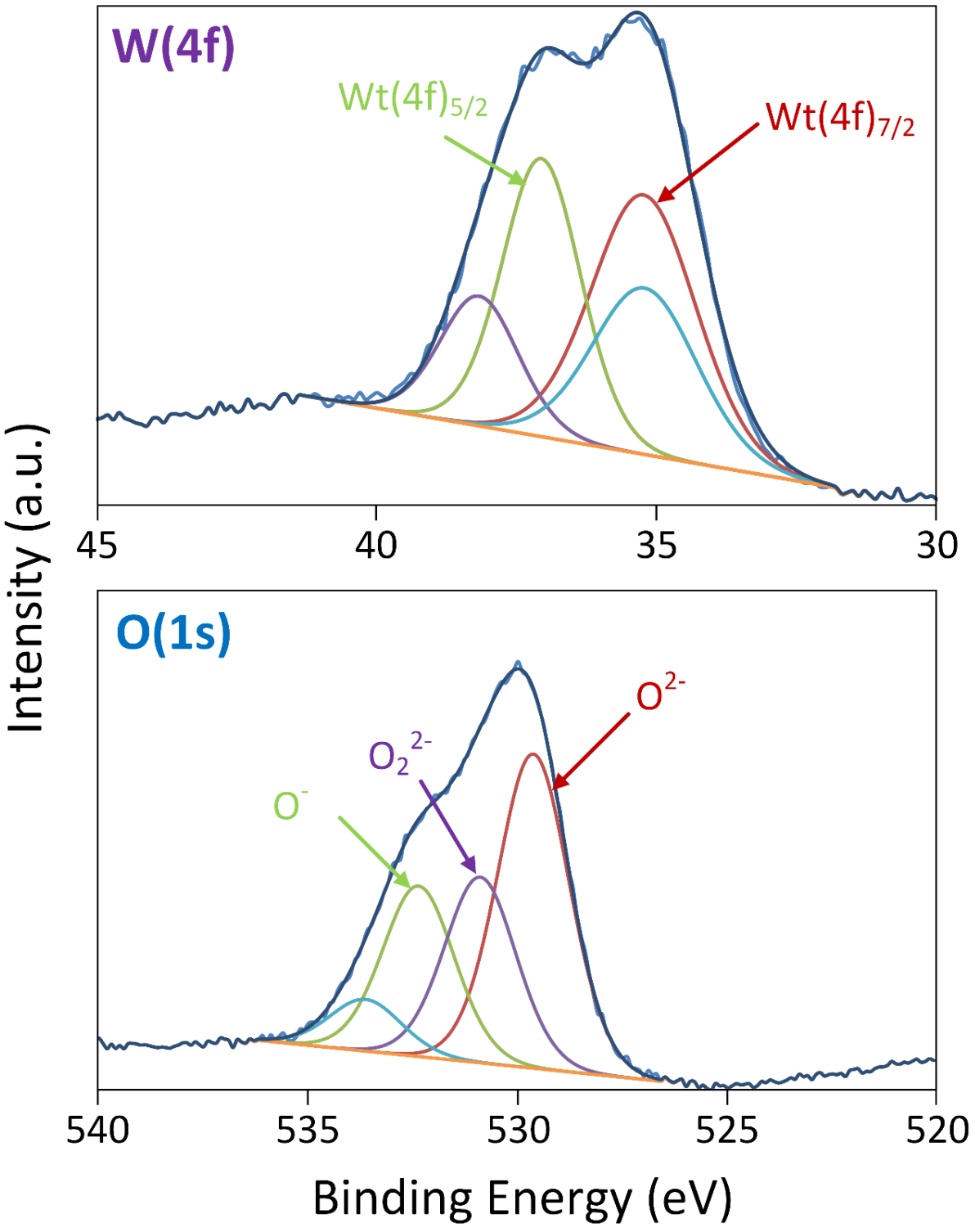

Fig. 9.5: XPS of core level region of O(1s), and W(4f) for WO_3 film.

9.6.4 Electron microscopy (SEM and TEM):

Fig. 9.6 (a), (b) and (c) shows the SEM micrographs of the WO_3 film as deposited on a Si wafer and gold electrode. The Si wafer was the chosen as a substrate because it can be easily fractured which enables the examination of the WO_3 film cross-section. From Fig. 9.6 (a) the film thickness was measured to be 2.5 μm. Fig. 9.6 (b) shows the WO_3 film directly deposited on the gold interdigitated electrode. Uniformly coated gold lines with WO_3 can be seen and it can be inferred that the film formation is conformal in nature. From Fig. 9.6 (c) it can be inferred that the WO_3 film surface is rough and porous with the formation of some agglomerates around 5–10 μm wide. Various open pores could be seen which is advantageous for the diffusion of gases in the bulk of the film [11]. The total WO_3 deposition area on the gold electrodes was 97.5 mm^2. The surface to volume ratio of the WO_3 film was 400 mm^{-1}. The images indicate high quality porous WO_3 films deposited by RSDT without any cracks, voids, dense regions or surface abnormalities. Fig. 9.6 (d) and (e) shows the bright field TEM and HRTEM micrographs of the WO_3 particles. Various oval shaped particles can be seen. From TEM point analysis, a particle size (d_{TEM}) distribution ranging between 20-30 nm was observed. No evidence of sintering of the nanoparticles was found which is attributed to the use of air quench in RSDT. The selected area diffraction patterns (SADP) of WO_3 is shown in the inset of Fig. 9.6 (d). The brightest diffraction ring corresponds to the (002), (220) and (114) planes. Fig. 9.6 (e) shows the HRTEM micrograph of one of the particle with the lattice fringes clearly visible. The lattice fringe spacing corresponds to the (002) plane of γ-WO_3.

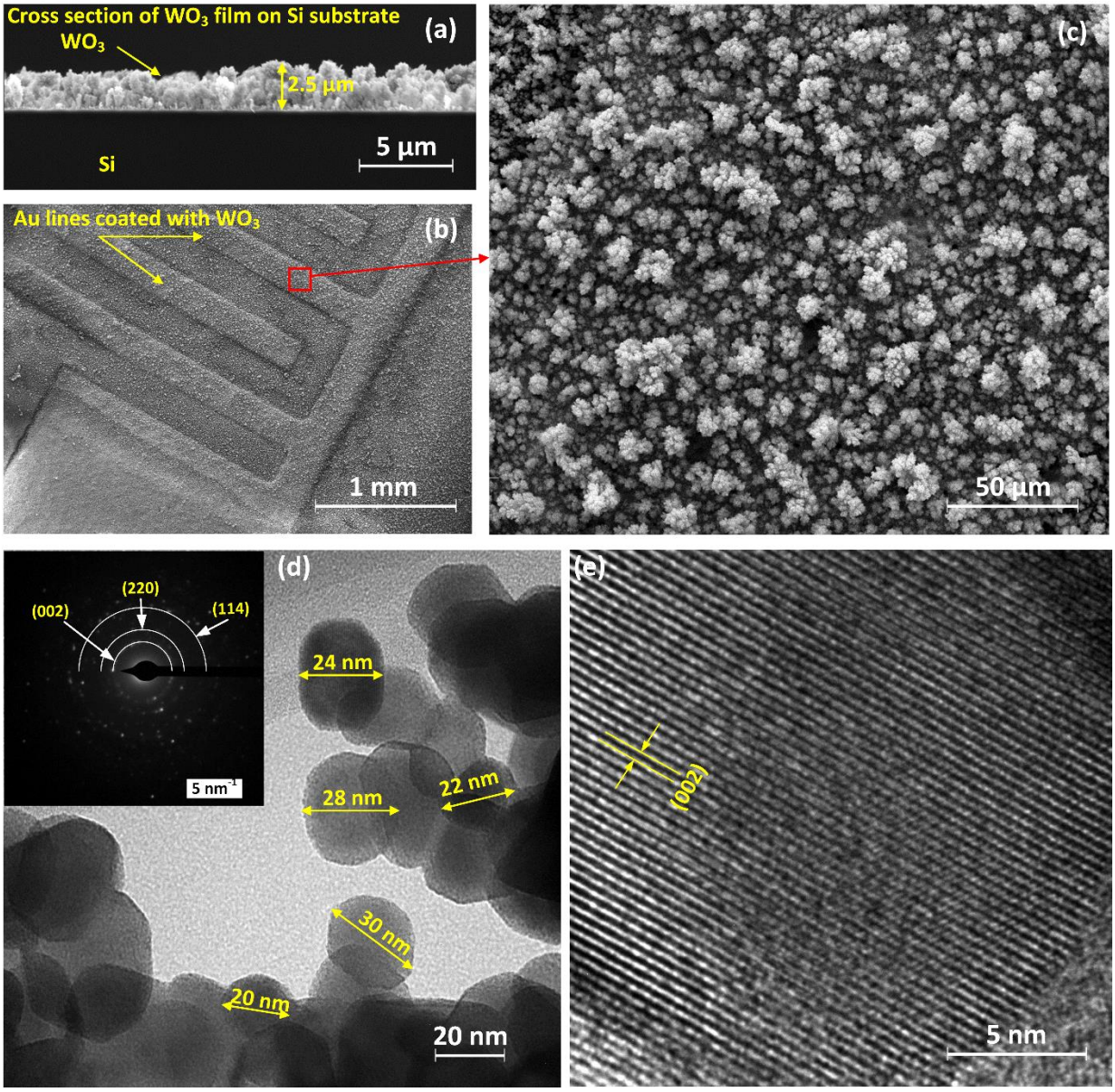

Fig. 9.6: Microscopy images of WO_3 deposited by RSDT: (a) Cross-section of the WO_3 film on a Si substrate showing a thickness of 2.5 µm, (b) WO_3 film deposited on gold interdigitated electrodes, (c) higher magnification view of the WO_3 film on a gold line. Transmission electron microscopy (TEM) images of WO_3 films deposited by RSDT: (d) WO_3 primary particle size in the range 20–30 nm. Selected area diffraction pattern (SADP) is shown in the inset (e) high resolution image of a WO_3 particle showing lattice fringes corresponding to the (002) plane.

9.6.5 BET surface area:

N_2 sorption measurements were performed for the WO_3 powder and the surface area was calculated by the BET method. The BET surface area was calculated as 46 m^2/g. An average particle diameter was estimated using the BET surface area and the density of WO_3 (7.16 g/cc) by making the assumption that the particles are uniformly sized spheres. Particle diameter (d_{BET}) was calculated to be 18 nm.

9.6.6 Response dependence on temperature:

The WO_3 film was tested for NO_2 response in the range of 0.17–5 ppm between 275–350°C to establish the relationship between NO_2 concentration and temperature, and to determine the working temperature at which the best response can be obtained. Fig. 9.7 (a) shows this relationship. It can be seen that as the temperature is increased, the response increases till it reaches the maximum value at 300°C. If the temperature is further increased, the response is reduced. This could be due to increased desorption of NO_2 at high temperature which reduces the concentration of ionosorbed oxygen at the WO_3 surface.

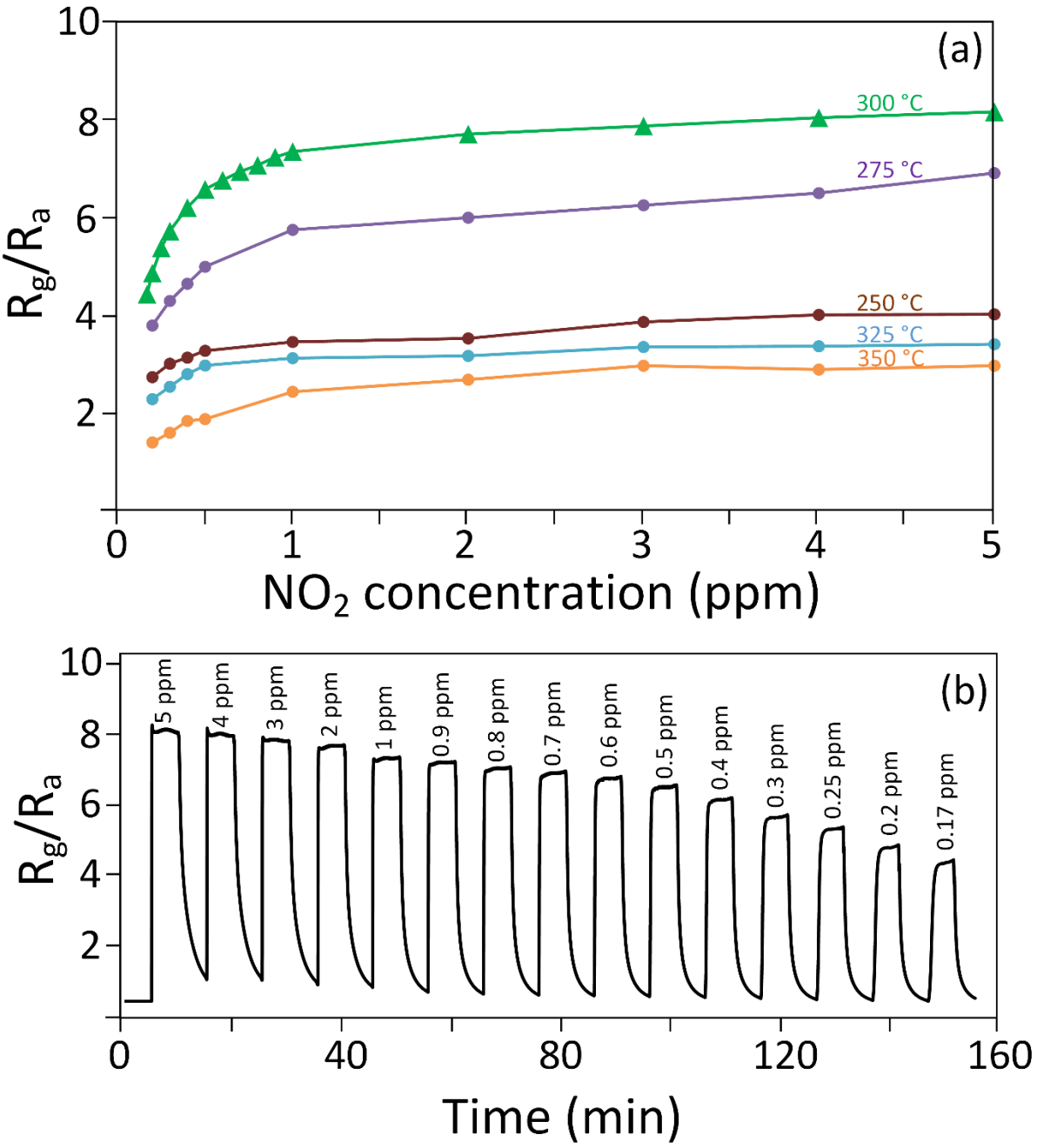

Fig. 9.7: (a) Relation between sensor response (R_a = resistance of WO_3 film in pure air, R_g = resistance of WO_3 film in NO_2) and NO_2 concentration at different temperatures. (b) NO_2 sensing tests conducted at 0.17-5 ppm NO_2 in the air conducted at 300°C at 100%.

9.6.7 Gas sensing results:

Fig. 9.7 (b) shows the normalized response-recovery curve vs time for the NO_2 concentration ranging from 0.17–5 ppm in the air at 300°C and 100% relative humidity. The measurable limit for our tests was 0.17 ppm. The response increases as the concentration of NO_2 is increased. This is because of the increased adsorption of NO_2 molecules at higher NO_2 concentration. The adsorption and desorption of the NO_2 molecules on the WO_3 film takes place simultaneously and is a reversible process. During the response stage, adsorption is higher than desorption and the resistance of the film increases. This is because NO_2 diffuses through the porous WO_3 film and oxidizes the WO_3 surface thereby increasing the ionosorbed oxygen concentration of the film. This causes an increase in electron scattering sites. NO_2 also captures electrons from the conduction band of WO_3 causing the formation of an electron depletion region, triggering an increase in its resistance. It was seen that the sensor response was spontaneous as the gas concentration in the test chamber was changed from pure air to NO_2 in the air. The response time was calculated to be 7.2 s. The sensor stabilized at the maximum value of resistance, very quickly. At this point, the adsorption rate is equal to the desorption rate. Maximum adsorption had taken place at that particular analyte concentration and the WO_3 film was in equilibrium with the NO_2 molecules. Recovery of the sensor started when pure air was switched back to the test chamber. At this point, adsorption was nil and desorption was the only process which was taking place. Presence of two vents in the test chamber expedited the exchange of the gas atmosphere. However it was seen that desorption was still slower than adsorption. A drift can be seen when the resistance of the film is measured in air after exposure to NO_2 at different concentrations. This is caused because of incomplete recovery during the 5 min. of recovery phase.

9.6.8 Stability tests:

Stability tests of the WO_3 films were conducted for 300 h. at 0.5 ppm NO_2 in the air at 300°C and 100% relative humidity which is 10 times lower than the workplace permissible exposure limit (PEL) as per the Occupational Safety and Health Administration (OSHA) specification. The sensor was tested below the PEL because it is desirable for the workplace atmosphere to remain below the PEL of NO_2. 0.5 ppm NO_2 was switched on every 5 min. (response) followed by 5 min. of pure air (recovery). Resistance of the film was measured every 100 ms to record the response and recovery cycle (response + recovery time = 10 min). A total of 2000 response-recovery cycles were recorded. Fig. 9.8 shows the resistance over time for WO_3 film in pure air (R_a) and 0.5 ppm NO_2 in air (R_g) respectively. The resistance is calculated as the moving average for the data collected every 24 h. It can be seen that the sensor is stable till day 6 (~150 h.). From day 6–14 (150–300 h.) the sensor began to degrade possibly due to the growth of the WO_3 nanoparticles. This shows that maximum degradation of the sensor occurred after day 8 (~200 h.) as evident from the fluctuation of resistance.

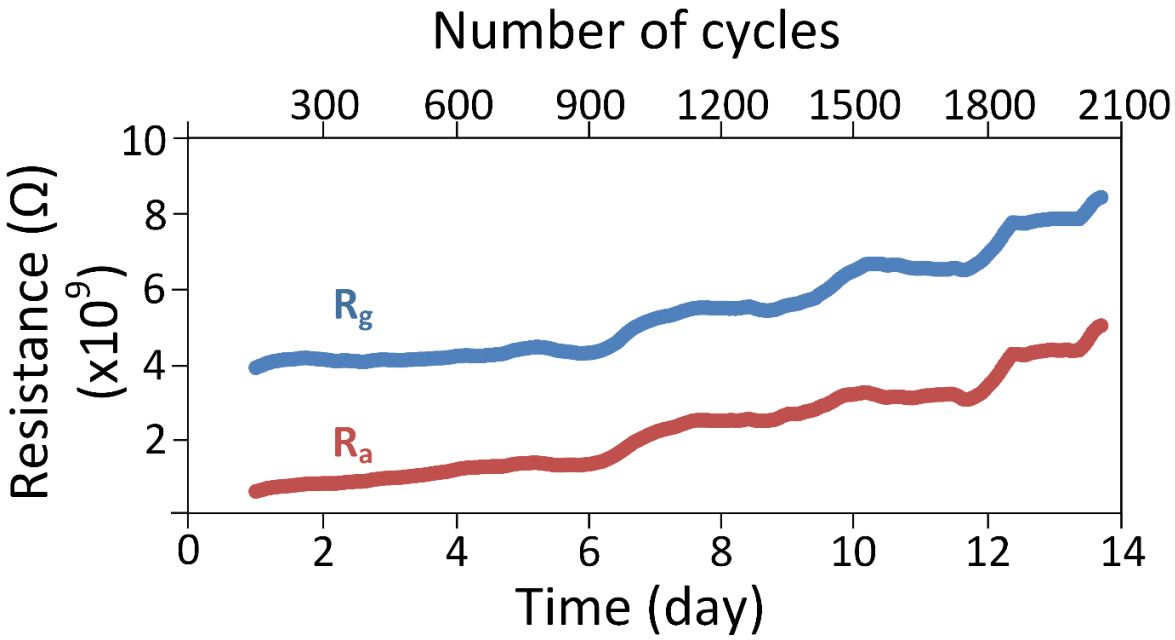

Fig. 9.8: Stability tests for WO_3 sensor conducted for 300 h. at 0.5 ppm NO_2 in the air at 300°C and 100% relative humidity.

9.6.9 Selectivity:

The response of 1 ppm NO_2 was compared with 10 ppm acetone, 100 ppm ethanol, 10–100 ppm H_2 and 10 ppm isoprene at 0.5 ppm NO_2 in air at 300°C and 100% relative humidity. This is shown in Fig. 9.9. It can be seen that the sensor had negligible response for acetone, ethanol and 10 ppm H_2. However the response is significant for 100 ppm H_2 and 10 ppm isoprene. Isoprene and H_2 are some of the major component exhaled from the human breath [12]. Typical values of isoprene in the breath of a healthy human range from 0.012–0.58 ppm [13] while H_2 range from 10–20 ppm [14].

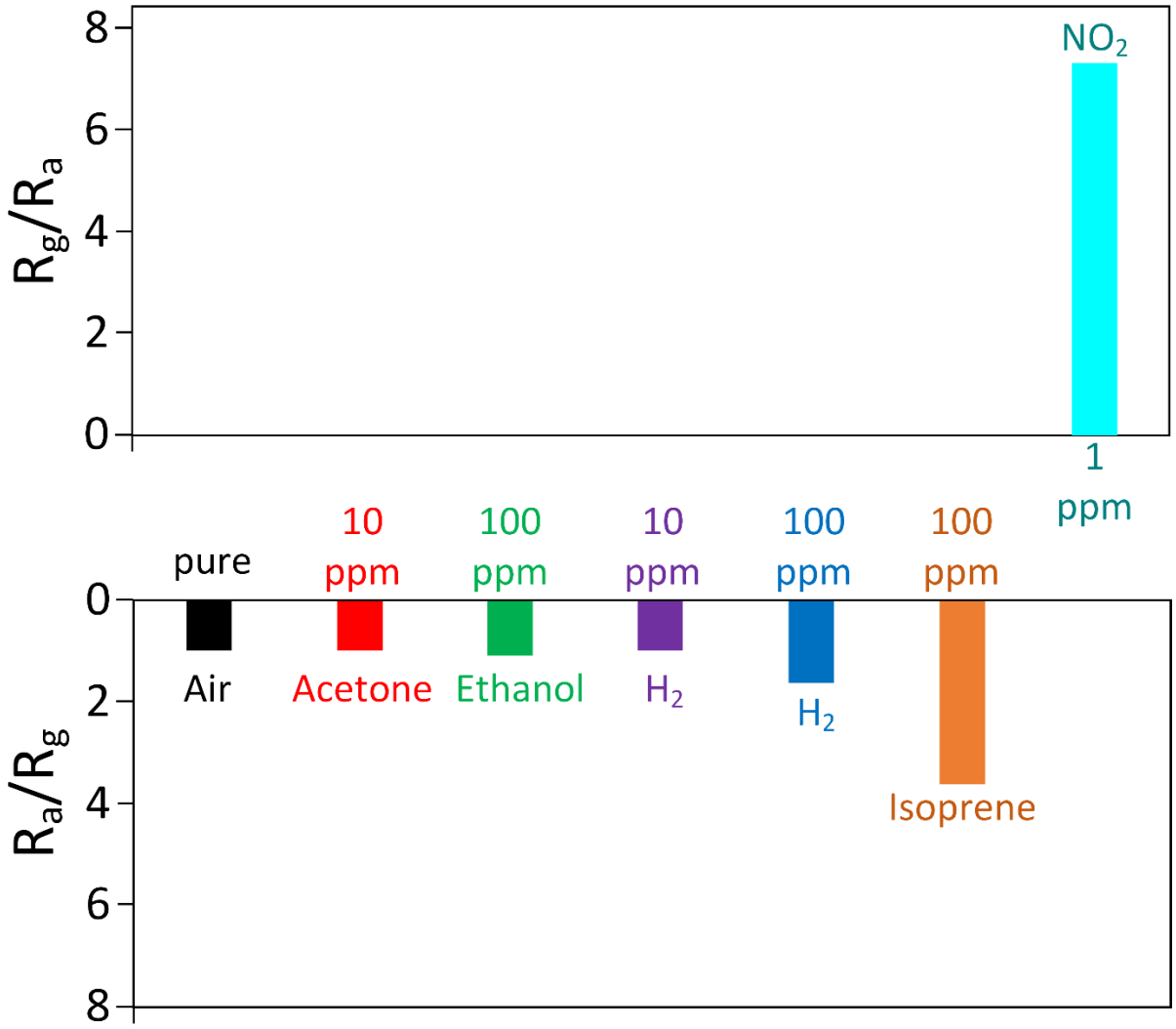

Fig. 9.9: NO_2 response as compared to other reducing analytes.

9.7 Discussions:

On the basis of the characterization and gas sensing results, we can conclude that RSDT can be used for the synthesis of NO_2 sensing films directly on gold interdigitated electrodes. Based on our previous work on WO_3 [2] and a review of the literature, it can be shown that the characteristics of the sensing device that are most important for good performance are: (1) high

porosity of the sensing film, (2) particle size of the sensing film smaller than the Debye length (λ_D), a characteristic of the semiconductor material, which is 25 nm for WO_3, (3) film thickness, (4) absence of impurities in the test atmosphere, (5) test chamber volume, and (6) time required for the exchange of gases in the test chamber. In this discussion we will identify the importance of these factors and show that the gas sensing test data presented in this work adheres to these requirements. We have also shown the comparison between the RSDT synthesized sensors and the sensors synthesized by other techniques as shown in table 9.1.

Table 9.1: Comparison of the WO_3 based NO_2 sensors prepared by different synthesis techniques.

Synthesis method	Limit of detection (ppm)	Working temperature (°C)	Response (R_g/R_a)	Response (used formula)	Response time	Reference
RSDT	**0.17–5**	**300**	**4.44 (0.17 ppm) 6.58 (0.5 ppm) 7.37 (1 ppm) 8.07 (5 ppm)**	**R_g/R_a**	**7.2 s**	**Present study**
Evaporation condensation	1–200	250	2 (1 ppm)	$(R_g-R_a)/R_a$	70 min	[15]
Drop coating	0.5–5	100 and 200	19.2 (1 ppm)	R_g/R_a	15 min	[16]
Glancing angle DC magnetron sputtering	0.1–2	250	4.4 (0.5 ppm)	R_g/R_a	15 min	[17]
Induction-heating oxidation of tungsten	1–8	110	5.5 (1 ppm)	R_g/R_a	10 min	[18]
PECVD	10–100	200	45 (10 ppm)	V_g/V_a (same as R_g/R_a)	50 s	[19]
Spray pyrolysis	10–100	200	1.5 (20 ppm)	$[(R_g-R_a)/R_a]*100$	3 s	[20]

Since the sensing is an adsorption-desorption process, gas diffusion through the film plays a major role in the sensor performance. The sensing film must be porous to effectively allow the diffusion process and extend the reaction between NO_2 and oxygen from the surface to the bulk. By assuming steady state conditions, it can be interpreted that the NO_2 concentration decreases with the film depth which causes the formation of various degree of reactions at different depths of the film. The resistance change data recorded by the electrochemical analyzer averages the resistances by providing the overall resistance change of the film. Ideally it would be beneficial to eliminate this variation. Film porosity, thickness, microstructure, and the electrode pattern are the factors which govern this variation [21, 22]. From the SEM micrographs in Fig. 9.6 (c) it can be seen that the WO_3 film synthesized by RSDT is highly porous and uniform.

Gas sensing response is dependent on the particle size of the sensing film. Smaller particles and increased surface area (higher surface to volume ratio) provides larger number of sites for the surface reaction to occur. At the same time, reducing the particle radius below Λ_{gas}, will converge the electron depletion layer ($2\Lambda_{gas}$) and the electrical conduction will be dominated by the presence of adsorbed NO_2^-. Λ_{gas} depends on the Debye length (λ_D) of the material which is 25 nm for WO_3. Sharma et al. has described the relationship between gas sensitivity and particle size with respect to the Debye length (λ_D). When the particle size is smaller than λ_D, the ionosorbed oxygen will extract all the electrons from the WO_3 particle causing an increase in film resistance [23]. It was also shown by Tamaki et al. that the sensitivity of 10 ppm NO_2 towards WO_3 particles were three fold higher when the particle size was smaller than 25 nm as compared to particles larger than 33 nm [1]. In this work, the WO_3 particle size were in the range 20–30 nm as determined by the TEM point analysis in Fig. 9.6 (d). BET surface area measurements revealed the average particle diameter (d_{BET}) to be 18 nm.

Working temperature is an important factor responsible for the performance of the sensor since sensing is an adsorption desorption process which is also influenced by kinetics [24]. At low working temperature, the activation barrier for the generation of ionosorbed oxygen is higher, while at high temperature, desorption of NO_2 exceeds adsorption resulting in lower response. Hence the optimum temperature at with balance kinetics and desorption is essential. In this work, the highest response was obtained at 300°C.

Selectivity with other gases is a major concern for a sensor to be commercially viable, which can lead to false alarm or incorrect gas concentration determination. In this study, it was found that the WO_3 film was responsive towards 10 ppm isoprene and 100 ppm H_2, while the response towards 10 ppm acetone, 100 ppm ethanol and 10 ppm H_2 was negligible. All the tests were performed in 100% relative humidity and sensitivity towards H_2O was not observed. There are various methods suggested in the literature to discriminate the interference towards these gases. The most common approach is to utilize a sensor array described by Albert et al. with various sensor electrodes to filter out the response from the interfering analytes [25]. The other method is to use filters upstream of the electrode to filter out the gases. One such activated charcoal filter is used by Figaro Inc. in their commercial CO sensor - TGS5042. Since the sensor response is a diffusion driven process, it can be easily applied to improve the selectivity. Porous layers in which gases may have different diffusion coefficient can be directly deposited on the sensing layer. These layers acts as molecular sieves to reject the interfering gases. Description of these porous layer filters have been provided in details in this reference [26]. Pre-calibration of the sensor for known cross contaminants has also been suggested [27].

The long recovery time and the drift of the metal oxides based sensors have been long recognized and various suggestions to counter this limitation have been proposed. From the

gas sensing tests in Fig. 9.7 (b), a drift can be seen when the resistance of the film is measured in the air after exposure to NO_2 at different concentrations. This is caused because of incomplete recovery during the 5 min. of recovery phase. As a gas molecule is chemically adsorbed on the surface of WO_3, it is in thermal equilibrium and resides at the bottom of the potential well (minimum potential energy). In order to desorb from the surface, the only driving force it experiences is the diffusion caused by the change in the concentration of gases in the test chamber on switching to pure air. However this energy is not sufficient and causes a long delay to achieve complete desorption. Further thermal or electrical energy is required to expedite this adsorption process. Different ways are suggested in literature to eliminate sensor drift. These include, using high-speed gas-switching system and smaller volume test chamber for enabling quicker gas exchange [28] pre exposing the sensing film to the analyte for a set period of time [29], use of mathematical function and modelling [30] to pre-estimate the steady state conditions and remove the time lag [31], use of multiple sensing electrodes in different test chamber to alter between response and recovery [32], use of neural network algorithm for the sensor to "self-learn" [33] use of strong negative field to electro-desorb the residual analyte molecules to "refresh" the sensor [34] and by illuminating the sensor with ultra-violet (UV) light [35]. Here we have used a two vent test chamber to expedite the atmosphere change. The test chamber volume was 85 cc. We are currently developing a prototype sensing device with a volume of 0.5 cc which will further eliminate this issue.

9.8 Conclusions:

In this study we have evaluated RSDT as a direct deposition technique for the synthesis of γ-WO_3 film for ultra-low NO_2 sensing. Air quenching was used to optimize the particle size and film morphology to tailor the film towards superior NO_2 sensing performance. Here our

main objective was to correlate the influence of the synthesis process, and the resultant structural properties of the γ-WO_3 film with the NO_2 gas sensing performance. We have highlighted these properties and their influence on the NO_2 sensing which will provide a platform for developing better sensors with improved performance compared to the currently used sensors. The reasons for the high response can be attributed to a number of factors, such particle size, porosity and pore size, and film thickness, all precisely controlled by the RSDT. Following conclusions can be made from this work:

1. RSDT synthesized WO_3 film based NO_2 sensor was responsive in the 0.17–5 ppm range, when tested at 300°C.

2. Response time was 7.2 s and recovery time was greater than 5 min. The response time was better than the WO_3 sensors synthesized by the traditional wet chemistry processes from literature.

3. The response was highest at the working temperature of 300°C.

4. The NO_2 sensors gave a steady response till 150 h. of continuous performance and started to degrade after 200 h. possibly due to increase in particle size.

5. Interference was negligible with 10 ppm acetone, 100 ppm ethanol, 10 ppm H_2 and humidity; however, it was significant with 10 ppm isoprene and 100 ppm H_2.

6. Response and recovery of the sensor is caused by adsorption and desorption respectively. Hence recovery time can be improved by expediting the desorption step.

7. WO_3 particle size of <25 nm attributes to better charge transfer which translates to superior NO_2 sensitivity.

9.9 Acknowledgements:

Financial support for the research in this chapter was provided from National Science Foundation (award number CMMI-1265893). Dr. Justin Roller at FEI Company is acknowledged for the HRTEM micrograph. R.J. acknowledges the 2015 General Electric (GE) graduate fellowship for innovation.

9.10 References:

[1] J. Tamaki, Z. Zhang, K. Fujimori, M. Akiyama, T. Harada, N. Miura, N. Yamazoe, Grain-Size Effects in Tungsten Oxide-Based Sensor for Nitrogen Oxides, Journal of Electroceramic Society. 141 (8) (1994) 2207-2210.

[2] R. Jain, Y. Wang, R. Maric, Tuning of WO_3 Phase Transformation and Structural Modification by Reactive Spray Deposition Technology, Journal of Nanotechnology and Smart Materials. 1 (2014) 1-7.

[3] R. Jain, R. Maric, Synthesis of nano-Pt onto ceria support as catalyst for water-gas shift reaction by Reactive Spray Deposition Technology, Applied Catalysis A: General. 475 (2014) 461-468.

[4] J.M. Roller, J. Arellano-Jiménez, R. Jain, H. Yu, R. Maric, C.B. Carter, Processing, Activity and Microstructure of Oxygen Evolution Anodes Prepared by a Dry and Direct Deposition Technique, ECS Transactions. 45 (21) (2013) 97-106.

[5] J. Roller, J. Renner, H. Yu, C. Capuano, T. Kwak, Y. Wang, C.B. Carter, K. Ayers, W.E. Mustain, R. Maric, Flame-based processing as a practical approach for manufacturing hydrogen evolution electrodes, Journal of Power Sources. 271 (0) (2014) 366-376.

[6] C. Bittencourt, E. Llobet, P. Ivanov, X. Vilanova, X. Correig, M.A.P. Silva, L.A.O. Nunes, J.J. Pireaux, Ag induced modifications on WO_3 films studied by AFM, Raman and x-ray photoelectron spectroscopy, Journal of Physics D-Applied Physics. 37 (24) (2004) 3383-3391.

[7] B. Mahut, C. Delacourt, F. Zerah-Lancner, J. De Blic, A. Harf, C. Delclaux, Increase in alveolar nitric oxide in the presence of symptoms in childhood asthma, Chest. 125 (3) (2004) 1012-1018.

[8] M. Arai, S. Hayashi, K. Yamamoto, S.S. Kim, Raman Studies of Phase-Transitions in Gas-Evaporated WO_3 Microcrystals, Solid State Communications. 75 (7) (1990) 613-616.

[9] C.D. Wanger, W.M. Riggs, L.E. Davis, J.F. Moulder, G.E. Muilenberg, Handbook of X-Ray Photoelectron Spectroscopy, Physical Electronics Division, Perkin-Elmer Corp, Eden Prairie, Minnesota, USA, 1979.

[10] Measurement Services Division of the National Institute of Standards and Technology (NIST) Material Measurement Laboratory (MML), Version 4.1 (National Institute of Standards and Technology, Gaithersburg, 2012), 2015 (2012).

[11] L. Filipovic, S. Selberherr, Performance and Stress Analysis of Metal Oxide Films for CMOS-Integrated Gas Sensors, Sensors. 15 (4) (2015) 7206-7227.

[12] M. Phillips, J. Herrera, S. Krishnan, M. Zain, J. Greenberg, R.N. Cataneo, Variation in volatile organic compounds in the breath of normal humans, Journal of Chromatography B: Biomedical Sciences and Applications. 729 (1–2) (1999) 75-88.

[13] J.D. Fenske, S.E. Paulson, Human breath emissions of VOCs, Journal of the Air & Waste Management Association (1995). 49 (5) (1999) 594-598.

[14] U.C. Ghoshal, How to Interpret Hydrogen Breath Tests, Journal of Neurogastroenterology and Motility. 17 (3) (2011) 312-317.

[15] T. Siciliano, A. Tepore, G. Micocci, A. Serra, D. Manno, E. Filippo, WO_3 gas sensors prepared by thermal oxidization of tungsten, Sensors and Actuators B: Chemical. 133 (1) (2008) 321-326.

[16] T. Akamatsu, T. Itoh, N. Izu, W. Shin, NO and NO_2 Sensing Properties of WO_3 and Co_3O_4 Based Gas Sensors, Sensors (Basel, Switzerland). 13 (9) (2013) 12467-12481.

[17] M. Horprathum, K. Limwichean, A. Wisitsoraat, P. Eiamchai, K. Aiempanakit, P. Limnonthakul, N. Nuntawong, V. Pattantsetakul, A. Tuantranont, P. Chindaudom, NO_2-sensing properties of WO_3 nanorods prepared by glancing angle DC magnetron sputtering, Sensors and Actuators B: Chemical. 176 (2013) 685-691.

[18] W. Gao, Y. Ling, X. Liu, J. Sun, Simple point contact WO_3 sensor for NO_2 sensing and relevant impedance analysis, International Journal of Minerals, Metallurgy and Materials. 19 (12) (2012) 1142-1148.

[19] M. Tong, G. Dai, Y. Wu, X. He, D. Gao, WO_3 thin film prepared by PECVD technique and its gas sensing properties to NO_2, Journal of Materials Science. 36 (10) (2001) 2535-2538.

[20] V.V. Ganbavle, S.V. Mohite, G.L. Agawane, J.H. Kim, K.Y. Rajpure, Nitrogen dioxide sensing properties of sprayed tungsten oxide thin film sensor: Effect of film thickness, Journal of Colloid and Interface Science. 451 (2015) 245-254.

[21] E. Comini, G. Faglia, G. Sberveglieri, Solid State Gas Sensing, 1st ed., Springer, US, 2009.

[22] N. Barsan, D. Koziej, U. Weimar, Metal oxide-based gas sensor research: How to? Sensors and Actuators B: Chemical. 121 (1) (2007) 18-35.

[23] S. Sharma, M. Madou, A new approach to gas sensing with nanotechnology, Philosophical Transactions of the Royal Society A. 370 (1967) (2012) 2448-2473.

[24] A. Kolmakov, D.O. Klenov, Y. Lilach, S. Stemmer, M. Moskovits, Enhanced Gas Sensing by Individual SnO_2 Nanowires and Nanobelts Functionalized with Pd Catalyst Particles, Nano Letters. 5 (4) (2005) 667-673.

[25] K.J. Albert, N.S. Lewis, C.L. Schauer, G.A. Sotzing, S.E. Stitzel, T.P. Vaid, D.R. Walt, Cross-reactive chemical sensor arrays, Chemical reviews. 100 (7) (2000) 2595-2626.

[26] G. Korotcenkov, Filters in Gas Sensors, in: R.A. Potyrailo (Ed.), Handbook of Gas Sensor Materials, 1st ed., Springer, New York, 2013, pp. 293-303.

[27] Tsuguyoshi Toyooka and Satoshi Hiyama and,Yuki Yamada, A prototype portable breath acetone analyzer for monitoring fat loss, Journal of Breath Research. 7 (3) (2013) 036005.

[28] T. Kida, T. Kuroiwa, M. Yuasa, K. Shimanoe, N. Yamazoe, Study on the response and recovery properties of semiconductor gas sensors using a high-speed gas-switching system, Sensors and Actuators B: Chemical. 134 (2) (2008) 928-933.

[29] Y. Liu, Y. Lei, Pt-CeO_2 nanofibers based high-frequency impedancemetric gas sensor for selective CO and C_3H_8 detection in high-temperature harsh environment, Sensors and Actuators B: Chemical. 188 (2013) 1141-1147.

[30] M. Holmberg, F. Winquist, I. Lundström, F. Davide, C. DiNatale, A. D'Amico, Drift counteraction for an electronic nose, Sensors and Actuators B: Chemical. 36 (1–3) (1996) 528-535.

[31] J.G. Monroy, J. González-Jiménez, J.L. Blanco, Overcoming the Slow Recovery of MO_X Gas Sensors through a System Modeling Approach, Sensors (Basel, Switzerland). 12 (10) (2012) 13664-13680.

[32] J. Gonzalez-Jimenez, J.G. Monroy, J.L. Blanco, The Multi-Chamber Electronic Nose--An Improved Olfaction Sensor for Mobile Robotics, Sensors (Basel, Switzerland). 11 (6) (2011) 6145-6164.

[33] M. Zuppa, C. Distante, P. Siciliano, K.C. Persaud, Drift counteraction with multiple self-organising maps for an electronic nose, Sensors and Actuators B: Chemical. 98 (2–3) (2004) 305-317.

[34] Z. Fan, J.G. Lu, Gate-refreshable nanowire chemical sensors, Applied Physics Letters. 86 (12) (2005) 123510.

[35] C. Li, D. Zhang, X. Liu, S. Han, T. Tang, J. Han, C. Zhou, In_2O_3 nanowires as chemical sensors, Applied Physics Letters. 82 (10) (2003) 1613-1615.

CHAPTER 10:

Ultra-low acetone detection by epsilon WO_3 synthesized by Reactive Spray Deposition Technology

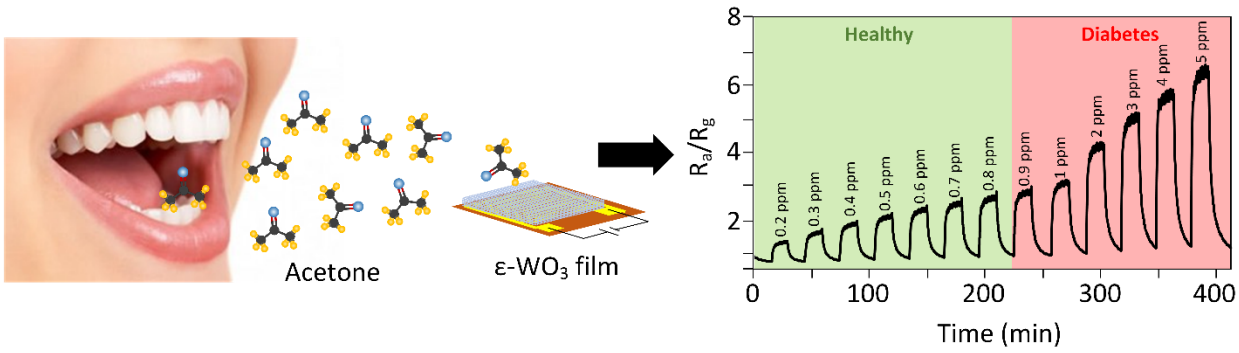

10.1 Highlights:

1. Monoclinic epsilon WO_3 thin film was synthesized by a single step flame based process.

2. The WO_3 film was tested with 0.2–5 ppm acetone in air at 400°C.

3. The structural properties of the WO_3 was correlated with the gas sensing data.

4. The WO_3 film showed quicker response time than similar films synthesized by traditional processes.

5. Test and stability data shows that performance improvements that approach 100% efficiency can be made.

10.2 Abstract:

A metastable monoclinic epsilon tungsten oxide (WO_3) film based acetone sensor was developed by the flame based process called Reactive Spray Deposition Technology (RSDT) depositing directly on gold interdigitated electrodes. The sensitivity of this acetone sensor was measured at the parts per million (ppm) level, (0.2–5 ppm in air) at 400°C. The sensors showed a relatively fast response time (~7 s) to acetone vapor. The stability of the sensor was evaluated for 450 h. in 0.5 ppm NO_2 in air (2700 response-recovery cycles). The sensor was stable up to 10 days (~250 h.) of continuous operation and degraded between 250 to 450 h. The selectivity of the sensor was tested in 90% relative humidity, 10 ppm H_2, 8 ppm CO, and 0.2 ppm ethanol. The morphology and surface properties of the WO_3 film were investigated with XRD, Raman spectroscopy, SEM, and TEM. In addition, operando XRD experiments were performed at the condition of the acetone tests to confirm the stability of the structure. We have also compared the test data of WO_3 based acetone sensors prepared by RSDT with the results reported in the literature.

10.3 Keywords:

Acetone sensor; diabetes; reactive spray deposition technology; flame combustion synthesis; tungsten oxide

10.4 Introduction:

In this chapter we have proposed an open atmosphere flame based process also known as Reactive Spray Deposition Technology (RSDT) for the synthesis of ε-WO_3 films directly on gold interdigitated electrodes. The RSDT process allows the flexibility to create ε-WO_3 with control of the particle size, porosity and thickness of the film. The sensitivity of porous WO_3 increases when the particle size is below its Debye length (λ_D) which is 25 nm [1]. In chapter 8, it had been shown that RSDT can be employed for the synthesis of γ-WO_3 films with precise control of particle size, film morphology, and crystal structure [2]. In this study, we have employed RSDT for the deposition of nano crystalline WO_3 thin films directly on a gold interdigitated electrode which is to be assembled into an acetone sensing device. Here we provide a brief description of the synthesis, fabrication and testing procedure of the acetone sensor. The microstructure of the tungsten oxide films, and the effect of the film structure, grain size, and the sensor response to the ppm level concentration of acetone will be described. Acetone response behavior on the tungsten oxide surface at various operating temperatures will also be presented. The properties of the WO_3 film was investigated by X-ray diffraction (XRD), Raman spectroscopy, transmission electron microscopy (HRTEM), and scanning electron microscopy (SEM). The structure of the WO_3 film was also probed by operando XRD studies at the condition of testing. The sensor film was ultimately performance tested for acetone sensitivity in the 0.17-5 ppm range at 400°C. The sensor was further tested for stability for 500 h. in 0.5 ppm acetone in air which is same as the breath

acetone concentration of a healthy individual [3,4]. The sensor was tested at this concentration because it is desirable that the breath acetone concentration remain below 0.5 ppm which is the diabetes threshold limit. In order to check the selectivity, the sensor was also tested for humidity, 10 ppm H_2, 0.2 ppm ethanol, and 8 ppm CO. We have also compared the test data of WO_3 based acetone sensors prepared by RSDT with the results reported in the literature.

10.5 Experimental:

10.5.1 Synthesis of WO_3:

An explanation of the RSDT equipment and process has been described in detail by Jain and Roller et al. [5, 6]. Tungsten hexacarbonyl [$W(CO)_6$] was obtained from Sigma Aldrich (Catalogue #AC221040100) and was dissolved in a tetrahydrofuran (THF) (enthalpy of combustion: 2501 kJ/mol) (Fisher Scientific # SHBD3901V). The precursor was chosen based on its low decomposition temperature of 170°C. Sulfur free liquefied propane (enthalpy of combustion: 2202 kJ/mol) (Airgas catalogue # PRCP350S) was added to the above to form a precursor solution resulting in a final concentration of 4.9 mmol/L $W(CO)_6$, and 18 wt% propane. THF has a dual role of an inexpensive solvent and fuel for the combustion of the [$W(CO)_6$]. Propane helps in atomization by increasing the pressure drop between the needle and the point of exit of the solution, thereby splitting the solution in tiny droplets approximately 15 μm in diameter as measured by Malvern Instrument's Spraytec laser diffraction system [7]. The increase in surface area of the overall droplets helps in efficient combustion of the precursor. The precursor solution was filled in a syringe pump (Teledyne Isco 500D, Lincoln NE) and directed at 4 mL/min to a series of stainless steel tubes of varying diameters: 0.025 cm inner diameter 316 stainless steel tube which is brazed to a capillary of 100 μm inner diameter (Vita Needle company). An Omega k-type thermocouple was placed at the junction of the tube and capillary, the temperature of which

is maintained at 170°C by means of an induction coil wrapped upstream of the flow of precursor solution based on our previous design of experiments to create nanometer sized Pt particles of 1–3 nm [8]. This caused the temperature of the precursor solution at the exit point to be 50–60°C and a pressure drop of 90–110 psi. The combined effect of liquefied propane, temperature, and reduction of diameter of the tube, causes the solution to shift into the supercritical regime and formation of sub-micron size droplets [7]. Six methane-oxygen flamelets (methane at 0.42 L/min and oxygen at 0.55 L/min) surround the capillary end, and ignites the combustible precursor mist. The precursor solution was atomized by oxygen (5 L/min). A circular air quench ring (Exair, Super Air Wipe®) with a compressed air flow rate of 76.8 L/min was positioned at 10 cm from the combustion nozzle. The distance between the combustion nozzle and the air quench is considered the reaction zone and the length of the reaction zone is proportional to the residence time of the nano-particles in that zone. Adjusting the length of the reaction zone and the flow rate of compressed air gives unique conditions to obtain different phases and crystalline structures of the material [9]. This also enables "nano quenching" thereby limiting the particle size growth in the flame. A gold interdigitated electrode on alumina base (Electronic design center-Case Western Reserve University item#102) was used as a substrate. This thick film printed electrode consists of interdigitated gold deposits on a 0.6 mm thick alumina substrate. The dimensions of the alumina base is 15 mm by 15 mm. The gold thick film screen printed electrode digits are 250 μm wide with 250 μm spacing between them. The gold digits are connected with a pair of gold bonding pads which allow wires to be threaded through them as an aid for electrical connection. Prior to WO_3 deposition, the electrode was cleaned with acetone, methanol and deionized water, in order and dried in an air oven operating at 80°C for 1 h. The substrate was mounted on a stainless steel block and, placed on an x-y-z platform. This substrate platform can be moved along a serpentine path in

front of the flame to deposit on a larger area if required, however because of the small area of deposition, this motion was not required. The total deposition area was only 2.25 cm^2. Post deposition, the sample was annealed in the air at 500°C for 5 h. in an oven to stabilize the WO_3 film. In a separate experiment, blank silicon plates (Nova Wafers, catalogue # 8289) were used as substrates, only for the evaluation of the film thickness since they can be easily fractured and can be mounted at 90° on an aluminum SEM stub. The characterization and gas sensing measurements were performed on the post annealed samples.

10.5.1.1 Role of air quench:

As discussed previously, quenching plays a very important role in obtaining the metastable monoclinic ε phase of WO_3. This was achieved by using the air quench in RSDT. By using air quench, the WO_3 particles were cooled from 500°C to 30°C in 7 ms. With this rapid cooling, the WO_3 particles did not get enough time to freeze in their stable state, and it also caused the formation of stresses in the WO_3 structure. Detailed description of the air quench has been provided in chapter 1 which will be briefly revisited here. The air quench is a circular ring with an internal annular chamber. Compressed air at room temperature enters two diametrically opposite nozzles and is directed into that chamber. The chamber has a narrow opening through which the air adopts the coanda profile and flows along the angled surface of the air quench. This also creates a low pressure region behind the air quench causing the entrainment of the surrounding air into the primary air stream. A 360° cone of cold air is formed which cools the nanoparticles instantly and prevents growth, agglomeration, and sintering, thereby keeping the particle size small and increasing the active surface area. The distance between the combustion nozzle and the air quench is considered the reaction zone and the length of the reaction zone is proportional to the residence time of the nanoparticles in that zone.

Adjusting the length of the reaction zone and the flow rate of compressed air gives unique conditions to obtain an assortment of phases and structures of WO_3. In this study the reaction zone was set at 10 cm. A schematic of the air quench is shown in Fig. 10.1.

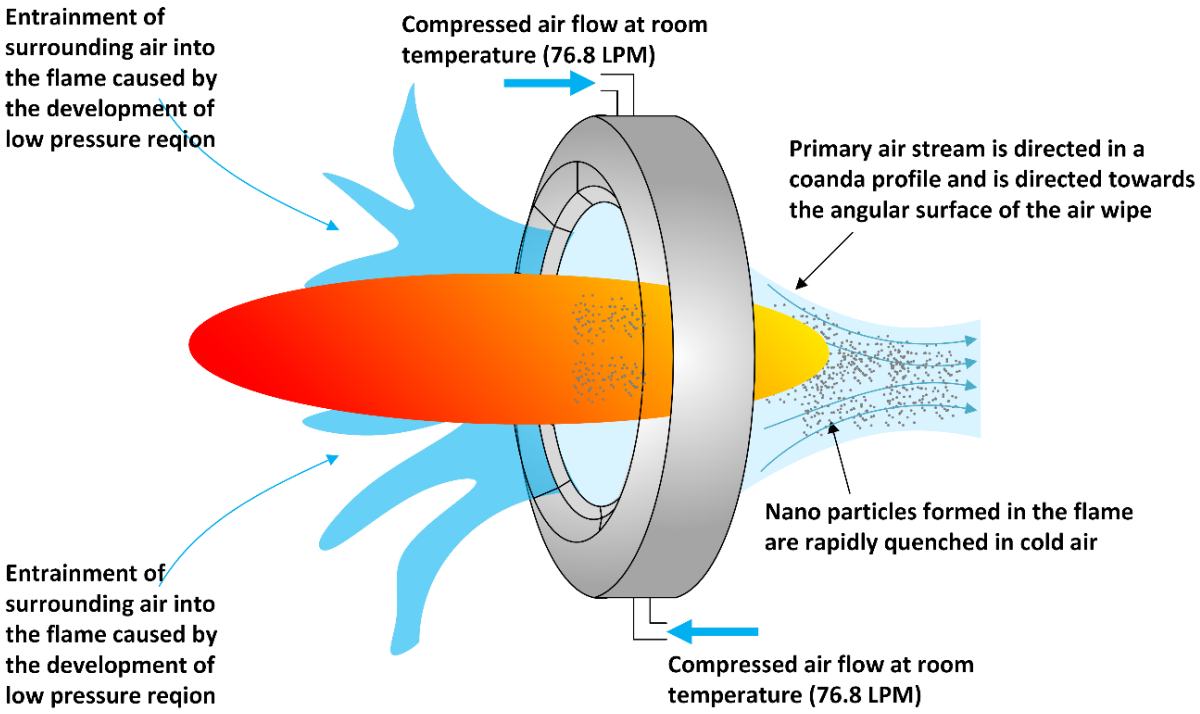

Fig. 10.1: Schematic of the air quench in RSDT.

10.5.2 Characterization:

XRD patterns of WO_3 films directly deposited on gold interdigitated electrodes were recorded in the air at 25°C on a Bruker D8 advanced powder diffractometer using CuKα radiation. The scans were taken in the 2θ range of 20–55° with a step size of 0.02° and time per step of 5 s. Operando XRD was also performed at the conditions of the acetone tests, from room temperature till 500°C both in air and air/acetone mixture to evaluate the phase transformation during the sensing process. For this purpose, a fresh sample was prepared with

the identical experimental conditions of the test sample. The sample was placed in a high temperature Anton Paar HTK1200 heating stage in the XRD. Heating rate of 5°C /min was used. Raman spectra were obtained in air at 25°C in the spectral range between 100 and 1200 cm^{-1} with a Renishaw Ramascope micro-Raman spectrometer fitted with a reflected light microscope using a 50 mW laser (514.5 nm) and exposure time of 10 s. Laser power delivered to the sample was set at 20% (10 mW) to avoid sample damage. Instrument alignment was optimized using a 521 cm^{-1} signal of a silicon wafer. Raman measurements for WO_3 is well known to provide structural and phase information of WO_3 material [10, 11]. The surface area of WO_3 particles was calculated by the Brunauer-Emmett-Teller (BET) method using N_2 sorption experiments on a Micromeritics ASAP 2020 BET system. Samples were degassed for 12 h. prior to N_2 sorption measurements. For obtaining the samples for BET, a separate experiment was performed in which, WO_3 nanoparticles powder was directly collected on a stainless steel substrate holder. The deposit was scrapped off using a plastic spatula and analyzed for N_2 sorption experiments. SEM micrographs were collected on an FEI ESEM Quanta 250 with a field emission gun at 5 kV accelerating voltage and 8 mm working distance. For determining the cross-sectional thickness of the film, the silicon substrate with WO_3 film was fractured, and mounted on a 90° aluminum stub. TEM micrographs and selected area diffraction pattern (SADP) of WO_3 particles were obtained on a 120 kV FEI Tecnai T12 S/TEM with a LaB_6 source. 300 mesh Cu grids coated with holey/thin carbon films (Pacific Grid Tech Cu-300HD) were used. A small portion of the film was scraped off from the gold interdigitated electrodes and was sonicated with ethanol. Few drops of the resulting solution were dropped on the grids and air dried before they were placed in the ultra-high vacuum (UHV) chamber of the TEM.

10.5.3 Gas sensing test:

Gas sensing tests were performed in a dynamic flow system, implemented in the laboratory as shown in Fig. 10.2. Prior to gas sensing, the electrode was annealed in the air at 500°C for 5 h. in an electric oven to stabilize the WO_3 film. A WO_3 coated gold interdigitated electrode was introduced in a quartz cylindrical test chamber (10 cm length, 3.2 cm inner diameter, volume of 80 cc) which was wrapped by a high temperature nozzle band heater (McMaster Carr item# 3594K981). The ends of the test chamber were sealed by stainless steel fittings. Several ports were introduced in the test chamber for (1) gas inlet, (2) two gas outlets, and (3) standard k-type thermocouple to monitor temperature. Gas flow to the furnace was controlled by Environics Series 4040 Computerized Gas Dilution System. Presence of two gas outlets in the test chamber allows a precisely controlled change in the atmosphere of the test chamber, as soon as the supply gas concentration is changed from acetone to pure air and vice versa. Dry synthetic air (Airgas #AI UZ300) was used as a diluent gas and 10 ppm acetone in air (Airgas # X02AI99C15A38K3) was used for adjusting the acetone concentration. Flow rate of 1.5 L/min was maintained in the test chamber, because it is same as the human expiratory flow rate [12] and it is expected that the results of this study could lead us to develop a sensor for human breath analysis. For the two probe amperiometric measurements, the ε-WO_3 coated electrode was connected with two Pt wires (99.9% metals basis) (0.127 mm diameter) (Alfa Aesar#F20X038) and connected to a CHI instrument's electrochemical analyzer (CHI6116E). Current (I) was measured as a function of time and gas flow concentration at a constant 1 V DC power supply. Resistance (R) was calculated by applying Ohm's law (R = V/I). The data was collected every 100 ms.

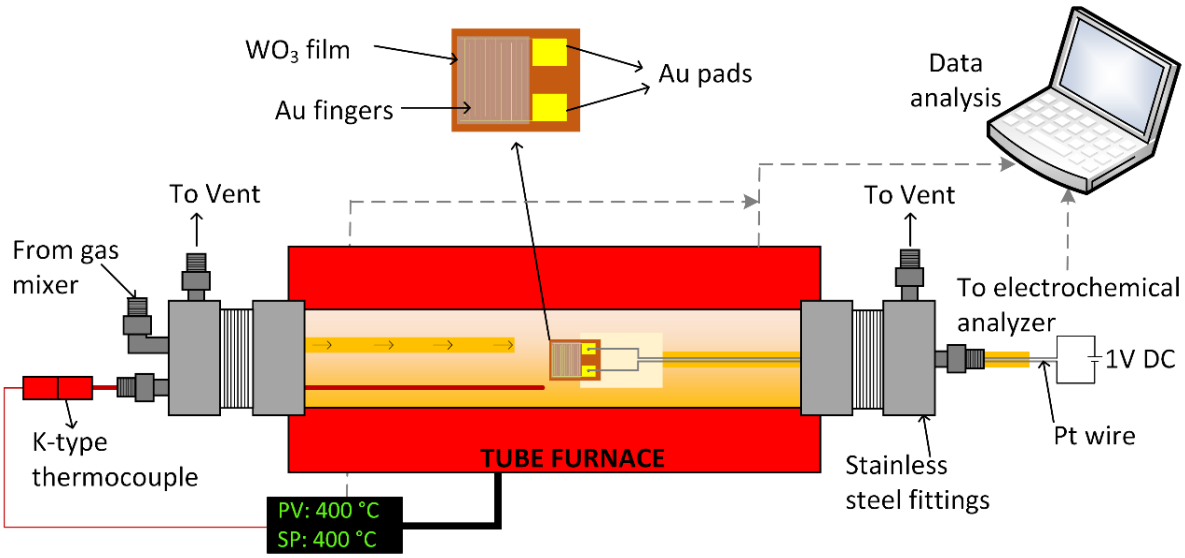

Fig. 10.2: Schematic of the gas sensing test setup.

10.6 Results:

10.6.1 X-ray diffraction (XRD):

Fig. 10.3 shows the XRD pattern of the WO_3 film coated on gold interdigitated electrodes pre acetone test and after 450 h stability test. The characteristic peaks of ε-WO_3 (ICDD# 01-087-2386), and γ-WO_3 (ICDD#01-043-1035) are shown. The characteristic main peaks for ε-WO_3 were seen at the 2θ value of 23.1°, 24.1°, 29°, 33.3°, 34°, and 49.4° and can be associated with the (002), (110), (012), (-112), (200) and (220) reflections respectively. However no change in the overall structure of the film was observed verifying that the film was stable under the acetone test conditions. Fig. 10.4 shows the XRD of sample at the conditions of the acetone test (operando XRD). It can be seen that the structure of the film has remained unchanged during the operando XRD confirming that the structure is stable during the acetone sensing experiments.

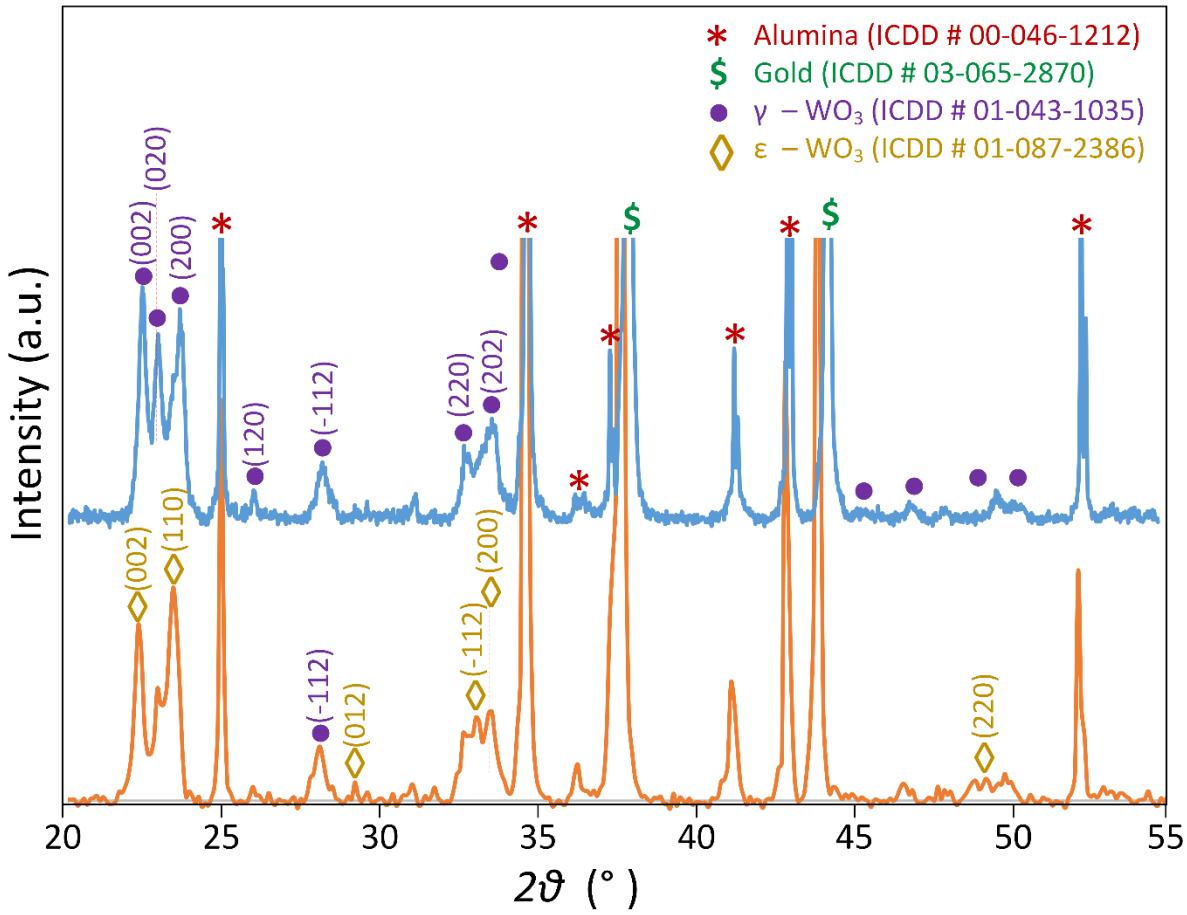

Fig. 10.3: X-ray diffraction of the WO_3 film before and after the acetone sensing stability test.

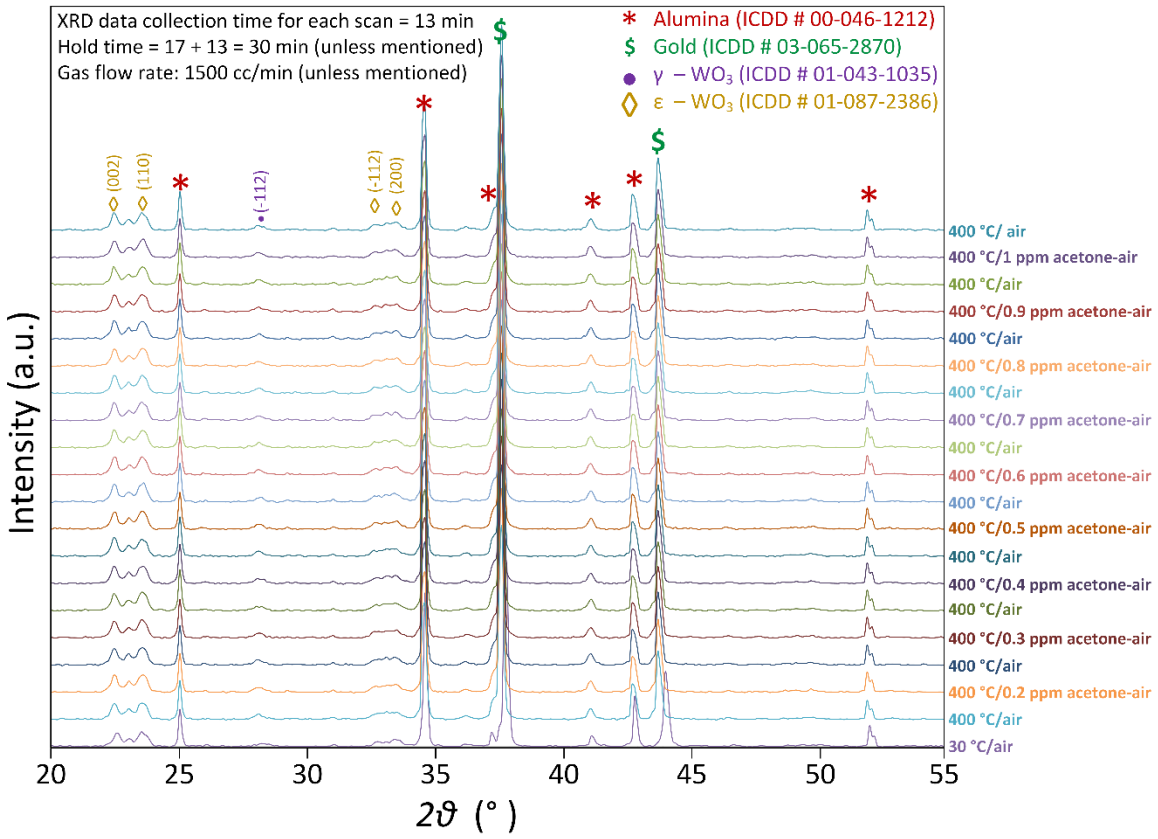

Fig. 10.4: Operando X-ray diffraction of the WO_3 film during 0.2–1 ppm acetone tests.

10.6.2 Raman Spectroscopy:

Raman spectroscopy technique was used for identifying the phases in the WO_3 film since this technique is well known to give the "fingerprint "of WO_3 material [10]. Fig. 10.5 shows the Raman spectroscopy results of the WO_3 film directly deposited on gold interdigitated electrodes, both pre and post acetone stability tests. The peaks were matched with the standards in references [10, 13]. The peaks for γ-WO_3 are at the Raman shift value of 808, 716, 328 and 275 cm^{-1} while the peaks for ε-WO_3 are at 808, 686, 646, 423, 373, 275 and 208 cm^{-1}. A relatively strong peak was observed below 150 cm^{-1} for all the samples which indicates the O-O deformation mode [13]. The strong γ-WO_3 peak at 715 cm^{-1} is weak in the as prepared sample

while the characteristic ε-WO_3 only peaks at 686, 646, 423, 373 cm^{-1} are stronger. On the basis of XRD and Raman spectroscopy results, it can be safely concluded that the structure of the WO_3 film in this study is monoclinic ε phase. Phase transformation from ε to γ is also evident after 450 h. of stability tests.

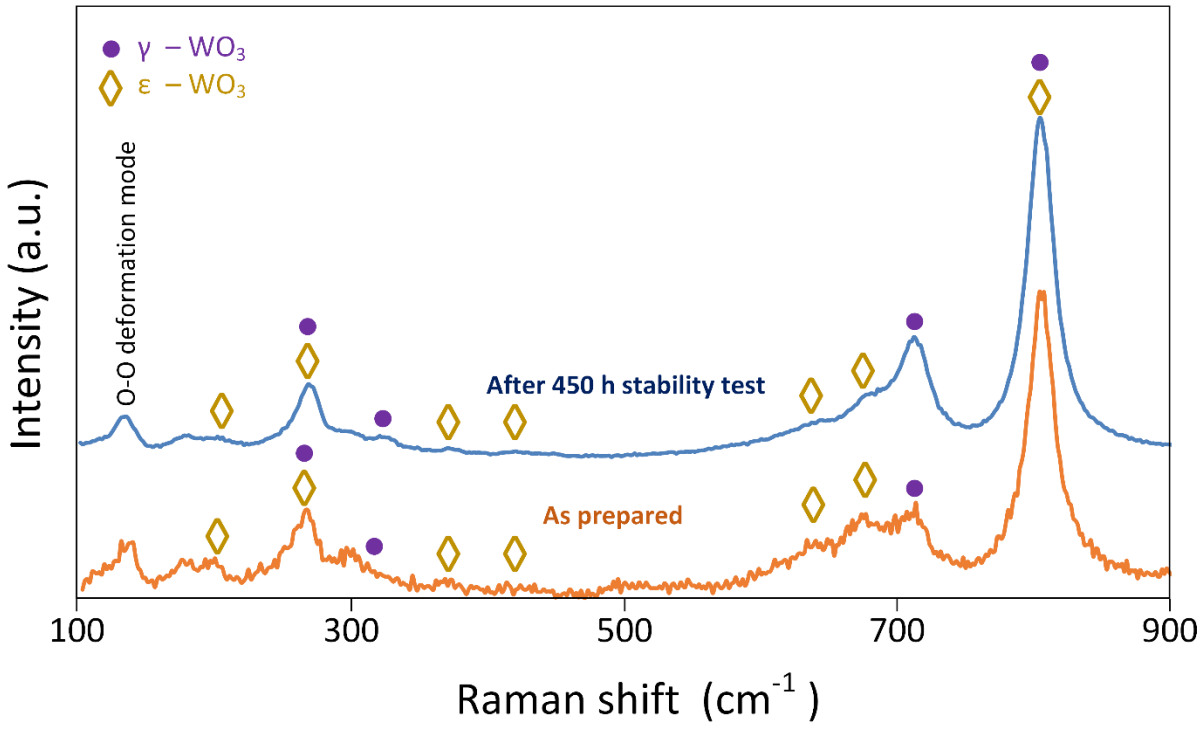

Fig. 10.5: Raman spectroscopy of the WO_3 film before and after the acetone sensing stability test.

10.6.3 Electron Microscopy:

10.6.3.1 Scanning Electron Microscopy:

Fig. 10.6 (a), (b), (c) and (d) shows the SEM micrographs of the WO_3 film as deposited on the gold electrode. Fig. 10.6 (a) and (c) shows the image after 8.5 h. acetone tests and it can be inferred from the images that the WO_3 film surface is rough and porous

with the formation of some agglomerates around 5–10 μm wide. Various pores could be seen which is advantageous for the diffusion of gases in the bulk of the film [14]. Fig. 10.6 (b) and (d) shows the image after 300 h. acetone tests. It can be clearly seen that there is a remarkable change in the morphology of the films after acetone stability tests. From Fig. 10.6 (a) and (b), uniformly coated gold lines with WO_3 can be seen and it can be inferred that the film formation is conformal in nature. The total WO_3 deposition area on the gold electrodes was 97.5 mm^2. The images indicate high quality porous WO_3 films deposited by RSDT without any cracks, voids, dense regions or surface abnormalities.

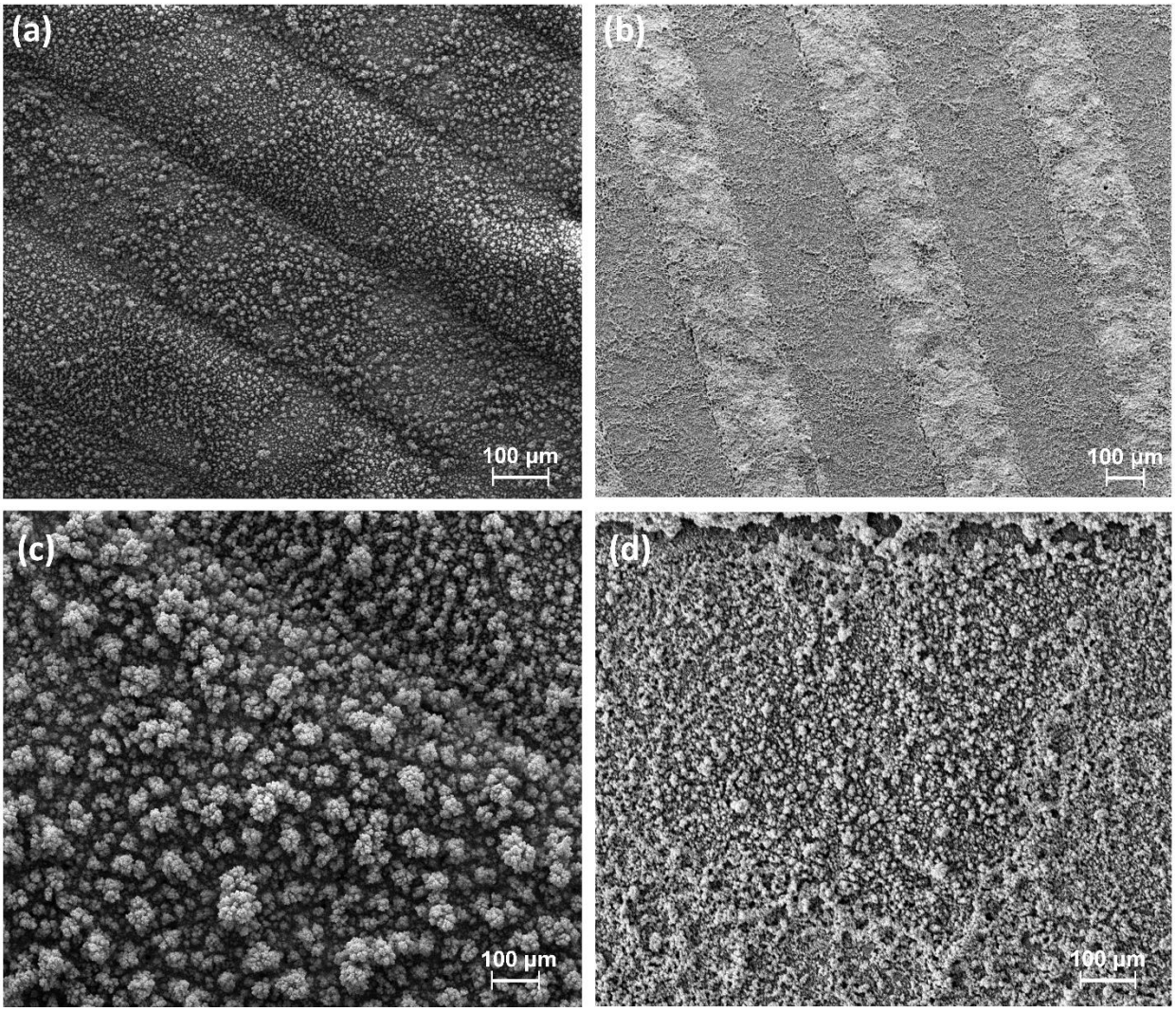

Fig. 10.6: SEM micrographs of the WO_3 film before and after the acetone sensing stability test.

10.6.3.2 Transmission Electron Microscopy:

Fig. 10.7 shows the bright field TEM micrograph of the WO_3 particles. Necking of the grains can be clearly observed which is advantageous for the enhanced electron transport through the percolation path (grain to grain contact) as described by Xu et al. [15]. Various oval shaped particles can be seen. From TEM point analysis, a crystallite size (d_{TEM}) distribution ranging between 12–25 nm was observed. It has been shown by Tamaki et al. that the

gas sensitivity is significantly enhanced when the crystallite size is smaller than the Debye length (λ_D). This is because both the surface and bulk of the grain contributes to the resistance and yields the largest gas sensor response. The Debye length for WO_3 is 25 nm [1]. No evidence of sintering of the nanoparticles was found which is attributed to the use of air quench in RSDT.

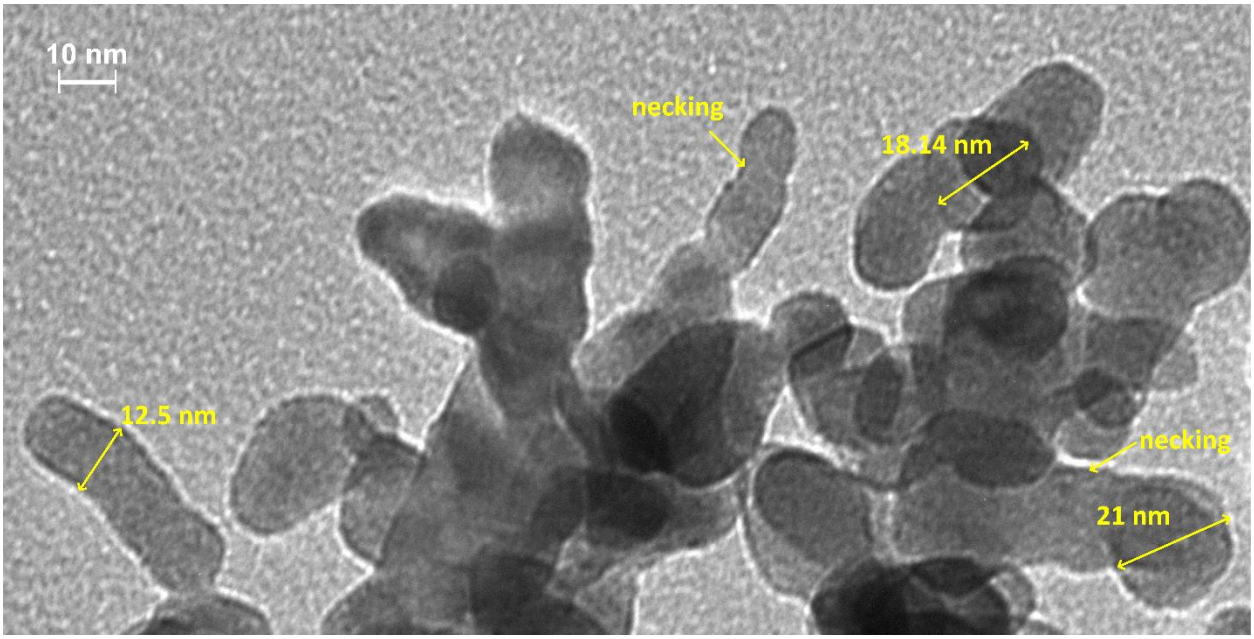

Fig. 10.7: TEM micrographs of the WO_3 crystallites showing necking and a crystallite size (d_{TEM}) distribution ranging between 12–25 nm.

10.6.4 Gas sensing results:

Fig. 10.8 shows the resistance vs time curve for the acetone concentration ranging from 0.2–1 ppm in the air at 400°C. The limit of detection for our tests was 0.2 ppm. The film resistance decreases as the concentration of acetone is increased. This is because of the increased adsorption of acetone molecules at higher acetone concentration. The adsorption and desorption of the acetone molecules on the WO_3 film takes place simultaneously and is a reversible process. During the response stage, adsorption is higher than desorption and the resistance of the

film increases. This is because acetone diffuses through the porous WO_3 film and reduces the WO_3 surface thereby depleting the ionosorbed oxygen concentration on the film. Acetone also captures electrons from the conduction band of WO_3 causing the formation of an electron depletion region, triggering an increase in its resistance. It was seen that the sensor response was spontaneous as the gas concentration in the test chamber was changed from pure air to acetone in the air. The response time was calculated to be 10 s. The sensor very quickly stabilized at the maximum value of resistance. At this point, the adsorption rate is equal to the desorption rate. Maximum adsorption had taken place at that particular analyte concentration, and the WO_3 film was in equilibrium with the acetone molecules. Recovery of the sensor started when pure air was switched back to the test chamber. At this point, adsorption was nil and desorption was the only process which was taking place. Presence of two vents in the test chamber expedited the exchange of the gas atmosphere. However it was seen that desorption was still slower than adsorption. A drift can be seen when the resistance of the film is measured in air after exposure to acetone at different concentrations. This is caused by incomplete recovery during the 15 min. of recovery phase. The test data was also compared with the data from other acetone sensors as given in literature. This is shown in table 10.1.

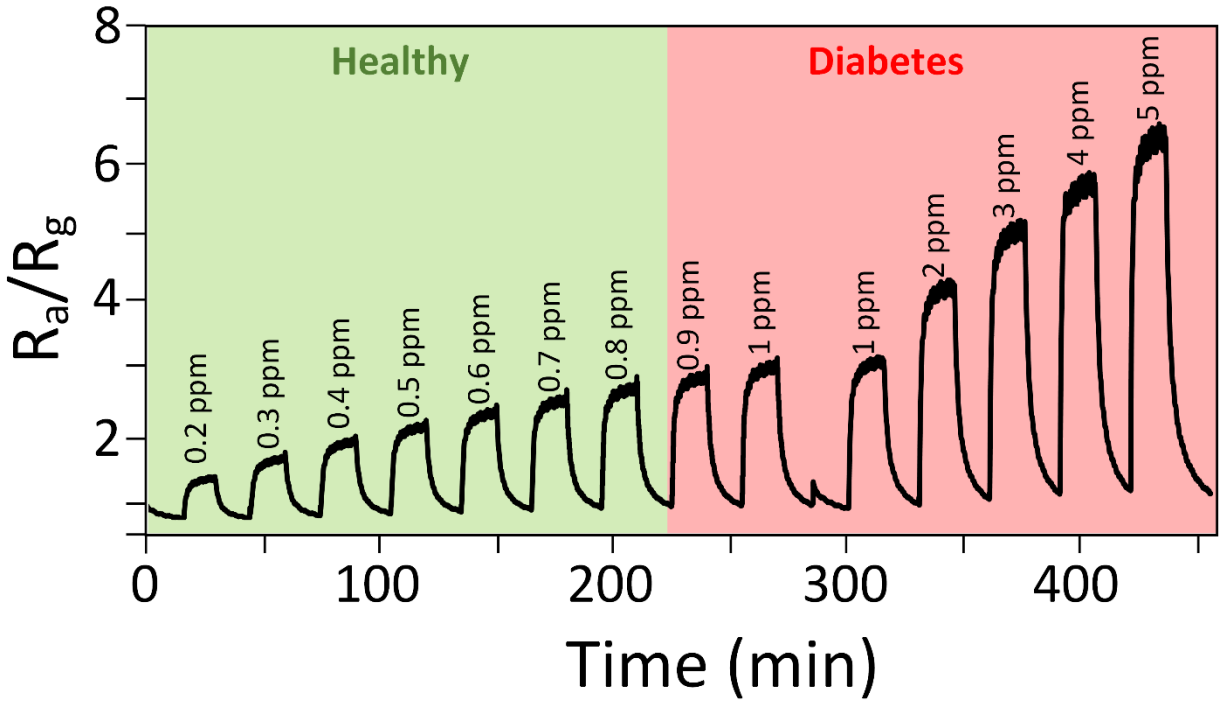

Fig. 10.8: Resistance vs time curve for acetone tests conducted at 400°C from 0.2–5 ppm acetone.

10.6.5 Stability tests:

Stability tests of the WO_3 films were conducted for 450 h. at 0.5 ppm acetone in the air at 400°C and which is same as the breath acetone concentration of a healthy individual [3, 4]. The sensor was tested at this concentration because it is desirable that the breath acetone concentration remain below the diabetes threshold limit. 0.5 ppm acetone was switched on every 5 min. (response) followed by 5 min. of pure air (recovery). Resistance of the film was measured every 100 ms to record the response and recovery cycle (response + recovery time = 10 min). A total of 2700 response-recovery cycles were recorded. Fig. 10.9 shows the resistance over time for WO_3 film in pure air (R_a) and 0.5 ppm acetone in air (R_g) respectively. It can be seen that the sensor is stable till day 10 (~250 h.). From day 10–21 (250–450 h.) the sensor began to degrade

possibly due to the growth of the WO_3 nanoparticles and the phase transformation to the γ phase as confirmed by XRD and Raman spectroscopy. This shows that maximum degradation of the sensor occurred after day 10 (~250 h.) as evident from the fluctuation of resistance.

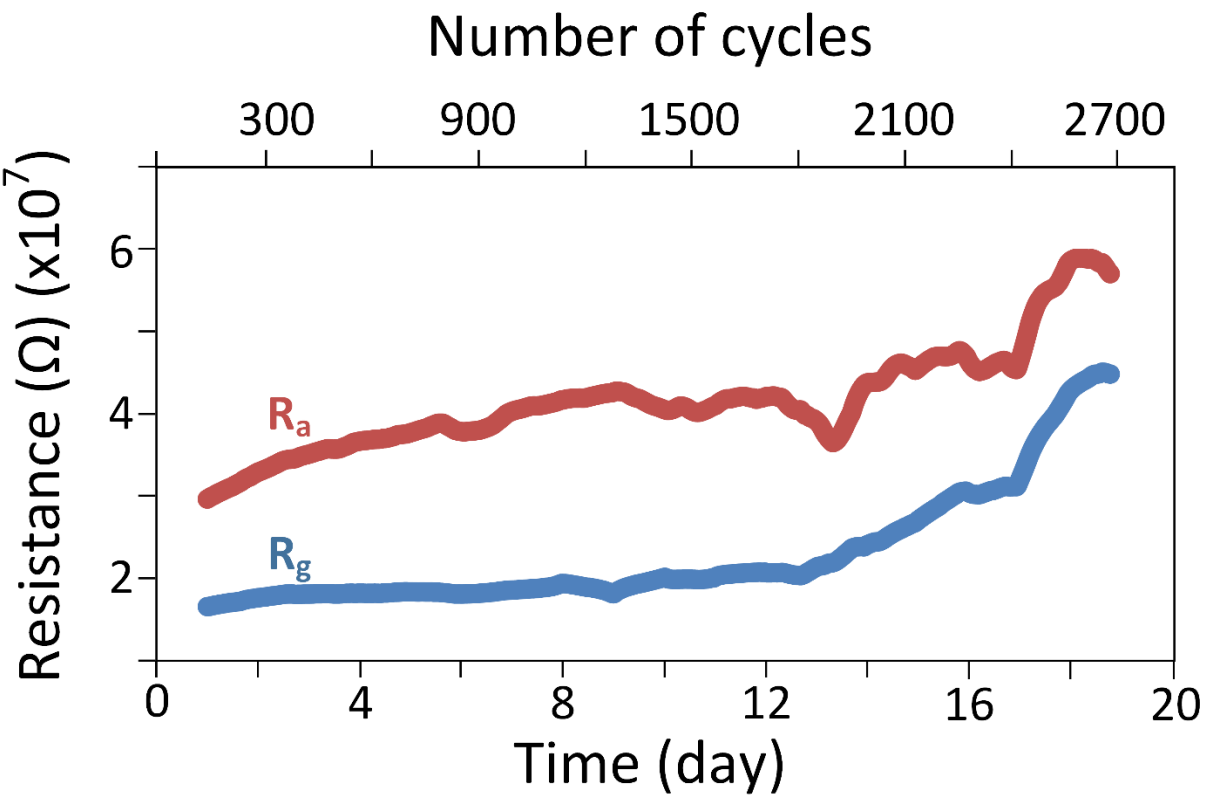

Fig. 10.9: Stability tests for WO_3 sensor conducted for 450 h. at 0.5 ppm acetone in the air at 400°C.

10.6.6 Selectivity:

The response of 0.5 ppm acetone was compared with 10 ppm H_2, 0.2 ppm ethanol, 8 ppm CO and 90% relative humidity in air at 400°C (data not shown here). It was seen that the sensor had negligible response for ethanol, CO and humidity, but significant response for

10 ppm H_2. H_2 is a major component exhaled from the human breath [16]. Typical values of H_2 in the breath range from 10–20 ppm [17].

10.7 Discussions:

On the basis of the characterization and gas sensing results, we can conclude that RSDT can be used for the synthesis of acetone sensing films directly on gold interdigitated electrodes. Based on our previous work on WO_3 [2] and a review of the literature, it can be shown that the characteristics of the sensing device that are most important for good performance are: (1) high porosity of the sensing film, (2) particle size of the sensing film smaller than the Debye length (λ_D), a characteristic of the semiconductor material, which is 25 nm for WO_3, (3) film thickness, (4) absence of impurities in the test atmosphere, (5) test chamber volume, and (6) time required for the exchange of gases in the test chamber. In this discussion we will identify the importance of these factors and show that the gas sensing test data presented in this work adheres to these requirements.

Since the sensing is an adsorption-desorption process, gas diffusion through the film plays a major role in the sensor performance. The sensing film must be porous to effectively allow the diffusion process and extend the reaction between acetone and oxygen from the surface to the bulk. By assuming steady state conditions, it can be interpreted that the acetone concentration decreases with the film depth which causes the formation of various degree of reactions at different depths of the film. The resistance change data recorded by the electrochemical analyzer averages the resistances by providing the overall resistance change of the film. Ideally it would be beneficial to eliminate this variation. Film porosity, thickness, microstructure, and the electrode pattern are the factors which govern this variation [18, 19]. From

the SEM micrographs in Fig. 10.6 it can be seen that the WO_3 film synthesized by RSDT is highly porous and uniform. For porous layers, the active surface area is much larger than the dense layers. Two different transport mechanism for the charge carriers were proposed for the porous layers by Barsan and Weimar [20]:

Diffusion theory:

According to the diffusion theory in porous layers, the conductance is calculated by the following equation:

$$C_{diff} = area * \left(\frac{q^2 n_b \mu_b}{k_B T}\right) * \sqrt{\frac{q n_b V_s}{2\varepsilon}} * exp\left(\frac{-q v_s}{k_B T}\right) \quad \text{(E10.1)}$$

Where "C" is the conductance and "area" has the dimensions in m^2 and represents the active area seen by the electrons while travelling from grain to grain. The subscript "b" represents bulk. The other symbols are as defined previously.

Thermoelectronic emission theory:

According to this theory, only the electrons which possess the kinetic energy greater than the band bending height can move across the boundary. The net current is the difference in the charge fluxes across the boundary from left to right and right to left respectively.

$$C_{thermo} = area * \left(\frac{q}{k_B T}\right) * q * \sqrt{\frac{8 * k_B * T}{\Pi * m'}} * exp\left(\frac{-q v_s}{k_B T}\right) \quad \text{(E10.2)}$$

Where, $\sqrt{\frac{8 * k_B * T}{\Pi * m'}}$ = mean thermal velocity of the carriers and m' is the effective mass. The other symbols are as defined previously.

Gas sensing response is dependent on the particle size of the sensing film. Smaller particles and increased surface area (higher surface to volume ratio) provides larger number of sites for the surface reaction to occur. At the same time, reducing the particle radius below Λ, will converge the electron depletion layer (2Λ), and the electrical conduction will be dominated by the presence of adsorbed acetone species. Λ depends on the Debye length (λ_D) of the material by the following equation:

Debye length by the following equation:

$$\Lambda = \lambda_D \left(\frac{2qV_s}{k_B T}\right)^{1/2} \quad \text{(E10.3)}$$

qV_s = height of band bending, λ_D = Debye length

k_B = Boltzmann's constant = $1.38 * 10^{-23} \frac{J}{K}$, T = temperature

Debye length of WO_3 is 25 nm. Sharma et al. has described the relationship between gas sensitivity and particle size with respect to the Debye length (λ_D). When the particle size is smaller than λ_D, the ionosorbed oxygen will extract all the electrons from the WO_3 particle causing an increase in film resistance [21]. In this work, the WO_3 particle size were in the range 12–25 nm as determined by the TEM point analysis.

Selectivity is a major concern for a sensor to be commercially viable, which may lead to false alarm or incorrect gas concentration determination. In this study, it was found that the WO_3 film was responsive to 10 ppm H_2, while the response to humidity, 0.2 ppm ethanol and 8 ppm CO was negligible. There are various methods to discriminate the interference to these gases that are suggested in the literature. The most common approach is to utilize a sensor array described by Albert et al. with various sensor electrodes to filter out the response from the

interfering analytes [22]. The other method is to use filters upstream of the electrode to filter out the gases. One such activated charcoal filter is used by Figaro Inc. in their commercial CO sensor - TGS5042. Since the sensor response is a diffusion driven process, filters can easily be applied to improve the selectivity. Porous layers in which gases may have different diffusion coefficients can be directly deposited on the sensing layer. These layers acts as molecular sieves to reject the interfering gases. Description of these porous layer filters have been provided in detail in this reference [23]. Pre-calibration of the sensor for known cross contaminants has also been suggested [24].

The long recovery time and the drift of the metal oxides based sensors have been long recognized and various suggestions to counter this limitation have been proposed. From the gas sensing tests in Fig. 10.8, a drift can be seen when the resistance of the film is measured in air after exposure to acetone at different concentrations. This is caused because of incomplete recovery during the 15 min. of recovery phase. As a gas molecule is chemically adsorbed on the surface of WO_3, it is in thermal equilibrium and resides at the bottom of the potential well (minimum potential energy). In order to desorb from the surface, the only driving force it experiences is the diffusion caused by the change in the concentration of gases in the test chamber on switching to pure air. However this energy is not sufficient and causes a long delay to achieve complete desorption. Further thermal or electrical energy is required to expedite this adsorption process. Different ways are suggested in literature to eliminate sensor drift. These include, using high-speed gas-switching system and smaller volume test chamber for enabling quicker gas exchange [25] pre exposing the sensing film to the analyte for a set period of time [26], use of mathematical function and modelling [27] to pre-estimate the steady state conditions and remove the time lag [28], use of multiple sensing electrodes in different test chamber to alter between

response and recovery [29], use of neural network algorithm for the sensor to “self-learn” [30] use of strong negative field to electro-desorb the residual analyte molecules to “refresh” the sensor [31] and by illuminating the sensor with ultra-violet (UV) light [32]. Here we have used a two vent test chamber to expedite the atmosphere change. The test chamber volume was 85 cc. We are currently developing a prototype sensing device with a volume of 0.5 cc which will further reduce this issue.

Table 10.1: Comparison of the metal oxide based acetone sensors prepared by different synthesis techniques.

Sensing film	Synthesis method	Limit of detection (LOD) (ppm)	Working temperature (°C)	Sensitivity (R_a/R_g)	Sensitivity (used formula)	Response time (s)	Reference
Pure WO_3	**RSDT**	**0.2**	**400**	**1.3 (0.2 ppm) 2.1 (0.5 ppm)**	R_a/R_g	**10**	**Present study**
Cr_2O_3-WO_3	Flame spray pyrolysis	0.2	400	1.5 (0.2 ppm)	R_a/R_g	333	[33]
5 mol% Cr_2O_3-WO_3	Sol-gel	0.5	320	1.2 (0.5 ppm)	R_a/R_g	182	[34]
SiO_2-WO_3	Flame spray pyrolysis	0.02	400	1.3 (0.02 ppm) 5.2 (0.5 ppm)	(R_a/R_g)-1	172	[35]
Pure SnO_2	Dip-coating	2	room temperature	4 (2 ppm)	R_a/R_g	30 s	[36]
Ce-SnO_2	Sol-gel and dip coating	100	210	79 (100 ppm)	R_a/R_g	not mentioned	[37]
SnO_2-ZnO	Wet method	200	300	2.3 (200 ppm)	R_a/R_g	233	[38]
ZnO	RF reactive sputtering	15	400	1.006 (15 ppm)	(R_a/R_g)-1	324	[39]
TiO_2	Flame spray pyrolysis	1	500	4 (1 ppm)	(R_a/R_g)-1	3	[40]
Fe_2O_3/Pt	Wet method	10	300	5.2 (10 ppm)	R_a/R_g	NM	[41]
Fe_2O_3/RuO_2	Wet method	10	300	2.5 (10 ppm)	R_a/R_g	NM	[41]
In_2O_3/Au	co-precipitation	0.1	250	2.8 (1 ppm)	R_a/R_g	72 s	[42]

10.8 Conclusions:

In this study we have evaluated RSDT as a direct deposition technique for the synthesis of ε-WO_3 film for ultra-low acetone sensing. Air quenching was used to optimize the particle size and film morphology to tailor the film towards superior acetone sensing performance. Here our main objective was to correlate the influence of the synthesis process, and the resultant structural properties of the ε-WO_3 film with the acetone gas sensing performance. We have highlighted these properties and their influence on the acetone sensing which will provide a platform for developing better sensors with improved performance compared to the currently used sensors. The reasons for the high response can be attributed to a number of factors, such particle size, porosity and pore size, and film thickness, all precisely controlled by the RSDT. Following conclusions can be made from this work:

1. RSDT synthesized WO_3 film based acetone sensor was responsive in the 0.2–1 ppm range, when tested at 400°C.
2. XRD and Raman spectroscopy confirmed the presence of ε-WO_3.
3. Operando XRD at the same conditions of acetone tests confirmed that the structure was unaltered during the tests.
4. Response time was 10 s and recovery time was greater than 15 min.
5. The acetone sensors gave a steady response till 450 h. of continuous performance and started to degrade after 450 h. possibly due to phase transformation to the thermodynamically stable γ-WO_3.

6. Interference was negligible with humidity, 0.2 ppm ethanol, and 8 ppm CO; however, it was significant with 10 ppm H_2.

7. Response and recovery of the sensor is caused by adsorption and desorption respectively. Hence recovery time can be improved by expediting the desorption step.

8. WO_3 particle size of <25 nm attributes to better charge transfer which translates to superior acetone sensitivity.

10.9 References:

[1] J. Tamaki, Z. Zhang, K. Fujimori, M. Akiyama, T. Harada, N. Miura, N. Yamazoe, Grain-Size Effects in Tungsten Oxide-Based Sensor for Nitrogen Oxides, Journal of Electroceramic Society. 141 (8) (1994) 2207-2210.

[2] R. Jain, Y. Wang, R. Maric, Tuning of WO_3 Phase Transformation and Structural Modification by Reactive Spray Deposition Technology, Journal of Nanotechnology and Smart Materials. 1 (2014) 1-7.

[3] Z. Wang, C. Wang, Is breath acetone a biomarker of diabetes? A historical review on breath acetone measurements. Journal of Breath Research. 7 (3) (2013) 037109.

[4] O.E. Owen, V.E. Trapp, C.L. Skutches, M.A. Mozzoli, R.D. Hoeldtke, G. Boden, G.A. Reichard Jr, Acetone metabolism during diabetic ketoacidosis, Diabetes. 31 (3) (1982) 242-248.

[5] R. Jain, R. Maric, Synthesis of nano-Pt onto ceria support as catalyst for water-gas shift reaction by Reactive Spray Deposition Technology, Applied Catalysis A: General. 475 (2014) 461-468.

[6] J.M. Roller, J. Arellano-Jiménez, R. Jain, H. Yu, R. Maric, C.B. Carter, Processing, Activity and Microstructure of Oxygen Evolution Anodes Prepared by a Dry and Direct Deposition Technique, ECS Transactions. 45 (21) (2013) 97-106.

[7] J. M. Roller. Flame Synthesis of Nanomaterials for Alternative Energy Applications (Doctoral dissertation). University of Connecticut. Retrieved from: http://digitalcommons.uconn.edu/dissertations/432/ (2014).

[8] R. Maric, J.M. Roller, R. Neagu, K. Fatih, A. Tuck, Low Pt Thin Cathode Layer Catalyst Layer by Reactive Spray Deposition Technology, ECS Transactions. 12 (1) (2008) 59-63.

[9] J. Roller, J. Renner, H. Yu, C. Capuano, T. Kwak, Y. Wang, C.B. Carter, K. Ayers, W.E. Mustain, R. Maric, Flame-based processing as a practical approach for manufacturing hydrogen evolution electrodes, Journal of Power Sources. 271 (0) (2014) 366-376.

[10] C. Bittencourt, E. Llobet, P. Ivanov, X. Vilanova, X. Correig, M.A.P. Silva, L.A.O. Nunes, J.J. Pireaux, Ag induced modifications on WO_3 films studied by AFM, Raman and x-ray photoelectron spectroscopy, Journal of Physics D-Applied Physics. 37 (24) (2004) 3383-3391.

[11] R. Garcia-Sanchez, T. Ahmido, D. Casimir, S. Baliga, P. Misra, Thermal Effects Associated with the Raman Spectroscopy of WO_3 Gas-Sensor Materials, Journal of Physical Chemistry A. 117 (50) (2013) 13825-13831.

[12] B. Mahut, C. Delacourt, F. Zerah-Lancner, J. De Blic, A. Harf, C. Delclaux, Increase in alveolar nitric oxide in the presence of symptoms in childhood asthma, Chest. 125 (3) (2004) 1012-1018.

[13] M. Arai, S. Hayashi, K. Yamamoto, S.S. Kim, Raman Studies of Phase-Transitions in Gas-Evaporated WO_3 Microcrystals, Solid State Communications. 75 (7) (1990) 613-616.

[14] L. Filipovic, S. Selberherr, Performance and Stress Analysis of Metal Oxide Films for CMOS-Integrated Gas Sensors, Sensors. 15 (4) (2015) 7206-7227.

[15] C. Xu, J. Tamaki, N. Miura, N. Yamazoe, Grain size effects on gas sensitivity of porous SnO_2-based elements, Sensors and Actuators B: Chemical. 3 (2) (1991) 147-155.

[16] M. Phillips, J. Herrera, S. Krishnan, M. Zain, J. Greenberg, R.N. Cataneo, Variation in volatile organic compounds in the breath of normal humans, Journal of Chromatography B: Biomedical Sciences and Applications. 729 (1–2) (1999) 75-88.

[17] U.C. Ghoshal, How to Interpret Hydrogen Breath Tests, Journal of Neurogastroenterology and Motility. 17 (3) (2011) 312-317.

[18] E. Comini, G. Faglia, G. Sberveglieri, Solid State Gas Sensing, 1st ed., Springer, US, 2009.

[19] N. Barsan, D. Koziej, U. Weimar, Metal oxide-based gas sensor research: How to? Sensors and Actuators B: Chemical. 121 (1) (2007) 18-35.

[20] N. Barsan, U. Weimar, Conduction Model of Metal Oxide Gas Sensors, Journal of Electroceramics. 7 (3) (2001) 143-167.

[21] S. Sharma, M. Madou, A new approach to gas sensing with nanotechnology, Philosophical Transactions of the Royal Society A. 370 (1967) (2012) 2448-2473.

[22] K.J. Albert, N.S. Lewis, C.L. Schauer, G.A. Sotzing, S.E. Stitzel, T.P. Vaid, D.R. Walt, Cross-reactive chemical sensor arrays, Chemical reviews. 100 (7) (2000) 2595-2626.

[23] G. Korotcenkov, Filters in Gas Sensors, in: R.A. Potyrailo (Ed.), Handbook of Gas Sensor Materials, 1st ed., Springer, New York, 2013, pp. 293-303.

[24] Tsuguyoshi Toyooka and Satoshi Hiyama and,Yuki Yamada, A prototype portable breath acetone analyzer for monitoring fat loss, Journal of Breath Research. 7 (3) (2013) 036005.

[25] T. Kida, T. Kuroiwa, M. Yuasa, K. Shimanoe, N. Yamazoe, Study on the response and recovery properties of semiconductor gas sensors using a high-speed gas-switching system, Sensors and Actuators B: Chemical. 134 (2) (2008) 928-933.

[26] Y. Liu, Y. Lei, Pt-CeO_2 nanofibers based high-frequency impedancemetric gas sensor for selective CO and C_3H_8 detection in high-temperature harsh environment, Sensors and Actuators B: Chemical. 188 (2013) 1141-1147.

[27] M. Holmberg, F. Winquist, I. Lundström, F. Davide, C. DiNatale, A. D'Amico, Drift counteraction for an electronic nose, Sensors and Actuators B: Chemical. 36 (1–3) (1996) 528-535.

[28] J.G. Monroy, J. González-Jiménez, J.L. Blanco, Overcoming the Slow Recovery of MO_X Gas Sensors through a System Modeling Approach, Sensors (Basel, Switzerland). 12 (10) (2012) 13664-13680.

[29] J. Gonzalez-Jimenez, J.G. Monroy, J.L. Blanco, The Multi-Chamber Electronic Nose-An Improved Olfaction Sensor for Mobile Robotics, Sensors (Basel, Switzerland). 11 (6) (2011) 6145-6164.

[30] M. Zuppa, C. Distante, P. Siciliano, K.C. Persaud, Drift counteraction with multiple self-organising maps for an electronic nose, Sensors and Actuators B: Chemical. 98 (2–3) (2004) 305-317.

[31] Z. Fan, J.G. Lu, Gate-refreshable nanowire chemical sensors, Applied Physics Letters. 86 (12) (2005) 123510.

[32] C. Li, D. Zhang, X. Liu, S. Han, T. Tang, J. Han, C. Zhou, In_2O_3 nanowires as chemical sensors, Applied Physics Letters. 82 (10) (2003) 1613-1615.

[33] L. Wang, A. Teleki, S.E. Pratsinis, P.I. Gouma, Ferroelectric WO_3 Nanoparticles for Acetone Selective Detection, Chemistry of Materials. 20 (15) (2008) 4794-4796.

[34] P. Gao, H. Ji, Y. Zhou, X. Li, Selective acetone gas sensors using porous WO_3-Cr_2O_3 thin films prepared by sol-gel method, Thin Solid Films. 520 (7) (2012) 3100-3106.

[35] M. Righettoni, A. Tricoli, S.E. Pratsinis, Si: WO_3 Sensors for Highly Selective Detection of Acetone for Easy Diagnosis of Diabetes by Breath Analysis, Analytical Chemistry. 82 (9) (2010) 3581-3587.

[36] J. Zhao, L. Huo, S. Gao, H. Zhao, J. Zhao, Alcohols and acetone sensing properties of SnO_2 thin films deposited by dip-coating, Sensors and Actuators B: Chemical. 115 (1) (2006) 460-464.

[37] Z. Jiang, Z. Guo, B. Sun, Y. Jia, M. Li, J. Liu, Highly sensitive and selective butanone sensors based on cerium-doped SnO_2 thin films, Sensors and Actuators B: Chemical. 145 (2) (2010) 667-673.

[38] K. Kim, P. Cho, S. Kim, J. Lee, C. Kang, J. Kim, S. Yoon, The selective detection of C_2H_5OH using SnO_2–ZnO thin film gas sensors prepared by combinatorial solution deposition, Sensors and Actuators B: Chemical. 123 (1) (2007) 318-324.

[39] N.H. Al-Hardan, M.J. Abdullah, A. Abdul Aziz, H. Ahmad, L.Y. Low, ZnO thin films for VOC sensing applications, Vacuum. 85 (1) (2010) 101-106.

[40] A. Teleki, S.E. Pratsinis, K. Kalyanasundaram, P.I. Gouma, Sensing of organic vapors by flame-made TiO_2 nanoparticles, Sensors and Actuators B: Chemical. 119 (2) (2006) 683-690.

[41] S.V. Ryabtsev, A.V. Shaposhnick, A.N. Lukin, E.P. Domashevskaya, Application of semiconductor gas sensors for medical diagnostics, Sensors and Actuators B: Chemical. 59 (1) (1999) 26-29.

[42] R. Xing, L. Xu, J. Song, C. Zhou, Q. Li, D. Liu, H. Wei Song, Preparation and Gas Sensing Properties of In_2O_3/Au Nanorods for Detection of Volatile Organic Compounds in Exhaled Breath, Scientific Reports. 5 (2015) 10717.

SECTION IV:

CONCLUSIONS

This thesis was produced as a result of two different research topics: catalysts and sensors. RSDT was explored as a single step approach to synthesize nanomaterials thin films for the catalyst and sensor. Pt/ceria catalysts was synthesized for the water-gas shift reaction while two distinct phases of WO_3 (γ and ε phase) were synthesized for the NO_2 and acetone sensing respectively. The work presented in this thesis opened up the avenue for further development of novel functional nanomaterials films for catalysts and sensors. It is clear from the work presented here that there is a large design space in RSDT to manipulate the nanomaterial structure, phase, chemistry, composition, porosity, density and particle size. Independent control of all the parameters provide additional flexibility to obtain the desired nanomaterial property. Based on various chapters presented in this thesis following conclusions can be made:

Pt was deposited on ceria support using RSDT. Composition of Pt on ceria was adjusted by adjusting the precursor composition. 1 wt% Pt on ceria catalyst was synthesized where solid nanoparticles were grown from the vapor phase and collected on glass fiber filter substrates. The catalyst was tested for water-gas shift reaction at various pretreatment and operating conditions. The activity was compared with the literature for the catalysts prepared by conventional processes. It was found that the RSDT synthesized catalyst performed better than most of the other catalysts. This is due to uniform distribution of Pt nanoparticles on the ceria surface and no agglomeration between particles. The catalyst activity depends strongly on the particle size of Pt, CO feed concentration, GHSV, water/CO ratio, ceria-Pt interaction, availability of surface oxygen vacancies in ceria, and catalyst poisoning by excess CO or sulfur.

Study on the effect of different ceria supports with similar Pt loading by RSDT resulted in the following conclusions:

Three different ceria support materials for were investigated for water-gas shift reaction studies on Pt/ceria catalysts. Reasons for the better catalytic activity of mesoporous Pt/ceria catalysts could be attributed to many factors such as noble metal loading, particle size of support and metal, porosity, pore size, concentration of defects, presence of active species etc. Here our main objective was to correlate the influence of the synthesis process, and the resultant structural properties of the ceria support with the performance of the Pt/ceria catalyst for the activity of low temperature water-gas shift reaction. We highlighted these properties and their influence on the WGS reaction which will provide a platform for generating catalyst with improved performance compared to the currently used catalysts. Three different ceria supports were chosen based on various syntheses techniques and 5 wt% Pt nanoparticles were applied onto them in the vapor phase using RSDT. The structure and crystallite size were determined using various characterization techniques. The catalysts were tested for WGS reaction in the temperature range of 150–450°C. Following conclusions can be made from this work:

1. C1/Pt mesoporous ceria had superior activity with complete CO conversion seen at 175°C followed by C2/Pt (225°C) and C3/Pt (450°C).
2. Increasing the Pt metal loading from 1% to 5% did not improve the WGS reaction activity of catalysts.
3. Catalytically active oxygen species [peroxides (O_2^{2-}) and superoxide (O_2^{-})] exist on the one-electron defect sites at the metal-support interface as observed from Raman spectroscopy.

4. Formation of OH, surface formate, surface carbonates, $CO–Ce^{4+}$ and $CO–Ce^{3+}$ species were seen by *in-situ* DRIFTS studies which prove the occurrence of both ceria mediated redox and formate mechanism in the WGS reaction.
5. Weak CO-Pt interaction was observed in C2/Pt by *in-situ* DRIFTS studies which could explain the poor WGS reaction activity.
6. Non-stoichiometry of ceria was noticed by Raman spectroscopy in C1/Pt and C3/Pt.
7. Crystallite size of <10 nm attributes to higher surface areas and lower activation rates for the WGS reaction.

Study on the synthesis of γ-WO_3 film for NO_2 sensing resulted in the following conclusions:

In this study we have evaluated RSDT as a direct deposition technique for the synthesis of γ-WO_3 film for ultra-low NO_2 sensing. Nano quenching was used to optimize the particle size and film morphology to tailor the film towards superior NO_2 sensing performance. Here our main objective was to correlate the influence of the synthesis process, and the resultant structural properties of the γ-WO_3 film with the NO_2 gas sensing performance. We have highlighted these properties and their influence on the NO_2 sensing which will provide a platform for developing better sensors with improved performance compared to the currently used sensors. The reasons for the high response can be attributed to a number of factors, such particle size, porosity and pore size, and film thickness, all precisely controlled by the RSDT. Following conclusions can be made from this work:

1. RSDT synthesized WO_3 film based NO_2 sensor was responsive in the 0.17–5 ppm range, when tested at 300°C.

2. Response time was 7.2 s and recovery time was greater than 5 min. The response time was better than the WO_3 sensors synthesized by the traditional wet chemistry processes from literature.

3. The response was highest at the working temperature of 300°C.

4. The NO_2 sensors gave a steady response till 150 h of continuous performance and started to degrade after 200 h possibly due to increase in particle size.

5. Interference was negligible with 10 ppm acetone, 100 ppm ethanol, 10 ppm H_2 and humidity; however, it was significant with 10 ppm isoprene and 100 ppm H_2.

6. Response and recovery of the sensor is caused by adsorption and desorption respectively. Hence recovery time can be improved by expediting the desorption step.

7. WO_3 particle size of <25 nm attributes to better charge transfer which translates to superior NO_2 sensitivity.

Study on the synthesis of ε-WO_3 film for acetone sensing resulted in the following conclusions:

In this study we have evaluated RSDT as a direct deposition technique for the synthesis of ε-WO_3 film for ultra-low acetone sensing. Nano quenching was used to optimize the particle size and film morphology to tailor the film towards superior acetone sensing performance. Here our main objective was to correlate the influence of the synthesis process, and the resultant structural properties of the ε-WO_3 film with the acetone gas sensing performance. We have highlighted these properties and their influence on the acetone sensing which will provide a platform for developing better sensors with improved performance compared to the currently used sensors. The reasons for the high response can be attributed to a number of factors, such particle

size, porosity and pore size, and film thickness, all precisely controlled by the RSDT. Following conclusions can be made from this work:

1. RSDT synthesized WO_3 film based acetone sensor was responsive in the 0.2-1 ppm range, when tested at 400°C.

2. XRD and Raman spectroscopy confirmed the presence of ε-WO_3.

3. Operando XRD at the same conditions of acetone tests confirmed that the structure was unaltered during the tests.

4. Response time was 180 s and recovery time was greater than 15 min.

5. The acetone sensors gave a steady response till 450 h. of continuous performance and started to degrade after 450 h possibly due to phase transformation to the thermodynamically stable γ-WO_3.

6. Interference was negligible with humidity, 0.2 ppm ethanol, and 8 ppm CO; however, it was significant with 10 ppm H_2.

7. Response and recovery of the sensor is caused by adsorption and desorption respectively. Hence recovery time can be improved by expediting the desorption step.

8. WO_3 particle size of <25 nm attributes to better charge transfer which translates to superior acetone sensitivity.

SECTION V:

RECOMMENDATIONS FOR FUTURE WORK

Results from this thesis opens up a whole new opportunity for the research which can be performed. Especially the research on the acetone sensors can be moved to the next level. Following are the recommendations for the future work for the acetone sensors:

1. Further study is required for the removal of the H_2 signal from the acetone. This is because the H_2 content of human breath is around 10 ppm which interferes with the acetone signal. This can be achieved by a number of ways as described in chapter 9 and 10.

2. The limit of detection (LOD) for the existing acetone sensors test was 0.17 ppm. With the addition of extra mass flow controllers, the LOD can be reduced to as low as 10 ppb.

3. The temperature control to the test chamber should be within ±0.01°C. This will significantly reduce the drift in the measurements.

4. The test chamber volume should be lowered to 1 cc to enable faster exchange of gas atmosphere.

5. It is essential to perform the tests in the real time conditions. This should be approached in the following steps:

   a. Testing the sensors with simulated breath. This can be achieved by mixing CO_2, O_2, N_2, H_2O, H_2, ethanol and acetone in correct proportion.

   b. Testing the sensors with actual breath from a patient.

6. Based on the results of the above it is essential to develop a prototype sensor. A description and schematic of such kind of sensor is given below:

The electrode chip with dimensions as given in the schematic was obtained for $28/piece from the Electronic Design Center of the Case Western Reserve University on January 2015. This chip has an onboard heater, resistance temperature detector to monitor the temperature

and Pt interdigitated lines to measure the sensor response under varying conditions. The chip can be heated to a temperature of up to 400°C in 15 s by supplying low dc voltage (<12V) to the heater. WO_3 film will be deposited on this chip using RSDT.

The chip can be placed in a small metal box (such as altoids mint box) and placed on the printed circuit board (PCB) as shown in the schematic shown below. The leads from the chip will be micro-bonded with the PCB at the clean room of IMS using gold wires. The reaction between WO_3 film and the sensing analytes will take place in the small metal box, the volume of which can be as low as 0.5 cc. The PCB will be connected with the electrochemical analyzer and multimeter using banana plugs. PCB will be placed inside a plastic housing which can be either 3D printed at C2E2 or machined. The size of the device will be half the size of an Apple iPhone 5S.

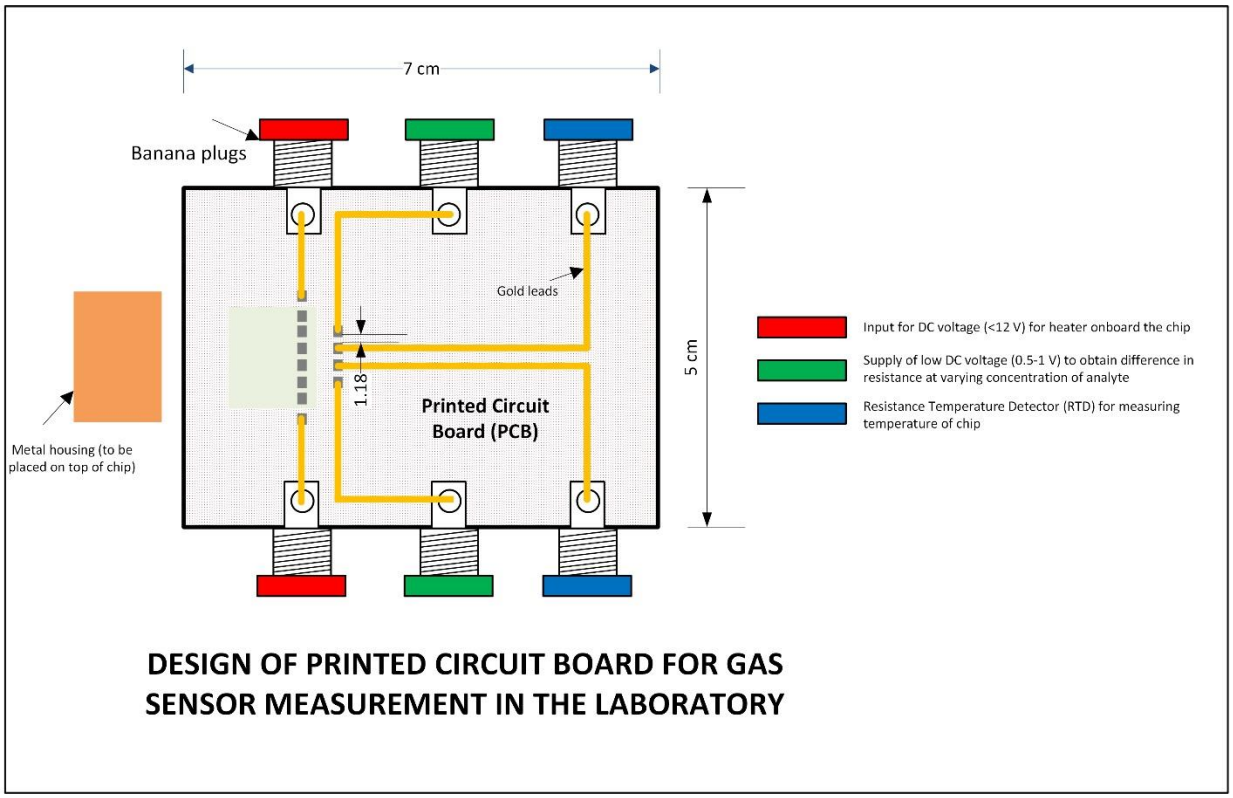

In-situ characterization of nanoparticles is essential in the RSDT for quick control of the nanomaterial properties and to maintain a state of the art quality control in the manufacturing of thin films. RSDT II is almost ready to be commissioned in the Maric group and following diagnostics and testing will be feasible:

1. Decreasing the deposition time by 30X by using multiple precursor flow capillary tubes.

2. 2D or 3D thermal profile of an oxy-THF-propane or flame (flame length ~15 cm and width 3-4 cm).

3. Velocity distribution and liquid droplet size exiting the atomizing portion of the nozzle prior to ignition.

4. Velocity distribution of ionized and non-ionized gases in the combustion zone up to the substrate.

5. Spatially resolved concentration map of pertinent active species in the flame.

SECTION VI:

APPENDICES

APPENDIX A:

SCHOLARLY ACTIVITIES

PEER REVIEWED PUBLICATIONS:

R. Jain, Y. Lei, R. Maric, Ultra-low NO_2 detection by gamma WO_3 synthesized by Reactive Spray Deposition Technology, (submitted to Sensors and Actuators B: Chemical on October 28th, 2015).

R. Jain, A. S Poyraz, D. P Gamliel, J. Valla, S. L. Suib, R. Maric, Comparative study for low temperature water-gas shift reaction on Pt/ceria catalysts: Role of different ceria supports, Applied Catalysis A: General. 507 (2015) 1-13.

R. Jain, R. Maric, Synthesis of nano-Pt onto ceria support as catalyst for water-gas shift reaction by Reactive Spray Deposition Technology, Applied Catalysis A: General. 475 (2014) 461-468.

R. Jain, Y. Wang, R. Maric, Tuning of WO_3 Phase Transformation and Structural Modification by Reactive Spray Deposition Technology, Journal of Nanotechnology and Smart Materials. 1 (2014) 1-7.

H. F. Garces, J. M. Roller, C. K. King'ondu, S. Dharmarathna, R. A. Ristau, R. Jain, R. Maric and S. L. Suib, Formation of Platinum (Pt) Nanocluster Coatings on K-OMS-2 Manganese Oxide Membranes by Reactive Spray Deposition Technique (RSDT) for Extended Stability during CO Oxidation, Advances in Chemical Engineering and Science, 01/2014; 4:23-35.

J. M. Roller, M. Josefina Arellano-Jiménez, R. Jain, H. Yu, C. Barry Carter, and R. Maric, Catalyst nanoscale assembly from the vapor phase on corrosion resistant supports, Electrochima Acta. 107, 632-655 (2013).

J.M. Roller, M. J. Arellano-Jiménez, R. Jain, H. Yu, C. B. Carter, R. Maric, Oxygen evolution during water electrolysis from thin films using bimetallic oxides of Ir-Pt and Ir-Ru, Journal of Electrochemical Society. 160 (6), F716-F730 (2013).

J. M. Roller, J. Arellano-Jiménez, R. Jain, H. Yu, R. Maric, C. B. Carter, Processing, Activity and Microstructure of Oxygen Evolution Anodes Prepared by a Dry and Direct Deposition Technique, ECS Transactions. 45(21), 97-106 (2013).

PATENT:

R. Jain, and R. Maric, Metal oxide based sensors for sensing low concentration of specific gases prepared by a flame based process. (In preparation)

PRESENTATIONS AT CONFERENCES AND SEMINARS:

R. Jain, V. Manthina, R. Maric, Antifogging Mirror by TiO_2 and Si Doped TiO_2 Thin Films Synthesized by Reactive Spray Deposition Technology, 2015 Materials Research Society (MRS) spring meeting and exhibit, San Francisco, CA. Symposium: UU: Titanium Oxides—From Fundamental Understanding to Applications. (Talk) Paper# UU4.04. Apr 6-10 (2015)

R. Jain, J.M Roller, R. Maric, The Control of particle size, adhesiveness, phase and structure of WO_3 film in the vapor phase by Reactive Spray Deposition Technology, 2014 Materials Research Society (MRS) fall meeting and exhibit, Boston, MA. Symposium: HH: Flame and High-Temperature Synthesis of Functional Nanomaterials — Fundamentals and Applications. (Talk) Paper#HH3.05. Dec 1-5 (2014)

R. Jain, Y. Liu, Y. Wang, Y. Lei, R. Maric, Synthesis of γ-WO_3 by Reactive Spray Deposition Technology for NO_x Sensing, 225th Electrochemical Society (ECS) meeting, Orlando, FL. Symposium: B1: Sensors, Actuators, and Microsystems General Session (Chemical and Biological Sensors). (Talk) Paper #441. May 11-16 (2014)

R. Jain, Y. Liu, Y. Wang, Y. Lei, R. Maric, Synthesis of WO_3 nanoparticles by Reactive Spray Deposition Technology for NO_2 sensing, Connecticut Microelectronics and Optoelectronics Consortium (CMOC), Storrs, CT. (Talk) Session V: Clean Energy /Storage/ Emerging Technologies. April 9 (2014).

R. Jain, A. Poyraz, S. L. Suib, R. Maric, Processing-structure-property relationship of different ceria supports for ceria/Pt catalysts for water-gas shift reaction, 2014 spring symposium of the Catalysis Society of Metropolitan New York, Lehigh University, Bethlehem, PA. Poster. March 12 (2014).

R. Jain, A. Poyraz, S. L. Suib, R. Maric, Processing-structure-property relationship of different ceria supports for ceria/Pt catalysts for water-gas shift reaction, 2013 Materials Research Society (MRS) fall meeting and exhibit, Boston, MA. Symposium AA: Catalytic Nanomaterials for Energy and Environment. Poster# AA6.05. December 1-6 (2013).

R. Jain, M. Janish, P. Kotula, C. B. Carter and R. Maric, TEM Characterization of Ceria Supported Pt Catalyst for Water-Gas Shift Reaction produced by Reactive Spray Deposition Technology, Microscopy and Microanalysis (M&M) 2013, Indianapolis, IN. Symposium P04.P1 Deriving Fundamental Catalyst Properties from Electron Microscopy. Poster# 198. August 4-8 (2013).

APPENDIX B:

COPYRIGHT PERMISSIONS

Chapter 5 of this thesis was obtained from the following article: R. Jain, R. Maric, Synthesis of Pt nanoparticles onto ceria support as catalyst for water-gas shift reaction by Reactive Spray Deposition Technology, Applied Catalysis A: General. 475 (2014) 461-468. The article was modified to match the style of this thesis. Permission to reuse was obtained from Elsevier provided by the Copyright Clearance Center. License number 3672710597663.

Chapter 6 of this thesis was obtained from the following article: R. Jain, A. S Poyraz, D. P Gamliel, J. Valla, S. L. Suib, R. Maric, Comparative study for low temperature water-gas shift reaction on Pt/ceria catalysts: Role of different ceria supports, Applied Catalysis A: General. 507 (2015) 1-13. The article was modified to match the style of this thesis. Permission to reuse was obtained from Elsevier provided by the Copyright Clearance Center. License number 3746640430648.

Chapter 7 of this thesis was obtained from the following article: R. Jain, Y. Wang, R. Maric, Tuning of WO_3 Phase Transformation and Structural Modification by Reactive Spray Deposition Technology, Journal of Nanotechnology and Smart Materials. 1 (2014) 1-7. The article was modified to match the style of this thesis. The article is open access and the author of this thesis owns the full copyright.

AUTHOR BIOGRAPHY

Rishabh Jain was born July 13th 1985 in Calcutta, India. He received his Bachelor of Technology (B.Tech) degree in Chemical Engineering from Haldia Institute of Technology (H.I.T) in 2007 and the Masters of Science (M.S.) in Chemical Engineering from University of Southern California

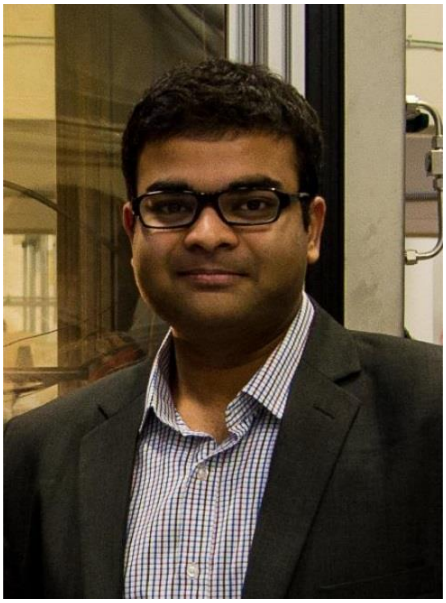

(USC) in 2009. Rishabh joined the Ph.D. program in Materials Science and Engineering (MSE) at the University of Connecticut (UConn) in August 2011 and worked at the Center for Clean Energy Engineering (C2E2) at the UConn's depot campus as a graduate research assistant (GA) under the guidance of Prof. Radenka Maric. His research is focused on the flame combustion synthesis, electron microscopy and microstructural characterization of nanomaterials for catalysts and sensors. He served as a teaching assistant (TA) in the MSE department for MSE 3001: Applied Thermodynamics of Materials (Aug–Dec 11) under Prof. Harold Brody and MSE 5309: Transport Phenomena in Materials Science and Engineering (Jan–May 12) under Prof. Radenka Maric. At UConn, Rishabh is the recipient of many awards including, fall 2011 pre-doctoral fellowship, fall 2014 doctoral dissertation fellowship, the 2015 General Electric fellowship for innovation, the 2015 Phi Kappa Phi graduate student award, and the honorary membership for Alpha Sigma Mu (ASM) society (University of Connecticut chapter). In addition to this he also received numerous travel grants for attending scientific conferences. At UConn Rishabh was actively involved in the outreach events because of his keen passion for interacting with young students to motivate them towards science and engineering. At the Center for Clean Energy Engineering, he has done more

than 15 presentations to students ranging from 5th grade till high school, explaining them about fuel cells and alternative fuel.

Prior to joining UConn, Rishabh decided to get some work experience as a Process Engineer at I Cube Nanotec India Pvt. Ltd (ICNI) at Noida where he worked from June 09-June 11. In his free time, he enjoys nature photography and hiking the mountains at New Hampshire, Maine and upstate New York.

Rishabh can be reached at rishabh.rjain@gmail.com.